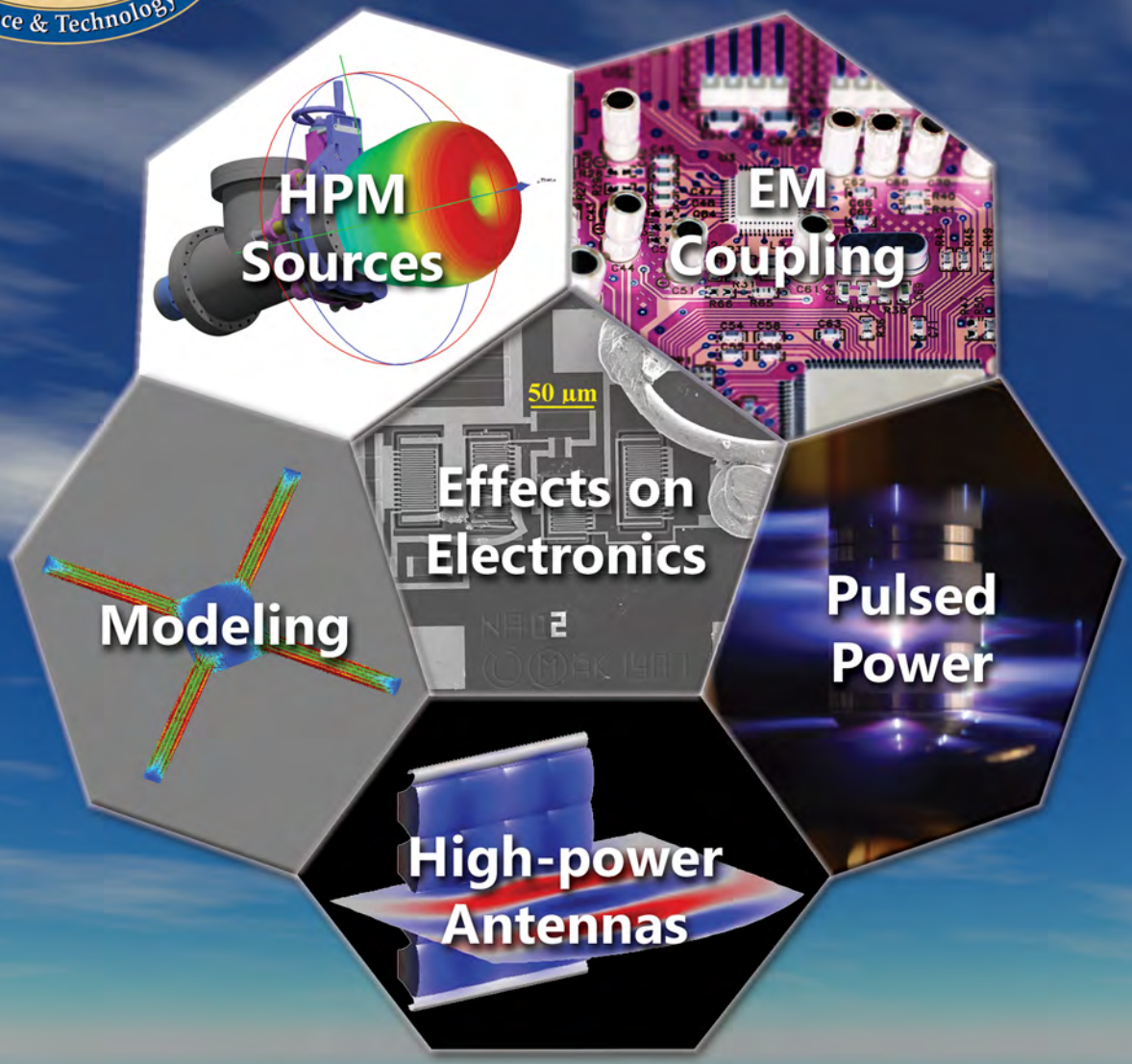


DIRECTED ENERGY WEAPONS (DEW)
HIGH POWER MICROWAVE (HPM)
6.1 PROGRAMS
FY22 ANNUAL REPORT

Mr. Ryan Hoffman, Program Manager

DISTRIBUTION STATEMENT A. Approved for public release; distribution is unlimited.
DCN#: 0543-1375-23

NAVAL SCIENCE & TECHNOLOGY

Directed Energy Weapons (DEW) High Power Microwave (HPM) Program
Annual Report for FY22

Table of Contents

Title	Pages
Introduction to ONR's HPM Program by Program Officer Ryan Hoffman, Office of Naval Research	3-4
ONR Grant Reports	
Improving Performance of Crossed-Field Amplifiers Through Modulation Injection (Dr. Allen Garner)	6-15
Distributed Coordination of Aerial Swarms for High-Gain Wireless Transmission (Dr. Jeffrey Nanzer)	16-28
Ultra-High-Efficiency Relativistic Magnetron and Improved MILO Capabilities (Dr. Edl Schamiloglu)	29-41
Pulsed Dielectric Breakdown of Solid Dielectric Insulation Materials (Dr. David Wetz)	42-51
ONR Industry Contract Reports	
Scaleup of Materials for Optimizing High Power RF Systems	53-65
ONR Young Investigator Program (YIP) Reports	
Surface Breakdown and Plasma Formation in Cross-Field High Power Microwave Sources (Dr. Ken Hara)	67-77
Direct Generation of Electromagnetic Radiation with a Compact, Air-Stable, Optically Modulated Electron Emitter (Dr. Rehan Kapadia)	78-89
Multi-frequency High Power Microwave Generation and Amplification via Optically Gated Electron Beams, MSU (Dr. Peng Zhang)	90-104
Infrared Optics with Engineered Materials (Dr. Mikhail Kats)	105-115
ONR Global Grant Reports	
Homoepitaxial Ga2O3 Structures for Power Device Applications, Japan (Dr. Akito Kuramata)	117-142
Compact High-power Microwave Oscillators, University of Strathclyde, UK (Dr. Alan Phelps)	143-152
Geodesic Luneburg Lenses for High Power Applications, KTH, Sweden (Dr. Oscar Quevedo-Teruel)	153-161
New Ideas for Advanced Relativistic Magnetrons, Technion, Israel (Dr. Yakov Krasik)	162-173

Directed Energy Weapons (DEW) High Power Microwave (HPM) Program
Annual Report for FY22

Table of Contents

Title	Pages
ONR FY22 Grant Summaries	
Novel High-Power Microwave System Designs Using Nonlinear Transmission Lines (Dr. Allen Garner)	175
Theory and Experiments on Magnetically Insulated Line Oscillator (MILO) (Dr. Ronald Gilgenbach)	175
A High Repetition Rate, Long Lifetime Magnetically Insulated Line Oscillator (MILO) (Dr.John Mankowski)	176
New Anode Materials for High Lethality HPM Sources (Dr. Ravi Joshi)	177
An Accessible platform for simultaneous Macro, Meso and Microscopic Measurements of Polymeric Materials at High Loading Rates and Temperatures (Dr. Sal Portillo)	177-178
ONR FY22 Industry Grant Summary	
Implementation of Tunable Dielectric and Multiferroic Materials For High Power Microwave Applications, Powerhouse Consulting (Dr. Somnath Sengupta)	179
ONR FY22 Industry Contract Summaries	
Active/Passive Limiters for High Power Radio Frequency (HPRF), Verus Research (Dr. Sameer Hemmady)	180
Leveraging Predictive Effects for Devising Collaborative HPRF/Cyber Engagement Paradigms, Verus Research (Dr. Sameer Hemmady)	180
SBIRs/STTRs Summaries	
Miniaturization of High Average Power, High Peak Power, Wide Bandwidth Antennas and DSRDs, ASR Corporation (Dr. Michael Abdalla)	182
Solid-state, Sub-nanosecond Pulse Sharpener for Generating High Power Impulses, Transient Plasma Systems Inc. (Dr. Jason Sanders)	183
Improved Marx Pulse Generator for HPM Systems Scientific Applications & Research Assoc., Inc. (SARA) (Dr**.** Sam Dickerson)	183
Drift Step Recovery Diode (DSRD) for Wideband (WB) and Ultra-Wideband (UWB) Pulse Generation, GeneSiC Semiconductor Inc. (Dr. Ranbir Singh)	184
Next-Gen Solid-State Power Module for High Power Microwave Drivers, Scientific Applications & Research Assoc., Inc. (SARA) (Dr**.** Landon Collier)	184
Navy-Electronic Battle Damage Indicator (eBDI) Tool for Non-Kinetic High-Power Radio-Frequency (RF) Engagements, Voss Scientific (Dr. Donald Voss)	185

Introduction

Ryan Hoffman
Program Officer, Office of Naval Research

The Directed Energy Weapons (DEW) Program of the Office of Naval Research (ONR) was initiated in response to the rapid development and growing threat of directed energy technologies by adversaries. Directed energy weapons are defined as electromagnetic systems capable of converting chemical or electrical energy to radiated energy and focusing it on a target, resulting in physical damage that degrades, neutralizes, defeats, or destroys an adversarial capability. The U.S. Navy uses HPM to gain and sustain tactical, operational, and strategic advantage in the arena of EM Maneuver Warfare and Integrated Defense for U.S. forces across the full range of military operations, including power projection and integrated defense missions. The ability to focus radiated energy reliably and repeatedly at range, with precision and controllable effects, while producing measured physical damage, is the measure of DEW system effectiveness. In anticipation of DEW advancements, the ONR HPM Program comprises a portfolio of initiatives and research projects which seek to provide the science and engineering basis for means and methodologies to provide the Navy advanced HPM technologies, systems, and techniques enabling a new class of weapons that will be highly effective in the battlespace. The goal is to be the most effective steward of DEW systems.

Asymmetric threats are proliferating worldwide and likely will continue to do so until such time as effective countermeasures are deployed. Often enough, Rules of Engagement will restrict kinetic engagement with asymmetric threats contingent on the particulars of the scenario. DEW systems – or more specifically for this report, HPM weapons – are expected to allow Naval commanders significantly more flexible responses to a number of asymmetric threats, including various small surface craft and unmanned aerial vehicle (UAV) threats. This flexibility is possible since the restrictions on engaging targets might be removed or reduced based on recognition of 1) the low collateral damage and 2) the non-lethal and reversible effects associated with HPM weapons.

HPM weapons create pulses of electromagnetic energy over a broad spectrum of known radio and microwave frequencies, causing either temporary or permanent results on electronics within targeted systems at scalable effects. HPM weapon systems can be used to disrupt, disable, or potentially destroy critical electronic circuitry in target systems, even in restricted scenarios, while also having the advantage of low cost per shot. HPM weapons deliver electromagnetic energy through coupling of the electromagnetic wave to target circuits through aperture or cable points of entry, thereby inducing currents in the circuitry capable of causing a variety of effects. Potential effects include erroneous signals, system lock-up, shutdown, loss of communications between systems, and physical damage.

As DEW falls within the Fundamental Research part of the broad ONR Science & Technology (S&T) investment portfolio, projects funded are long-term initiatives, covering basic research or applied science. These investigations can have a five to twenty year horizon. Across the HPM technology thrust areas, research projects within the program include performers from academia, industry, government laboratories, and small businesses. Moreover, the program includes performers whose research is financed through Navy SBIR/STTR funding. In addition, S&T solutions from an international technical community are afforded through ONR Global, which funds projects that foster cooperation in areas of mutual interest with global partners. The program encourages the cross-pollination of ideas and collaboration among performers worldwide, and offers an annual review where performers provide updates on the status of their research

and present results to their DEW peers. Furthermore, data and facilities sharing are encouraged within the program. This approach contributes to increased success for the program and for the Navy.

Focus areas cover HPM sub-systems that optimize power and/or energy density at the electronic target for a variety of platform sizes and capabilities while minimizing size, weight, power and cost. Examples of related areas for S&T investment and research include supporting technologies such as power electronics, pulsed power drivers, power modulators, as well as frequency agile RF sources and antennas.

Additional research focus areas include research into electronic system coupling, interaction, and effects with the first goal of enabling development of predictive effects tools for current systems. A second goal of this work includes an exploration of in band and out of band coupling and interaction mechanisms. This exploration will exploit developing advances in frequency and bandwidth agility both to identify new potential weapon system possibilities as well as to achieve significant improvements in size, weight, power, and cost in new variants of existing systems.

Research Challenges and Opportunities

- RF coupling and modeling tools to capture complex EM wave interactions with electronics and associated enclosures, RF component disruption, along with novel techniques for experimental validation. Prediction of effects on electronics with improved techniques for HPM lethality testing and analysis. Analysis of HPM coupling mechanisms, electronic device interaction physics, and component level effects validated through experiment. Development of tools and techniques for more efficient identification and utilization of novel RF waveforms.
- Pulsed power/power electronics; including high energy density capacitors, power conditioning, high voltage switches, dielectric insulators, 3D printed/novel materials and power modulator pulse forming networks that enable higher duty cycle operation
- Solid state and vacuum electronic based HPM sources that provide frequency and waveform parameter tunability and are reconfigurable to adapt to changing requirements; computer codes for modelling HPM physics to enable the next generation of devices
- Wide bandwidth high power amplifiers that provide the ability of very rapid waveform adjustment.
- High power, low profile, or conformal antenna designs and capable radome materials, novel array concepts, high power beam steering techniques and distributed beam forming approaches.
- Novel HPM sensors, instrumentation and algorithms are of interest for measurement of waveforms and diagnosing system performance as well as applied to Electronic battle damage indication (eBDI).

ONR Grant Reports

Improving Performance of Crossed-Field Amplifiers Through Modulation Injection

Grant No. N00014-21-1-2024

Annual Report for Fiscal year 2022

Period of Performance: October 1, 2021 to September 30, 2022

Prepared by:

Dr. Allen L. Garner, Principal Investigator
Associate Professor and Undergraduate Program Chair, School of Nuclear Engineering
Purdue University
363 N. Grant St.
West Lafayette, IN 47907
Email: algarner@purdue.edu

This work was sponsored by the Office of Naval Research (ONR), under grant number N00014-21-1-2024. The views and conclusions contained herein are those of the authors only and should not be interpreted as representing those of ONR, the U.S. Navy or the U.S. Government.

Grant or Contract Number: N00014-21-1-2024
Date Prepared: 29 January 2023
Project Title: Improving Performance of Crossed-Field Amplifiers Through Modulation Injection
Annual Summary Report: FY22
Principal Investigator: Allen L. Garner, algarner@purdue.edu Purdue University

Section I: Project Summary

1. Overview of Project

Abstract: Crossed-field devices, such as crossed-field amplifiers (CFAs), offer high efficiency, high power density, and robust performance. Improved CFA gain-bandwidth product and reduced noise would contribute to greater use and operational capabilities. This report highlights our progress toward benchmarking the particle-in-cell (PIC) codes ICEPIC and VSim to assess a commercial CFA, our completion of theoretically linking field emission and thermionic emission with space-charge limited current in a crossed-field diode to assess behavior, and our progress toward using two-dimensional PIC to understand the fundamental difference in transitions between cycloidal and Brillouin flow in one- and two-dimensional crossed-field diodes.

Objective: This effort will study the effects of electron modulation on a high power (1 MW) L-Band CFA using theory (Purdue University) and simulation using the particle-in-cell codes ICEPIC (Confluent Sciences) and V-Sim (Boise State University and Tech-X). The first task entails developing and validating a CFA model using thermionic emission models. This result will next be combined with secondary emission models and theories and validated. This will subsequently permit the examination of the causes of drive saturation and gain-bandwidth limitations. This combined theory and simulation will then be used to characterize the effects of electron modulation with and without secondary emission on gain, bandwidth, saturation, and noise on CFA efficiency, pulse width, output power, bandwidth, and frequency timing. Finally, an assessment on the impact of noise in the CFA will be performed by examining how particle orbits are impacted based on the thermionic and secondary emission models and the impact of space-charge on the electromagnetic properties of the device. This will involve including sensitivity analysis into the theoretical studies of single electron orbits, including second emitter into the theory and studying the interaction between electrons emitted from each source, and using simulation to examine electromagnetic mechanism in more detail.

The electromagnetic spectrum is becoming both congested and contested, requiring greater flexibility in electromagnetic sources. As platforms become much more loaded with electronics and technology, the compactness, efficiency, capability, and controllability of individual electromagnetic sources must increase. Therefore, this proposal strives to both maintain the high amplitude operation associated with DE technology and determine ways in which DE devices can provide information rich signals with choices in center band frequency, high bandwidth frequency modulation, and exquisite phase control. Traditional crossed-field DE devices, such as magnetrons, operate at high amplitude, but with only modest bandwidth or shot-to-shot frequency control. In contrast, the CFA provides bandwidth and phase control, but with orders-of-magnitude lower power. Thus, the CFA characterization proposed here will determine the limitations in gain-bandwidth product and enhance CFA tunability, which is critical for electromagnetic warfare.

Introduction: Microwave vacuum electron devices (MVEDs) are critical for military infrastructure from radar and communications to electronic warfare, including emerging directed energy applications. While MVEDs are dominant in high frequency and high power regimes, improved device performance is essential to maintain the advantage over solid state devices. In particular, crossed-field devices, such as crossed-field amplifiers (CFAs), offer high efficiency, high power density, and robust performance. Improved CFA gain-

bandwidth product and reduced noise would contribute to greater use and operational capabilities. Currently, there are no high-power CFA models available for public research studies at universities. This gap is especially important as we try to realize the promise of higher power devices represented by directed energy high-power radiofrequency (HPRF) devices. Almost every type of HPRF device is an oscillator. While these sources produce very high-power pulses, the waveform control, typically measured in the bandwidth, is insufficient for radar or communications. This restricts these directed energy (DE) sources to jamming and counter-electronics missions, rather than the more information-intense full-fledged electronic warfare. This effort goes to the heart of the question "what are the limits to high-power amplifiers?"

Background: Crossed-field devices, such as crossed-field amplifiers (CFAs), offer high efficiency, high power density, and robust performance. Improved CFA gain-bandwidth product and reduced noise would contribute to greater use and operational capabilities. Currently, there are no high-power CFA models available for public research studies at universities. This gap is especially important as we try to realize the promise of higher power devices represented by Directed Energy High-Power RF (HPRF) devices. Almost every type of high-power radiofrequency (HPRF) device is an oscillator. While these sources produce very high-power pulses, the waveform control, typically measured in the bandwidth, is insufficient for radar or communications. This restricts these directed energy (DE) sources to jamming and counter-electronics missions, rather than the more information-intense full-fledged electronic warfare. This proposal goes to the heart of the question "what are the limits to high power amplifiers?" The university community currently lacks the well characterized, high power sources with intense space-charge that can mimic a HPRF device to address these questions. This problem becomes more acute for CFAs. CFAs are the highest power amplifiers widely used; however, they suffer from the limits of the gain-bandwidth product. The lack of a publicly available CFA model using first-principles, particle-in-cell simulations to serve as a benchmark for research hinders the examination of potential methods to improve design.

We use a model of the L3 Technologies L4953 CFA (discontinued) that was operated by the Federal Aviation Administration (FAA). Because this model is discontinued and unclassified, L3 Technologies is willing to allow our team to use the design to develop a high-power CFA model. This CFA model would become a benchmark for CFA research in universities, industry, and national laboratories to allow comparing future simulations and modifications to CFAs and other amplifiers. After developing the model, we would then study the effects of electron modulation on gain, bandwidth, and noise. We can study, via simulation, the saturation effects that occur in CFAs and determine whether techniques such as current modulation can improve the gain-bandwidth performance including performance at higher input powers. This would include studying the cause of saturation and techniques to maintain/increase gain-bandwidth product for HPRF production. Table 1 summarizes our team's overall research concept. We propose using VSim and ICEPIC and theoretical analysis to (1) develop and validate CFA models using emission-based cathodes, (2) extend the validated model using a combined thermionic emission and simple secondary emission model to approximate the secondary emitting component, (3) apply simulation and theory to analyze the saturation of gain-bandwidth in high power CFAs, (4) study the effects of a modulated cathode and electron back-bombardment on the gain-bandwidth product, and (5) analyze the effects of electron modulation and electron back-bombardment on noise generation and noise reduction with simulation and theory.

From this effort, studying the back-bombardment of field emission cathodes and out of band noise suppression will enhance the effectiveness of radar/communications/electronic warfare by removing spurious signals that degrade source performance for a given application and providing a signature to adversarial platforms. By providing high power, multi-frequency operation, this study could reduce SWAP-C (size, weight, power and cost) of the system.

2. Activities and Accomplishments

Last year, we reported the initial establishment of the CFA geometry in VSim and the application of the built-in Child-Langmuir emission model (CLEM) to emit from the cathode at the space-charge limit. This year, we (Boise State University) extended the VSim model by using a "virtual" current source with feedback for the DC voltage, which previously depended strongly on device operating conditions and required unique calibration factors for each initial condition. We also corrected an issue in the DC port feedback implementation in VSim 11 that did not account for Dey-Mittra cut-cells by slightly altering DC port dimensions to align perfectly with the grid, making the DC electric fields agree with the analytic solution for concentric cylinders and invariant with cell size. An instability due to an interaction between the CLEM and Dey-Mittra was mitigated by increasing the distance from the cathode where electrons were born so that they were less affected by the instability.

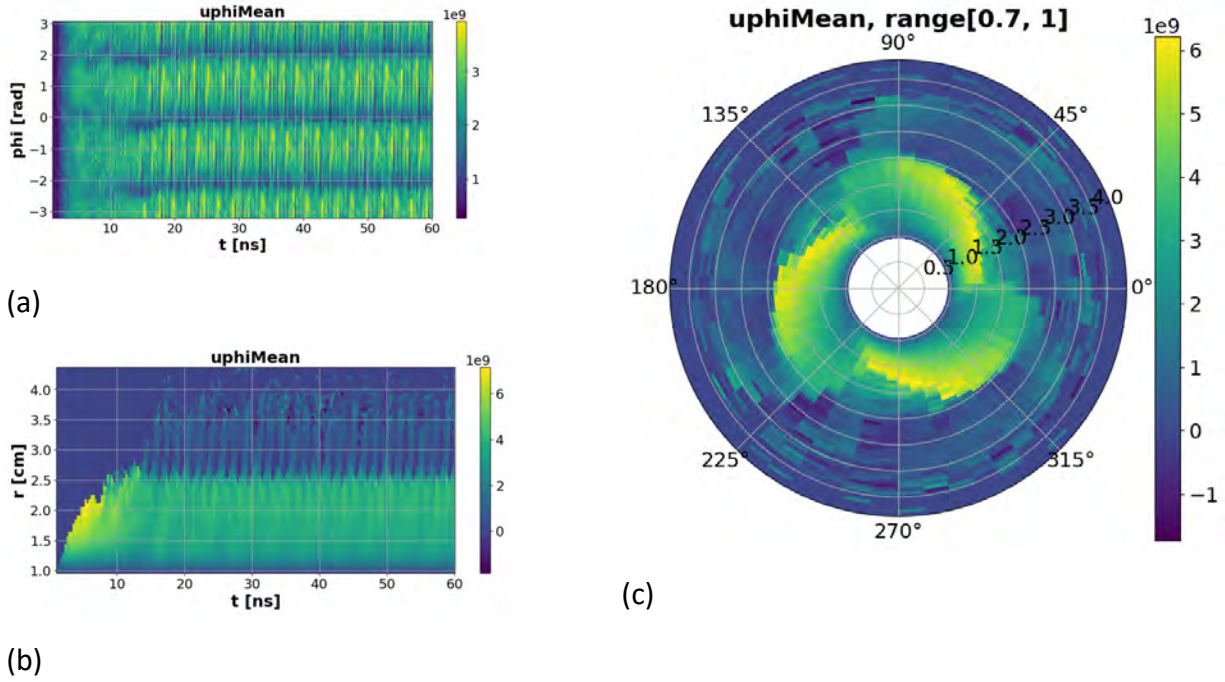


Fig. 1. Angular velocity in a rotating frame of reference for (a) angle vs. time, (b) radius vs. time, and (c) angle vs. radius

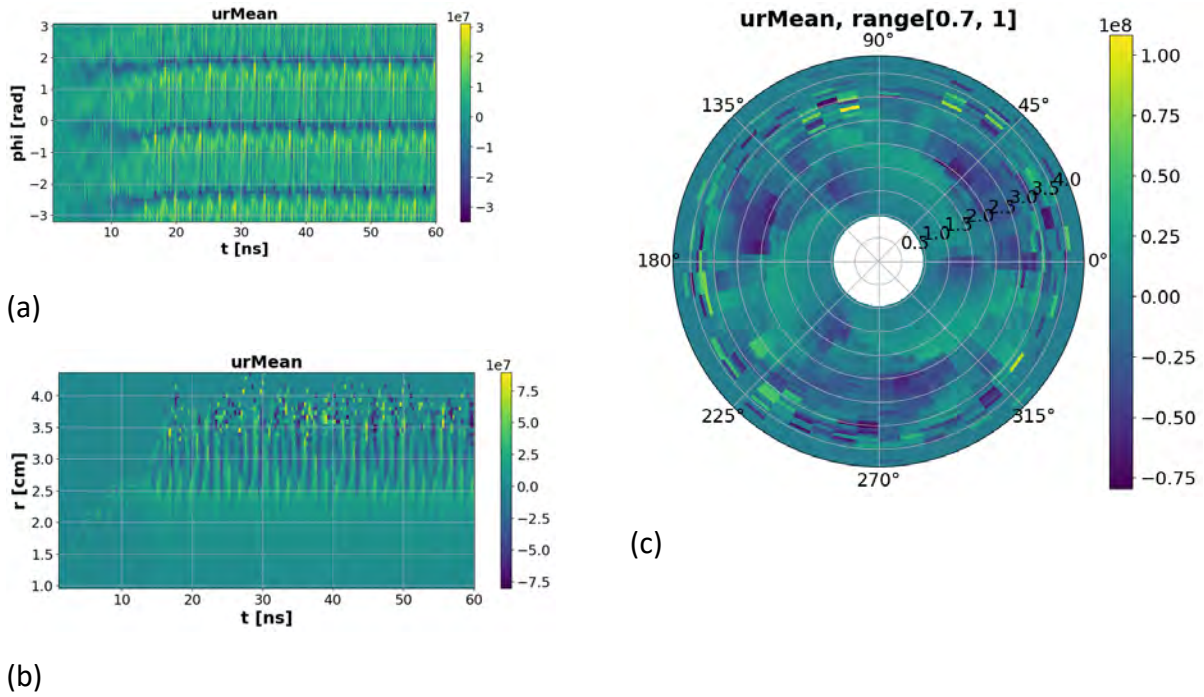


Fig. 2: Radial velocity in a rotating frame of reference for (a) angle vs. time, (b) radius vs. time, and (c) angle vs. radius

These corrections, as well as the development of new diagnostics, allowed us to study the electron population statistics and emission characteristics. **Fig. 1**-2 show a full simulation with $B = 0.137$ T and $V = 91$ kV. These plots are in a frame of reference that rotates with the electron spokes to allow a stationary view of the spoke for analysis. The spokes rotate in the counterclockwise direction. Electrons move up the back side of the spoke and move down the leading side.

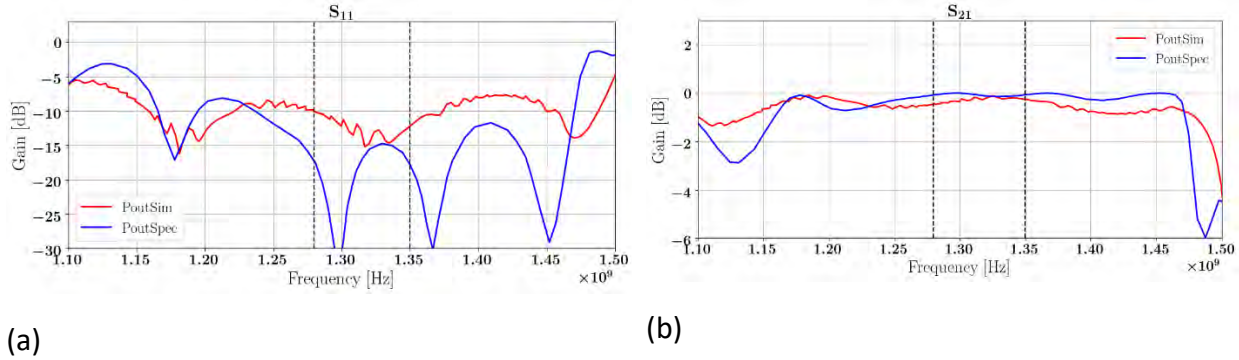


Fig. 3. (a) S_{11} and (b) S_{22} for a frequency sweep

Figure 3 shows S_{11} and S_{21} for frequencies between 1.1 and 1.5 GHz for both the device and simulation. The device and simulated transmission (S_{21}) are both low from 1.1-1.45 GHz with a cutoff region (full reflection) between 1.45 and 1.50 GHz. The cutoff region for the device and simulation occurs at 1.47 GHz and 1.49 GHz, respectively. This 0.02 GHz shift in the cutoff frequency is 28% of the specified bandwidth of the device, so this shift is notable. The simulated S11 plots do not show the large dips in gain observed

in the device data, but the reflected power remains below -10 dB throughout the operation region. Overall, S_{11} and S_{21} match relatively well between simulation and experiment; however, there seems to be a 0.02 GHz shift in bandwidth, which may explain the outlier observed at 1.28 GHz in the device tuning data shown later. These results were presented at the 2022 IEEE International Conference on Plasma Science (ICOPS) and submitted to the *IEEE Transactions on Electron Devices* for publication.

Confluent Sciences identified and eliminated the remaining difference between ICEPIC and VSim predictions of device performance, making significant progress toward creating an ICEPIC version of the L-4953 that matched VSim results. In the process, Confluent improved the methods to directly compare geometric features, developed a tool for extracting an annular subset of planar simulation data (which is immediately applicable for other high-power microwave device development and analysis), and provided other team members with data on space-charge-limited emission in the presence of an applied axial magnetic field that can be used to theoretically describe the process.

In the preceding annual reporting period, we had built the ICEPIC L-4953 geometry up to a point where we purposefully omitted several debatably unimportant details. An important instance of that involved the anode vane tips. However, the true anode vane tip geometry used by BSU was more involved. We revised the ICEPIC model of the anode vane tips to conform to the VSim version and compared the two geometries using a "cold static sweep," which does not allow electron emission. Figures 4 and 5 show the average power passing into the device through the input port in the cold static sweep series before and after, respectively, the anode vane tips geometry correction. The results show that entire response curve downshifts in frequency by about 200 MHz. The downshift is reasonable on the basis that the anode vane tip geometry correction creates a longer path length along the cross-section of the geometry.

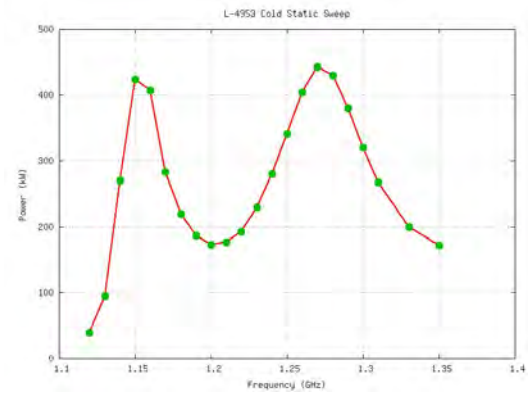


Fig. 4. Cold static sweep from ICEPIC using the original simplified anode vane tip geometry.

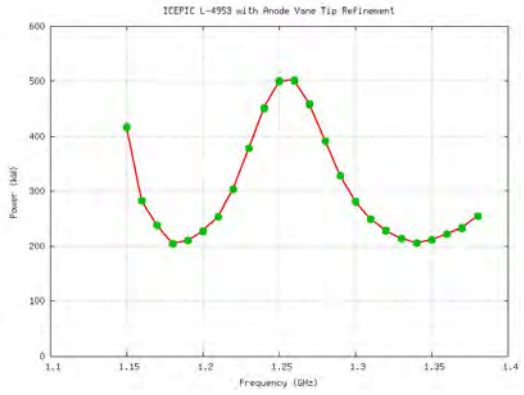


Fig. 5. Cold static sweep using anode vane tips with cross-section conformed to that used in VSim.

Further modifying ICEPIC to account for both the connector geometry and the straps to the outer housing resulted in agreement with measurements of the L-3 (Stellant) L-4953 CFA. As a an example, Figure 6 shows the S_{11} calculated using ICEPIC and Figure 7 shows laboratory measurements of the L-4953 CFA. The comparison shows considerable qualitative agreement between ICEPIC results and laboratory measurements. The dips in the laboratory S_{11} measurement at 118 and 1.30 GHz occur at 1.22 and 1.37 GHz in the latest ICEPIC calculations, but the broad, relatively flat spot where the operating region resides agrees well between calculation and measurement. The S_{12} calculation (not shown) also agrees well with the laboratory measurement.

Purdue University completed the development of a theory unifying thermionic, field, and space-charge limited emission in a crossed-field diode, publishing this work as an invited paper in the *IEEE Transactions on Plasma Science*. This work was also part of an invited talk at the 2022 IEEE International Power Modulator and High Voltage Conference (IPMHVC). As discussed last year, this paper developed first-principles based equations linking electron motion with the general thermo-field emission theory to determine the transitions between thermionic, field emission, and SCLC for a crossed-field diode under appropriate limits. The major results were presented in the FY-2021 report and are not repeated here.

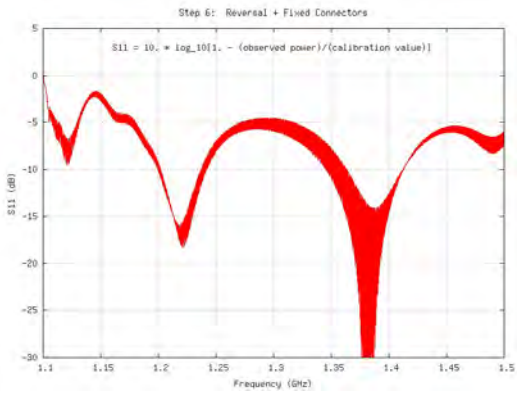


Fig. 6. S_{11} from ICEPIC calculations including the rebuilt/corrected strap/port connector.

Most of FY-2022 focused on examining the difference in electron trajectories in 1-D and 2-D. In 1-D, the limited current in a crossed-field diode is characterized by the transition from a cycloidal orbit to Brillouin flow superimposed upon a turbulent background. Using the 2-D PIC code OOPIC, we have noted that a true Brillouin state does not exist in 2-D – a cycloidal component always exists, unlike 1-D.

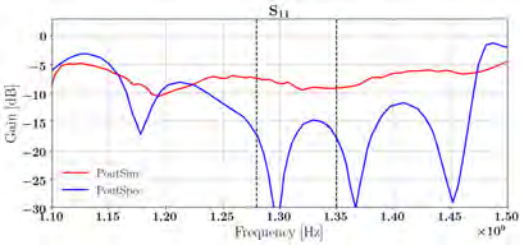


Fig. 7. L-3 laboratory measurement of L-4953 S_{11} (blue curve).

We developed a metric based on the particle distribution with respect to velocity across the diode gap and quantified the level of Brillouin flow by the number of particles with zero velocity across the gap (v_x). Raising the injection current increase the number of particles with v_x=0, indicating more Brillouin flow. Current work is assessing the meaning of the electron velocity v_y in the direction along the electrodes. For low current densities, $v_y$increases in magnitude with position x across the gap, as expected for both cycloidal and Brillouin flow. Raising the current density shifts the particles closer to the anode and causes more spread in the distribution of v_y, rather than all the particles being located linearly when plotting $v_y(x)$. Increasing the current density causes the virtual cathode to form earlier, which causes the electrons the electrons to remain closer to the cathode and reduces the variation in v_y.

Figure 8 shows C_B and C_T, which represent the deviation from $v_x = 0$ and $v_y = -\Omega x$ (where Ω is the cyclotron frequency) to represent the contribution of Brillouin flow and noise, respectively, for $W = 0.5D$, D, $2D$, $4D$, $8D$ without and with periodic boundary conditions (PBCs), and 1D models from XPDP1. A smaller C_B and a larger C_T represent more Brillouin contribution and more noise, respectively. The longer emission width, the higher the C_B for the same injection current density. For a longer emission width, C_T peaks and decreases with lower injection current density. The variations and their physical meanings of the two quantities match with the trajectories ($x - y$ phases) and velocity profiles (v_x vs. x and v_y vs. x) in raw XOOPIC data. Note that the two quantities exhibit sudden changes around J_c that marks the transition from a stable cycloidal flow to the near-Brillouin flow in 1D. For $J > J_c = 2.1 \times 10^5$ A/m^2 in XPDP1, $\overline{\left(v_x(x_q)\right)^2} \to 0$ and $\overline{\left(\Delta v_y(x_q)\right)^2} \to 0$ indicate good agreement between the numerical velocity profiles and analytical Brillouin velocity profiles, which can be observed in the raw data. However, the decrease in C_T as J_{in} increases in both 1D and 2D models may require further explanation.

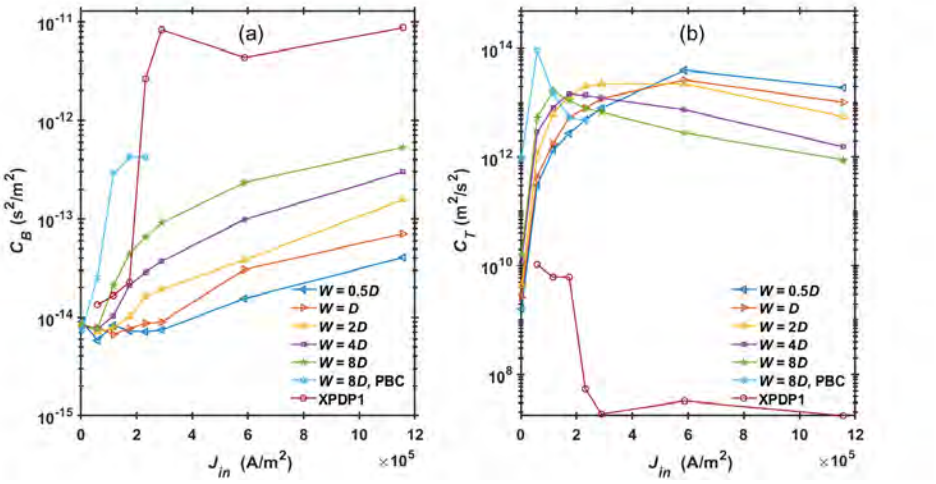


Fig. 8. (a) C_B and (b) C_T for $W = 0.5D$, D, $2D$, $4D$, $8D$ without and with periodic boundary conditions (PBCs), and 1D models from XPDP1.

3. Findings and Conclusions

We have successfully completed benchmarking ICEPIC and VSim to each other and to Stellant's L-4953 crossed-field amplifier. We have also identified dispersion and eigenmodes demonstrated device oscillations and implemented a temporally modulated emission source to improve efficiency in VSim, although the gain was limited by the space-charge limit. BSU and Tech-X worked significantly to improve VSim by resolving computational issues and updating the code. Purdue completed the development of theoretically unifying thermionic and field emission with SCLC in a crossed-field diode to guide device designs and one transitions from a thermionic to cold cathode. Ongoing work using a 2-D PIC simulation has demonstrated that strong emission currents do not lead to the collapse of cycloidal flow to a Brillouin state, as in 1-D. Instead, a combination of these flows exists, for which we have developed metrics for quantification. Ongoing work is finalizing these metrics with the goal of extending to multiple beams to assess the implications on flow and noise.

4. Plans and Upcoming Events

Boise State (BSU) will study the gain limit caused by mode interface by first sweeping both the DC potential (V) and magnetic field (B) to map the VB-space with regards to power, stability and the oscillatory modes excited in unstable regions, similar to the mode maps often used with gyrotrons. This process may elucidate the power saturation mechanisms; at a minimum, it will properly characterize the device under "normal" operation for comparison with future attempts at improving device performance. New modulated emission profiles, guided by the analysis performed previously, will be implemented and studied. These efforts will be coordinated with Confluent's ICEPIC simulations for benchmarking.

Confluent Sciences will continue to compare progressively finer levels of details between ICEPIC predictions and VSim predictions of L-4953 behavior. Confluent will also begin to implement modulation of emission as per the statement of work. Confluent will continue to interface with BSU for comparisons between ICEPIC and VSim as each group progresses in their efforts.

Purdue University will complete the assessment of 2-D electron flow using XOOPIC to characterize the transition from cycloidal to Brillouin flow and the transition to noise. From a first principles perspective, understanding the implications of the 2-D geometry on these conditions and how closely one can approach the idealized 1-D behavior is of fundamental interest. From a device operation perspective, the next step is to characterize the interactions of a second emitted beam with the first beam, particularly concerning the

relative contributions of Brillouin flow and noise and whether the second beam may be valuable for tuning output.

Recommendations for Future Work: Experimental studies with CFAs or other crossed-field devices to benchmark the experiments. This could lead to further modifications of the simulations to test potential new designs, potentially with devices at NRL, NSWCDD, or AFRL. Extension of the simulations to include propagation from an antenna to explore a system level device.

5. Transitions and Impacts

None.

6. Collaborations

John Luginsland, AFOSR, Ongoing discussions with Stellant Systems (formerly L3 Harris now). Indirected related, Purdue is working with Sandia National Laboratories on developing nexus theory for crossed-field physics with collisions, and in discussions with Avalanche Energy concerning crossed-field physics nexus theory for fusion applications.

7. Personnel

Principal investigator: Allen L. Garner, Purdue University, 1 person-month, N
Co-investigator or Co-PI: Jim Browning, Boise State University, 1 person-month, N
Jack Watrous, Confluent Sciences, 5 person-months, N
Business Contact: Michelle Williams, Purdue University, N (not paid from grant)
Team Members: Amanda Loveless (Post-Doc), Purdue University, 1 person-month, N
Marcus Pearlman (Post-Doc), Boise State University, 4 person-months, N
Adam Darr (Graduate student), Purdue University, 1 person-month, N
Nilesh Maker (Graduate student), Boise State University, 6 person-months, N
Xiaojun Zhu (Graduate student), Purdue University, 4 person-months, N
Subs: Christine Roark, Tech-X, 1 person-month, N
David Smithe, Tech-X, 1 person-month, N
Peter Stoltz, Tech-X, 1 person-month, N

8. Students

3 graduate students/0 undergraduate students.

9. Technology Transfer

Working with Sandia National Laboratories on applying crossed-field nexus theory to their efforts on magnetically insulated transmission lines (MITLs).

10. Products, Publications, Patents, License Agreements, etc.

Publications resulting from this project:

Archival Publications (publication reference information (article title, authors, journal, date, volume, issue) can be automatically entered using a DOI)

[INVITED] A. M. Loveless, A. M. Darr, and A. L. Garner, "Theoretical Linkage of Thermionic, Field, and Space-Charge Limited Emission for a Vacuum Crossed-Field Gap," *IEEE Transactions on Plasma Science* **50**, 2609-2620 (2022). {Peer-reviewed, acknowledged funding}

Conference Presentations (non-archived, presenter italicized)

[INVITED] *L. I. Breen*, A. M. Loveless, A. M. Darr, K. L. Cartwright, A. L. Garner, "Crossed-field nexus theory: Incorporating collisions, field emission, thermionic emission, and space-charge," 2022 IEEE International Power Modulator Conference (IPMHVC), Knoxville, TN, Analytical Methods Section, 22 June 2022.

M. Pearlman, J. Watrous, C. Roark, D. Smithe, A. L. Garner, M. Worthington, and J. Browning, "Characterization of Stellant Systems L-4953 crossed-field amplifier via simulation," IEEE International Conference on Plasma Science, Seattle, WA, PO 2.06, PO 2.0 -2.0, 25 May 2022.

X. Zhu, A. M. Darr, J. W. Luginsland, and A. L. Garner, "Stability of electron cycloid in a crossed field gap under the effect of secondary emission," IEEE International Conference on Plasma Science, Seattle, WA, PO 1.09, PO 1.01 -1.0, 25 May 2022.

Submitted Refereed Papers

M. Pearlman, D. Smithe, C. Roark, M. Worthington, J. Watrous, A. L. Garner, and J. Browning, "Simulation of the pulsed 4.7 MW, L-band crossed-field amplifier," Submitted in FY-22 [subsequently accepted to *IEEE Transactions on Electron Devices*, Vol. 69, pp. 7053-7058 (2022). ***DOI:*** *10.1109/TED.2022.3218267* {Peer-reviewed, acknowledged funding}]

11. Point of Contact in Navy

Kevin Jensen, NRL, kevin.jensen@narl.navy.mil, 19JUL2022.

12. Acknowledgement/Disclaimer

This work was sponsored by the Office of Naval Research (ONR), under grant number N-00014-21-1-2024. The views and conclusions contained herein are those of the authors only and should not be interpreted as representing those of ONR, the U.S. Navy or the U.S. Government.

Distributed Coordination of Aerial Swarms for High-Gain Wireless Transmission

Grant No. N00014-20-1-2389

Annual Report for Fiscal year 2022

Period of Performance: October 1, 2021 to September 30, 2022

Prepared by:

Dr. Jeffrey Nanzer, Principal Investigator
Associate Professor, Electrical and Computer Engineering
Michigan State University
428 S Shaw Lane, Room 2120 Engineering
East Lansing, MI 48824
Email: nanzer@msu.edu





This work was sponsored by the Office of Naval Research (ONR), under grant number N00014-20-1-2389. The views and conclusions contained herein are those of the authors only and should not be interpreted as representing those of ONR, the U.S. Navy or the U.S. Government.

Grant or Contract Number: N00014-20-1-2389
Date Prepared: March 19, 2023
Project Title: Distributed Coordination of Aerial Swarms for High-Gain Wireless Transmission
Annual Summary Report: FY22
Principle Investigator: Jeffrey Nanzer, nanzer@msu.edu,
Michigan State University, 428 S Shaw Lane, Room 2120 Engineering, East Lansing, MI 48824

Section I: Project Summary

1. Overview of Project

Abstract: This report provides a summary of progress made towards distributed synchronization of separate wireless systems for distributed beamforming operations. Distributed beamforming requires accurate synchronization of the electrical states of the nodes in a distributed array to ensure that transmitted signals arrive sufficiently aligned at the intended destination so that the signals add constructively, yielding significant increases in signal power at the destination. In this report, we summarize the objectives of this effort and report on advancements made in the areas of decentralized electrical state coordination, distributed localization, and experimental implementations of the concepts developed in this effort.

Objective: In this effort, we will develop novel decentralized coordination techniques for high-gain transmission from swarms of hundreds of nodes and evaluate the possibilities of achieving high-gain signal transmission using existing commercial off-the-shelf (COTS) microwave technologies. In particular, we will investigate new techniques for the coordination of large arrays using decentralized consensus algorithms based on physical-layer coordination of array element location, frequency, phase, and time. We will assess the feasibility of achieving high-power transmission under realistic system-level constraints, such as coordination errors, noise, array motion, amplifier efficiencies, and beamsteering errors, among others. The results of this effort will inform future high-gain microwave transmission concepts and identify any technology areas for future development to achieve greater capabilities than COTS technologies can provide. The proposed research directions are two-fold:

- Develop a distributed approach enabling the coherent coordination of the spatio-electrical states of arrays consisting of hundreds of nodes, investigate the possibilities of using distributed optimization for high-gain microwave signal transmission, and demonstrate distributed signal transmission in a scaled testbed.
- Develop system design rules for achieving specified high-gain signal requirements, determine bounds on achieving high levels of coherent gain given system specifications, provide notional designs based on COTS technologies, and identify areas for future technology development.

Introduction: Current and future wireless applications, including sensing, communications, and high-power transmission, have driven the need for continual increases in transmitted signal gain. However, the ability to achieve high-gain wireless transmission of microwave signals is restricted by the traditional platform-centric model used to develop wireless systems, where single, large platforms are limited by aperture size, device power handling and efficiency, and heat dissipation, among other factors. Achieving increases in signal gain under the current platform-centric model requires redesigns of devices, apertures, or entire systems, an approach that is not only costly but time-consuming. To overcome these platform-centric challenges, we propose a novel approach to high-gain microwave signal transmission using distributed, scalable arrays of small, low-cost platforms, each with individually low-power transmitters. In particular, coordinating separate wireless systems to create a coherent distributed phased array can yield dramatic system-level gains that cannot feasibly be achieved with a single platform, or even with non-coherent signal coordination on multiple platforms. These benefits include transmit power gains proportional to the number of platforms squared, significant spatial diversity affording robustness to interference and failures, and the ability to directly scale capabilities by simply adding or removing nodes in the array. The ultimate level of

flexibility is achieved in an open-loop array, where the nodes self-align without using feedback from the target location. Whereas closed-loop distributed arrays are possible with signal inputs from the target, such approaches are limited in that the array can only direct signals back to the point of the emanating signal. In contrast, open-loop distributed phased arrays can arbitrarily steer beams to any desired angle.

Background: Achieving coherent transmission in distributed arrays requires coordination of the spatio-electrical states of the elements in the array; our group has pioneered efforts in developing technologies for high-accuracy coordination for distributed beamforming in small arrays of 2-4 platforms. Our group has extensive experience developing open-loop distributed phased arrays through our prior efforts developing and demonstrating critical technologies enabling fully open-loop coherent distributed transmission, which have demonstrated the feasibility of achieving and maintaining sufficient phase stability between separate platforms. In prior efforts, a high-accuracy microwave ranging technique using a novel spectrally sparse waveform achieved sub-mm range accuracy and was used to experimentally demonstrate the first open-loop coherent distributed transmission. Other efforts developed a novel one-way wireless frequency locking approach, which was used to demonstrate the first fully wireless open-loop distributed phased array. Current efforts are focused on building cognitive-enabled adaptive coordination algorithms that are robust to changing environmental conditions. The outcome of these efforts is that the basic coordination technology to achieve distributed phase coherence with small array sizes has been largely proven. The challenge for high-gain microwave applications is in creating a framework amenable to coordinating hundreds of nodes or more. The proposed effort is, to our knowledge, the first to investigate approaches to implementing distributed coordination in large-scale arrays of tens to hundreds of nodes, and to explore the implications of array scalability.

2. Activities and Accomplishments

In this reporting period, we made significant progress in the development of decentralized coordination and localization algorithms that will support distributed coherent operation in large arrays, and in centralized localization algorithms that will enable near-term experimental measurements of distributed beamforming. Specifically, in this reporting period we:

- Developed approaches to mitigate bias in internode ranging;
- Developed a wireless time synchronization algorithm obtaining tens of picosecond time alignment between separate nodes;
- Continued the development of decentralized frequency syntonization algorithms.

Our results on these topics are described in the following.

Bias Mitigation in Centralized Localization

Localization is key for phase alignment in open-loop coherent distributed array architectures. As mentioned in the previous report, we are currently working on localizing the primary node using the range estimates between the nodes in a centralized array architecture. This can be done by implementing multilateration algorithms to localize the target, which in our case is the primary node. Localizing the primary node is essential since in the centralized topology that we are interested in, all the secondary nodes (in relative motion) need to localize their phases to that of the primary node.

To ensure that localization errors will not hinder the coherent operation of distributed phased arrays, the range estimates used in the multilateration algorithm need to be accurate and unbiased. Two-tone waveforms offer the highest ranging accuracy, however, once pulse compression is used for time delay estimation, the peak of the matched filter output is prone to bias due to discretization errors. This problem was addressed in [1] using a computationally expensive least squares estimation approach. To reduce this computation time, a novel method that relies on a lookup table is employed.

Quadratic Least Squares (QLS) is used for estimating the refined time delay from the matched filter output [2,3]. This peak estimator is commonly used in the literature to refine the peaks of a given waveform or a matched filter output. However, the bias of this peak estimator was rarely addressed, especially the ranging biases in radars that use two-tone ranging waveforms. The anticipated ranging bias using QLS is shown in Fig. 1 for the case where a sampling rate of 10 MSps and a pulse width of 0.1 ms. The bias for multiple instances between two discretization points is shown for varying bandwidth. Depending on the bandwidth, the anticipated bias can be on the order of meters which is problematic for our application. To reduce or eliminate the ranging bias from QLS we generate a table that includes the estimated bias for a given range estimate and a given ranging waveform (with a specific pulse width and frequencies). Once the range is estimated, the anticipated bias is extracted for the estimated range and is subtracted from that value to obtain an unbiased estimate. The results are shown in Fig. 2. As can be seen the bias is removed from most of the cases where the bandwidth is below 3.3 MHz (5 MHz is the Nyquist rate). This method does not work for bandwidths from 3.3 MHz to 5 MHz because at these frequencies, initial range estimates are ambiguous, corresponding to multiple values.

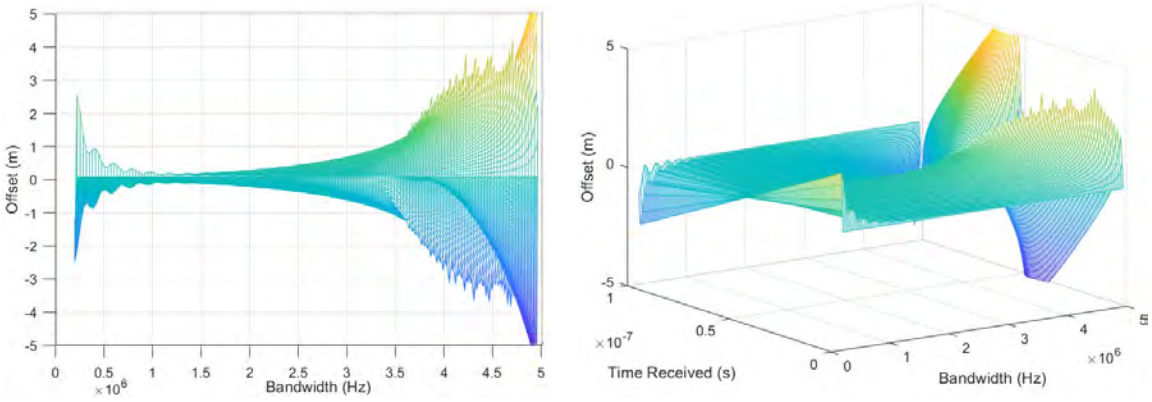


Figure 3: Anticipated ranging bias for radars employing two-tone ranging waveforms with pulse compression and QLS peak estimator.

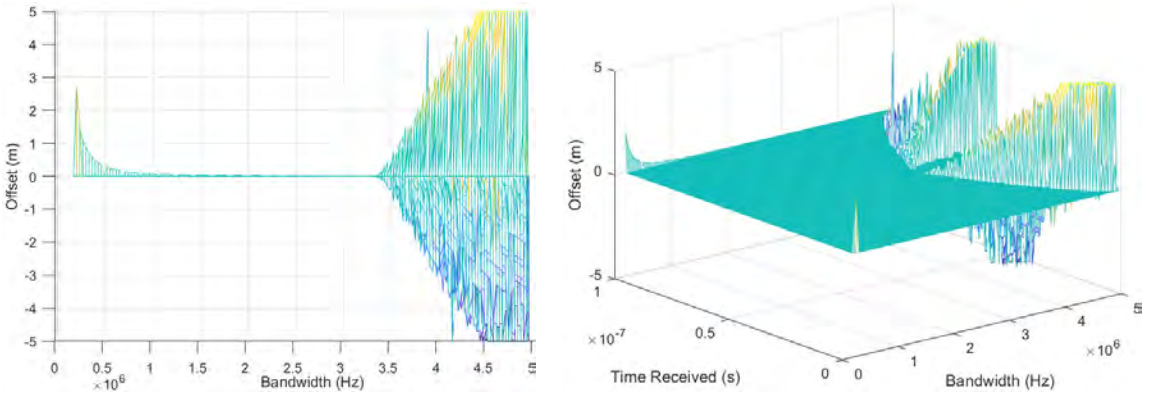


Figure 4: Ranging offset once the bias in QLS is corrected for using a lookup table that includes the anticipated bias for every estimated range. Offset is still high for the cases where multiple solutions are present for a given range estimate.

Given that pairing QLS with bias correction using a lookup table only allow non-biased ranging for bandwidths up to 3.3 MHz for sampling rate of 10 MBps, it is important to investigate other peak estimators that can push this boundary further. Sinc nonlinear least-squares (NL-LS) is another peak estimator that offers little to no bias for ranging using linear frequency modulated (LFM) waveforms [4]. Nevertheless, biases are observed when implementing NL-LS with two-tone ranging pulses, such as shown in Fig. 3. These biases can also be eliminated by employing bias correction using a lookup table. The bias elimination for NL-LS estimators is shown in Fig. 4. It was possible to obtain non-biased range estimates for frequencies up to 4.5 MHz, compared to 3.35 MHz for the case where QLS was employed. Some biases were observed for low tone separations, however in practice, large tone separations are needed to achieve accurate range estimates, making these biases less significant.

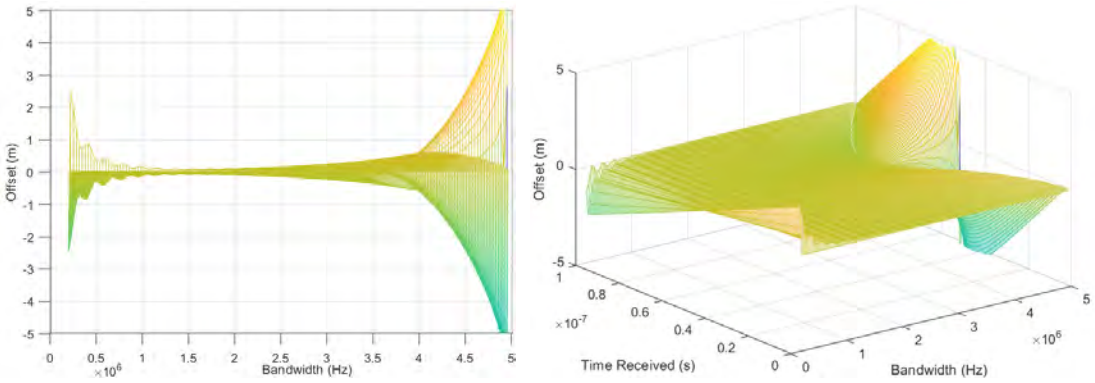


Figure 5: Anticipated ranging bias for radars employing two-tone ranging waveforms with pulse compression and NL-LS peak estimator.

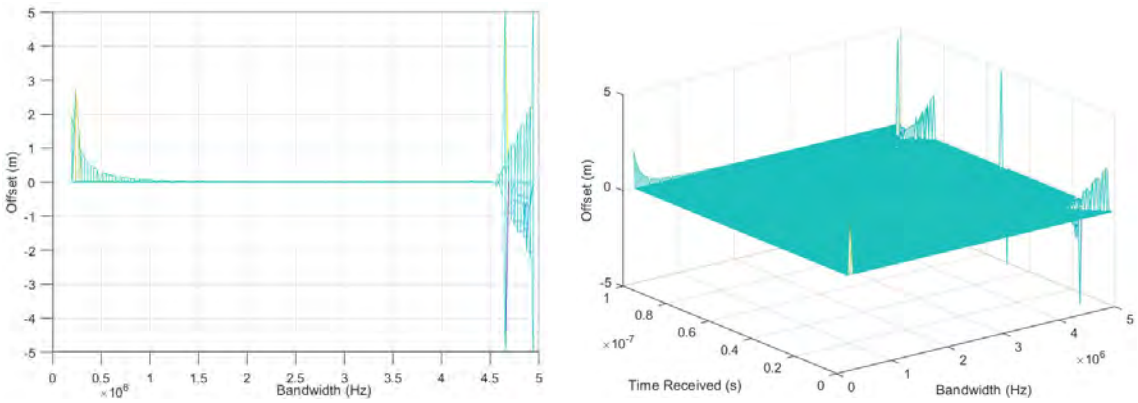


Figure 6: Ranging offset once the bias in NL-LS is corrected for using a lookup table that includes the anticipated bias for every estimated range. Offset is still high for the cases where multiple solutions are present for a given range estimate.

High-Accuracy Internode Time Synchronization

To achieve high bandwidth coherent distributed array operation, the systems must be tightly synchronized in frequency, phase, and time. A common metric for evaluating the overall system

performance is the probability of achieving a certain coherent gain value $P(G_C > X)$; commonly, a G_C value of 0.9 is chosen $G_C > 0.9$, i.e., 0.5 dB less than the ideal coherent gain with perfect phase alignment. This translates to phase accuracies of below 18° to achieve $P(G_C > X) \geq 0.9$, where λ is the carrier wavelength. For timing synchronization, the alignment requirements are waveform dependent; continuous-wave (CW) amplitude modulated waveforms may achieve $P(G_C > X) \geq 0.9$ by simply achieving 90% overlap, however for continuously phase-modulated waveforms such as the linear frequency modulation (LFM) waveform the timing requirements are considerably more stringent, typically resulting in overlap requirements of « 1% of the signal duration, for typical chirp-rates, thus very high accuracy synchronization is required for wide-band modulations.

In general, the local time at each node in a system of N wireless nodes with independent clocks can be modeled as $T_n(t) = t + \delta_n(t) + v_n(t)$, where $\delta_n(t)$ is a time-varying offset from the global true time, and $v_n(t)$ is a zero-mean time-varying noise term due to device noise from all components in the timing chain. The goal of timing synchronization is to determine the offset $\delta_n(t)$ of each node. For simplicity, it may be assumed that node 0 has the true time; thus, we must correct offset relative to node 0, i.e., $\Delta_{0n} = \delta_0 - \delta_n$, where $\delta_0 = 0$.

To estimate this offset, a two-way time transfer (TWTT) technique is used based on the assumptions that the channel is quasi-static during the synchronization epoch and the systems are syntonized (aligned in frequency). The synchronization process begins when node n transmits a ranging waveform to node 0 which it locally timestamps at $T_n(t_{\mathrm{TX}n})$ which we will denote as $T_{\mathrm{TX}n}$ for brevity. Node 0 will timestamp the received waveform with its local time $T_{\mathrm{RX}0}$ and will then respond with another locally timestamped ranging waveform at $T_{\mathrm{TX}0}$ after some arbitrary processing delay τ_{proc}. Finally, node n will timestamp the received waveform at $T_{\mathrm{RX}n}$ and estimate its offset Δ_{0n} using

$$\Delta_{0n} = \frac{(T_{\mathrm{RX}0} - T_{\mathrm{TX}n}) - (T_{\mathrm{RX}n} - T_{\mathrm{TX}0})}{2}$$

To validate the time and frequency transfer techniques in a real-world environment, the system was placed in a cluttered outdoor courtyard. The full system schematic and experimental setup are shown in Figs. 5 and 6. The nodes were separated by a distance of 2.1 m and the beamforming target was placed 41 m downrange. For this experiment, a Keysight DSOS804A 20 GSa/s oscilloscope was used with a 10-dBi L-Com HG72710LP-NF log-periodic antenna as the ranging target, pictured in the inset of Fig. 6, to digitize the waveforms at the carrier and estimate the time delay, phase, and coherent gain of the beamforming pulses. Each array node had a single Ettus Research X310 SDR with two UBX-160 daughterboards each to perform the time transfer and beamforming; the SDRs were configured to operate at 200 MSa/s and transmitted two-tone waveforms with 40 MHz tone separation for time transfer, and orthogonal 40 MHz LFMs for beamforming accuracy estimation, described in Section IV. The cart used for node 0 contained a desktop PC running GNU Radio to control the SDRs; the secondary node SDR was connected via a long fiber-optic cable for sending control signals, however a wireless link could be used. Each node had two antennas, one 8-dBi L-Com HG2458-08LP-NF log-periodic used for time transfer, and one 10-dBi L-Com HG72710LP-NF log-periodic antenna used for beamforming (the same as the target). SDR channel 0 on each node was connected to an Analog Devices EV1HMC849ALP4C transmit-receive switch, controlled by the time-transfer direction, which was connected to a power combiner/splitter and finally an antenna used for time and frequency transfer.

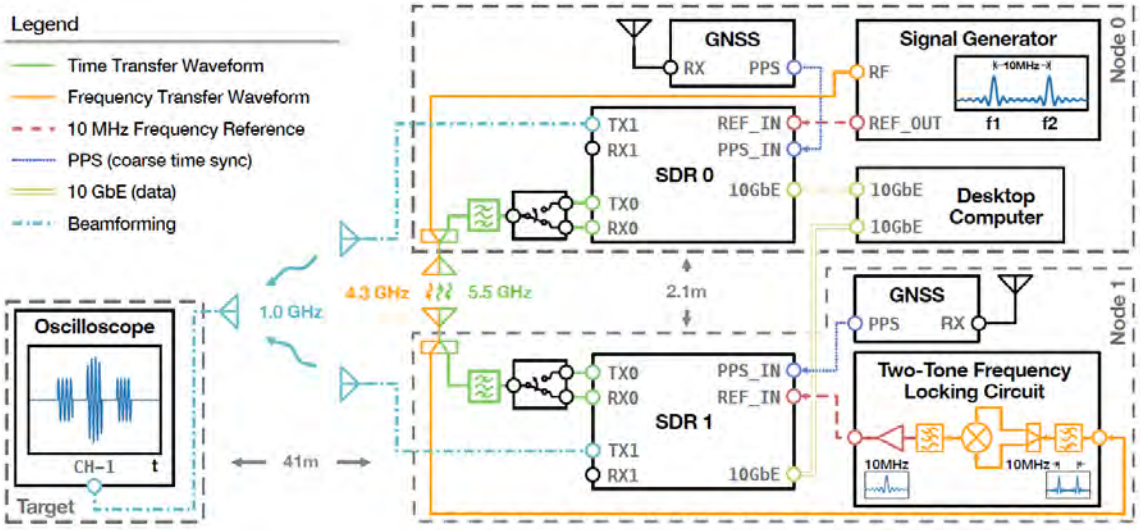


Figure 5. System schematic showing target node (left), and distributed array nodes 0 and 1 (top and bottom, respectively). Node 0 held the coordination computer running GNU Radio which was connected via 10 GbE to each node for control. Node 0 also contained the signal generator for frequency reference which generated a 10 MHz two-tone waveform at 4.3 GHz to be transmitted to the two-tone frequency locking circuit on node 1 used to lock SDR 1, as well as generated the 10 MHz frequency reference for the SDR on node 0. Each node also contained a GNSS receiver for coarse initial time synchronization between platforms (only used once on initialization). Finally, channel 0 on each SDR was connected to a transmit-receive switch to controlled via timing synchronization pulse direction which was connected to the 8-dBi log-periodic time-frequency transfer antennas, and channel 1 on each SDR was connected to a 10-dBi log-periodic beamforming antenna.



Figure 6. Experimental configuration of the distributed beamforming system in a fully enclosed courtyard. Node 0 is on the left and node 1 is on the right, separated by 2.1 m. The ranging target, shown in the inset is located 41 m downrange, below the blue walkway. A 20 GSa/s sampling oscilloscope was used to digitize the waveforms at the carrier to estimate time delay, phase, and coherent gain at the beamforming location.

A one-way wireless frequency transfer circuit was used to syntonize the platforms. This technique provides a 10 MHz frequency reference using two tones modulated onto a carrier frequency spaced 10 MHz apart. Once it is received, the signal is split and mixed with a copy of itself, and then low-pass filtered resulting in only a signal at the frequency of the tone separation, in this case, 10 MHz. This two-tone signal was generated at node 0 at a carrier of 4.3 GHz by a Keysight E8267D and connected to the second side of the splitter. The reference 10 MHz output of the signal generator was then connected to SDR 0 so they were frequency locked. The two-tone signal was received at node 1 and split into the two-tone self-mixing frequency locking circuit to produce a single 10 MHz square wave which SDR 1 was locked to, to ensure the same frequency reference as SDR 0.

Finally, because the nodes have random initial start times, the nodes must first be coarsely time aligned to ensure the 30 µs transmit and receive windows for the high-accuracy pulses will overlap. To accomplish this, a single pulse-per-second (PPS) pulse from a global navigation satellite system (GNSS) reference is used to align the system clocks on the order of ten to one hundred nanoseconds at system initialization—the PPS signal is not used afterwards. From here, the system exchanges τp = 30 µs two-tone pulses centered in a 30 µs window to perform the time offset correction described in Section II.

To characterize system performance, the beamforming waveforms were chosen to be two orthogonal LFM waveforms—an up-chirp and a down-chirp; this provides the ability to determine time delay and phase of each platform. The initial inter-node beamforming bias was used to calibrate the time-of-flight difference due to beamforming angle. From these, the standard deviation of each quantity was also calculated to evaluate accuracy, shown in Fig. 7; the standard deviation was computed over a ten-sample moving window. Because the cycle rate was ∼4 s, the accuracy plot starts at ∼40 s into the 110 s experiment windows. From Fig. 7 it is shown that over the duration of the experiment, the time transfer synchronization accuracy reached a minimum of 36.7 ps with an SNR of ∼21 dB while the beamforming reached an accuracy of 27.6 ps. The beamforming is expected to have a lower standard deviation as it is run directly after (∼300 ms) the system performs a time alignment. The phase stability was also measured, shown in the bottom row of Fig. 4, which was ∼0.1π radians, or ∼18°. Based on the beamforming delay and phase accuracies, this implies the system should be capable of transmitting data with a data modulation bandwidth of up to 2.415 GBd and maintaining a carrier frequency of up to 1 GHz with P (Gc > 0.9) ≥ 0.9.

Finally, to demonstrate the beamforming performance of the system, a set of coherent pulse measurements were performed after the system was aligned, shown in Fig. 8. Each node transmitted two 6 µs pulses separated by 6 µs with the center pulse being overlapped; the sharp rising edge indicates a high level of time alignment. The power level indicates the phase coherence of the system which was estimated by first taking the magnitude of Hilbert transform of the RF waveform to find the signal envelope, then performing a 50 ns low-pass moving average, plotted as a dashed pink line in Fig. 8. The coherent gain was computed by taking the ratios of the power levels at the center of each pulse, indicated by the X marks in Fig. 5. For the given measurement, the coherent gain was determined to be Gc = 0.954.

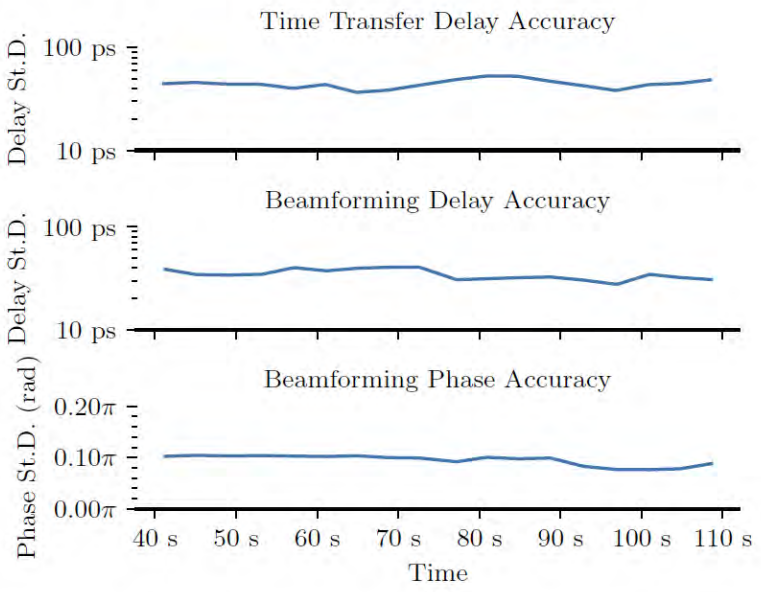


Figure 7. Time standard deviation measured between the two systems (top) and time and phase standard deviation measured at the beamforming target (middle and bottom).

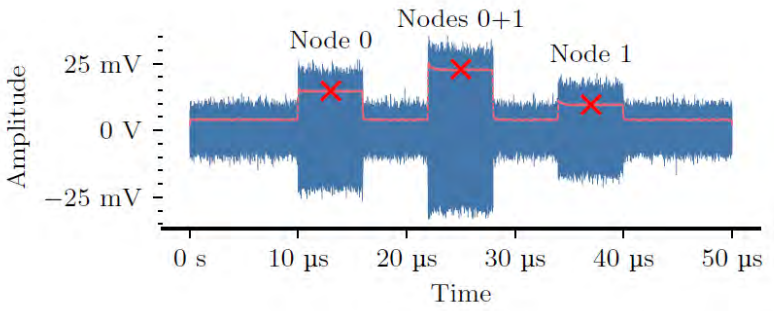


Figure 8. Coherent summation of CW pulses from two nodes. First and third pulses are from nodes 0 and 1 respectively, second pulse is the summation of both nodes. The pink dashed line indicates the smoothed signal envelope, and the X marks indicate the sample location for the coherent gain estimation, found to be 95.4%.

Decentralized Phase and Frequency Synchronization

In a distributed phased array, the evolution of the electrical states (i.e., frequencies and phases) of the nodes can be modeled using a state-space model wherein the process noise at each time instant can be described by the oscillator induced frequency drifts and phase jitters, and the measurement noise can be defined using the electrical states' estimation errors. With such modeling of the electrical states, we previously proposed a distributed Kalman filtering (KF) based frequency and phase synchronization algorithm wherein it was shown that the use of KF with consensus averaging significantly reduces the residual phase error, particularly when faster update rates are used for synchronization. In that algorithm, the nodes iteratively share their filtered frequency and phase estimates as well as the error covariances with their neighbors, and then update these parameters by computing a weighted average of the shared values in each iteration to reach the consensus, a scheme we refer to as consensus on estimates and error covariances (CEEC). An

existing distributed consensus scheme close to CEEC is the consensus on estimates (CE) as used in distributed KF algorithms in which the nodes only share their filtered estimates of the electrical states with their neighbors. The CE scheme reduces the amount of data shared between the nodes, but it results in a poorer convergence speed of the KF algorithm as compared to the CEEC-based filtering algorithm. Note that a rapidly converging consensus algorithm reduces the latency in achieving the synchronized state of the array, as well as it implies fewer exchanges of the data packets between the nodes, which in turn prolongs the lifetime of low-powered antenna nodes in an array network.

Another two families of the distributed Kalman filtering algorithms that are found in the literature use either a consensus on measurements (CM) scheme or a consensus on information (CI) scheme. In CM-based KF algorithms, the nodes perform consensus on their locally shared measurements and the innovation noise covariance matrices to approximate the centralized Kalman filtering. On the other hand, in CI-based KF algorithms, the nodes perform consensus on the locally shared predicted information matrix (the inverse of the predicted error covariance matrix) and the predicted information vector (information matrix multiplied with the predicted state estimate). Thus, exploiting the interesting features of both CM and CI techniques, a hybrid consensus on measurement and consensus on information based KF algorithm, referred to herein as the HCMCI-KF algorithm, has been explored in the literature, and has been shown to perform better than the distributed KF algorithms based only on either the CM or CI scheme. We are thus investigating a higher accuracy distributed Kalman filtering algorithm where HCMCI-KF is modified to also include the CEEC scheme, referred to herein as the HA-DKF algorithm. Both CM and CI schemes are complementary to each other, and by adding the CEEC scheme to further improve the synchronization performance of the filtering algorithm. In a nutshell, performing consensus on the filtered estimates of the electrical states provides a better estimate of the states as it averages out the zero mean normally distributed process and measurement noises. Furthermore, by computing the weighted average of the estimates and the error covariance at each node we obtain a better prior distribution for the next iteration of KF which in turn results in an improved KF estimates.

In Fig. 9 we illustrate the synchronization performance of the HA-DKF algorithm and compare it to the closely related hybrid consensus on measurement and consensus on information (HCMCI) algorithm, the distributed Kalman filter (DKF) algorithm, and the Kalman filter distributed frequency and phase consensus (KF-DFPC) algorithm. In this figure, we show the total residual phase error upon the convergence of these algorithms by varying the number of nodes N in the array network, when the update interval is set to T=0.1 ms and the SNR=30 dB. We consider different connectivity c between the nodes for comparison purposes. It is observed that for all the considered N and c values, our proposed HA-DKF algorithm significantly reduces the residual phase error as compared to the other algorithms.

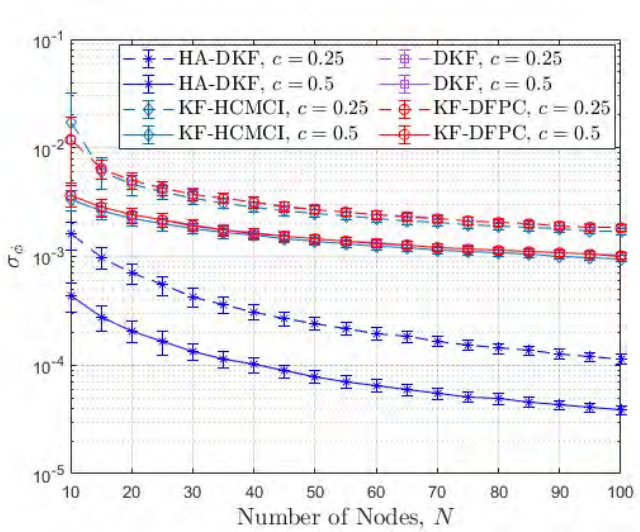


Figure 9. Standard deviation of the total residual phase error of the proposed HA-DKF algorithm, the KF-HCMCI algorithm, the DKF algorithm, and the KF-DFPC algorithm vs. varying the number of nodes N in the array when different connectivity c is assumed and the update interval is $T = 0.1$ ms and SNR $= 30$ dB.

3. Findings and Conclusions

The results of this reporting period provide critical pieces of the foundation of a distributed approach to phase coherent transmission of microwave signals. Localization is a challenging aspect of distributed array coordination, and even very small errors in internode range estimation can yield significant degradation in distributed beamforming performance. The bias mitigation approaches discussed in this report will allow improved range estimation accuracy as well as time synchronization accuracy. By using similar estimation techniques as implemented for internode range estimation, relative time between nodes can also be synchronized. The two-way time transfer approach discussed in this report relies on accurate estimates of the time of reception of the waveforms, and is thus based on the same principle as relative range estimation (time of flight estimation). The bias mitigation approach allows synchronization within tens of picoseconds. Our ongoing decentralized coordination algorithms have focused principally on frequency and phase synchronization, and have shown significantly improved performance in terms of theoretical bounds on coordination accuracy. These algorithms will be leveraged to include time synchronization in future work.

4. Plans and Upcoming Events

In the next year we will focus on three principal topics: advanced decentralized coordination algorithms for aligning frequency, phase, and time; hardware implementations of wireless coordination to support distributed beamforming, and investigating bounds and limitations on transmit power.

5. Transitions and Impacts

N.A.

6. Collaborations

N.A.

7. Personnel

Principal investigator

- Jeffrey Nanzer
- ~1 person month of effort in the reporting period
- National Academy Member: No

Postdoctoral Fellow

- Mohammed Rashid
- ~4 person months of effort in the reporting period
- National Academy Member: No

8. Students

This project supported three PhD students during the reporting period:

- William Torres
- Jason Merlo
- Naim Shandi

9. Technology Transfer

N/A

10. Products, Publications, Patents, License Agreements, etc.

Publications resulting from this project:

Archival Publications

M. Rashid and J. A. Nanzer, "A Message Passing Based Consensus Averaging Algorithm for Decentralized Frequency and Phase Synchronization in Distributed Phased Arrays," MILCOM 2022

M. Rashid and J. A. Nanzer, "Push-Sum Protocol Based Frequency and Phase Synchronization in Distributed Phased Arrays," IEEE International Symposium on Phased Array Systems & Technology, 2022

W. R. Torres, S. R. Mghabghab, and J. A. Nanzer, "Channelized Frequency Synchronization Using Consensus Averaging for Distributed Phased Arrays," IEEE International Symposium on Antennas and Propagation and USNC-URSI Radio Science Meeting, 2022

J. Merlo and J. A. Nanzer, "High Accuracy Wireless Time Synchronization for Distributed Antenna Arrays," IEEE International Symposium on Antennas and Propagation and USNC-URSI Radio Science Meeting, 2022

A. Bhattacharyya, S. R. Mghabghab, S. Vakalis, and J. A. Nanzer, "Experimental Implementation of Microwave Multi-Objective Linear Constrained Minimum Power Beamforming in the Near Field." IEEE International Symposium on Antennas and Propagation and USNC-URSI Radio Science Meeting, 2022

11. Point of Contact in Navy

N/A

12. Acknowledgement/Disclaimer

This work was sponsored by the Office of Naval Research (ONR), under grant (or contract) number N00014-20-1-2389. The views and conclusions contained herein are those of the authors only and should not be interpreted as representing those of ONR, the U.S. Navy or the U.S. Government.

Ultra-High-Efficiency Relativistic Magnetron and Improved MILO Capabilities

Grant No. N00014 -19-1-2155

Annual Report for Fiscal year 2022

Period of Performance: October, 1, 2021 to September 30, 2022

Prepared by:

Professor Edl Schamiloglu, Principal Investigator
University of New Mexico
Department of Electrical and Computer Engineering
Albuquerque NM 87131-0001
Email: edls@unm.edu

This work was sponsored by the Office of Naval Research (ONR), under grant number N00014 -19-1-2155. The views and conclusions contained herein are those of the authors only and should not be interpreted as representing those of ONR, the U.S. Navy or the U.S. Government.

Grant or Contract Number: N00014-19-1-2155
Date Prepared: January 03, 2023
Project Title: Ultra-High-Efficiency Relativistic Magnetron and Improved MILO Capabilities[1]
Annual Summary Report: FY2022
Principle Investigator: Edl Schamiloglu, edls@unm.edu, University of New Mexico, Department of Electrical and Computer Engineering

Section I: Project Summary

1. Overview of Project

The relativistic magnetron is the most compact and efficient high power microwave source. The University of New Mexico (UNM) has been studying relativistic magnetrons for over 20 years. We published a review article on the topic in 2019. Our recent work has focused on techniques to mitigate axial leakage current, and through a very productive collaboration with our colleagues at The Technion, we have made substantial progress through the introduction of the split cathode. In addition, the split cathode has made it possible to perform joint studies with NSWC using their superconducting magnet.

UNM has also been developing a magnetically insulated line oscillator (MILO) over the past few years to study plasma formation and evolution in the device and mitigating such plasmas to achieve higher efficiency operation. Additional funds were requested and received to construct a transmission line to facilitate MILO experiments. In addition, collaborations are ongoing with several partners on cathode development, theoretical studies of desorption, and spectroscopic diagnostics.

In terms of the Navy relevance of the project, this project extends the UNM/University of Michigan (UM) successful HPRF partnership to MILOs, that were largely developed in the USA (1980's-2000), but recently have seen intensive research and development by near-peer adversary nations. Our goal is to address, via focused and transitional HPRF research, some of the critical problems facing Navy operations due to asymmetric electronic threats, such as those faced by Marine warfighters in forward operating bases to those in littoral waters, and protection of high value targets, such as U.S. embassies in potential hot spots around the globe. These asymmetric electronic threats can come in the form of small airborne electronic drones, perhaps even COTS-type devices employed in boat or automobile-sized machines.

Abstract: This annual report summarizes activity on the recently awarded ONR grant "Ultra-High-Efficiency Relativistic Magnetron and Improved MILO Capabilities" covering the period October 01, 2021-June 30, 2022

Objective: The objectives of this research are to i) increase the HPRF power/electron beam power efficiency of relativistic magnetrons and explore the MILO to further improve its performance. The relativistic magnetron portion of this research is in collaboration with The Technion, Israel. The MILO portion of this research is in collaboration with UM.

Introduction: The UNM group excels in designing novel HPRF source concepts of relevance to the Navy, and then validating the source designs in experiment. We are pushing the boundaries on the relativistic magnetron through the use of a split cathode, an idea originally proposed by our colleagues at The Technion but investigated jointly. In addition, UNM is seeking to further the magnetically insulated line oscillator (MILO) through basic studies of surfaces plasmas within the device. This project seeks to continue this

[1] This work was sponsored by the Office of Naval Research (ONR), under grant number N00014-19-1-2155. The views and conclusions contained herein are those of the authors only and should not be interpreted as representing those of ONR, the U.S. Navy or the U.S. Government.

basic research program that has been in collaboration with our colleagues at UM. Investigating frequency agile magnetrons with diffraction output (MDOs) and MILOs is an important consideration of our work.

Ultra-High-Efficiency Relativistic Magnetron

In our original proposal we were planning on studying the MDO with virtual cathode (VC) and the MDO with magnetic mirror. However, in FY20, Q3 we decided to abandon this approach for the following reasons:

1. Experiments at UNM with the MDO and VC resulted in some RF generation, but mostly dead shorts and a considerable amount of concomitant bremsstrahlung radiation generation. Particle-in-cell (PIC) simulations had indicated that this approach was promising. However, in experiments, the electric field stress in the radial A-K gap far exceeded the threshold for breakdown so this approach was not viable and was abandoned.
2. Although we were still considering moving forward with the MDO with magnetic mirror at UNM, the magnetic field distribution from the NSWC DD cryomagnet (which was purchased specifically for the ORION relativistic magnetron) has a very long uniform magnetic field region (Fig. 1) which would have resulted in axial loss current from the MDO streaming to the output window which would have destroyed it.
3. In addition, implementing a magnetic mirror would require i) additional magnetic field-producing coils, ii) an additional power supply, and would result in a heavier, less efficient system, making it less attractive for a mobile platform.

At about the same time, we initiated a collaboration with Yakov Krasik and John Leopold at The Technion in Haifa, Israel (Technion funded by ONR Global). This collaboration led to an extremely fruitful direction, resulting in the development and implementation of what we call the split cathode. The split cathode is an elegant, lightweight, passive (no power needed) solution to eliminating axial leakage current from the MDO. The split cathode enabled the successful demonstration of the NSWC DD MDO (clone of the UNM MDO) with the cryomagnet arranged in Helmholtz coil configuration. Without the split cathode, experiments at NSWC DD on the MDO would have been impossible! Furthermore, simulations indicate that the split cathode is more effective at eliminating axial leakage current compared to a magnetic mirror.

The Magnetically Insulated Line Oscillator (MILO)

The MILO is a crossed field HPM generator comprised of two structures, an inner conductor that serves as an electron field emitter and an outer conductor that contains the slow wave structure and ultimately where the electromagnetic energy is generated.

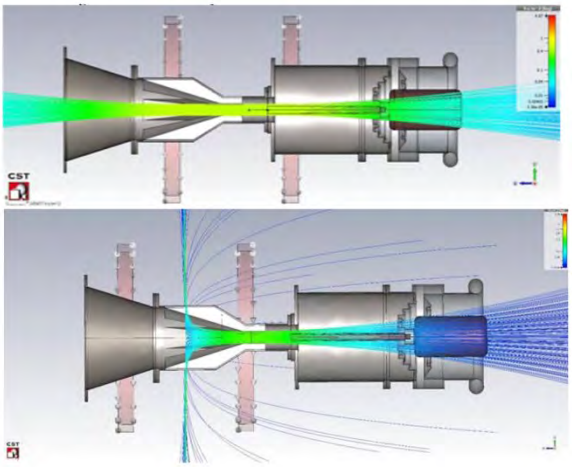


Figure 1. NSWC DD cryomagnet operating in Helmholtz coil mode (top) and cusp mode (bottom).

The Magnetically Insulated Line Oscillator (MILO)

The initial idea put forward in our grant proposal was that we would have a multipronged approach to addressing the main issues with crossed-field devices, specifically with the MILO. Although much thought as well as much effort has gone into understanding what the optimal electromagnetic output parameters are for an effective electronically lethal source, it often is not possible to reach a consensus or provide that information to academic researchers. Nonetheless, one can take the approach that energy, and it is energy, that goes into a device should be used to generate whatever that device was meant to provide (in this case electromagnetic waves) with as little energy loss as possible. Additionally, it would be good if that electromagnetic energy is not tied to a single frequency but rather could somehow be swept on command to a different monochromatic frequency – or perhaps even spread out over some broadband range. The ideal would be to provide the targeting team with a single source that could put energy at specific frequency to match the weaknesses of the target. Ideally the same single source could fire as many times as needed within 1 s to paint that target with as much energy at the right frequency as required to increase electronic lethality.

Background: The approach that is being followed in the research under this grant is to i) utilize comprehensive PIC simulations using UNM's various virtual prototyping tools (ICEPIC, MAGIC, LSP – which can handle surface plasmas in the MILO) and then validate the simulations using experiments. A modified PI-110A accelerator is used for the MDO and relativistic magnetron experiments, and a Marx/PFL for the MILO. The MILO is fitted with spectroscopic diagnostics to compare experimental results with LSP simulations. Novel cathodes are also being developed for the MILO.

2. Activities and Accomplishments

The current reporting period is October 01, 2021 – June 30, 2022.

Ultra-High-Efficiency Relativistic Magnetron

Figure 2 presents an idealized simulation of how the split cathode works (without being in the MDO's interaction regime for simplification). The split cathode consists of a series of annular cathode emitters made out of carbon nanotubes in epoxy located outside of the MDO interaction region. A small diameter central rod connects the emitters to the downstream reflector. An electron beam is injected into the interaction region and, instead of forming a VC (as we had proposed earlier – here we do not form a VC), the electrons flow downstream, are reflected from the reflector and flow upstream, are reflected from the cathode and flow downstream, and so on. (Not requiring a VC enables us to significantly increase the radial A-K gap, resulting in much lower electric field stress on the anode and avoiding electrical breakdown.) Over several transit times, the electrons gradually lose energy, forming a "squeezed state," as originally described by Ignatov and Tarakanov.[2] Figure 3 presents MAGIC PIC simulations that show the evolution of the squeezed state for the geometry in Fig. 2

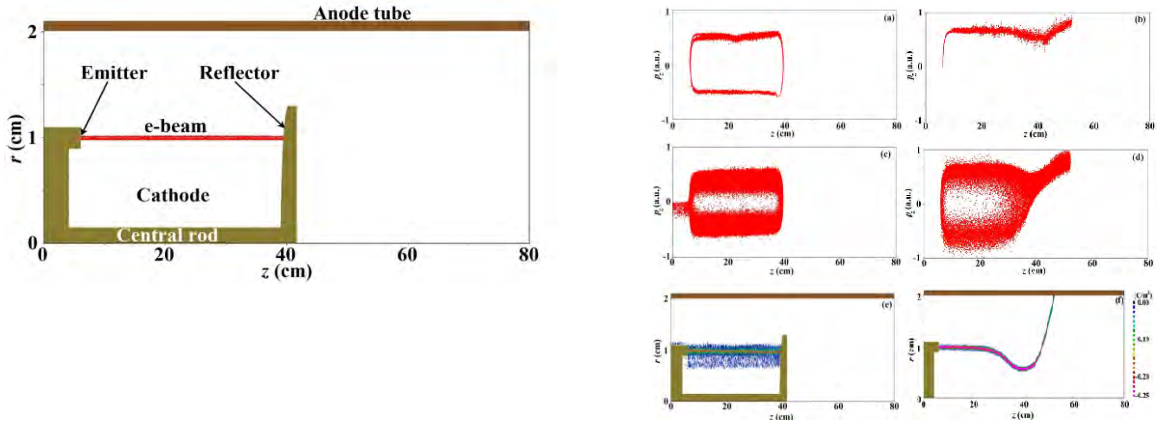


Figure 2 (left). A cross section of an axially symmetric arrangement of a split cathode made up from an emitter, a reflector, and a central rod placed coaxially inside an anode tube. The beam snapshot is at 6 ns. (right). [z, pz] phase space for the reflector [(a) at 6 ns and (c) at 45 ns] and for the magnetic mirror [(b) at 6 ns and (d) at 45 ns] cases. Electron charge density distribution at 45 ns for the reflector (e) and the magnetic mirror (f) cases. The color bar is the same for (e) and (f).

Considerable effort was also invested in updating the pulsed power system on the PI-110 electron beam accelerator. SPICE was used to model the circuit and optimize the Marx generator. In addition, all liquid resistors were replaced with solid state resistors.

Experiments were performed at UNM on the PI-110A accelerator. The results of the experiments were summarized in our final technical report submitted July 28, 2022. We have document MDO operation in the $2\pi/3$ mode at 2.2 GHz with no mode competition.

[2]A.M. Ignatov and V.P. Tarakanov, "Squeezed State of High-Current Electron Beam," Phys. Plasmas 1, 741 (1994).

Experiments were also performed at NWSC DD. The pulsed power system in the NSWC DD laboratory[3,4] is very different from UNM's. However, the MDO and the split cathode geometries are identical to those used in the UNM setup and were designed by UNM. NSWC DD researchers performed single shot, long pulse experiments as well as shots at 20 Hz repetition rate.

Figure 3 shows a typical result from single shot operation of the NSWC DD experiments. The pulsewidth of the NSWC DD driver was set to 150 ns and the maximum voltage amplitude was set at 200 kV. We can observe similar behavior to the UNM experiments: during the risetime of the pulse, charge accumulates in the interaction region, then electrons drift azimuthally and start interacting with the SWS where they start generating RF. The frequency of the RF is relatively clean; however, some mode competition is present.

Researchers at The Technion also performed several experiments with the split cathode that were jointly designed with UNM. The geometry of their magnetron differed from the UNM A6 MDO, but the working principle remains the same.[5,6] The first experiments were performed on a magnetron structure without an output cavity. Figure 4 shows a comparison of different cathodes in the magnetron: solid cathode, solid cathode with reflector, and finally the split cathode. With the solid cathode without the reflector, the electric field has low amplitude and is generated during the interval 25-150 ns, while the input signal is over 300 ns long. This behavior is a sign of high leakage current in the system. The second case partially resolves this behavior and the amplitude of the RF is much higher; however, the pulselength of the electric field is similar to the first case. Figure 4(d) shows the input current in the system increasing while the RF signal decays. This behavior is explained by A-K gap closure.

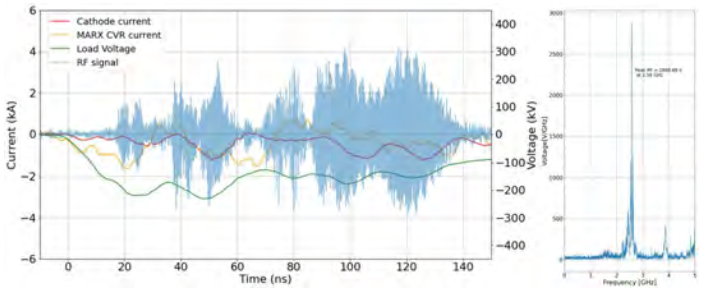


Figure 3. NSWC DD single shot results for the MDO with split cathode.

When the physical cathode is removed from the interaction region, as is the case for the split cathode, the RF signal exists for the entire duration of the voltage pulse. The mode looks to be consistent, yet slightly shifting frequencies as time progresses, as shown in Figure 4(i).

The experiment described above was performed on a magnetron structure with no output cavity. The electric field was measured inside of one of the cavities using a B-dot. The next experiment was performed

[3]A.J. Sandoval, *Experimental Verification of A6 Magnetron with Permanent Magnet* (M.S. Thesis, University of New Mexico, Albuquerque, NM, 2018).
[4]D. Andreev, A. Kuskov, D. Reass, A. Sandoval, E. Schamiloglu, Y.-J. Chen, J. Kreger, and J. Chaparro, "Rep-Rated Testing of a Compact Magnetron with Diffraction Output (MDO) and Plans for Testing the full MDO," IEEE PPPS-2019 (Orlando, FL, June 23-28, 2019).
[5]J. Leopold, M.S. Tov, S. Pavlov, V. Goloborodko, Y.E. Krasik, A. Kuskov, D. Andreev, and E. Schamiloglu, "Experimental and Numerical Study of a Split Cathode Fed Relativistic Magnetron," J. Appl. Phys., vol. 130, 034501 (2021).
[6]Y.E. Krasik, J. Leopold, Y. Hadas, Y. Cao, S. Gleizer, E. Flyat, Y. Bliokh, D. Andreev, A. Kuskov, and E. Schamiloglu, "An Advanced Relativistic Magnetron Operating with a Split Cathode and Separated Anode Segments." J. Appl. Phys., vol. 131, 023301 (2022).

on a magnetron with separated anode segments and a split cathode.[6] The segmented anode segments facilitated rapid penetration of a fast magnetic field.

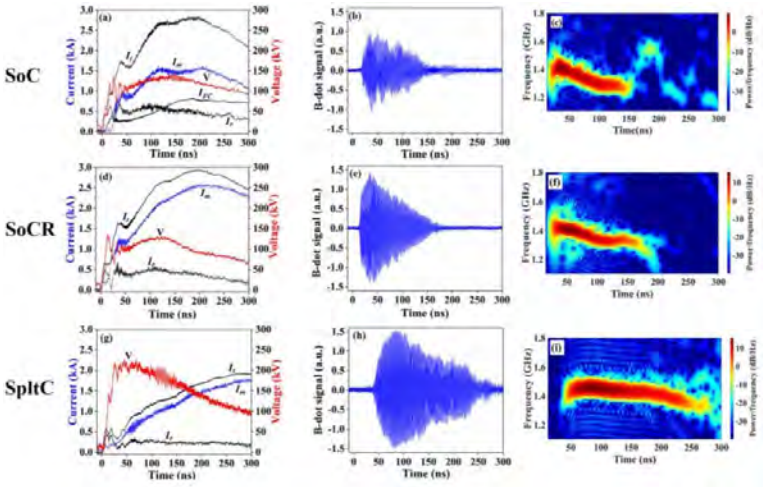


Figure 4. Summary of results from The Technion comparing cathodes: solid cathode (top), solid cathode with a reflector (middle), and the split cathode (bottom).[5]

MAGIC PIC simulations of the MDO with split cathode revealed the formation of spoke patterns with n-fold symmetry. The n-fold symmetric shapes are attributed to the diocotron instability.

We have only just begin studying the diocotron instability in our continuing collaboration with The Technion. We believe that this instability can lead to faster turn on of the MDO. We anticipate further investigations of this instability as part of a follow-on effort investigating the MDO for X-band and higher frequency generation. Our preliminary findings have been submitted for publication.[7]

The Magnetically Insulated Line Oscillator (MILO)

This portion of the final report gives an overview of the past efforts of the MILO group at UNM. Some of these were quite successful – yielding three patent applications, some are a work in progress but establishing strong collaborations, yet other novel efforts provided tantalizing clues as to path forwards for ultimately yielding an electronically lethal HPM source. Although described in discrete steps it is worth mentioning once again that our mantra was a multipronged effort to address the core issues and so all experiments and simulations are tied together.

Because a MILO is a low impedance device, the currents called for to self-insulate are very high. The MILO does not need an external magnetic field as it is self-produced but the critical current in order to achieve self-magnetic insulation is rather high, on the order of 30-40 kA. This means that we need a cathode that produces a large current density, does it again and again, turns on very fast, and outgasses very little. On this topic we partnered with Dexmat and Drexel University, as well as with a material scientist, Dr. Steven Fairchild of AFRL/RX. The first generation cathodes utilized felt cathodes (which we named Elvis regardless of constitution as there are many, many varieties of felt) and later generation electron emitters utilized CsI as an adulterant on a carbon nanotube substrate.

[7]Y.P. Bliokh, Ya.E. Krasik, J.G. Leopold, and E. Schamiloglu, "Observation of the Diocotron Instability in a Diode with a Split Cathode," accepted and to appear in Phys. Plasmas (2023).

Dexmat produced centimeter-long carbon fibers using a proprietary process and Drexel university employed their advanced material assembly techniques to yield a tufted sewn cathode structure. Dr. Fairchild provided additional cathodes based on similar structures but bonded to substrates that outgas less. We were the principal group leading the high voltage experiments with our LTD accelerator and with our spectroscopic diagnostics. We found that the cathodes did turn-on readily and provided large currents. We also were able to ascertain that these cathodes could be built to a modest size, 4" diameter, with the promise that this could be extended to longer lengths for use in HPM cathodes, especially for MILOs in the 1.2 GHz range. Our work, however, does indicate that the material still outgasses and more work is being done by Dr. Fairchild and UNM to mitigate this. Additionally, we found that the anode, as expected, emitted neutrals which resulted in a large ion load very easily.

3. Findings and Conclusions

For the ultra-high-efficiency relativistic magnetron work, the split cathode and related work has been a major breakthrough that is enabling experiments at NSWC and advancing the relativistic magnetron and MDO work at UNM. The collaboration with colleagues at The Technion has been extremely fruitful.

For the MILO, some of our initial key findings are:

1. Plasma formation occurs very fast
2. Various spectral lines show adsorbates of various compositions (this is in the visible regime and additional measurements need to be taken in the UV range).
3. Measurements are azimuthally resolved but not temporally resolved
4. Initial density measurements show densities are on the order of 1.4×10^{15} cm^{-3}.

It is worth noting once again that these plasmas keep the pulselength short – mitigating these plasmas will increase the effectiveness by at least 50%.

4. Plans and Upcoming Events

This effort has ended and the UNM group is now pursuing HPM sources from X-band to Ka-band. MDOs and MILOs are being considered.

5. Transitions and Impacts

As part of its collaboration with NSWCDD, UNM is transitioning its MDO with split-cathode. In addition, we are presently developing/designing a new MILO for use in irradiation of targets of interest to the Naval warfighter. This will include our novel frequency agile design. We will transfer any cathode developments for this design which will be fielded at Dahlgren Navy facilities.

6. Collaborations

Agency/Org	Performer	Project Name	Purpose of Research/ Collaboration
NSWCDD	John Kreger, Jack Chen, and Jon Cameron Pouncey	HPM collaboration	We discussed proceeding with MDO and transparent cathode testing at NSWC
AFRL/RX	Steven Fairchild	HPM cathode collaboration	We are discussing collaborative research on HPM cathodes
AFRL/RD	Brad Hoff and Sterling Beeson	HPM cathode and switch collaboration	We are discussing collaborative research on HPM cathodes and pulsed power switches/CsI coatings
Technion, Haifa, Israel	Yakov Krasik and John Leopold	Comparison of magnetic mirror vs. cathode rod and reflector	Optimize suppression of magnetron leakage current via an electron beam in a squeezed state
Weizmann Institute of Science	Yitzhak Maron	Diagnostics	Time-resolved spectroscopic diagnostics in high power, cross-field devices
Drexel University	Genevieve Dion	Cathodes	Large area cathode assembly
DexMat	Dmitri Tsentalovich	Cathodes	Providing base material for sewn cathodes
Verus Research	Sameer Hemmady	MILO	High impact outcomes
Stanford University	Ken Hara	Cathodes, MILO, MDO	Spectroscopy
Texas Tech University	Ravi Joshi	Cathodes, MILO, MDO	Effects of outgassing
Institute for Radiophysics and Electronics, National Academy of Sciences of Ukraine, Kharkiv	Kostyantyn Ilyenko	MILO and beam physics theory	MILO theory

7. Personnel

Principal investigator – Edl Schamiloglu (0.5 person month), National Academy Member (N).
Co-investigator or Co-PI – Salvador Portillo (2.5 person months), National Academy Member (N).
Business Contact – Timothy Wester, National Academy Member (N).
Team Members – none
Subs – none

8. Students

Artem Kuskov (Ph.D. student – 6 person months)

Dmitrii Andreev (Ph.D. student – 6 person months)

Robert Beattie Rossberg (M.S. student – 6 person months)
Eli Bartlit (B.S. student – 4 person months)
Chris Rodriguez (B.S. student – 4 person months)

9. Technology Transfer

N/A – except for ongoing collaboration with NSWC DD on MDO and MILO, and joint experiments.

10. Products, Publications, Patents, License Agreements, etc.

Peer-reviewed publications acknowledging this grant:

a. An Axial Output Relativistic Magnetron Fed by a Split Cathode and Magnetically Insulated by a Compact Low Power Solenoid
b. IEEE Transactions on Electron Devices
c. J.G. Leopold, Y. Hadas, Ya. E. Krasik, and E. Schamiloglu
d. Keywords: high power microwaves, virtual cathode, magnetron with diffraction output, MDO, squeezed state
e. Distribution Statement: Unlimited release
f. Publication Status: published
g. Publication Identifier Type: DOI
h. Publication Identifier: 10.1109/TED.2021.3105942
i. Publication Date: October 2021
j. Volume: 68
k. Issue: 10
l. First Page Number: 5227
m. Publication Location: Piscataway, NJ
n. Acknowledgement of Federal Support? Yes
o. Peer Reviewed? Yes

Peer-reviewed publications acknowledging this grant:

a. PIC Simulation of the Coherent Cerenkov-Cyclotron Radiation Excited by a High-Power Electron Beam in a Crossed-Elliptical Metamaterial Oscillator at S-band
b. IEEE Transactions on Plasma Science
c. Y. Li, M. Liu, C. Wang, E. Schamiloglu, C. Liu, M.I. Fuks, W. Jiang, and J. Feng
d. Keywords: crossed-elliptical metamaterial (MTM), high power microwaves (HPMs), mode switching, particle-in-cell (PIC) simulations, slow-wave structure (SWS)
e. Distribution Statement: Unlimited release
f. Publication Status: published
g. Publication Identifier Type: DOI
h. Publication Identifier: 10.1109/TPS.2021.3112660
i. Publication Date: November 2021
j. Volume: 49
k. Issue: 11
l. First Page Number: 3351
m. Publication Location: Piscataway, NJ
n. Acknowledgement of Federal Support? Yes
o. Peer Reviewed? Yes

Peer-reviewed publications acknowledging this grant:

a. An Advanced Relativistic Magnetron Operating with a Split Cathode and Separated Anode Segments
b. Journal of Applied Physics
c. Ya.E. Krasik, J.G. Leopold, Y. Hadas, Y. Cao, S. Gleizer, E. Flyat, Y.P. Bliokh, D. Andreev, A. Kuskov, and E. Schamiloglu
d. Keywords: high power microwaves; relativistic magnetron, split cathode, squeezed state
e. Distribution Statement: Unlimited release
f. Publication Status: published
g. Publication Identifier Type: DOI
h. Publication Identifier: 10.1063/5.0080421
i. Publication Date: January 2022
j. Volume: 131
k. Issue: 023391
l. First Page Number: 023301-1
m. Publication Location: College Park, MD
n. Acknowledgement of Federal Support? Yes
o. Peer Reviewed? Yes

Peer-reviewed publications acknowledging this grant:

a. Numerical Evaluations of Hydrogen Outgassing from Cesium Coated Carbon Fiber Electrodes
b. Vacuum
c. S.N. Sami, R. Islam, S. Portillo, E. Schamiloglu, and R.P. Joshi
d. Keywords: outgassing, carbon fiber, density functional theory, molecular dynamics simulation, Cs coating
e. Distribution Statement: Unlimited release
f. Publication Status: published
g. Publication Identifier Type: DOI
h. Publication Identifier: 10.1016/j.vacuum.2022.110869
i. Publication Date: April 2022
j. Volume: 198
k. Issue: 110869
l. First Page Number: 110869-1
m. Publication Location: United Kingdom
n. Acknowledgement of Federal Support? Yes
o. Peer Reviewed? Yes

Peer-reviewed publications acknowledging this grant:

a. PIC Simulations of a Frequency Agile Multicavity Relativistic Magnetron Using Irregular Ring Metamaterials Driven by a Transparent Cathode

b. Physics of Plasmas
c. Y. Li, M. Liu, J. Feng, C. Wang, E. Schamiloglu, C. Liu, and W. Jiang
d. Keywords: high power microwaves, metamaterials, transparent cathode, relativistic magnetron
e. Distribution Statement: Unlimited release
f. Publication Status: published
g. Publication Identifier Type: DOI
h. Publication Identifier: 10.1063/5.0089115
i. Publication Date: July 2022
j. Volume: 29
k. Issue: 073107
l. First Page Number: 073107-1
m. Publication Location: College Park, MD
n. Acknowledgement of Federal Support? Yes
o. Peer Reviewed? Yes

Peer-reviewed publications acknowledging this grant:

a. Observation of the Diocotron Instability in a Diode with a Split Cathode
b. Physics of Plasmas
c. Y.P. Bliokh, Ya.E. Krasik, J.G. Leopold, and E. Schamiloglu
d. Keywords: high power microwaves, relativistic magnetron, split cathode, diocotron instability
e. Distribution Statement: Unlimited release
f. Publication Status: published
g. Publication Identifier Type: DOI
h. Publication Identifier: accepted and to appear 2023
i. Publication Date: 2023
j. Volume: TBD
k. Issue: TBD
l. First Page Number: TBD
m. Publication Location: College Park, MD
n. Acknowledgement of Federal Support? Yes
o. Peer Reviewed? Yes

Conference Papers

None

Conference Presentations

J.G. Leopold, Y.E. Krasik, Y. Hadas, Y. Cao, S. Pavlov, V. Goloborodko, S. Gleizer, E. Flyat, Y.P. Bliokh, D. Andreev, A. Kuskov, and E. Schamiloglu, “Experiments on a Segmented Axial Relativistic Magnetron Fed by a Split Cathode,” IEEE International Conference on Plasma Science (Seattle, WA, May 22-26, 2022).

Books

J.W. Luginsland, J.A. Marshall, A. Nachman, and E. Schamiloglu, Eds., *High Power Microwave Sources and Technologies using Metamaterials* (IEEE Press/John Wiley and Sons, New York, NY, 2021).

Theses

Artem Kuskov - 2022 *Relativistic Magnetron with Diffraction Output and Split Cathode* (Artem is with Verus Research in Albuquerque, NM)

Dmitrii Andreev - 2022 *Relativistic Magnetron Powered by Electrons in a High-Energy State* (Dmitrii is with Momentus Space in San Jose, CA)

Websites

MILO HPM laboratory: www.unm.edu/~sportil. MILO HPM laboratory web site showcasing some of the work being carried out on pulsed power and HPM source development.

Other Products:

None

11. Point of Contact in Navy

NSWCDD – John Kreger, Jack Chen, Jon Cameron Pouncey – we have periodic (at least quarterly) telecons.

Pulsed Dielectric Breakdown of Solid Dielectric Insulation Materials

Grant No. N00174-20-1-0025

Annual Report for Fiscal Year 2022

Period of Performance: October 1, 2021 to 30, September, 2022

Prepared by:

Professor David Wetz, Principal Investigator
Associate Professor Electrical Engineering Department
University of Texas at Arlington
Department of Electrical and Computer Engineering
416 Yates Street, Rm. 537
Arlington, TX 76019
Email: wetz@uta.edu

This work was sponsored by the Office of Naval Research (ONR), under grant (or contract) number N00174-20-1-0025. The views and conclusions contained herein are those of the authors only and should not be interpreted as representing those of ONR, the U.S. Navy or the U.S. Government.
Grant or Contract Number: N00174-20-1-0025
Date Prepared: 1/14/2023

Project Title: Pulsed Dielectric Breakdown of Solid Dielectric Insulation Materials
Annual Summary Report: FY22
Principle Investigator: David Wetz, wetz@uta.edu
The University of Texas at Arlington
416 Yates St. 537 Nedderman Hall
Arlington, Texas 76019

Section I: Project Summary

1. Overview of Project

Overall Goals:

The overall goal of this effort is to identify and study solid dielectric materials that can be employed to replace gas and liquid insulators in high voltage pulsed power systems. The team is using modeling and simulation (M&S) and experimental techniques to characterize the dielectric properties and pulsed dielectric strength of solid dielectric materials that are both raw and altered using nano additives.

Future Naval Relevance:

There is significant tactical advantage to being able to deploy directed energy weapon (DEW) systems on the battlefield. Many DEW systems employ high voltage pulsed power supplies that drive the DE source. Typically, gas and liquid (oil) dielectrics are used to insulate high voltage systems, which have advantages such as high dielectric strength and self-healing properties when breakdown events occur. However, these dielectrics pose many challenges when it comes to sealing, maintaining, and storing them for extended periods of time. Solid dielectrics solve many of these issues but face many of their own challenges. The significance of finding suitable solid dielectric materials pertains to reduction in size, weight, and maintenance of fielded high voltage pulsed power systems; solid dielectrics require no maintenance under normal storage or operational conditions and can lead to reductions in size and weight of fielded systems. A primary concern comes with a solid dielectric's inability to self-heal, as a single dielectric breakdown can cause electrical and mechanical failure that results in the need for replacement of the entire system. It is imperative that the insulator is well understood and properly designed to ensure reliability under high electric fields. Identifying methods to tune dielectric properties of insulator materials enables functionally graded dielectrics to be employed, which aims to reduce electric field enhancements along with the size of the system. The experimental and M&S work being performed here is aimed at advancing our understanding of solid dielectrics and their ability to make DEW systems more easily fieldable within the near future.

Abstract:

In high voltage pulsed power systems, liquids and gases are often used as insulating materials. Regardless of the material used, dielectric breakdown is always a concern. Gas and liquid materials are conforming and self-healing, but they introduce significant engineering challenges and restrictions when it comes to sealing and/or pressurizing them. Liquid dielectrics are heavy so they may reduce a system's power and energy density, and their dielectric properties are unable to be functionally graded which can lead to boundary conditions that create high electric-field enhancements. Solid dielectrics can be more attractive from a maintenance, power density, and energy density perspective, but they are not self-healing and can be difficult to manufacture, especially around complex geometries. Epoxies have been studied to some extent but much more work is needed to fully understand their future uses. The rapid rise of additive manufacturing has also opened new avenues that need to be better explored. Epoxy, thermoset plastics, and additively manufactured materials can be functionally graded using nano-particle additives, introducing the ability to potentially minimize electric-field enhancements across boundaries. In the work presented here, solid dielectric materials that are both raw and dielectrically altered have been modeled using finite element

techniques and experimentally studied under pulsed experimental conditions to evaluate their dielectric strength.

Introduction:

This project serves to investigate the feasibility of using solid dielectric materials as replacements for conventional liquid or gas dielectrics in high voltage pulsed power applications, including high power microwave (HPMs) systems. The solid dielectrics of interest include epoxies and plastic materials. Epoxies are of especially high interest due to their ability to pot complex geometries, since they are formulated and cast in a liquid state that hardens as a solid. Composite solid dielectric materials, which are produced by introducing particulate filler materials into a base material of interest during its formulation, are also being investigated. The motivation for investigating composites is to determine how the dielectric properties of solids can be tuned to achieve specific desired dielectric characteristics that may reduce high electric field enhancements in complex geometries. This effort focuses on using experimental as well as M&S techniques to characterize the dielectric properties and pulsed dielectric strength of raw and altered epoxy materials. Over the course of the three-year project period of performance, several tasks have been executed, listed below, and those performed in this reporting period will be described in detail later.

Task 1: Technology, Raw Epoxy Material, and Dielectric Additives Literature Survey

A review of previously performed research investigating dielectric breakdown of epoxies and plastics has been performed in year 1 and materials to be studied have been chosen.

Task 2. Testbed Design and Fabrication

A testbed has been designed and fabricated to apply continuous and pulsed electric fields to epoxy and thermoset plastic samples. A 30 stage, 600 J/pulse marx generator is employed as the pulsed power source and a load fixture is utilized to apply the pulsed electric fields to the samples manufactured in house. This was completed in year 1.

Task 3. Existing Pulsed Power System Survey

UTA has worked with NSWC-DD to identify a marx topology that has been employed in HPM studies and M&S tools are being used to evaluate how solid dielectrics can be employed and functionally graded to reduce the size and weight of the system.

Task 4. M&S and Pulsed Dielectric Breakdown of Raw and Additively Manufactured Dielectrics

EPON 815C base epoxy material is initially being studied. Several pulsed dielectric breakdown experiments have been performed to characterize its pulsed dielectric strength in raw and dielectrically altered forms. Novel M&S techniques have been developed to quickly study the electric field profile of the materials being studied.

Task 5: Reporting

Reporting has been completed monthly to satisfy the requirements of the ONR and NEEC contracting vehicles.

Background:

In preparation for the execution of this effort, many research papers were found in which epoxy dielectrics have been studied in their natural form or with dielectric modification. The results of all these previously published works suggest that it is very feasible to alter the dielectric properties of epoxy resins by using many different types of micro and nano sized particles. Most of the previously documented work is focused on studying only low-voltage dielectric properties of altered materials, not on studying their dielectric strength. The work here is focused on not only studying how material properties are altered when they are dielectrically altered, but also what impact the alteration has on the dielectric strength. When coupled with the M&S approaches being taken, a wholistic approach to studying solid insulator materials is being taken. Epoxy materials are being altered and cast in-house using careful techniques to minimize the presence of

air bubbles. The work with thermoset plastics is limited to date but techniques have been developed and verified for creating dielectrically altered samples for study.

2. Activities and Accomplishments

Experimental Setup

In FY21, a companion DURIP grant was awarded to support the procurement of a high voltage pulsed power supply and load fixture. Near the end of FY21, the marx and load fixture procured from Applied Physical Electronics (APELC) in Austin, Texas was delivered. It is comprised of a 30-stage, 600kV marx generator along with a matched electrical load in which samples can be installed and dielectrically loaded. A planetary mixer was also procured so that epoxy materials can be well mixed, including homogeneous dispersion of any nanoparticles introduced, while under a vacuum. In early FY22, a rack was constructed to house the Marx and testbed near the APELC controls cabinet. Breakdown samples are loaded into the testbed such that when the marx is fired, current will flow either through the matched load or through the sample if the electric field is great enough to cause a breakdown event to occur. The testbed came equipped with a CVR (current viewing resistor) for monitoring current through the matched load, but nothing was installed to measure current through the sample being studied. That diagnostic was added after it was received and setup. The marx, test fixture, and sample CVR assembly are shown in Figure 1.

The epoxy samples are manufactured in house using a custom mould assembly designed and fabricated this FY, seen in Figure 2. The mould casts epoxy around two parallel electrodes at a fixed separation distance that is set by the thickness of the middle section of the mould. The epoxy is mixed in the planetary mixer

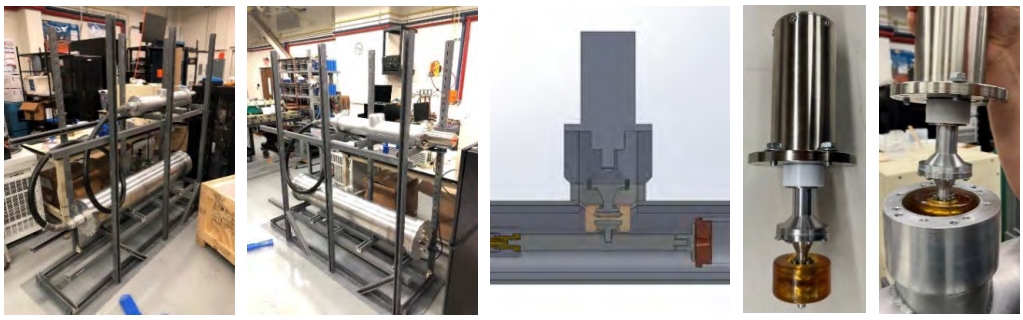


Figure 1. Marx and test fixture (left, second left), rendering of the dielectric sample holder and CVR, (third left), fabricated assembly (second right), sample assembly being loaded into testbed (right).

and then injected into the mould from the bottom using a large syringe. There is a disposable reservoir installed above for ensuring the mould is filled and for degassing it as shown in Figure 3. The three-piece mould design originally utilized an acrylic body but was redesigned using an aluminum body after having several of the acrylic bodies crack during sample removal. EPON 815C epoxy samples with a 0.1” electrode spacing were made but those samples were not able to be broken down, even when a field enhanced electrode pair was used. The spacing was reduced to 0.050” but they still were unable to be broken down. Reducing the gap further to 0.025” and 0.015” has led to reliable breakdown events occurring. Mould bodies have been fabricated to manufacture multiple 0.015”, 0.025”, 0.050”. or 0.100” samples at a time to speed

up testing. Initially, electrodes with a center-located field enhancement were used. The concern with using those is that it is difficult to derive the applied electric field since the field enhancement factor of a machined electrode is impossible to precisely define. More recently, electrodes with a Bruce profile have been used to apply a uniform electric field across the sample.

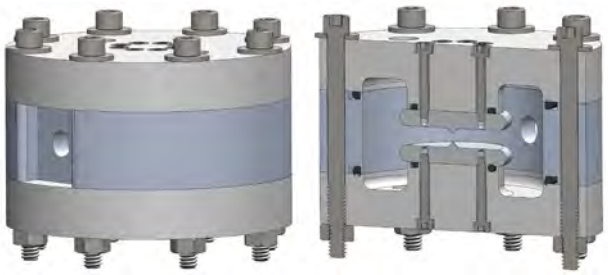


Figure 2. Rendering of epoxy sample mould assembly (left), section view of assembly where electrodes can be seen mounted inside the mould (right).

In Figure 3, an epoxy sample is seen after it was potted, both before (left) and during (center) the degassing phase. Also shown in the right side of Figure 3 is a sample made using field enhanced electrodes, circled in red, that have a visible carbon track left behind from a breakdown experiment. Simulations were performed to characterize the field enhancement factor as a function of varying tip radii, seen in Figure 4. The results, seen in Figure 5, plot the simulated enhancement factor when the radii are varied while keeping the separation between the flat sections of the electrodes constant (left), and while keeping the distance between the tip of the enhancement kept constant (right). Enhancement factors as high as 25 are feasible for the arrangement studied here. Figure 6 shows an epoxy sample fabricated using Bruce profiled electrodes before (left) and after (center) an electrical breakdown event. In the right side of Figure 6, a plot of the electrical data showing the breakdown voltage and current measured during testing.



Figure 3. Epoxy samples before and during degassing (left, center), and after breakdown (right).

In FY21, significant effort was invested to fabricate custom additive manufacturing filaments with and without additives. It will not be discussed in detail here but in short, the effort was not successful. Later in FY21 and into FY22, effort was spent identifying vendors that that could supply thermoset plastics with and without additives. Techmer PM in Knoxville, TN has been able to produce and supply limited composite plastic stock with and without additives. Their difficulty in supplying more has been the supply chain issues and low quantity needed to complete the proposed research. The material supplied by Techmer PM comes in thin sheets that are cut and compressed to produce samples to be broken down. A plastic pressing assembly was modeled and fabricated, seen in Figure 7, which compresses the material between the electrodes. This material sample with embedded electrodes is then potted in epoxy for rigidity. Figure 8 shows the process of creating a graded dielectric sample of fiberglass filled polycarbonate. Figure 9 shows a photograph of the sectioned sample after it was broken down, and the electrical data collected during that experiment.

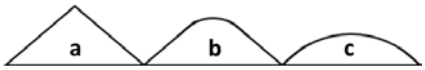


Figure 4. (a) Tip geometry with no smoothing. (b) Tip geometry with some smoothing. (c) Tip geometry with full smoothing, with a sphere at a 45-degree tangent to the electrode surface.

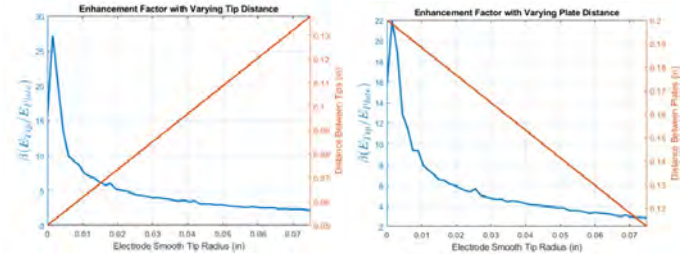


Figure 5. (left) Plot of the enhancement factor on the electrode tip versus the radius of the smoothed portion of the tip. As this radius increases, the inherent distance between the electrode tips also increases. (right) Plot of the enhancement factor on the smoothed electrode tip for a fixed electrode tip distance. Compared to a fixed plate distance, the enhancement factor does not reach as high and does not roll off as much.

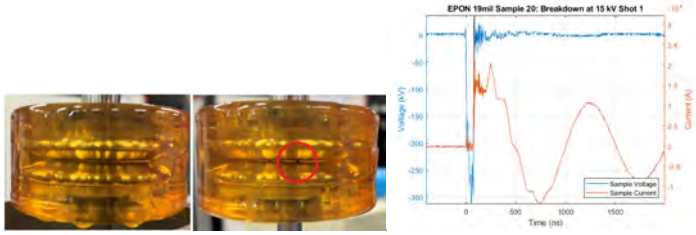


Figure 6. Epoxy sample before (left) and after (center) breakdown testing, carbon tracking (circled) can be seen between broken down sample's Bruce electrode faces. Breakdown voltage and current through the sample (right).



Figure 7. Plastic pressing assembly model cross-section, open assembly (left), compressed assembly (right).

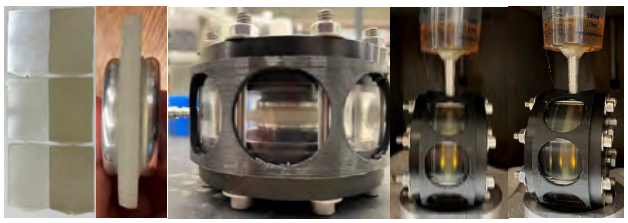


Figure 8. Compression and potting of 2-layer composite plastic sample (left), compressed layers between electrodes (second left), sample placed in epoxy mould (middle), mould filled with epoxy in vacuum chamber (right two)

M&S Efforts

Simulation efforts in FY22 focused on developing new M&S techniques to optimize the grading of dielectric constants in both simple and complex geometries. The model adjusts the dielectric constants of multiple layers of material at one or more hotspots/triple points to minimize the peak electric field at that location. This is performed by function minimization using fmincon in MATLAB. By having the dielectric constants as the input to the function f(ϵ_1…ϵ_n), MATLAB finds the minimum simulated E-Field with specified costs and constraints. Bounds are set as the expected maximum and minimum dielectric constants that are feasible for use and the output is the local maximum electric field observed in the area where the layers are generated. An example of this process is shown in Figure 10 where the solver is tasked with generating the nine layers of anonymous dielectric and optimizing their dielectric properties within a limiting range of ϵ = 2:20. The simple model shown consists of two rounded electrodes separated by up to nine layers of dielectric. The simple geometry was chosen to understand the optimization process and reduce simulation complexity, as numerous iterations of dielectric constants are needed, especially with many layers. The M&S development, and validation of it, is taking place in three stages. The first is using this simple geometry. The second has been performed using a more complex geometry with multiple hotspots. Eventually the plan is to study representative complex geometric models. Complex geometries are taking several days to complete so making sure the results are valid is important.

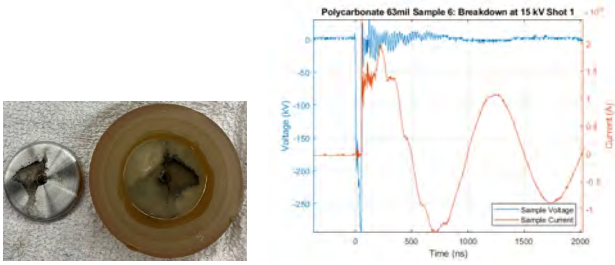


Figure 9. Visible carbon tracking from broken down sample after sectioning (lower-left) and breakdown voltage and current through the sample (bottom-right).

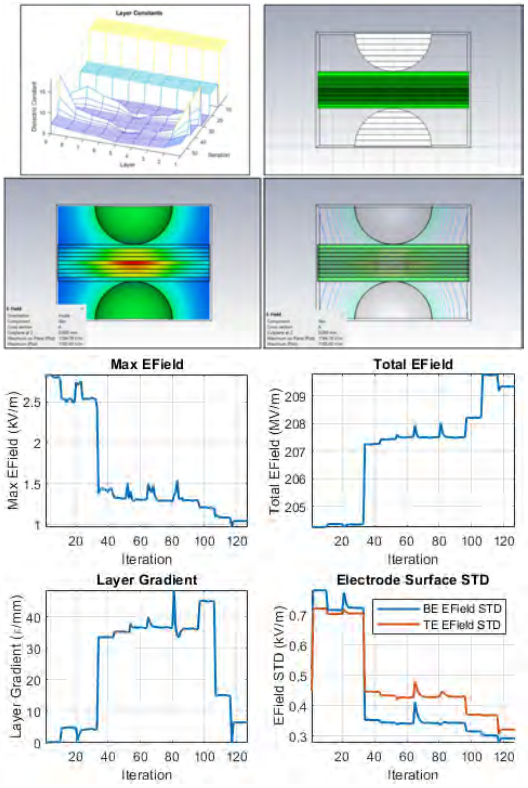


Figure 10. (row 1 left) Values of the dielectric constants for each layer from each iteration of the solver as it attempts to minimize the electric field of the model. (row 1 right) Electrode geometry with nine layers. The darker the layer, the lower the dielectric constant, etc. (row 2 left) E-Field. (row 2 right) Isoline display of fields. (row 3 left) Max E-Field for each iteration, the lower the value is from the first point, the better. (row 3 right) Total E-Field (summed value of the E-Field in the result file). The lower this is the better. (row 4 left) Gradient of the dielectric constants. The smoother the transition between different layers, the smaller the value. (row 4 right) Smoothness of the E-Field on the electrodes.

Dielectric Characterization

For the results collected here to be meaningful, it's critical that the dielectric properties of each sample be well characterized. The permittivity properties are most often measured using a vector network analyzer (VNA) connected to a dielectric test fixture in which samples are placed. Initially, it was desirable to measure the frequency dependent permittivity across a frequency range of 10s of MHz to 400 MHz, which represents what is typically measured in high voltage marx generators. Towards the end of FY22, additional funds were added to the grant to support the study of new dielectrics for use in non-linear transmission line (NLTL) applications, for which frequencies as high as 12 GHz are of interest. To simultaneously support characterization across both frequency ranges, a coaxial airline fixture was procured from MuEpsln. A 20GHz Anritsu Shockline VNA was ordered to be used with this test fixture. The samples loaded into the airline are coaxial samples with an outer diameter of 7 mm, inner diameter of 3 mm, and length of 5 cm, seen in the left side of Figure 11. Casting epoxy samples with these small dimensions and tight tolerances has proven to be difficult, but more recently success has been achieved using a mould fixture designed in-house as seen in the right side of Figure 11. This clam shell design appears to be working well and results will be shown in FY23.

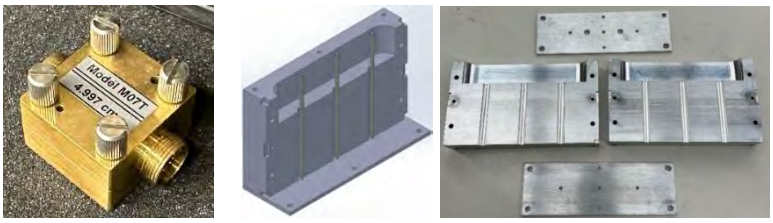


Figure 11. Coaxial airline (left), VNA mould split solid model (middle) and fabricated version (right).

3. Findings and Conclusions

A total of 32 samples were fabricated and tested in FY22. The samples were mostly EPON 815C epoxy samples with either 0.015" or 0.025" electrode spacing, utilizing either enhanced profile or Bruce profiled electrodes. Of the 32 samples, 3 of them were polycarbonate samples with glass fiber loading. Figure 12 shows a selection of breakdown data that has been collected using raw epoxy and Figure 13 shows data collected from all samples, including outliers, tested to date. This data includes samples that had physical issues, such as bubbles or cracking, and samples with odd behavior in the waveforms. Recently, sample preparation and testing has accelerated quickly as many samples are necessary for characterization of these materials due to the probabilistic nature of dielectric breakdown. Its very

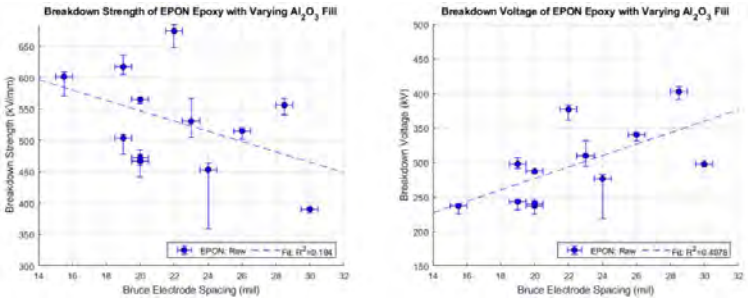


Figure 12. (left) Breakdown Strength for raw EPON. (right) Breakdown voltage for raw EPON.

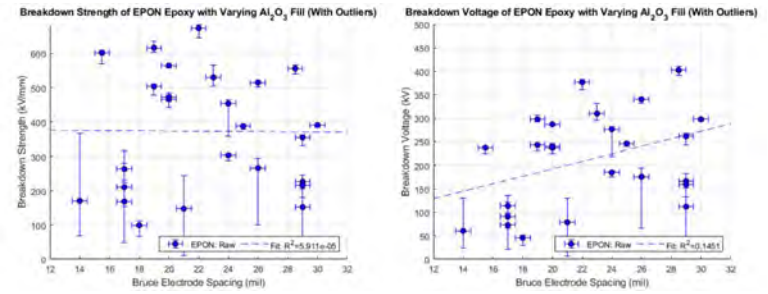


Figure 13. (left**)** Breakdown strength for all raw EPON samples. (right) Breakdown voltage for all EPON samples.

difficult to provide any definitive conclusions from the results collected to date. There have not been enough samples tested in each of the configurations presented to be statistically conclusive. The focus of FY23 work is to test at least 10 samples in each configuration and more results and conclusions will be made tests are complete.

4. Plans and Upcoming Events

In FY23, the plan is to significantly accelerate sample production and pulsed electrical breakdown testing. Samples with varying nanoparticle additives are being created to obtain a statistically relevant sample size. As described in the report, additional work was added towards the end of FY22 to study the frequency dependent dielectric properties of high permittivity materials that are of interest to the NLTL community. That work is being performed in collaboration with Purdue University and results will be presented in the next FY report.

5. Transitions and Impacts

There are many ways to transition this work including starting to apply it to relative HPM pulsed power supplies. A proposal has recently been submitted to the Joint Directed Energy Transition Office Center of Excellence proposing additional work studying potted dielectrics and particle suspension in liquid dielectrics for employment in pulsed power supplies and especially pulsed transformers. There is significantly more work to do studying raw and altered thermoset plastics that should also be explored based on the methods and preliminary results obtained here.

6. Collaborations

Collaborations are occurring with Cameron Pouncey (NSWC-DD), Jordan Chaparro (NSWC-DD), Matthew McQuage (NSWC-DD), Andrew Fairbanks (NSWC-DD), and Allen Garner (Purdue University).

7. Personnel

Principal Investigator: David Wetz, 2.9 months (504 hours of effort assuming a 2080-hour year), National Academy Member (N)
Co-investigator or Co-PI: None this FY, Allen Garner (Purdue Univ) added in FY23
Business Contact: Sarah Panepinto, Director of Grant and Contract Services, ogcs@uta.edu
Team Members: Listed as students below
Subs: None this FY (Purdue added at the start of FY23)

8. Students

Tyler Scoggin (2nd Year PhD Student), Hayden Atchison (3rd Year PhD Student), Scott Turpin (Student Asst. who only helped for one month), Alex Johnston (3rd Year PhD Student)

9. Technology Transfer

None to report

10. Products, Publications, Patents, License Agreements, etc.

Archival Publications

No Journal papers have been submitted to date but some are planned for FY23

Conference Papers

a. Title: ‘Finite Element Modeling (FEM) of Altered Dielectric Epoxy and Plastic Insulation Materials’
b. Authors: H.L. Atchison, D.A. Wetz, PhD, and S.T. Scoggin
c. Conference Name: 2021 IEEE Pulsed Power Conference
d. Conference Dates: December 13 – 16, 2021
e. Conference Location: Held virtually
f. Publication Status: Presentation only with no archival publication other than presentation
g. Publication Date: December 15, 2021
h. Publication Identifier Type: None
i. Publication Identifier: None
j. Acknowledgment of Federal Support: Yes

a. Title: ‘DC and Pulsed Evaluation of Altered Dielectric Insulation Materials’
b. Authors: S.T. Scoggin, D.A. Wetz, PhD, and H.L. Atchison
c. Conference Name: 2021 IEEE Pulsed Power Conference
d. Conference Dates: December 13 – 16, 2021
e. Conference Location: Held virtually
f. Publication Status: Presentation only with no archival publication other than presentation
g. Publication Date: December 15, 2021
h. Publication Identifier Type: None
i. Publication Identifier: None
j. Acknowledgment of Federal Support: Yes

a. Title: ‘High Voltage Breakdown of Altered Dielectrics’
b. Authors: S.T. Scoggin, D.A. Wetz, PhD, and H.L. Atchison
c. Conference Name: 2022 ONR 6.1 Basic Research Conference
d. Conference Date: September 6, 2022
e. Conference Location: Held virtually
f. Publication Status: Presentation only with no archival publication other than presentation
g. Publication Date: September 6, 2021
h. Publication Identifier Type: None
i. Publication Identifier: None
j. Acknowledgment of Federal Support: Yes

Books, Book Chapter, Theses, Websites, and Patents
None

11. Point of Contact in Navy

Mr. Ryan Hoffman, ryan.hoffman@navy.mil, ONR Directed Energy Weapons: High Power Microwaves Program Manager (Code 351), Last Contacted on November 20, 2021
Mr. Matthew McQuage, matthew.mcquage@navy.mil, NSWC-DD, Last Contacted on November 20, 2021

12. Acknowledgement/Disclaimer

This work was sponsored by the Office of Naval Research (ONR), under grant (or contract) number N00174-20-1-0025. The views and conclusions contained herein are those of the authors only and should not be interpreted as representing those of ONR, the U.S. Navy or the U.S. Government.

ONR Industry Grant Reports

Scaleup of Materials for Optimizing High Power RF Systems

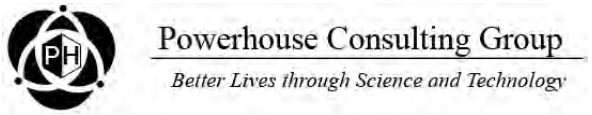
Grant No. N00014-21-1-2019

Annual Report for Fiscal Year 2022

Period of Performance: October 1, 2021 to May 30, 2022

Prepared by:

Dr. Somnath Sengupta, Principal Investigator
Powerhouse Consulting Group
3210 Boones Lane
Ellicott City, MD 21042-2138
Email: somnath@powerhouseconsultinggroup.com





This work was sponsored by the Office of Naval Research (ONR), under contract number N00014 -21-1-2019. The views and conclusions contained herein are those of the authors only and should not be interpreted as representing those of ONR, the U.S. Navy or the U.S. Government.

Grant Number: N00014-21-1-2019
Date Prepared: February 2023
Project Title: Scale up of materials for optimizing high power RF systems
Annual Summary Report: [FY22] – 10/1/2021 through 05/30/2022
Principle Investigator: Somnath Sengupta; somnath@powerhouseconsultinggroup.com, Powerhouse Consulting Group

Section I: Project Summary

1. Overview of Project

The purpose of this report is to provide an overall summary of the goals, objectives, and achievements of this program. It is not meant to be a compilation of the monthly reports, rather a broad view of the attributes of the scaleup of a class of low loss tunable dielectric materials for high power RF systems.

There were two primary **goals** for this grant: (a) **Scale up** of a family of novel tunable dielectric materials, and (b) **Assess** a family of magnetodielectric materials for high power RF applications. We have established that the scalability of the tunable dielectric materials is limited only by the size of the equipment available for scale up. As for the assessment of the magnetodielectric materials we have shown that with compositional variation one can avail of both phases of the materials through its magnetoelectric coupling coefficient when the dielectric material is in its low loss paraelectric composition. The secondary goals of testing the dielectric materials for high power applications showed that at 400 PEP of RF power, the materials are linear in their performance. Tunable thick films of the dielectric materials were also demonstrated for future high power RF electronics applications.

The benefits of frequency agility and beam shaping utilizing electronically tunable materials have been demonstrated in communication systems and sensing systems; for communication systems such advances have led to the 5G implementation. For high power microwave (HPM) such advances could mean avoiding equipment fratricide and tunable radomes that could switch its transmittance, as needed, to protect sensitive equipment. Sidelobe emission reduction may also reduce the radar cross section (RCS) of Naval antennas. Development of such a capability will assist in reducing EMI/EMC issues and assist in the transition of HPM DEW to the warfighter. Additionally, frequency and temporal agility can also enable HPM sources to generate unique waveforms leading to the defeat of electronic devices.

2. Activities and Accomplishments

The **approach** included the fabrication of the different form factors (bulk and thick film) of the materials and then measuring the material's response functions (ε', ε'', tunability, intermodulation products (IP3), and breakdown voltages). Tunability is defined as the % change in dielectric constant of the material with applied electric field. The simulation pathways were investigated by researching different machine learning algorithms for the data set that was available from our past work. The magnetodielectric materials were synthesized and the magnetic (inductance, saturation magnetization, and others) and dielectric properties (mentioned above) were measured.

The **results** showed that the material is manufacturable in a wide variety of form factors and can support many applications. We also showed that the material response was linear for high RF power incidence. A

two tone (114.6 W each signal) measurement with 400 W Peak Envelope Power (PEP) showed that the third harmonics were about -25.8 dBc from the two signals that were separated by 500 kHz @ 300 MHz frequency. So, it suffices to say that devices designed from our material will not have any significant impact on the IMD3 performance of the entire system. A modeling and simulation task for forecasting material properties concluded that to proceed further and develop a complete learning model one would need to collect data on all features of this material family *for many compositions*. Once those features are collected, the algorithm will determine the important feature sets to develop a learning model. As for the magnetodielectric materials, we were able to identify, *for the first time*, a magnetoelectric coupling coefficient that would enable high power RF devices where both the phases of the materials may be tuned by simply applying a DC voltage.

There were five tasks for the program- (a) to fabricate large pieces of tunable dielectric materials and measure the RF properties of the materials, (b) high power RF characterization of the tunable materials, (c)develop thick films of the novel tunable dielectric for future applications, (d) investigate a simulation pathway for discovery of new materials, and (e) assess a low loss magnetodielectric family of materials for high power RF applications.

a. **Scale up of dielectric materials**- Powerhouse has machined ceramics to pieces as small as 2 mm x 2 mm x 1 mm and as large as 4" x 4" ceramics. We have polished our ceramics to optical flatness to assure that these ceramics can be metallized and soldered for electrical connection. As for different shapes for potentially different applications, we have made annular rods, puck, flat panel pucks, and blocks (**Figure 1**).

.

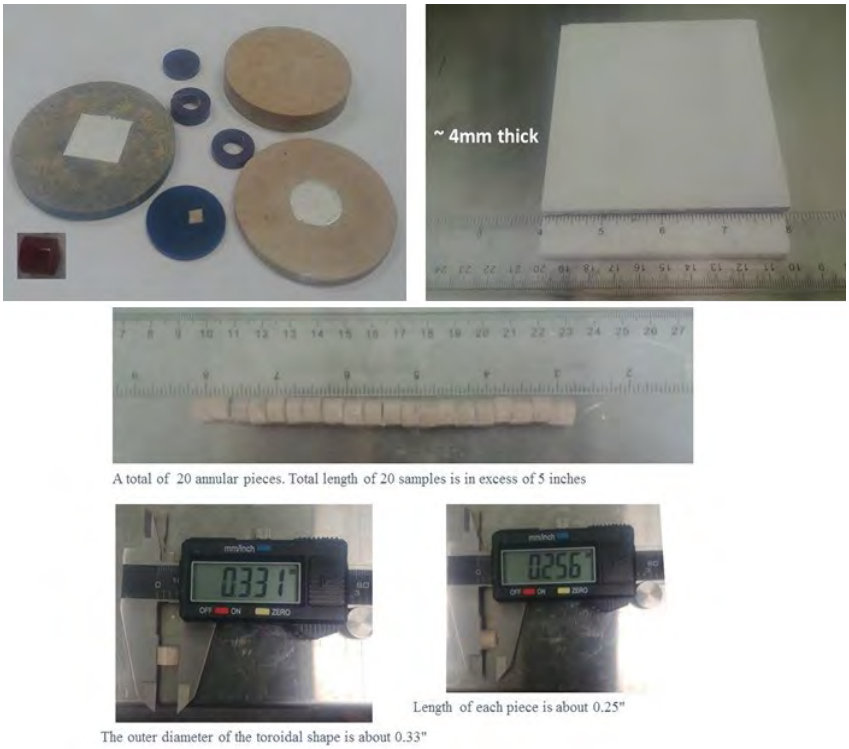


Figure 1. Powerhouse has demonstrated that our processes are repeatable and limited only by the availability of the processing equipment

As a future activity, we would suggest the development of slurry-based 3D printing of near net shapes for antenna and other subsystem applications.

b. **Development of thick film processes-** Thick films provide coplanar design opportunities along with the ability to integrate drop in components (passive and active) for compact RF designs. Thick films can withstand harsh and rugged environments and are considered extremely reliable in higher frequency circuits**.** The thick film had a 100-micron coplanar gap in its top electrode (silver) pattern. **Figure 2** shows the X-ray diffraction data for the thick film. All the peaks have been identified in reference to previously published data of x-ray diffraction patterns of BST and MgO.

As for the dielectric parameters of the thick film, the data showed (**Figure 3**) a clear voltage tunability on the capacitance of the film. There is also a clear effect in the down sweep (0V to -30V), at all frequencies. It must be emphasized that the maximum electric field applied across the gap was 0.3 V/micron (30 V/100 microns).

Figure 4 shows the insertion loss (tan δ) of the thick film. The thick films are very low loss across the frequency sweep and the insertion loss decreases with applied DC voltage since the capacitance decreases too.

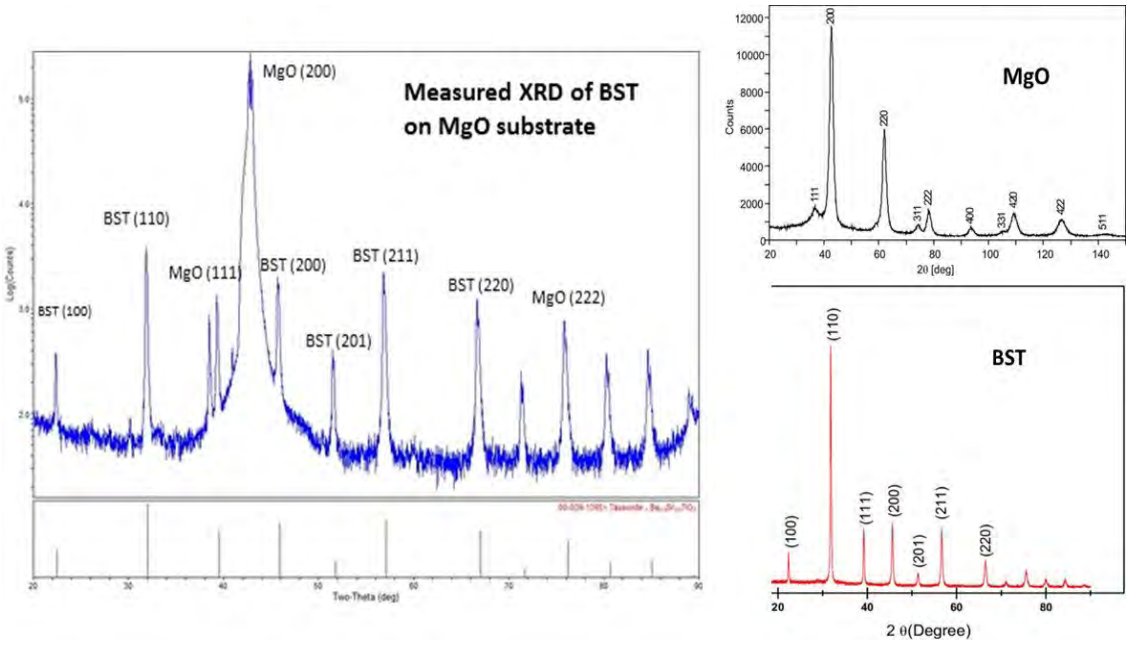


Figure 2. Xray diffraction data of the thick films show that the thick film attained the desired BST composition

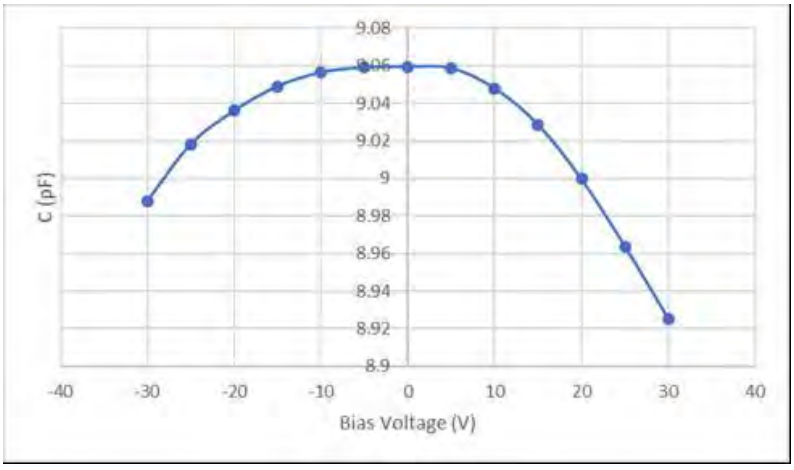


Figure 3. Tunability of the BST thick films at 1 MHz

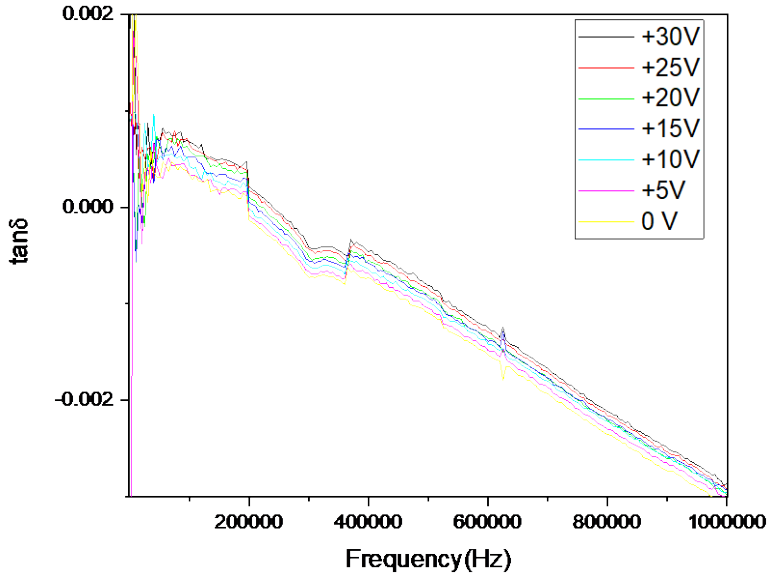


Figure 4. Low insertion loss was measured for the thick films across a kHz to MHz frequency range

So, in summary, we have demonstrated a commercial technique of printing thick films of the tunable materials and shown that the thick films can attain the tunability and maintain low insertion loss across a wide spectrum of frequency. For future work, our suggestion would be to identify a high-power RF application for thick film-based circuits to demonstrate the viability of these materials for such applications.

c. RF measurements of the ceramic materials

Powerhouse incorporates oxides in the BST matrix to modify its dielectric parameters. The variation of the dielectric parameters as a function of the wt% oxide incorporated in the BST matrix has been reported in the previously. An important step was to determine the temperature excursion of the dielectric materials. So, we decided to perform a Capacitance versus Temperature study of three compositions. Our study

showed that the doped samples are more stable in voltage cycling and show much less charge retention. ; *compositional variation can indeed reduce the hysteresis of the material over a wide temperature range*.

We performed 2-tone high power RF measurements to determine the 3rd order intermodulation products for our ceramic materials. During our previous contract we had performed similar experiments at 35 dBm and less input power for each tone. In our current experiments each tone of the experiment was at 50.6 dBm. The set up was a 50-ohm load in parallel with the dielectric material at the output of an amplifier.

The relevant parameters were:

- Tone 1: 300MHz
- Tone 2: 300.5MHz
- Output power (Peak Envelope Power): 400W
- Tone power: 114.6W/ea (50.6 dBm)

Table 1 compares the results of the previous and current measurements.

Composition A (60/40 BST with ~9 wt% dopant)			
F1 (dBm)	**F2 (dBm)**	**2f2-f1 (dBc)**	**2f2-f1 (dBc)**
35	35	-33	-33
Composition B (60/40 BST with ~16 wt% dopant)			
26.4	26.4	-32	-32
Composition C (60/40 BST with ~60wt% dopant)			
24.9	24.9	-31.7	-31.8

BST			
F1 (dBm)	F2(dBm)	2f1-f2(dBc)	2f2-f1(dBc)
50.6	50.6	-25.8	-30.3
Air			
50.6	50.6	-25.9 dBc	-30.5 dBc

These results show that 100W CW signals are not enough to distort the response of the ceramic. There was no heating observed in the ceramic sample although one may want to measure larger pieces for investigating the thermal effects. *The pulsed power tests to be performed at NRL will further establish the viability of these tunable ceramics for high power RF applications.* Peak envelope power (PEP) is the average power over a single RF cycle at the crest of the modulation the power level for the INSTANT that all the voltage vectors line up in phase to a max value. That is where circuits and component clip the signal and cause IMD. ***It is significant that our material performed without any issue at 400W PEP.***

d. Development of modeling and simulation pathways

To perform any machine learning approach, we would need copious amount of data points (values of epsilon and loss tangent for a multitude of compositions) AND the relevant features for all these material

compositions. The machine learning algorithm would then forecast the relevant feature set for the material compositions. One would then interpolate compositions that were not in the data set, synthesize the compositions and compare the measured and predicted properties to validate the model. Most regression models just end up learning a function that includes all the data points, the region between data points is just linear extrapolation. **Table 2** shows the relevant features[8].

To develop a "learning" model, we chose 29 different compositions at a single frequency and annotated them numerically (**Table 3**). The composition IDs are in ascending order of barium %

in that case what the models learnt was the target values as barium % keeps increasing. (Numerically larger composition ID = higher barium % = different target value). We interpolated the composition IDs in 0.1 value increments, so if `-1` = 0% barium, `0` = 5% barium, `-0.9` = 0.5% barium, `-0.8` = 1% barium, etc . With these new IDs `[-1, -0.9, -0.8.... 27.8, 27.9, 28]`, we had the models predict the target values for each, and plot them against actual known values, to better visualize the function the models had learnt from the training data.

The article by J.Qin, Z.Liu, and M.Maetal. titled "Machine learning approaches for permittivity prediction and rational design of microwave", Dielectric ceramics, Journal of Materiomics, https://doi.org/10.1016/j.jmat.2021.02.012 provided us with a path forward to utilize the Gaussian process regressor (**Figure 5 and 6**).

Table 2. Relevant features for developing the machine learning algorithms

- **Ppv (polarization per unit volume)-** 0.165 C/m^2 (for Barium Titanate)
- **d- theoretical density-** between 6.02 gm/cm^3 (for Barium Titanium Oxide) to about 4.96 gm/cm^3 (for Strontium Titanium Oxide)
- **bg- Bandgap-** 1.725 eV (Barium Titanate) to 1.827 eV (for Strontium Titanate)
- **Blm- average bond length-** 2 to 3 angstroms
- **fepa – Formation energy per atom (eV)-** -3.477 eV (for Barium Titanate) to -3.551 eV (for Strontium Titanate)
- **Bpa- number of bonds per atom**- 8 for the center Barium atom to 4 for the corner oxygen atom
- **Ord- order of symmetry-** Tetragonal (for Barium Titanium Oxide) to Cubic (for (Strontium Titanium Oxide)
- **Ne- number of elements-** 3 (when it is Barium Titanium Oxide) to 4 (when it is Barium Strontium Titanium Oxide)
- **na- number of atoms-** 3 atoms (in Barium Titanium Oxide) to 4 atoms (in Barium Strontium Titanium Oxide)
- **cat- number of cations-** 2 (in Barium Titanium Oxide) to 3 (in Barium Strontium Titanium Oxide)
- **ani- number of anions-** 3 (in Barium Titanium Oxide) to 3 (in Barium Strontium Titanium Oxide)
- **Vm- primitive cell volume**- 64.36 $angstroms^3$ (for Barium Titanate) to 61.402 $angstroms^3$ (for Strontium Titanium Oxide)
- **M- molecular mass-** 233.192 g/mol (for Barium Titanate) to 183.49 g/mol (for Strontium Titanium Oxide)
- **Dielectric permittivity range-** 7000 (for Barium Titanium Oxide) to 300 (for Strontium Titanium Oxide)
- **Insertion loss-** 0.03 to 0.003

[8] J.Qin,Z.Liu,M.Maetal.,Machine learning approaches for permittivity prediction and rational design of microwave Dielectric ceramics, Journal of Materiomics, https://doi.org/10.1016/j.jmat.2021.02.012

Table 3. A wide variety of compositions and their respective dielectric parameters were chosen from past data

Composition		Frequency (1 MHz)
		ε
	-1	350
	0	4448.1
	1	1047.33
	2	1566.22
	3	1167.18
	4	895.78
	5	886.45
	6	650.91
	7	433.43
	8	425.18
	9	306.92
	10	188.65
	11	89.35
	12	2256.5
	13	2193.2
	14	1386.5
	15	649.9
	16	263.52
	17	198.25
	18	3299.1
	19	2267.4
	20	1264.6
	21	842.23
	22	413.04
	23	76.7
	24	2515.3
	25	1868.9
	26	1016
	27	389.06
	28	93.591

Composition		Frequency (1 MHz)
		tanδ
	-1	0.0008
	0	0.0002
	1	0.00149
	2	0.00141
	3	0.00118
	4	0.00106
	5	0.00096
	6	0.00076
	7	0.00087
	8	0.00065
	9	0.00092
	10	0.01176
	11	0.00065
	12	0.0014
	13	0.0021
	14	0.0022
	15	0.0021
	16	0.0056
	17	0.0085
	18	0.0066
	19	0.005
	20	0.0057
	21	0.0146
	22	0.0313
	23	0.0125
	24	0.0011
	25	0.0013
	26	0.0327
	27	0.0009
	28	0.0022

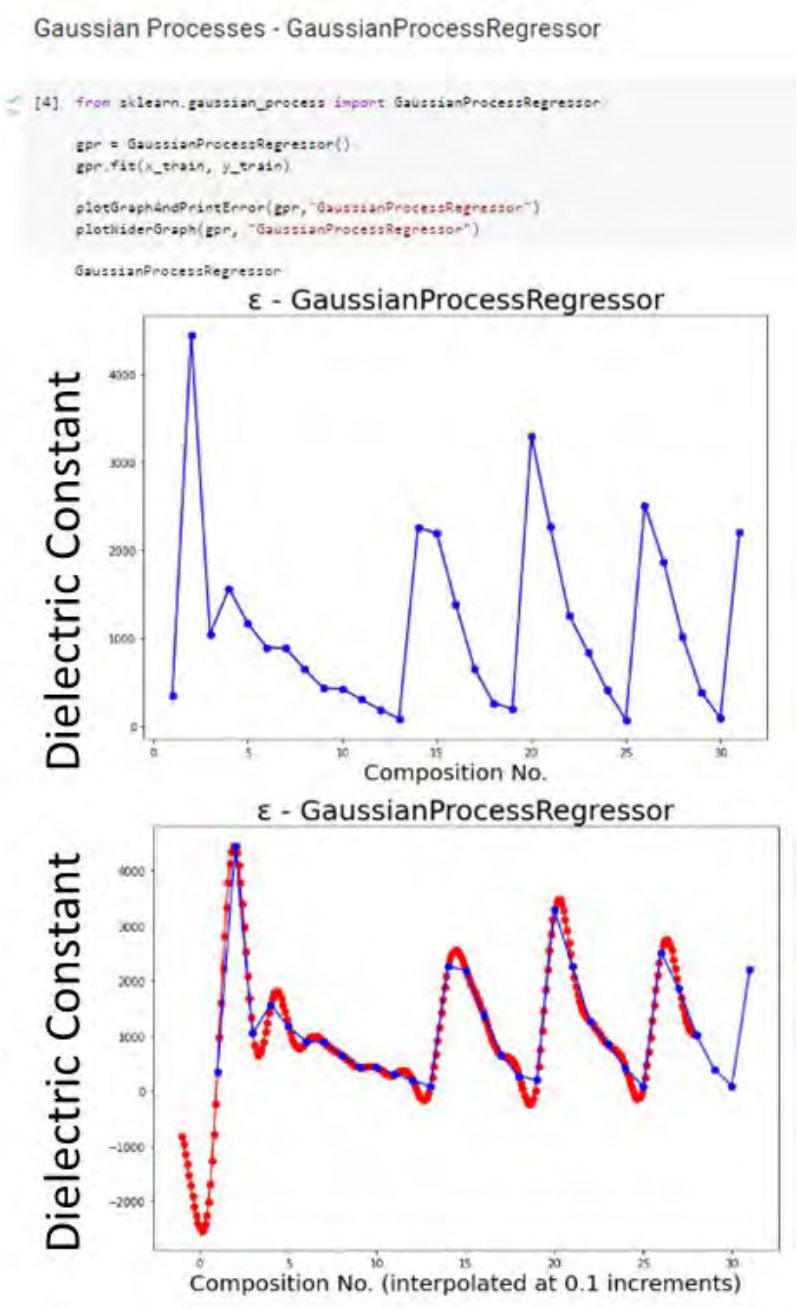


Figure 5. The Gaussian regressor model fit for the tunable dielectric material epsilon data shows a decent fit for forecasting future compositions

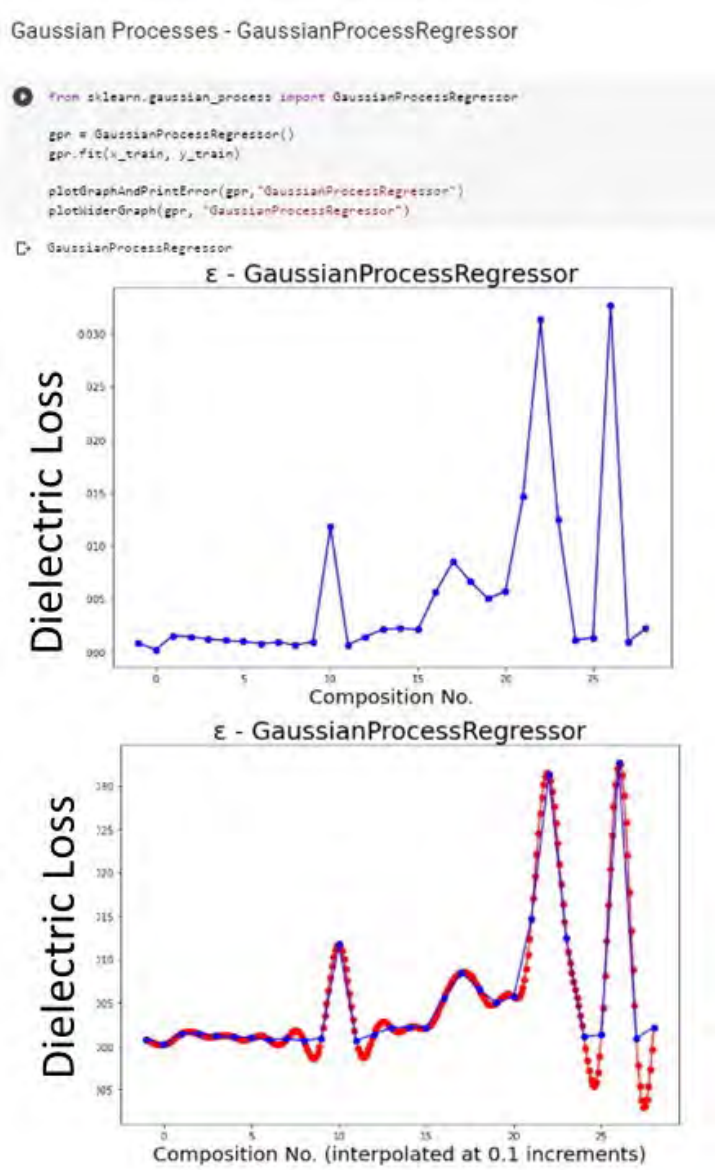


Figure 6. The Gaussian regressor model fit for the tunable dielectric material loss data shows a decent fit for forecasting future compositions

Although these were encouraging data to proceed further, we have to collect the data for the feature set for ***all material compositions***. Those data were not available in the literature.

At this point, we can surmise that we can utilize the gaussian process regression model to develop a systematic learning and material discovery model for the Barium Strontium Titanate family of tunable dielectric materials provided we can collect the data for the feature sets as shown in Table 1.

e. **Assessment of magnetodielectric materials for RF applications**

Magneto-dielectric or multiferroic materials are those which offer the advantage of dielectric and magnetic properties in one material. The task was oriented towards studying magnetodielectric materials whose saturation magnetization values were 0.2 Tesla or higher and the dielectric part will be a lead-free tunable material. ***The objective of this task was to observe and understand the trends of magnetic and dielectric properties of these magnetodielectric materials.***

Conventional ceramic processing techniques were used to fabricate discs and toroids of the materials (**Figure 7**). Sintering temperatures were chosen from literature based on highest saturation magnetization values. X-ray diffraction technique was utilized to study the compositional characteristics of the materials.



Figure 7. Three different compositions of BST/YIG; toroids (for L measurements), and discs (for C measurements). All compositions were measured via toroidal and disc samples.

The cylinders were screen printed with silver contacts for dielectric measurements while the toroids were wound with wires to form the coils for magnetic measurements. The minimum number of turns for coils was 14. The formulae used for calculating the dielectric constant and loss were:

$$C = (\in_r * \in_0 * A)/d$$

where C is the measured capacitance by a LCR meter in Farads, ε_r is the relative permittivity to be calculated, ε_0 is the absolute permittivity= $8.854*10^{-14}F/m^2$, A is the area of the material under the electrode (m^2) and d is the thickness in meters. This renders a dimensionless value for ε_r. The LCR meter calculates the tanδ value of the material by taking a ratio of the complex part of ε_r and the real pat of ε_r.

The μ_r values were calculated using the formula:

$$L = \frac{\mu\ N^2 H ln(b/a)}{2\pi}$$

where L= measured inductance in Henry, N is the number of turns of the coil, H is the thickness of the toroidal ceramic, b is the outside radius of the toroid, and a is the inside radius of the toroid. The μ_r is obtained by dividing the μ value from the above equation by μ_0=- $4\pi*10^{-7}$. A DE 5000 LCR meter was used for dielectric and magnetic measurements. To verify our magnetic measurements, we purchased a commercial toroid rated with a μ_r value of 900. Our measurements produced a value of 910, *a good match to proceed with confidence in measuring newly fabricated magneto dielectric materials.*

As CoFe did not produce any intermediate phase, we hypothesized that any effect on the magnetic properties of the $CoFe_2O_4$ might occur due to the inclusion of the dielectric phase in the magnetic material. As such, three $CoFe_2O_4$ samples were created- Sample A1, Sample A2, and a Sample A3. A calibrated Microsense VSM EZ11 HF magnetometer was used for the measurements. The hysteresis measurements were made along both the in plane (IP) and out of plane (OOP) directions. Sample rod and

tape correction ignored since the rod measured 4-5 orders of magnitude lower than sample signal; 10^{-5} emu for rod/tape, compared to 10^{0}-10^{-1} emu for samples. The saturation magnetization (M_s) values were extracted from linear regression of the saturated region that corresponds to the linear paramagnetic response; thus the y-intercept of a linear fit will give M_s. The saturation magnetization (M_s), coercivity (Hc), and squareness ration (M_r/M_s) were extracted for each sample both IP and OOP. H_c is the field at which the magnetization switches sign. M_r is the remnant magnetization at 0 field while Ms values differed for the IP and OOP directions but were all within 10% of each other. Coercivities were effectively identical regardless of field direction. The squareness ratios were similar regardless of material composition, with IP being squarer than OOP. **Table 4** is a summary of the calculated data.

Table 4. Saturation magnetization values of magnetodielectric materials

Sample	$M_s\ (emu/cm^3)$		$H_c\ (Oe)$		Squareness (M_r/M_s)	
	IP	OOP	IP	OOP	IP	OOP
A1	261 ± 1	277 ± 1	767	767	0.46	0.34
A2	98.2 ± 0.2	89.3 ± 0.3	422	419	0.48	0.39
A3	156.3 ± 0.7	160.2 ± 0.8	826	825	0.47	0.39

We observed that

1. The saturation magnetization (M_s) is the maximum magnetic moment per unit volume for a magnetic material; a higher value indicates potential for miniaturization. In our data, we see an about 60% drop in the M_s value of the CoFe (Sample A) with the additive (Sample A2) whereas the drop in the M_s value with the same wt% of additive amounts to about 40% for Sample A3.

2. The coercive field (H_c) or coercive force, is a measure of the ability of a ferromagnetic material to withstand an external magnetic field without becoming demagnetized. The addition of Sample A2 results in a 45% drop in the H_c value of the mixture whereas in Sample A3 **increases** the coercive field by about 8%.

Although these are very few data points, it provides some insight into the direction of the future research for selecting compositions for low loss magnetodielectric materials. It is clear that the wt% of BST must be in 10% of less; addition of other oxides for lowering the loss must also occur at low wt% (5 wt% or less).

3. Findings and Conclusions

The **outcome** of the work has provided us with an understanding of the scalability of the tunable dielectric materials for high power RF applications. RF power handling characteristics are also understood; *they have much lower inter modulation products than active components at similar power levels even at a 100W CW level.* As for manufacturability, the robust nature of the material was proven through machining of a wide variety of shapes and sizes. The results from the assessment of the magnetodielectric materials opens a whole new domain of fabricating and designing components and systems based on these materials. The **key technology advancement/payoff** are to demonstrate the scalability of the tunable material such that the system designers can conceptualize frequency agile systems for directed energy applications. In summary, the scalability questions were answered to justify a Phase 3 proposal to investigate application specific measurements of tunable dielectric material-based delay lines for ultrawide band pulse generators.

4. Plans and Upcoming Events

We surmise that for the next phase of the work we will be utilizing the compositions to fabricate the delay line components for high power RF testing and incorporation into an ultrawide band generator to create different waveforms.

5. Transitions and Impacts

Not Applicable

6. Collaborations

1. NRL High Power Microwave Section, Code 5745 - The Code 5745 HPM team has been the cornerstone of our work with regards to HPM applications; locating adequate measurement facilities within NRL, and discussing future applications to steer the work towards meaningful data collection. The collaboration continues. Powerhouse and Code 5745 team will perform application specific measurements of these tunable materials for ultrawide band pulse generators.
2. NRL Advanced Materials Section, Code 6127- The Code 6127 team has been a great collaborator during the fledgling days of this program and through the COVID-19 ordeal. Under a CRADA, the team has provided help with sintering, XRD, and other analysis techniques.
3. Softronics, Ltd.-Softronics is a radio manufacturer. They have extensive experience in the measurements of properties like intermodulation distortion and high bias field performances.
4. NSWCDD E13, HPM Technology Development Branch -NSWCDD and Powerhouse has continued their collaboration throughout this phase. Powerhouse has shared our data with him to enable him to develop concepts for applications.

7. Personnel

Key Personnel- Somnath Sengupta
Category- Principal Investigator
Nearest Person Month- 900 hours of effort over 18 months
National Academy Member- N

8. Students

Although not part of the official program, Powerhouse trains adults with autism on the laboratory skills related to this project.

9. Technology Transfer

None

10. Products, Publications, Patents, License Agreements, etc.

None

11. Point of Contact in Navy

Dr. Zachary Drikas; Code 5745; Naval Research Laboratory. Last Contact: August 2022.
Dr. Andrew Fairbanks; Naval Surface Warfare Center - Dahlgren Division. Last Contact: August 2022
Dr. Matthew Laskoski, Code 6127; Naval Research Laboratory. Last Contact: July 2022.

ONR Young Investigator Program (YIP) Reports

Surface Breakdown and Plasma Formation in Cross-Field High Power Microwave Sources

Grant No. N00014-21-1-2698

Annual Report for Fiscal Year 2022

Period of Performance: October 1, 2021 to September 30, 2022

Prepared by:

Professor Ken Hara, Principal Investigator
Assistant Professor, Department of Aeronautics and Astronautics
Stanford University
DURAND 252
Stanford, CA 94305
Email: kenhara@stanford.edu

This work was sponsored by the Office of Naval Research (ONR), under grant number N00014-21-1-2698. The views and conclusions contained herein are those of the authors only and should not be interpreted as representing those of ONR, the U.S. Navy or the U.S. Government.

Grant or Contract Number: N00014-21-1-2698
Date Prepared: February 18, 2023
Project Title: Surface breakdown and plasma formation in cross-field high power microwave sources
Annual Summary Report: FY22
Principle Investigator: Ken Hara, kenhara@stanford.edu, Department of Aeronautics and Astronautics, Stanford University

Section I: Project Summary

1. Overview of Project

Abstract: In this annual report, we summarize the activities on the recently awarded ONR (YIP) grant "Surface breakdown and plasma formation in cross-field high power microwave sources" covering the period October 01, 2021 – September 30, 2022.

Objective: The goal of this proposed research project is to advance the understanding of surface breakdown and plasma formation in cross-field HPM devices. Specific research objectives include: (i) to develop and test electromagnetic plasma fluid and kinetic models; (ii) to characterize the space charge limited sheath due to the plasma formation near explosive emission cathodes; and (iii) to investigate the anode plasma formation and radiofrequency wave-driven surface breakdown mechanisms.

Introduction: Plasma dynamics in high power microwave (HPM) sources are considered a detriment to the operation of vacuum electronic devices (VED) to generate electromagnetic signals. The formation and existence of the plasma flows become more and more critical, particularly when operating the HPM sources at a high-frequency range, which is of great interest to the future of U.S. naval missions. While HPMs theoretically must operate in high vacuum conditions, due to available materials and operating conditions, outgassing can occur from materials. This issue becomes more problematic for compact HPM devices because the volume-to-area ratio worsens, and the plasma-wall interactions greatly influences the electromagnetic wave properties. For instance, pulse shortening of the microwave output signal due to gap closure and lifetime of the device can highly depend on the charged particles. The breakdown processes in atmospheric conditions on the surfaces (e.g., antenna) is another area in which such plasma formation is problematic.

Background: We are developing high-order (five- and ten-moment) fluid models and particle-based kinetic models to study plasma formation, providing an efficient model for the dense plasma formation around the anode, cathode, and window surfaces, such as the antenna. The fluid and hybrid fluid-kinetic models will be benchmarked against particle simulation results to assess whether reduced-order description can be constructed to model the beam-plasma interactions in the HPM devices.

Naval relevance: The research outcomes can help (i) address existing issues in the HPM sources developed and deployed by the U.S. Navy, and (ii) improve the optimization and design processes of the future HPM sources using the predictive modeling capabilities developed through this project. In addition, advancing the fundamental understanding of the interaction between plasma flows, electromagnetic waves, and plasma-immerse materials possesses further immense impacts to other DoD applications and missions, including space propulsion, fusion energy, space weather, aerodynamics, combustion, and material processing.

2. Activities and Accomplishments

In the present project, we aim to understand and characterize the plasma sheaths so that a high-fidelity model can be constructed to understand the time-dependent plasma behavior as well as the electron emission characteristics. The emitted electron flux, the ion flux from the plasma, the electron from the plasma, and neutral flux due to outgassing can contribute to the plasma formation near the electrodes. It is expected that in the presence of large electron emission (such as due to field emission, ion/electron-induced secondary electron emission, thermionic emission) the plasma sheath becomes space charge limited (SCL). The structure of the plasma sheath will likely play an important role in the plasma formation and how much electron emission occurs within the vacuum electronic device (VED).

A. Magnetized plasma sheath

The set up that we consider is a 1D (one dimensional) plasma sheath in the presence of an oblique magnetic field, as shown in Figure 1. The amplitude is denoted using α and the angle with respect to the normal direction to the wall is θ. What we have observed is that the gyrating electrons will go back to the buffer zone, considering x = 0 to be the injection plane.

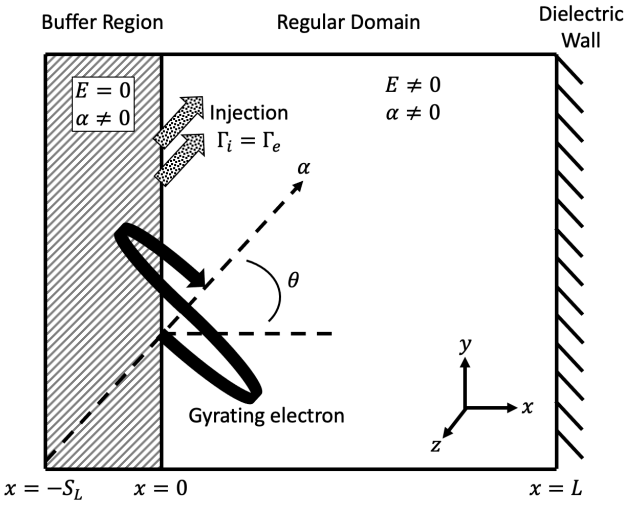


Figure 1. Magnetized plasma sheath setup.

The key parameters that dictate the plasma flow into the plasma sheath include:

- Ion bulk velocity. Here, the ion bulk velocity in the x direction (direction normal to the wall) is $u_{ix} = Au_B$, where A is a coefficient and u_B is the Bohm velocity that is equivalent to the ion acoustic speed.
- Electron velocity distribution function (VDF). Usually, in plasma sheath theory, a Maxwellian distribution is considered. However, with the magnetic field, electrons with different velocities can experience different Larmor radii, resulting in some considerations at the injection plane. Here, we observed that the electrons with larger Larmor radius are rarer as these correspond to the high-energy tail of the distribution function. Once these electrons gyrate back to injection plane, then they are lost and another electron is reinjected. This reinjection can create a discontinuity in the plasma properties near the injection plane, leading to a numerical oscillation, as shown in Figure 2. Thus, to mitigate the effects of reinjection, we have defined a cutoff velocity v_c in the velocity parallel to the magnetic field, over which the high energy electrons remain their trajectory.

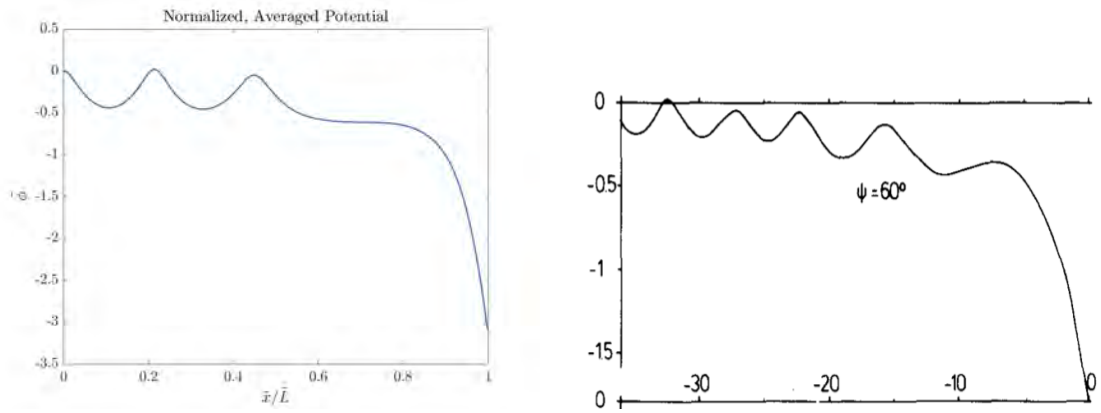


Figure 2. Normalized potential distribution, $\theta = 60°$ (magnetic field is becoming parallel to the wall). Left: our result (with $m_i/m_e = 1836$). Right: Chodura's result ($m_i/m_e = 100$).

Figure 2 shows the results of the plasma sheath simulation when assuming the angle of the magnetic field with respect to the direction normal to the wall is 60 degrees. It is interesting to observe thay there are some plasma oscillations that appear the plasma sheath edge, while the potential drops near the wall similar to the nonmagnetized case. Chodura named this oscillatory region to be a *magnetic presheath*. However, our recent simulations and analysis show that these oscillations may be due to the fixed injection scheme.

One of the key observations is that the wall generates a loss cone for the electron loss mechanism, as shown in Figure 3. The electrons are sampled based on its velocity along the magnetic field $v_{\parallel}$ and its velocity across the magnetic field $v_{\perp}$. Considering that there is a potential distribution as shown in Figure 2, the minimum velocity is based on the magnitude of the potential drop. However, the minimum velocity line is also dependent on the electron trajectories as the gyromotion allows for the electrons to be absorbed at the wall.

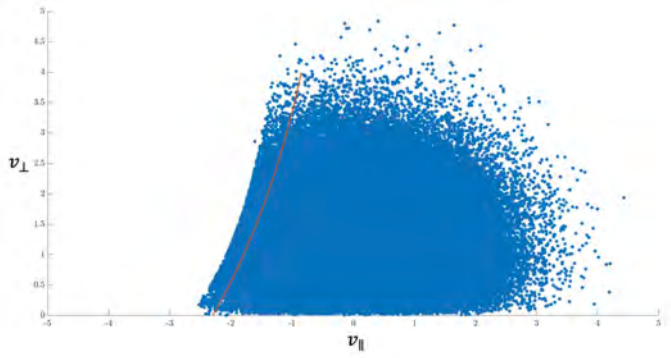


Figure 3. The electrons in the quasineutral region for the oblique magnetic field case. Red line indicates the theoretical line of the cutoff.

By changing the ion bulk velocity and the electron cutoff velocity, we were able to observe that the plasma oscillation is significantly dampened. As shown in Figure 4, when the ions are injected slower (blue line) there is a plasma potential profile that accelerates the ions into the domain and when the ions are injected faster (red, yellow, and purple lines) there is a plasma potential profile that decelerates the ions. Thus, indicating that there is an optimal ion injection velocity.

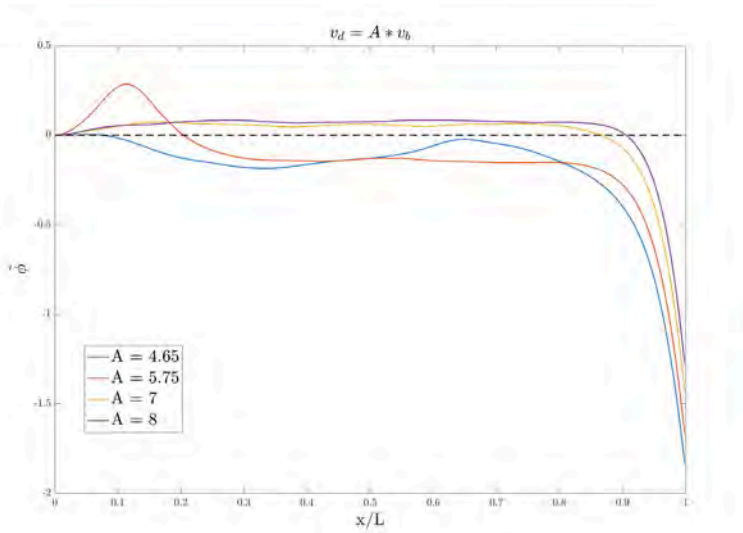


Figure 4. Averaged normalized potential distribution for a large magnetic field (almost parallel to the wall) $\theta = 80°, \frac{m_i}{m_e} = 1836, \text{and } T_i = 0.$

Similarly, Figure 5 shows the plasma potential profile when modifying the electron cutoff velocity. In the new boundary condition, when an electron returns to x = 0, if its parallel velocity, $v\|$, is less than a prescribed cutoff velocity, v_c, the electron is deleted and a new electron is injected sampling from the appropriate distribution. However, if the parallel velocity is greater than the cutoff velocity, the electron is immediately re-injected using the velocity that it would have if it was returning to the injection plane after gyrating in the $x \leq 0$ region. Larger v_c results in a potential increase near the injection plane, indicating that the electrons are too slow. However, when v_c is chosen to be smaller, the electrons are too fast, resulting in a decelerating potential profile. We can conclude that the choice of the ion and electron injection velocities play an important role in minimizing the potential oscillations in the computational domain.

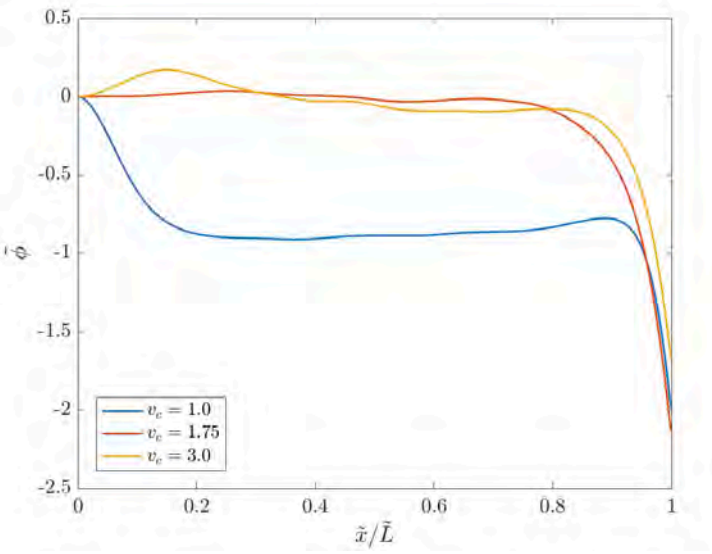


Figure 5. Potential distribution for different cutoff velocity values, which essentially changes the bulk velocity for the injected electrons.$\theta = 80°$, $\frac{m_i}{m_e} = 1836$, and $T_i = 0$.

B. Full fluid moment (FFM) modeling and rotating spokes

We are also developing a full fluid moment (FFM) model for low-frequency cross-field plasma discharge oscillations. Figure 6 shows the application of a 5-moment model that accounts for the electron inertia term showing rotating spokes on the order of 100 kHz. The spoke propagates in the diamagnetic drift direction. This have led to revisiting of the so-called modified Simon-Hoh instability that is often cited for rotating spoke studies. This work resulted in two peer-reviewed journal articles, one of which acknowledges the ONR support.

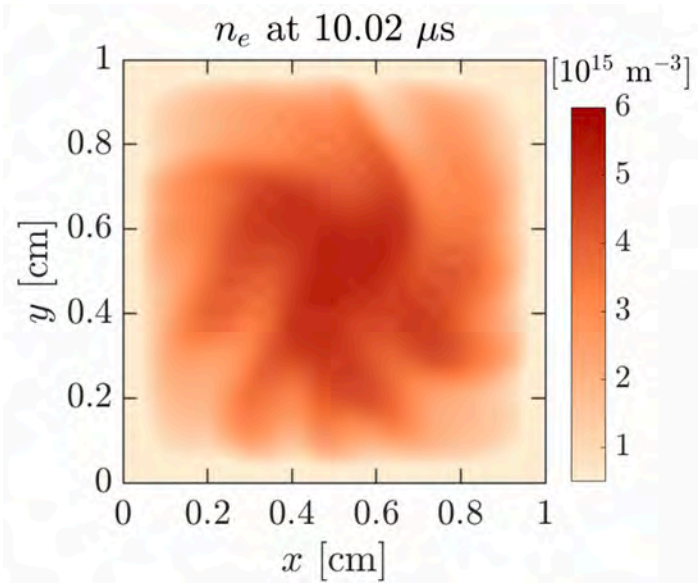


Figure 6. Plasma density of a rotating spoke. The magnetic field is into page and the boundaries are at 0V, setting up a quasineutral plasma and a rotation of the spokes in the azimuthal direction.

C. Plasma formation study

We have started diode simulations with the goal to reproduce the results from Welch's work [Phys. Plasmas 16, 123102 (2009); https://doi.org/10.1063/1.3270471]. The referenced work accomplishes the modelling of a simple planar diode using a 2D cylindrical, collisional, electromagnetic PIC simulation. The cathode injection scheme is a simplification of a process where field emitted electrons ionize the surrounding neutral gas, creating a region of weakly ionized gas followed by a quasineutral region. The ionization due to emitted electrons is simplified through a two-part injection scheme; from the cathode, electrons are injected according to field emission and neutral particles are injected with a constant flux. The neutral particles then uniformly become and electron-ion pairs within two computational cells of the cathode, establishing the two regions of weakly ionized gas and quasineutral plasma near the cathode.

Our initial simulations aim to build a 1D representation of this model. We first developed the electron field emission component of Welch's injection scheme. Considering the cathode injection scheme is based on cold cathode electron emission and its similarity to explosive electron emission, the Fowler-Nordheim equation is chosen for the injection of electrons. According to this relation, the current density of emitted electrons is defined as

$$J_{FN} = \frac{A(\beta E_C)^2}{\phi_W t^2(y)} \exp\left(-\frac{B v(y) \phi_W^{1.5}}{\beta E_C}\right) \left[\frac{A}{m^2}\right],$$

where E_c is the electric field on the cathode surface, β is a local enhancement factor, ϕ_W is the material work function, $y = \sqrt{\frac{eE_c}{4\pi\epsilon_0}}/\phi_W$, $v(y) \approx 1 - y^{1.69}$, $t(y) \approx 1 + 0.1107y^{1.33}$. The latter two factors are corrections for image charge effects. The constants A and B are defined as $A \approx 1.53 \times 10^{-6}$ $\left[\frac{A\ eV}{V^2}\right]$ and $B \approx 6.83 \times 10^9$ $\left[\frac{V}{eV^{1.5}m}\right]$. The emission model is based on this equation and is verified with work by Feng and Verboncoeur [Physics of Plasmas 13, 073105 (2006); https://doi.org/10.1063/1.2226977].

Assuming a work function of 2 eV and a diode length of 10^{-6} m, a constant anode voltage leads to a constant applied electric field on the cathode surface to initiate the emission model. Figure 7 shows the simulation results of the steady-state emitted current density for a range of applied electric field. For comparison, the Fowler-Nordheim current density calculated using the applied electric field and Child's law for space-charge limited current density, $J_{CL} = \frac{4\epsilon_0}{9}\sqrt{\frac{2e}{m_e}}\left(\frac{V^{1.5}}{d^2}\right)$, is also plotted. This result shows good agreement with Feng and Verboncoeur. It also exemplifies that for applied electric field's below $2 \times 10^9\ V/m$ the electron injection is limited by the field emission process. For higher applied electric field, the injection is limited due to space-charge effects. Figure 8 further aids in the verification of the field emission model by comparing the transient electric field at the cathode for one of the simulated cases with Feng and Verboncoeur.

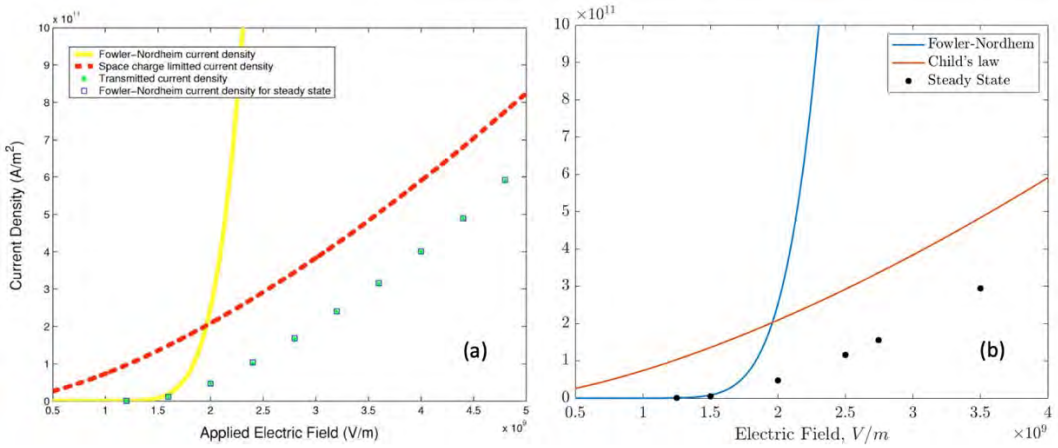


Figure 7. Steady-state emitted current density. (a) PIC from Feng and Verboncoeur. (b) Our result. Compared with Fowler-Nordheim and Child's law relations.

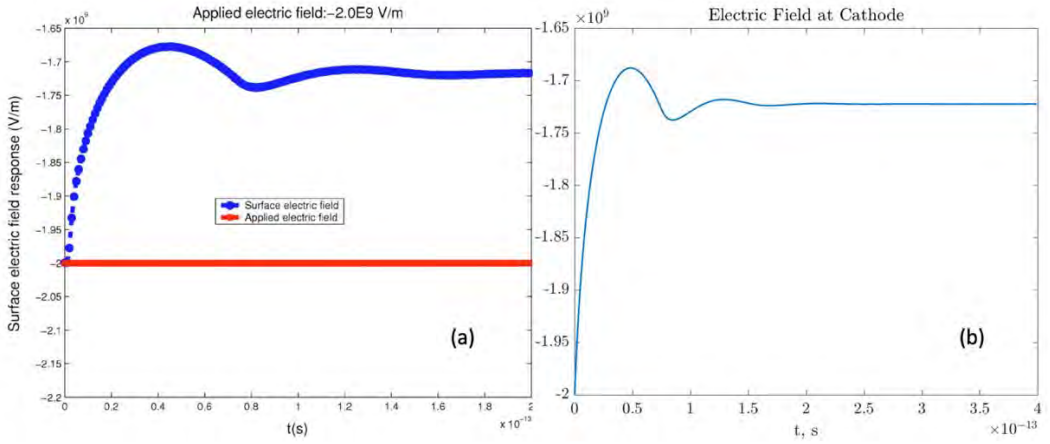


Figure 8. Transient electric field at the cathode surface. The applied electric field is 2×10^9 V/m. (a) Result from Feng and Verboncoeur. (b) Our result.

3. Findings and Conclusions

We have made significant progress with the magnetized plasma sheath study. We are currently writing a journal article.

4. Plans and Upcoming Events

We have identified our major activity for the FY2022 is to proceed with the benchmarking of various fluid models in the lab against the PIC/MCC simulation results. The test case used will be from Welch et al. [Welch et al., "Hybrid simulation of electrode plasmas in high-power diodes," Phys. Plasmas **16**, 123102, (2009).] We will be having more results related to the research idea in the next reporting period.

PI Hara has given multiple invited talks (in GEC, ICOPS, ESCAMPIG) and is planning to give an invited talk at University of Texas at Austin in November 2022 and Georgia Institute of Technology near year. In addition, PI Hara has visited NRL in September 2022 to have a discussion with the Pulsed Plasma group (Ian Rittersdorf and Joe Schumer). PI has also been invited as a lecturer at the 2nd US Low temperature plasma summer school.

5. Transitions and Impacts

Graduate student Andy Castillo has been selected as a year-round intern at Sandia National Laboratories, where he will work on plasma global model for high-power switches.

6. Collaborations

- AFRL: Peter Mardahl – we visited AFRL and had discussion about state-of-the-art HPM computational models, including ICEPIC.
- Sandia National Laboratories: Matt Hopkins – collaboration regarding high power switch simulation using a plasma global model (PI's student is selected for a year-long internship).
- Lam Research: Saravanapriyan Sriraman – we are collaborating with Lam research to study RF breakdown in low-pressure capacitively coupled plasma source. We have been awarded Lam internal funding, called the Unlock Ideas and Elevate Ideas.

- Applied Materials: Jason Kenney and Shahid Rauf – we collaborate on development of a 2D cylindrical PIC-MCC model for low-temperature plasmas.
- Georgia Institute of Technology: Sedina Tsikata – collaboration on cross-field plasma discharge physics, particularly focusing on the kinetic and fluid instabilities in partially magnetized plasmas.
- NRL: Ian Rittersdorf – been invited to the give a talk.

7. Personnel

- Principal investigator: Ken Hara, 0.3-person month, National Academy Member (N)
- Business Contact: Thomas Merritt, Associate Research Administrator

8. Students

3 graduate students (two post-quals PhD candidates and one master student) are supporting this research.

- One PhD candidate is developing the plasma sheath simulations and theory.
- One PhD candidate is developing the full-fluid moment (FFM) model.
- The master student is developing the simulations of plasma formation in anode-cathode gap.

1 undergraduate student was involved during the summer of 2022.

1 postdoc, not supported by this ONR project directly, is in charge of the RF breakdown simulations.

9. Technology Transfer

We discussed our research with Joe Schumer, Ian Rittersdorf, Alexander Vlasov, and Simon Cooke at NRL before the proposal. PI visited NRL in September 2022. We hope to continue the relationship.

PI visited the Air Force Research Laboratory to visit the ICEPIC team in Albuquerque in 2021.

PI has strong connection with AFRL in Edwards AFB (In-space propulsion branch), e.g., Justin Koo, Dan Eckhardt, and David Bilyeu.

10. Products, Publications, Patents, License Agreements, etc.

Publications resulting from this project:

Archival Publications

a. Title: Theory of gradient drift instabilities in low-temperature, partially magnetized plasmas
b. Journal: Journal of Plasma Physics
c. Authors: K. Hara, A. R. Mansour, and S. Tsikata
d. Keywords: plasma devices, plasma dynamics, plasma instabilities
e. Distribution Statement: Open Access
f. Status: Published
g. Publication Identifier Type: DOI
h. Publication Identifier: doi:10.1017/S002237782200068X
i. Publication Date: 2022
j. Vol: 88
k. Issue: -
l. Number: 905880408

m. Publication Location: The city and country where article was published
n. Acknowledgement of Federal Support? Yes
o. Peer Reviewed? Yes

Conference Papers

a. Title: Kinetic modeling of plasma-wall interactions with magnetic field and secondary emission effects
b. Authors: A M Castillo and K Hara
c. Conference Name: International Electric Propulsion Conference
d. Conference Date: June 2022
e. Conference Location: Cambridge MA
f. Publication Status: Published
g. Publication Date: June 2022
h. Publication Identifier Type: none
i. Publication Identifier: IEPC-2022-382
j. Acknowledgement of Federal Support? Yes

a. Title: Kinetic simulation of plasma sheath relevant to cross-field diodes
b. Authors: A M Castillo and K Hara
c. Conference Name: International Conference on Plasma Sciences
d. Conference Date: May 2022
e. Conference Location: Seattle WA
f. Publication Status: Abstract Published
g. Publication Date: May 2022
h. Publication Identifier Type: none
i. Publication Identifier: none
j. Acknowledgement of Federal Support? Yes

a. Title: Kinetic simulation of magnetized plasma sheaths with oblique magnetic fields
b. Authors: A M Castillo and K Hara
c. Conference Name: APS Far West Section Fall 2022 Meeting
d. Conference Date: October 2022
e. Conference Location: Honolulu HI
f. Publication Status: Abstract Published
g. Publication Date: October 2022
h. Publication Identifier Type: none
i. Publication Identifier: none
j. Acknowledgement of Federal Support? Yes

11. Point of Contact in Navy

Joe Schumer and Ian Rittersdorf, Naval Research Laboratory.
Last contact: September 2022. PI visited NRL for a discussion.

12. Acknowledgement/Disclaimer

This work was sponsored by the Office of Naval Research (ONR), under grant (or contract) number N00014-21-1-2698. The views and conclusions contained herein are those of the authors only and should not be interpreted as representing those of ONR, the U.S. Navy or the U.S. Government.

Direct Generation of Electromagnetic Radiation with a Compact, Air-Stable, Optically Modulated Electron Emitter

Grant No. N00014-21-1-2634

Annual Report for Fiscal Year 2022

Period of Performance: October 1, 2021 – September 30, 2022

Prepared by:

Prof. Rehan Kapadia, Principal Investigator
University of Southern California
Dept. of Electrical and Computer Engineering
3737 Watt Way, PHE 626
Los Angeles, CA, 90089-0271
Email: rkapadia@usc.edu

This work was sponsored by the Office of Naval Research (ONR), under grant (or contract) number N00014-21-1-2634. The views and conclusions contained herein are those of the authors only and should not be interpreted as representing those of ONR, the U.S. Navy or the U.S. Government.

Grant or Contract Number: N00014-21-1-2634

Date Prepared: 1/29/2023
Project Title: Direct Generation of Electromagnetic Radiation with a Compact, Air-Stable, Optically Modulated Electron Emitter
Annual Summary Report: FY22
Principle Investigator: Rehan Kapadia, rkapadia@usc.edu, University of Southern California

Section I: Project Summary

1. Overview of Project

1.1 Abstract

In this report, we will cover the objectives, background, accomplishments, and future plans for the grant titled “Direct Generation of Electromagnetic Radiation with a Compact, Air-Stable, Optically Modulated Electron Emitter”. Through this grant we aim to demonstrate a new type of electron source that enables rapid modulation of emitted electron density but allows the use of established telecommunications photon sources to excite the electron source. In this way, an optical signal imprinted on the incident photon source can be converted into an elecron density modulation. Using this density modulated electron beam, we then aim to design a vacuum electron device that can convert the density modulated electron beam into a high-power RF signal.

1.2 Objective

The first goal of this proposal is to continue to develop and demonstrate a simple *planar* silicon-insulator-graphene structure to create an air-stable, *electrically tunable*, negative electron affinity surface by applying a bias between the graphene and silicon, termed Hot Electron Light Assisted Cathode (HELAC). A continuous or pulsed photon source may then be used to excite electrons in the silicon, which will then be emitted into vacuum when a small (4-10 V) bias is applied across the device. This electron source can be compact, environmentally robust, and use low energy photons in the near-IR to visible range. Based on initial simulations, modulation frequencies of >250 GHz and 1 A/cm^2 emission currents should be achievable through device optimization. Initial experimental prototypes have already demonstrated 1 mA/cm^2, despite a relatively unoptimized structure.
Using this electron source, we will then design and build a device similar to an Inductive Output Tube (IOT), where an electron beam is density modulated by incident light, then accelerated to a desired voltage, and finally RF power is extracted from the beam using an output cavity. We refer to this device as a Light Modulated IOT (LM-IOT). Unlike IOTs, which have frequency and total current limitations due to the grid-cathode spacing and uniformity, this approach is expected to overcome those issues by eliminating the need for a grid and input cavity. We will build a prototype LM-IOT, where the beam generation, confinement, and collector segments are fixed, and the output frequency will be determined by swapping output cavity. Specifically, we will carry out simulations to establish basic operation principles, design the overall device, and then fabricate and assemble the device. This will be used to establish the proof of principle operation for LM-IOTs as well as make projections about device parameters.

Finally, we aim to explore multi-frequency devices, where we simultaneously excite the electron emitter with multiple modulation frequencies, creating an electron beam with multiple frequencies, and then use multiple output cavities to extract and emit those frequencies separately. In this task, the goal is to understand interaction between multifrequency beams and multiple cavities, the limitations in power distribution between frequencies, and any non-linear effects due to the electron source itself that could take two input frequencies and generate different output frequencies. These limits would be driven by a combination of the physics of the electron source and the beam-cavity interactions.

1.3 Background

The modern day congested and contested electromagnetic spectrum has placed stringent demands on electronic systems[1, 2]. A single electromagnetic (EM) source that change transmission bands, multiple frequencies, or even frequency bands, and be able to quickly switch frequencies when the desired communication channels becomes contested is of value in a contested environment. Additionally, directed EM sources which can temporarily or permanently deny communications are of significant value. One approach to this may be the direct generation of EM radiation from a modulated electron source. This

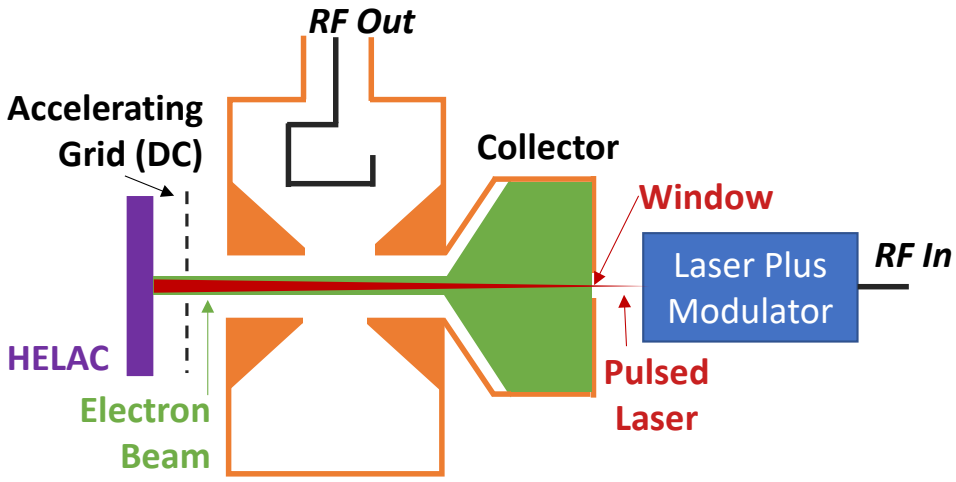


Figure 1: A schematic view of our device. In this structure, the cathode (HELAC) is excited by a modulated laser beam, generating a density modulated electron beam. This beam is accelerated by a grid held at a DC bias. The beam will then pass through an RF cavity to extract the high frequency content of the beam. The HELAC will be excited by a laser beam that travels in reverse through the electron beam tunnel. The size of the laser spot on the cathode, and therefore the area of the beam will be determined by the divergence of the spot, which can be tuned by an optical lens at the source.

approach could enable compact, high-frequency, high-power HPM sources which could serve the needs of directed energy systems[3-14]. An Inductive Output Tubes (IOT) is a source which utilizes a directly modulated, where a continuous beam of electrons is modulated by a grid, and an output cavity converts the high frequency component in the beam to electromagnetic radiation. IOTs, however, use a high voltage grid which couples to an input RF signal, this limits the frequency of operation due to electron transit time between the grid and cathode, and also limits scaling of the cathode due to grid spacing uniformity requirements. Here, we propose utilizing an optically modulated cathode technology to directly create a density modulated electron beam, and then extract the high frequency content from the beam using an output cavity. By eliminating the use of a grid to modulate the electron density, this approach would enable (i) higher frequency operation, (ii) larger cathodes for increased drive current, (iii) higher beam voltages, (iv) a reduction in size and weight, and (v) multi-frequency operation from a single device.

Electron emission cathodes are used in a wide variety of applications, including but not limited to, electron microscopes[15, 16], electron beam lithography[17], space propulsion[18], high power microwave (HPM) devices[19-21], free electron lasers[22], and displays[23]. HPM sources for millimeter-wave and terahertz radiation are of great interest for military and defense applications such as radar, electronic counter measures, and communications[20, 24]. While photo-assisted field emission devices have been explored in the past[25,26,27,28,29], as promising high frequency emitter, these are generally studied utilizing free-space optics to directly focus

a laser on a tip or tip array, and use p-type silicon to enable photogating of field emission. Recently, simulation and experimental results have shown that optically driven emitters[30-37] could play a valuable role in cathodes for high power microwave and vacuum electron devices in general.

2. Activities and Accomplishments

We have made progress on a variety of topics focused on improving the measured performance of the HELAC devices:

2.1 Post Fabrication Anneal

We have been carrying out studies on the effect of post device fabrication heat treatments affect the performance of our devices. We have found that a rapid thermal annealing (RTA) step of 400 ^{o}C or higher in forming gas (H_2/N_2) improves the emission current by a factor of ~2-3 as shown in Figure 2. We hypothesize this occurs due to (i) desorption of contaminants on the surface and (ii) improved adhesion between the graphene and underlying SiO_2. This is expected to improve the probability of carriers tunneling out of the graphene into vacuum and reduce scattering for carriers tunneling into the graphene from the SiO_2.

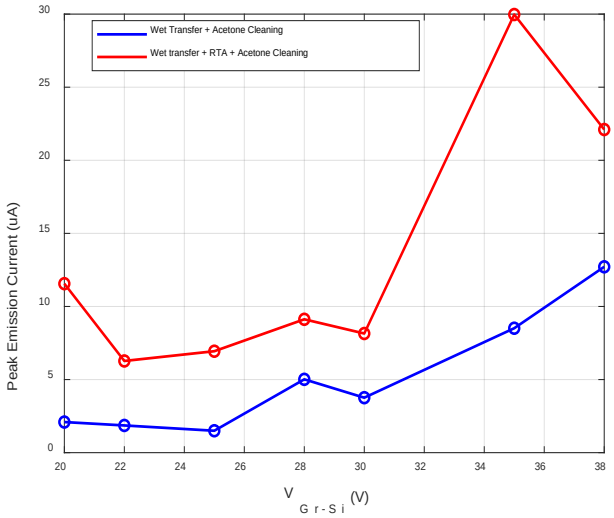


Figure 2: Effect of post fabrication anneal on resulting currents.

Previously, we noted that when using the diamond device, we observed current, but we did not observe any light modulated current, when using two terminals. One key difference between the diamond device and previous HELAC devices is the substrate. The diamond device was fabricated on intrinsic silicon, while previous devices have been fabricated on p-type silicon. We have been fabricating Si/oxide/graphene devices on intrinsic silicon and found that these diodes are operating in the reverse polarity of our standard

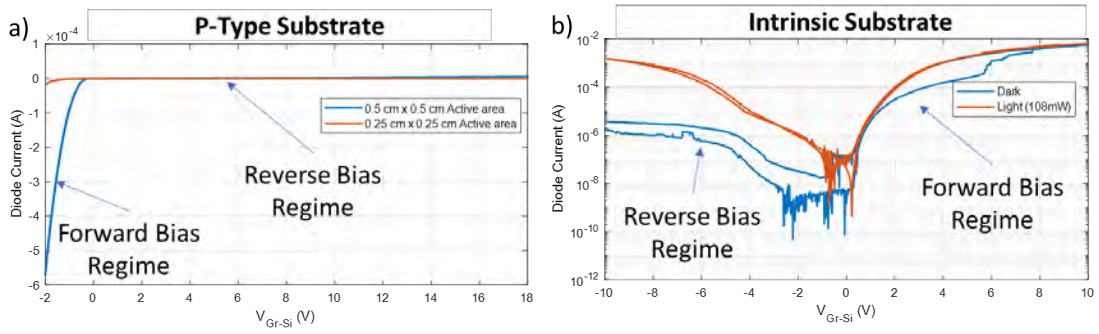


Figure 3: a) Dark diode I-V characteristics for p-substrate devices. b) Dark and light diode I-V characteristics for intrinsic substrate devices.

p-type devices. This can be seen in Figure 3, where the reverse bias and forward bias regimes are reversed. Thus, we are in a regime where electrons are the majority carriers. This is an issue caused by our back contact. Specifically, we will need to carry out back contact doping/annealing schemes to enable a thin layer of p-dopants at the rear contact. We anticipate that this will return the polarity of the diodes to the expected. In order to fix this, we are currently exploring different contact doping and metallization schemes.

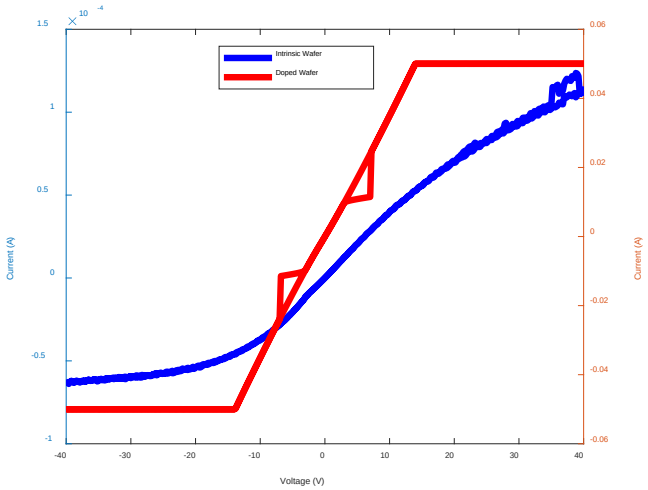


Figure 4: Current–voltage characteristics comparison of the back surface of intrinsic Si before and after boron spin-on doping.

Specifically, we are exploring pre-contact deposition doping using a boron doped spin-on-glass (SOG). With this process we would first spin coat a thermally curable glass with a high concentration of boron on the backside of the wafer, then carry out a high temperature (~700-900 ^{o}C) anneal to create a highly p-doped layer at the bottom surface. Next we may use a light etch to clean up any damaged layers, and finally we would deposit the back contact metal (e.g. aluminum) and use a lower temperature rapid-thermal annealing step (i.e 400-450 ^{o}C)

2.2 Intrinsic Device Back-Contact Doping

In order to fabricate, Si/oxide/graphene devices on intrinsic silicon, we have carried out back contact doping and metallization schemes to enable a thin layer of p-dopants at the rear contact of intrinsic Si. Specifically, we have performed pre-contact deposition doping using a boron doped spin-on-glass (SOG). With this process, we first spin coated a thermally curable glass with a high concentration of boron on the backside of the wafer, then carried out a high temperature (850 ^{o}C) anneal in N_2 gas to create a highly p-doped layer at the bottom surface. Next, we performed HF etching to remove the unwanted borosilicate glass followed by HNO_3 treatment at 80 ^{o}C to oxidize the boron precipitates. Finally, we deposited the back contact metal (i.e. aluminum) and characterized the contact resistance which showed that the contact resistance significantly decreased due to the doping scheme. The linear I-V characteristics also confirmed the ohmic nature of the contact as shown in Figure 4.

2.3 HELAC Post-Fabrication Rapid Thermal Annealing

We are trying to find out the best temperature for performing the Rapid Thermal Annealing (RTA) on our devices. RTA improves the graphene adhesion to SiO_2 and helps to remove polymethyl methacrylate (PMMA) residues from graphene surface. But applying high temperature during this step makes the device

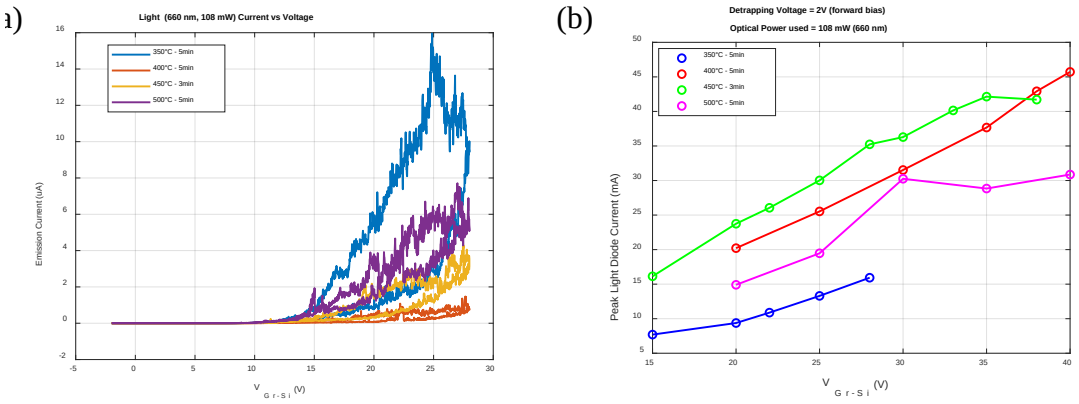


Figure 5: (a) Emission current comparison between devices with different temperature RTA performed on them; (b) Light diode current comparison between devices with different temperature RTA performed on them.

leaky resulting in lower emission current. We have observed that applying a lower temperature during RTA and then using acetone to remove the remaining PMMA layer gives us better results. The devices on which we performed higher temperature RTA showed higher diode currents in both light and dark conditions. In Figure 5 and Figure 6 we can see that the diode currents reach high levels for the devices with higher temperature RTA during pulsed voltage measurement where we alternate between operating and de-trapping voltages in order to get maximum emission current.

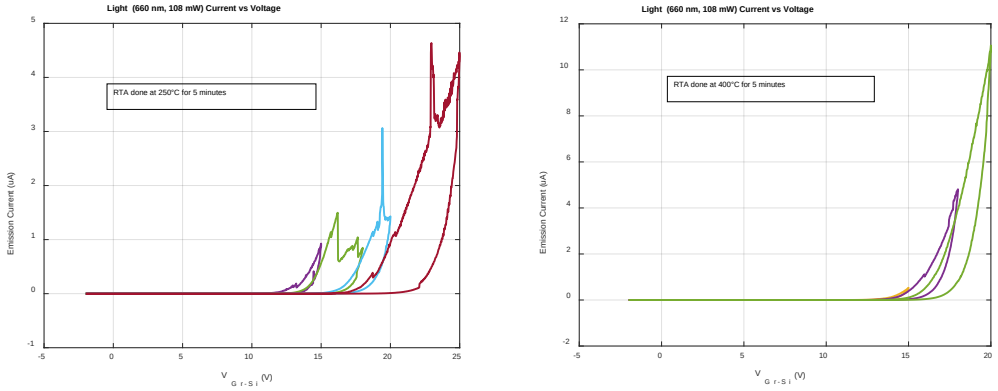


Figure 6: Stable Emission current comparison between devices with different temperature RTA performed on them

2.4 HELAC Material Variation

We are exploring different materials and structures to identify what gives us the best performance. Recently we changed the oxide material of HELAC from SiO_2 to Al_2O_3 and observed clean emission as shown in Figure 5. We have observed that applying a higher temperature during RTA gives us better results. A distinguishing property of Al_2O_3 is the field-effect passivation induced by negative fixed charges. Also, low interface defect density and adequate stability during processing might be the reason behind it. We are investigating more with these devices.

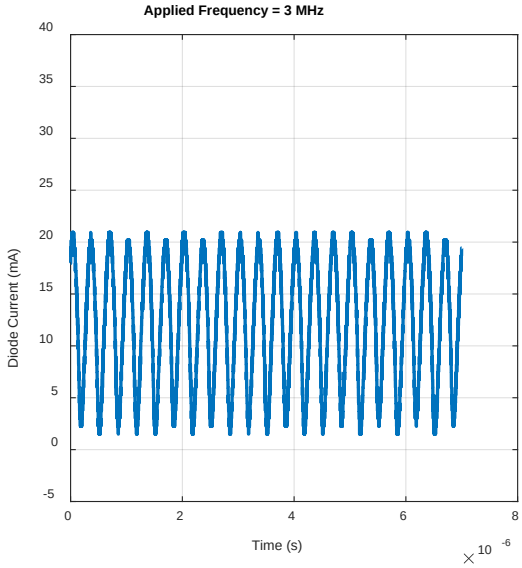


Figure 7: Modulated light diode current response of HELAC. Applied frequency for modulating light was 3MHz

Additionally, we have worked on improving the frequency response performance of our devices. One limiting factor was the series resistor (R_s) that we were using for observing the current in oscilloscope. The high resistance value was increasing the RC constant of the overall system and as a result we were seeing slower response. By reducing the R_s we were able to get optical modulation response up to 3 MHz for the diode current of our HELAC device. This is shown in Figure 7.

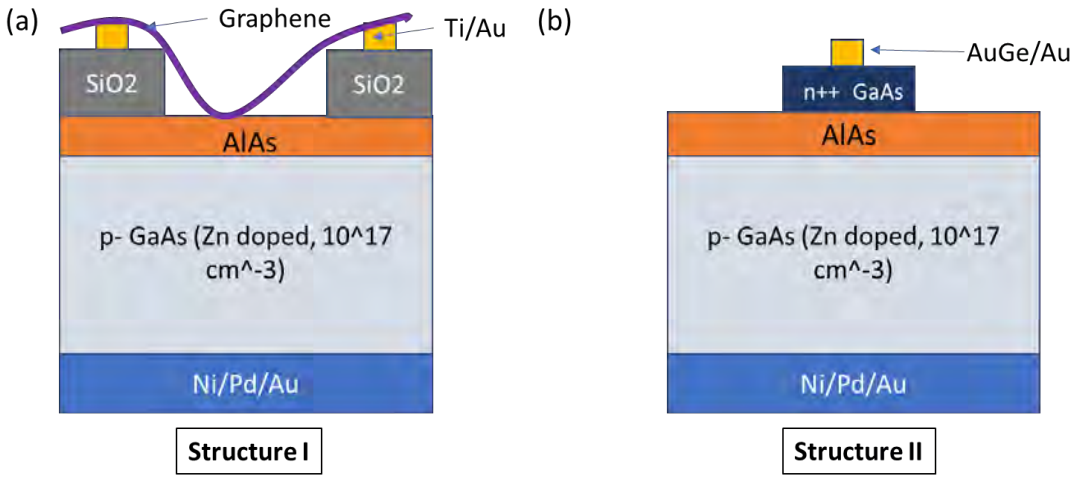


Figure 8: Two different HELAC structures on p-GaAs substrates.

We are working on the fabrication of HELAC devices on III-V substrate. We have designed two different HELAC structures on moderately p-doped GaAs substrate (doping concentration ~10^{17} cm^{-3}). For the first structure, (**Structure I** in Fig. 8), we will use AlAs grown by MOCVD (metal organic chemical vapor deposition) technique as the tunneling dielectric. We expect that AlAs will act as the passivation layer on

p-GaAs substrate and reduce electron recombination at the interface. As the insulation layer, we will use SiO_2 deposited by PECVD method and will transfer monolayer of graphene on top as the gate of the device.

Likewise, in the second HELAC structure, (**Structure II** in Fig.8), MOCVD grown AlAs will act as the tunneling dielectric, but for this device, we have grown heavily n doped GaAs on top of the AlAs layer by MOCVD. We anticipate that this n++ GaAs layer will act as the gate of the device mimicking the graphene in the typical HELAC structure. We will complete the fabrication of the devices and explore their performance.

2.5 LM-IOT Component Design

One important part of our LM-IOT is the output cavity. In order to get the suitable dimensions and structure of the output cavity we are performing simulations. For mimicking the light modulated electron beam's characteristics, we have used a gaussian source emitting bunched electrons. We have observed that increasing the number of electrons in a bunch significantly improves the output gained. This is shown in Fig.9.

a) b)

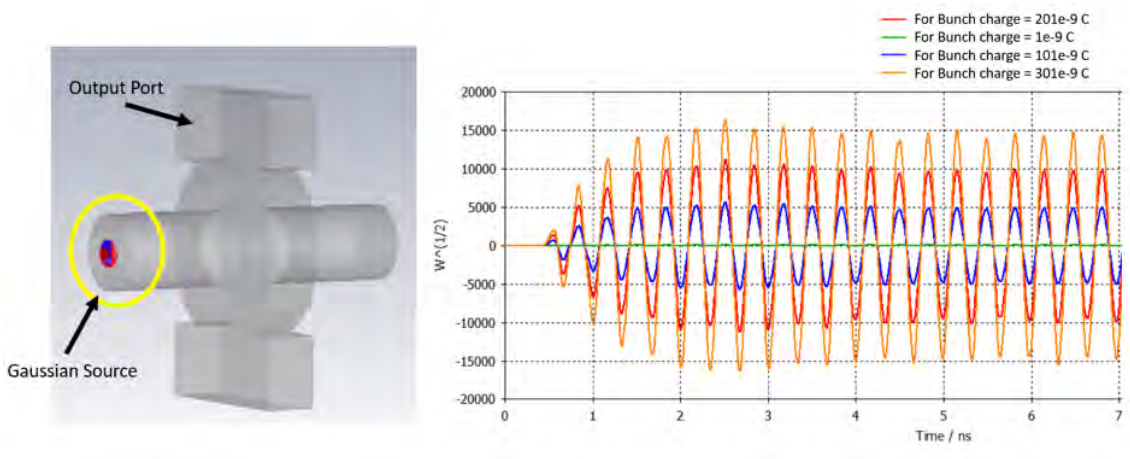


Figure 9: a) Output Cavity structure. b) Output signal observed in the output port for various bunch charge.

3. Findings and Conclusions

We have several important findings that have emerged from the previous year of work. First, we have found that the type and preparation of the insulator plays a critical role in the behavior of the device. It is hypothesized that the key feature which determines the behavior is the ease of defect formation while under tension. These defects then serve to trap charges which oppose the applied field. This reduced field causes a time dependent reduction in emission current. As such, we have determined that there are three structures which can eliminate this issue and still provide the benefits desired of HELACs.

4. Plans and Upcoming Events

We plan to continue carrying out the work detailed here, and plan to add three additional structures that can address some of the challenges that tunneling through an oxide/insulator poses. Specifically, we plan on

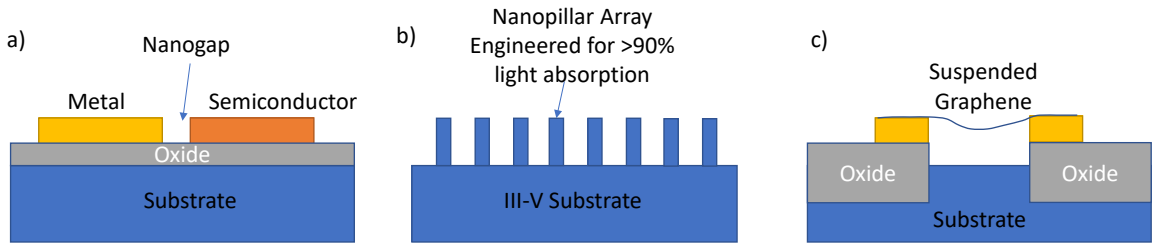


Figure 10: Examples of devices structures which can provide similar behavior with presently explored solid-insulator HELACs while using a vacuum dielectric. a) Metal-semiconductor nanogap device. b) III-V substrate with engineered nanopillar structures. c) Suspended graphene on a substrate.

implementing three additional device structures. First a metal-semiconductor nanogap device where the metal applies an extraction field to the semiconductor (Fig. 10a, Fig 11a), but using a magnetic and electric field, emitted electrons will be diverted upwards for collection. The idea of this device is to essentially use p-type semiconductors which are excited by light to serve as the emitters, and laterally spaced metal contacts act as the gates. By applying a significant field between the semiconductor and metal, carries will be extracted. However, as the semiconductor will be p-type, the emission will be modulated by light. Additionally, to ensure emission of the carries orthogonal to the plane of the substrate, these will be on a magnet which accelerates the carriers away from the gate.

Second, a III-V substrate with engineered nanopillar structures (Fig. 10b, Fig. 11b) to ensure light absorption in an array of nanowires is considered. The concept behind this device structure is to use a more traditional field emission device architecture but with a p-type semiconductor and a limited light absorption region. Specifically, one of the main challenges that p-type emitters have faced is the relatively low quantum efficiency and longer emission times. This is due to the need to make relatively sharp tips that are significantly spaced out. However, there have been previous studies that show that wire geometries can be designed to interact resonantly with incident light giving very high absorption despite the wire geometries. Using this approach we plan on designing and testing p-type InGaAs on InP devices for emission.

Finally, a device with suspended graphene on a substrate (Fig 10c), which is a structure similar to the present HELAC devices, but using a vacuum gap as the dielectric. This will eliminate the issue with electron trapping in the oxide.

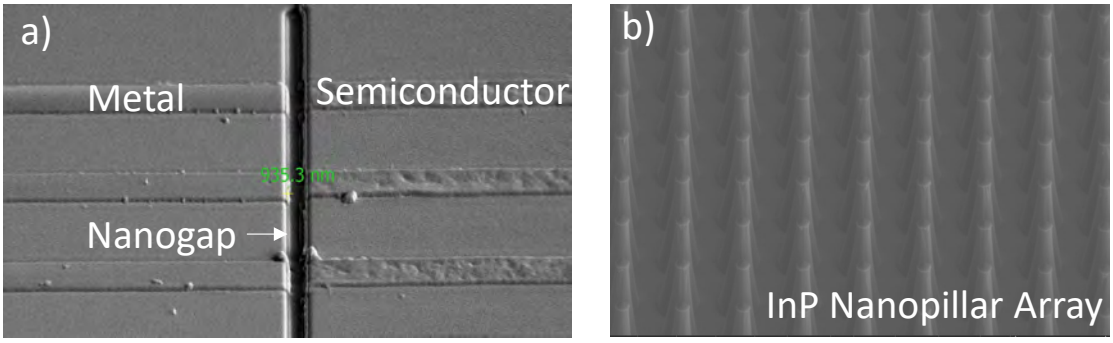


Figure 11: Examples of fabricated a) nanogap devices and b) nanowires to be used to test structures shown in Figure 10.

5. Transitions and Impacts

We presently do not have any transitions, but aim to share the emission devices fabricated in our group beyond the present collaborations as noted in section 6.

6. Collaborations

Our collaboration with Prof. Peng Zhang at MSU where his team is theoretically exploring material combinations and structures that may be used to improve our device performance is continuing. We are presently in the process of submitting a theory paper on how a tunneling can be used to dramatically improve emission energy spread for field emitters.

We also have an on-going collaboration with Prof. John Booske and Prof. Nader Behdad that is where we will be sending them HELAC devices for use in x-ray generation devices for the purposes of communications. We have sent them some initial generation HELACs, and they are doing testing on those devices.

7. Personnel

Principal investigator: Rehan Kapadia, 2 person months, NA Member: N
Business Contact: Cindy Huynh (cynthimh@usc.edu)

8. Students

A total of 4 Graduate students have assisted with this work: Subrata Das, Hyun Uk Chae, Ragib Ahsan, and Anika Tabassum.

9. Technology Transfer

We have applied for a patent on the general HELAC structure, U.S. Serial No. 17/940,113.

10. Products, Publications, Patents, License Agreements, etc.

Conference Papers

a. Hot Electron Laser Assisted Cathode using Electronically Tunable Negative Electron Affinity Surfaces – Prospects and Challenges
b. Subrata Das, Hyun Uk Chae, Ragib Ahsan Rehan Kapadia
c. International Vacuum Electronics Conference
d. 4-25-2022
e. Monterey, CA
f. Publication Status: Awaiting publication
g. Publication Date
h. Publication Identifier Type
i. Publication Identifier
j. Acknowledgement of Federal Support? Yes

Patents

a. Inventor: Ragib Ahsan, Subrata Das, Hyun Uk Chae, Rehan Kapadia
b. Assignee: USC
c. Title: Electronically-Tunable Air-Stable, Negative Electron Affinity Semiconductor Photocathode
d. Patent Number: U.S. Serial No. 17/940,113.
e. Date of Award: Applied

11. Point of Contact in Navy

Matthew McQuage, updated via email Dec. 19th 2022.

12. Acknowledgement/Disclaimer

This work was sponsored by the Office of Naval Research (ONR), under grant (or contract) number N00014-21-1-2634. The views and conclusions contained herein are those of the authors only and should not be interpreted as representing those of ONR, the U.S. Navy or the U.S. Government.

References

1. Spezio, A. E. *IEEE Trans. Microwave Theory Tech.* **2002,** 50, (3), 633-644.
2. Schleher, D. C. *Dedham* **1986**.
3. Beunas, A.; Bel, C.; Robert, C.; Racamier, J. C.; Bussiere, D.; Bariou, D.; Khlifa, K. H.; Hermann, V.; Yates, C.; Halatsis, N. In *Manufacturing and performance results of a 1.2 MW peak, 704 MHz multi-beam inductive output tube*, 2017 Eighteenth International Vacuum Electronics Conference (IVEC), 2017; IEEE: pp 1-2.
4. Freund, H.; Miner, W.; Verboncoeur, J.; Li, Y.; Wright, E. *IEEE transactions on plasma science* **2007,** 35, (4), 1081-1088.
5. Jensen, M. **2004**.
6. Heppinstall, R.; Clayworth, G. *EBU Technical Review* **1997**, 43-52.
7. Lau, Y.; Chernin, D. P.; Wilsen, C.; Gilgenbach, R. M. *IEEE transactions on plasma science* **2000,** 28, (3), 959-970.
8. Caryotakis, G. *Physics of Plasmas* **1998,** 5, (5), 1590-1598.

9. Lau, Y.; Friedman, M.; Krall, J.; Serlin, V. *IEEE transactions on plasma science* **1990,** 18, (3), 553-569.
10. Sessler, A. M.; Simon, S. Y. *Physical review letters* **1987,** 58, (23), 2439.
11. Nyaiesh, A. R.; Garwin, E. L.; King, F. K.; Kirby, R. E. *Journal of Vacuum Science & Technology A* **1986,** 4, (5), 2356-2363.
12. Girard, B.; Lapierre, Y.; Ortega, J.; Bazin, C.; Billardon, M.; Elleaume, P.; Bergher, M.; Velghe, M.; Petroff, Y. *Physical review letters* **1984,** 53, (25), 2405.
13. Lau, Y.-Y. *Physical review letters* **1984,** 53, (4), 395.
14. Chodorow, M.; Wessel-Berg, T. *IRE Transactions on electron devices* **1961,** 8, (1), 44-55.
15. Goldstein, J.; Newbury, D. E.; Echlin, P.; Joy, D. C.; Romig Jr, A. D.; Lyman, C. E.; Fiori, C.; Lifshin, E., *Scanning electron microscopy and X-ray microanalysis: a text for biologists, materials scientists, and geologists*. Springer Science & Business Media: 2012.
16. Reimer, L., *Transmission electron microscopy: physics of image formation and microanalysis*. Springer: 2013; Vol. 36.
17. Vieu, C.; Carcenac, F.; Pepin, A.; Chen, Y.; Mejias, M.; Lebib, A.; Manin-Ferlazzo, L.; Couraud, L.; Launois, H. *Applied Surface Science* **2000,** 164, (1), 111-117.
18. Goebel, D. M.; Katz, I., *Fundamentals of electric propulsion: ion and Hall thrusters*. John Wiley & Sons: 2008; Vol. 1.
19. Benford, J.; Swegle, J. A.; Schamiloglu, E., *High power microwaves*. CRC Press: 2007.
20. Gold, S. H.; Nusinovich, G. S. *Review of Scientific instruments* **1997,** 68, (11), 3945-3974.
21. Barker, R. J.; Luhmann, N. C.; Booske, J. H.; Nusinovich, G. S. *Modern Microwave and Millimeter-Wave Power Electronics, by Robert J. Barker (Editor), Neville C. Luhmann (Editor), John H. Booske (Editor), Gregory S. Nusinovich, pp. 872. ISBN 0-471-68372-8. Wiley-VCH, April 2005.* **2005,** 1.
22. Brau, C. A. **1990**.
23. Wang, Q.; Setlur, A.; Lauerhaas, J.; Dai, J.; Seelig, E.; Chang, R. *Applied Physics Letters* **1998,** 72, (22), 2912.
24. Kartikeyan, M. V.; Borie, E.; Thumm, M., *Gyrotrons: high-power microwave and millimeter wave technology*. Springer Science & Business Media: 2013.
25. Yanagisawa, H.; Hengsberger, M.; Leuenberger, D.; Klöckner, M.; Hafner, C.; Greber, T.; Osterwalder, J. *Physical review letters* **2011,** 107, (8), 087601.
26. Wimmer, L.; Herink, G.; Solli, D.; Yalunin, S.; Echternkamp, K.; Ropers, C. *Nature Physics* **2014,** 10, (6), 432-436.
27. Jensen, K.; Lau, Y.; McGregor, D. *Applied Physics Letters* **2000,** 77, (4), 585-587.
28. Jensen, K. L.; Lau, Y.; McGregor, D. *Solid-State Electronics* **2001,** 45, (6), 831-840.
29. Hagmann, M. J. *Ultramicroscopy* **1999,** 79, (1), 115-124.
30. Xiong, X.; Zhou, Y.; Luo, Y.; Li, X.; Bosman, M.; Ang, L. K.; Zhang, P.; Wu, L. *ACS nano* **2020,** 14, (7), 8806-8815.
31. Luo, Y.; Zhang, P. *Physical Review Applied* **2019,** 12, (4), 044056.
32. Zhang, P.; Lau, Y. *Scientific reports* **2016,** 6, (1), 1-12.
33. Rezaeifar, F.; Ahsan, R.; Lin, Q.; Chae, H. U.; Kapadia, R. *Nature Photonics* **2019**, 1-6.
34. Blankemeier, L.; Rezaeifar, F.; Garg, A.; Kapadia, R. *Journal of Applied Physics* **2019,** 126, (3), 033102.
35. Rezaeifar, F.; Kapadia, R. In *Cavity coupled photon-enhanced thermionic electron emitter*, Vacuum Electronics Conference (IVEC), 2016 IEEE International, 2016; IEEE: pp 1-2.
36. Ahsan, R.; Sakib, M. A.; Chae, H. U.; Kapadia, R. *Physical Review Applied* **2020,** 13, (2), 024060.
37. Rezaeifar, F.; Chae, H. U.; Ahsan, R.; Kapadia, R. *Applied Physics Letters* **2021,** 118, (7), 071108.

Multi-frequency High Power Microwave Generation and Amplification via Optically Gated Electron Beams

Grant No. N00014-20-1-2681

Annual Report for Fiscal Year 2022

Period of Performance: October 1, 2021 to September 30, 2022

Prepared by:

Prof. Peng Zhang, Principal Investigator
Department of Electrical and Computer Engineering
Michigan State University
428 S. Shaw Ln
East Lansing, MI 48824
Email: pz@egr.msu.edu





This work was sponsored by the Office of Naval Research (ONR), under grant (or contract) number N00014-20-1-2681. The views and conclusions contained herein are those of the authors only and should not be interpreted as representing those of ONR, the U.S. Navy or the U.S. Government.

Grant or Contract Number: N00014-20-1-2681

Date Prepared: Dec 28, 2022

Project Title: Multi-frequency High Power Microwave Generation and Amplification via Optically Gated Electron Beams

Annual Summary Report: FY2022

Principle Investigator: Peng Zhang, pz@egr.msu.edu
Department of Electrical and Computer Engineering, Michigan State University

Section I: Project Summary

1. Overview of Project

Abstract: Electron beam based high power microwave (HPM) devices are critical to a variety of defense applications for Navy and more broadly the Department of Defense (DOD). This project explores the fundamental physics of density modulation of electron beam emission via combined mechanisms of thermionic/field/photo-emission and the interaction of such premodulated beams with circuits for HPM generation and amplification. This report provides an executive summary of our recent theoretical modeling efforts. We constructed an analytical solution for nonlinear photoelectron emission in a nanoscale metal–vacuum–metal junction driven by a single-frequency laser field. Our results show the transition from direct tunneling to multiphoton induced electron emission as gap distance increases. We developed an exact quantum model for photoemission from metal surfaces coated with an ultrathin dielectric, by solving the 1D time-dependent Schrodinger equation subject to an oscillating double-triangular potential barrier. It is found that a flat metal surface with dielectric coating can photoemit a larger current density than the uncoated case when the dielectric has smaller relative permittivity and larger electron affinity. We extended our exact theory for nonlinear photoelectron emission in a dc-biased metallic nanovacuum gap triggered by a laser field. Our results demonstrate that, besides the dc bias, varying the gap spacing could strongly influence the rectification on the photoelectron emission in a dc-biased metal-vacuum-metal gap. We also analyzed quantum pathways interference in two-color coherent control of photoemission. The theory includes all possible quantum pathways and their interference terms. It is found that increasing the intensity ratio of the second harmonic (2ω) to fundamental (ω) lasers results in less contribution from the ω pathway (absorption of ω photons only) and more contribution from multicolor pathway (simultaneous absorption of both ω and 2ω photons) and 2ω pathway (absorption of 2ω photons only), and therefore stronger pathways interference. Our results will be useful to the development of advanced cathodes and electron sources with density modulation, enabling new advances for the development of high power electromagnetic sources and amplifiers.

Objective: The objective of this project is to provide a foundational understanding of the underlying physics in optically gated electron emission and its interaction with microwave circuits. The goal is to provide a guideline for the design of compact HPM devices with the ultimate high power output and extremely flexible frequency tunability. The ultrafast electron emission due to pulsed lasers, or optical gating, would potentially provide unrivaled precision in phase-control of electromagnetic signals from electron based HPM devices. The potential of selective gating of multiple beams would provide strong flexibility for multi-frequency HPM applications.

Introduction: Traveling wave devices utilize the collective interaction of an electron beam with a periodic structure to convert electron beam energy into electromagnetic radiation. They are key elements in telecommunication systems, satellite-based transmitters, military radar, communication data links, and electronic countermeasures. There continues to be strong interests in increasing the output power, frequency tunability, and bandwidth of traveling wave devices, for uses as radiation sources and power amplifiers, from GHz to THz and beyond. For the development of coherent radiation sources, it is desirable to minimize

the threshold beam current for triggering oscillation. In contrast, for high power traveling wave tube (TWT) amplifiers, unwanted oscillations pose a major threat to their operation. For novel contemporary traveling wave devices, such as metamaterial-, photonic crystal- and advanced Smith-Purcell-based traveling wave devices, improving efficiency remains a major challenge.

In vacuum microwave tubes, the energy conversion from electron beams into electromagnetic radiation relies on beam modulation, by either density modulation or velocity modulation. Density modulation is achieved by controlling the electron emission from the cathode. Velocity modulation is achieved by passing the electrons through an RF electric field that modulates the velocities of the electrons. At present, TWTs mainly rely on velocity modulation of the electron beam for power amplification. After the electron velocities are modulated, there is a substantial delay before velocity modulation becomes density modulation, until useful gain is produced. Significant improvements in TWT performance can be enabled by density modulation during emission. In particular, with density modulation, velocity dispersion in the beam can be minimized and the substantial portion of the interaction circuit for the purpose of converting velocity modulation into density modulation can be eliminated. This would result in compact devices with reductions in overall dimensions and weight, through the elimination of the premodulation circuit. Furthermore, density modulation during emission would eliminate the launching loss of the input RF signal, which is a serious intrinsic problem in TWTs based on velocity modulation.

In this project, we will explore density modulation in optically gated electron emission. This is motivated by the recent rapid development in ultrafast lasers and photonics, which has opened up unprecedented advances to control electron beam dynamics at ultrashort spatial-temporal scales. The research on implementing both high power and frequency tunability in HPM devices will provide a critical disruptive capability using high power microwaves. The theory will also be valuable to neighboring fields such as novel miniaturized electromagnetic radiation sources, nano-optoelectronics, ultrafast physics, material science, and accelerator technology.

Background: The idea of using direct current modulation of electron beams in microwave amplifiers has existed for decades. Historically, density modulation was accomplished with a grid that lays over the surface of a thermionic emitter to control the electron emission. Because of the finite transit time of the electrons across the cathode-grid space, this modulation technique is only effective up to 2 GHz for state-of-the-art devices. With the advancement of vacuum microelectronics and field emitter arrays (FEAs), the gate-to-emitter spacing has been reduced into submicron scale, which significantly decreases the electron transit time. Density modulation about 5 GHz by gate modulating of the FEA has been demonstrated; however, there are significant challenges for using FEAs in high power tubes, because the premature failure due to arcing often occurs at current levels much smaller than the design requirements. Breakdown is a major challenge for FEAs because of the high fields within the structure and the thin-film gate electrode. An electrical short between the gate and any individual emitter will burn out the entire FEA and render it unusable. While shields can be added to mitigate the damaging effects of the electrical shorts, high operating voltage is needed to field emitter arrays to draw sufficient current.

Photoemission provides an alternative method to generate premodulated electron beams, which relaxes the requirement of high operating voltage in field emission, thus eliminating possible arcing and circuit breakdown. More importantly, pulsed laser induced (or assisted) electron emission offers the possibility of manipulation and control of coherent electron motion in ultrashort spatiotemporal scales. These advantages would greatly benefit the development of advanced compact HPM devices.

2. Activities and Accomplishments

The main new activities and accomplishments during this performance period (1 October 2021 to 30 September 2022) include: 1) An exact analytical formulation for ultrafast optical-field-induced photoelectron emission in a vacuum nanoscale gap; 2) Theory of laser-induced photoemission from a metal surface with nanoscale dielectric coating; 3) Optical-field-induced electron emission in a dc-biased nanogap; and 4) Unraveling quantum pathways interference in two-color coherent control of photoemission with bias voltages.

ULTRAFAST OPTICAL-FIELD-INDUCED PHOTOELECTRON EMISSION IN A VACUUM NANOSCALE GAP: AN EXACT ANALYTICAL FORMULATION

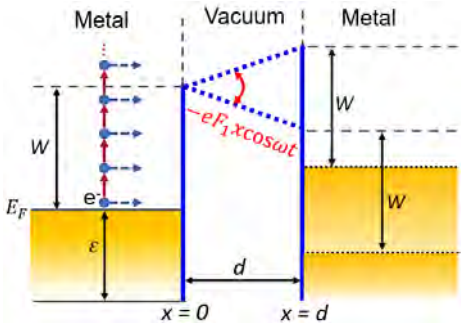


Figure 1. Energy diagram for photoelectron emission in a nanoscale metal-vacuum-metal junction under a single-frequency laser field. Electrons with the initial energy ε are emitted from the surface at $x = 0$, with an energy of $\varepsilon + n\hbar\omega$, due to n-photon contribution [1].

By exactly solving the one-dimensional time-dependent Schrodinger equation (TDSE), we constructed an analytical solution for nonlinear photoelectron emission in a nanoscale metal–vacuum–metal junction driven by a single-frequency laser field [1], where the impact of image and space charges is neglected. Based on the analytical formulation, we examine the photoelectron energy spectra and emission current under various laser fields and vacuum gap distances. Our calculation shows the transition from direct tunneling to multiphoton induced electron emission as gap distance increases. In the multiphoton regime, the photoemission current density oscillatorily varies with the gap distance, due to the interference of electron waves inside the gap. Our model reveals the energy redistribution of photoelectrons across the two interfaces between the gap and the metals. Additionally, we find that decreasing the gap distance (before entering the direct tunneling regime) tends to extend the multiphoton regime to higher laser intensity. This work provides clear insights into the underlying photoemission mechanisms and spatiotemporal electron dynamics of ultrafast electron transport in nanogaps and may guide the future design of ultrafast nanodevices, such as photoelectron emitters, photodetectors, and quantum plasmonic nanoantennas.

Our one-dimensional (1D) model (see Fig. 1) considers electrons with initial energy ε emitted from the surface at $x = 0$, under the action of laser field $F_1\cos(\omega t)$, where F_1 is the amplitude of the laser field and ω is the angular frequency. The laser field is assumed to be perpendicular to the flat emitter surface, and cuts off abruptly at the surface. Note that, by symmetry, electron emission from the surface at $x = d$ can be modeled in the same way (but with an opposite sign of instantaneous laser field). This indicates no net time-averaged photoemission current, but only net instantaneous current is generated in a symmetric nanogap. Note further that generating non-zero net time-averaged photocurrent requires some sort of symmetry breaking of the nanogap, e.g. by using dissimilar materials on the two sides of the gap, dc bias, or spatially or temporally inhomogeneous optical fields. Here, we focus only on a symmetric nanogap, which is applicable to a broad range of plasmonic and ultrafast optoelectronic devices, where direct measurement of

the gap current is typically infeasible. This makes the theoretical investigation even more valuable. The time-dependent potential energy in Fig. 1 reads,

$$\Phi(x,t)=\begin{cases}0 & x<0\\ E_F+W-eF_1 x\cos(\omega t) & 0\le x<d\\ -eF_1 d\cos(\omega t) & d\le x,\end{cases} \qquad (1)$$

here E_F and W are the Fermi energy and work function of the left metal respectively, and e is the elementary charge. Here, the impact of image and space charges is neglected for simplicity. The above potential barrier is inserted into TDSE to analytically solve the emission current exactly.

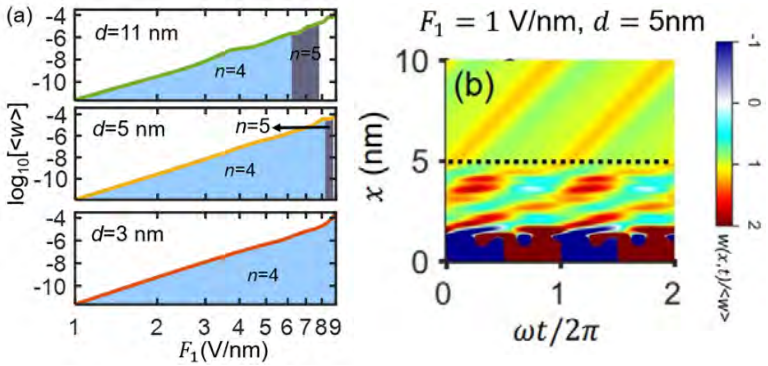


Figure 2. (a) Normalized total time-averaged emission current density $\langle w\rangle$ as a function of F_1 for d = 3, 5, and 11 nm. Here, laser field regimes are labeled with n = 4 and n = 5 (cf. the areas filled with different colors), meaning the dominant emission process here is four- or five- photon absorption; (b) Total time-dependent current density $w(x,t)$ as a function of time t and space x, under F_1 = 1 V/nm and d = 5nm. Here, $w(x,t)$ is normalized in terms of the time-averaged $\langle w\rangle$. The dotted line is at $x=d$. [1].

Our calculations show that the transition location between the dominant four- and five- photon absorption shifts to larger laser field F_1 for smaller gap distance d (Fig. 2a). This indicates that decreasing the gap distance (before entering the direct tunneling regime) can extend the multiphoton regime to higher laser intensity. This may be explained by the fact that the shape of the potential barrier becomes less sensitive to the laser field strength for a smaller gap distance, thus allowing the dominant n-photon process to remain over a larger range of laser fields (or laser intensities).

Figure 2b shows the time-dependent current density $w(x,t)$ as a function of space x and time t. It is seen that, besides the surface oscillation current near the metal-vacuum interface at $x=0$, some electrons are back reflected from the vacuum-metal interface at $x=d$ into the vacuum gap. The full width at half maximum (FWHM) of the emission current pulse is about 0.63 fs, which is greatly shorter than laser period of 2.67 fs.

The work is published in Applied Physics Letters [1] and is selected as a Featured article.

THEORY OF LASER-INDUCED PHOTOEMISSION FROM A METAL SURFACE WITH NANOSCALE DIELECTRIC COATING

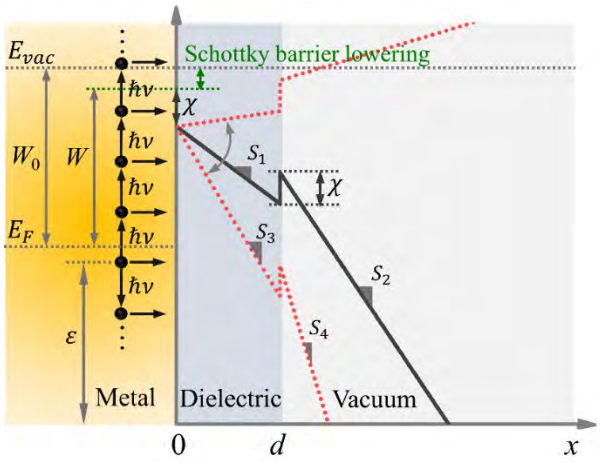


Figure 3. Photoemission from a flat metal surface coated with a dielectric under laser electric field and dc bias. The metal-dielectric interface is located at $x = 0$, and the coating's thickness is d. The metal has Fermi energy E_F and nominal work function of W_0. The effective work function $W = W_0 - \Delta W$, with the Schottky barrier lowering $\Delta W = 2\sqrt{e^3 F_0^{diel}/16\pi\varepsilon_0\varepsilon_{diel}}$ when the maximum of the potential barrier including image charge potential is in the coating or $\Delta W = 2\sqrt{e^3 F_0/16\pi\varepsilon_0}$ when the potential maximum is in the vacuum. The dielectric has the electron affinity of χ and the relative permittivity of ε_{diel}. The laser field strengths are F_1 in the vacuum and F_1^{diel} in the coating. The dc field strengths are F_0 in the vacuum and F_0^{diel} in the coating. The electron incident longitudinal energy is ε. The black solid line represents the potential profile under the dc field F_0 only, and the red dotted lines are for the time-dependent potential profile due to both F_0 and F_1. Slopes of the potential profile, denoted as S_1, S_2, S_3, and S_4, are $-eF_0^{diel}$, $-eF_0$, $-e(F_0^{diel} + F_1^{diel})$, and $-e(F_0 + F_1)$, respectively. [2]

The work develops an analytical quantum model for photoemission from metal surfaces coated with an ultrathin dielectric, by solving the 1D time-dependent Schrödinger equation subject to an oscillating double-triangular potential barrier [2]. The model is valid for an arbitrary combination of metal (of any work function and Fermi level), dielectric (of any thickness, relative permittivity, and electron affinity), laser field (strength and wavelength), and dc field. The effects of dielectric properties on photoemission are systematically investigated. It is found that a flat metal surface with dielectric coating can photoemit a larger current density than the uncoated case when the dielectric has smaller relative permittivity and larger electron affinity. Resonant peaks in the photoemission probability and emission current are observed as a function of dielectric thickness or electron affinity due to the quantum interference of electron waves inside the dielectric. Our model is compared with the effective single-barrier quantum model and modified Fowler–Nordheim equation, for both 1D flat cathodes and pyramid-shaped nanoemitters. While the three models show quantitatively good agreement in the optical field tunneling regime, the present model may be used to give a more accurate evaluation of photoemission from coated emitters in the multiphoton absorption regime.

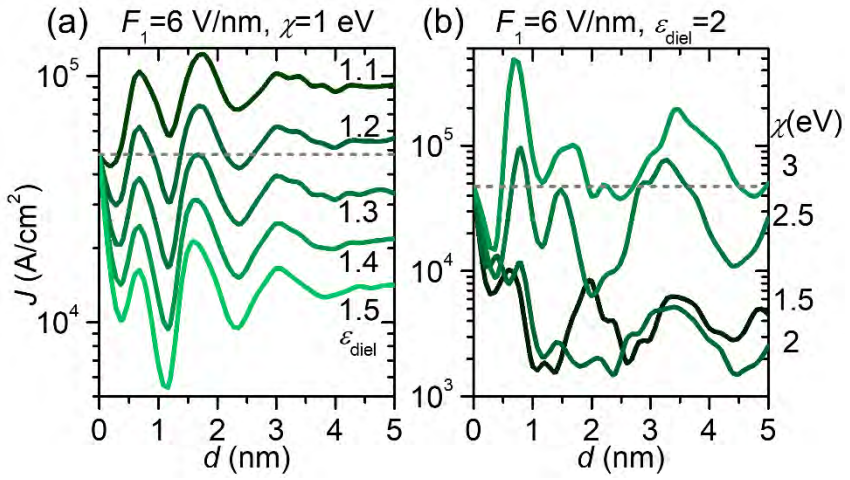


Figure 4. The photoemission current density J from a dielectric-coated flat metal surface as a function of dielectric thickness d under different (a) relative permittivity ε_{diel}; (b) electron affinity χ. The dc electric field $F_0 = 0$. [2]

The model under consideration is shown in Fig. 3 with the energy diagram at the metal-dielectric-vacuum interfaces. Importantly, it is found that a flat cathode surface with dielectric coating can emit a larger current density than an uncoated case, when the dielectric has sufficiently small relative permittivity ε_{diel} or large electron affinity χ, which would result in a narrowed or lowered potential barrier. Figures 4(a) and 4(b) provide examples of such cases, as shown in the region above the gray dashed lines. It should be pointed out that scattering of electrons with phonons, impurities, and even with other electrons inside the dielectric is not considered in the model. Photoelectron emission from ultrathin oxide covered devices shows an exponential attenuation behavior for the relatively thicker oxide layer (2.5~15.3 nm), with the dominant mean-free-path of the photoexcited electrons inside the SiO_2 ~1.2 nm. Therefore, for dielectric thicker than the mean-free-path, electron scattering effects cannot be neglected and require further investigations.

The work is published in Journal of Applied Physics [2].

OPTICAL-FIELD-INDUCED ELECTRON EMISSION IN A DC-BIASED NANOGAP

We extended our analytical formulation for nonlinear photoelectron emission in a dc-biased metallic nano-vacuum gap triggered by a laser field [3]. We theoretically investigate the photoelectron energy spectra and emission current from left- and right-side surfaces of the asymmetric nanojunction with various dc biases, laser fields and gap distances. The underlying photoemission mechanisms transitioning form multiphoton over-barrier emission to photon-assisted field tunneling, and the spatiotemporal dynamics of electron transport inside the gap are analyzed in detail. Our calculation shows applying a dc field could greatly reduce the interference oscillation in the transmission current in the nanogap, due to the shift of dominant emission away from multiphoton over-barrier regime. Our results demonstrate that, besides the dc bias, varying the gap spacing could strongly influence the rectification on the photoelectron emission in a dc-biased metal-vacuum-metal gap. Our study provides useful guideline to the design of ultrafast nanogap-based signal rectification devices, such as photoelectron emitters and photodetectors, by choosing optimal combination of dc bias, gap spacing, and material properties.

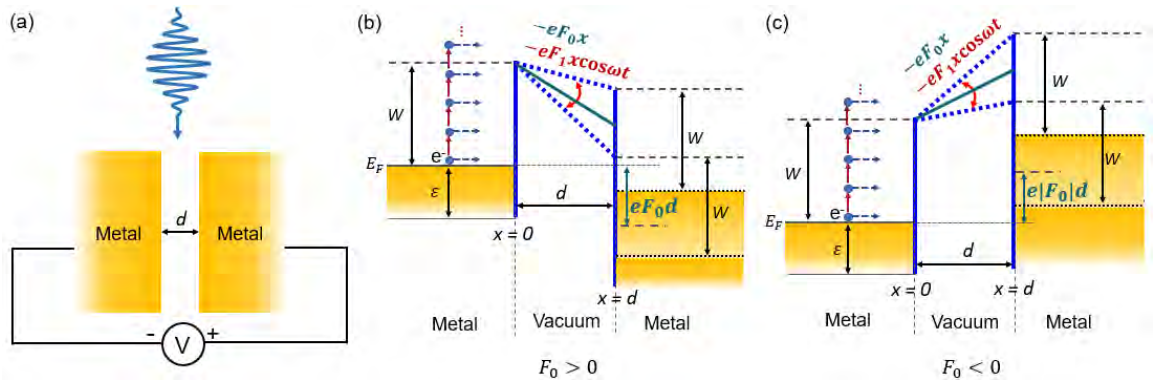


Figure 5. (a) Schematic of metal-vacuum-metal nanogap with a dc bias V under the illumination of laser field. d is the gap distance. (b) Energy diagram for photoelectron emission from left metal-vacuum interface of the gap in (a). Electrons with the initial energy ε would see a potential barrier subjected to a positive dc electric field $F_0 = V/d$ (> 0) and laser field $F_1\cos(\omega t)$. (c) Energy diagram for photoelectron emission from right metal-vacuum interface of the gap in (a). Electrons would see a potential barrier with a negative dc electric field $F_0 = -V/d$ (< 0) and laser field $F_1\cos(\omega t)$ with F_1 of opposite sign of that in (b) at any time instant for a given laser field.[3]

The schematic of the configuration for a metal-vacuum-metal nanogap with a dc bias under the illumination of optical field is shown in Fig. 5(a). With the external applied dc voltage V, the symmetry of the metal-vacuum-metal system is broken. This means that under the same illumination condition, the left and right metal-vacuum interfaces of the nanogap in Fig. 5(a) have different photoemission properties, whose energy diagrams are shown in Figs. 5(b) and 5(c), respectively.

In Figs. 6(a) and 6(b), we plot the total time-averaged transmission current density $<w>$ as a function of dc field F_0 under different laser fields F_1. In Fig. 6(c), we display the net emission current density $<w>_{net}$, defined as the difference between the left-to-right and the right-to-left emission current, as a function of external dc bias V for laser field F_1 = 0.4, 0.8 and 1 V/nm. For zero dc bias voltage, by symmetry, emission current density from left and right metal surfaces are equal, thus no net photocurrent $<w>_{net}$ is generated. Due to the nonlinear emission process with respect to dc field F_0 shown in Figs. 6(a) and 6(b), the photoemission from right surface of gap is gradually suppressed with the increasing dc bias while that from the left increases, which leads to the rectification response caused by applied dc bias to the photoemission (Fig. 6 (c)). The calculated increasing trend in Fig. 6(c) is in good agreement with the experimental measurement of photocurrent versus applied dc voltage in the periodic metal-vacuum nanotip array.

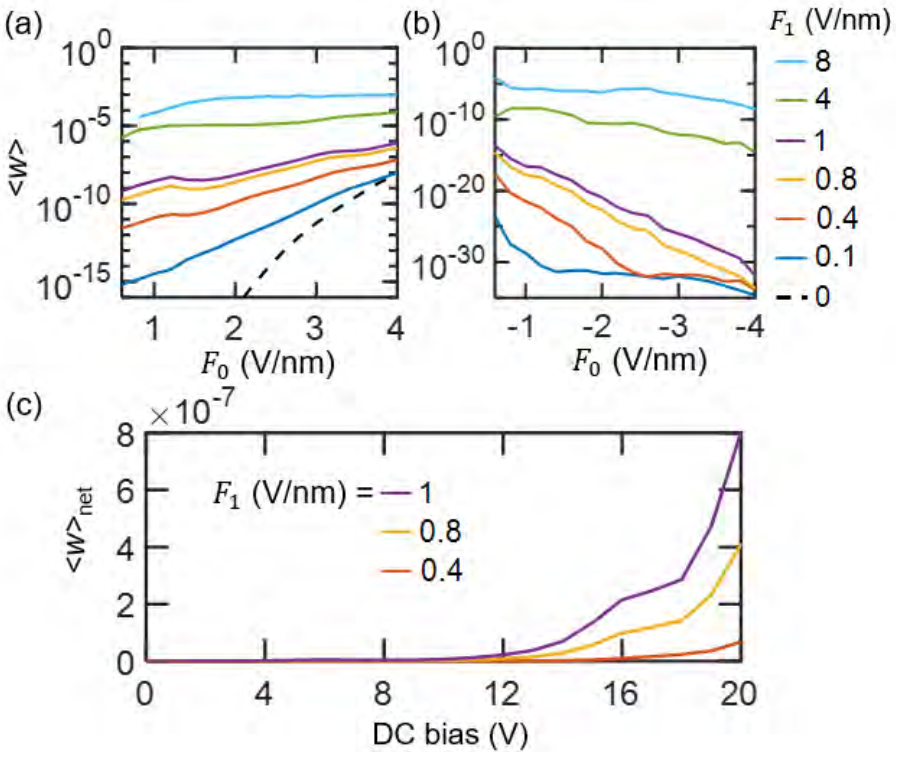


Figure. 6. (a), (b) Normalized total time-averaged emission current density $\langle w \rangle$ as a function of dc field F_0 for different laser fields F_1. (c) Dependence of net emission current density $\langle w \rangle_{\text{net}}$, defined as the difference between the left-to-right and the right-to-left emission current, on the applied dc bias for different laser fields F_1. Here, gap distance d is fixed at 5 nm. [3]

The work is published in Physical Review Applied [3].

UNRAVELING QUANTUM PATHWAYS INTERFERENCE IN TWO-COLOR COHERENT CONTROL OF PHOTOEMISSION WITH BIAS VOLTAGES

Coherent control steers a quantum system from an initial state to a target state by controlling quantum interference phenomena via an external field, which is central to vast applications ranging from quantum information processing to attosecond physics. For electron sources, coherent control enables precise manipulation on the electron emission process, and therefore the emitted beam properties. Here, we analyzed the quantum pathways interference in two-color coherent control of photoemission using exact analytical solutions of the time-dependent Schrödinger equation [4]. The theory includes all possible quantum pathways and their interference terms. Constructive (or destructive) interferences among the pathways leads to the maximum (or minimum) emission with varying phase delay of the two-color lasers. It is found that increasing the intensity ratio of the second harmonic (2ω) to fundamental (ω) lasers results in less contribution from the ω pathway (absorption of ω photons only) and more contribution from multicolor pathway (simultaneous absorption of both ω and 2ω photons) and 2ω pathway (absorption of 2ω photons only), and therefore stronger pathways interference and increased visibility larger than 95%. Increasing bias voltages shifts the dominant emission to processes with lower-order photon absorption, which sequentially decreases the interference between the ω and the 2ω pathways, and between single-color and multicolor pathways, leading to two peaks in the visibility.

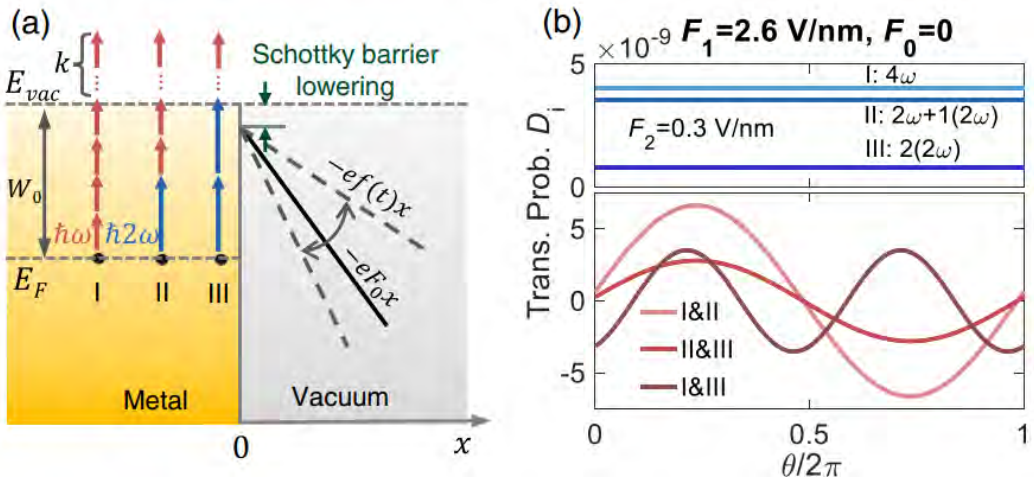


Figure 7. (a) Energy diagram for photoemission from metal surfaces induced by two-color laser fields $f(t) = F_1\cos(\omega t) + F_2\cos(2\omega t + \theta)$ under a dc field F_0. Red and blue arrows depict quantum pathway model, with pathway I: absorption of (4+k) fundamental photons (red arrow); pathway II: absorption of (2+k) fundamental photons and 1 second-harmonic photon (blue arrow); pathway III: absorption of 2 second-harmonic photons and k fundamental photons. (b) Electron transmission D_i through each quantum pathway (top) and their interference terms (bottom). [4]

The one-dimensional (1D) model is illustrated in Fig. 7(a). Electrons with initial energy of ε emit through the metal-vacuum interface ($x = 0$) due to dc field F_0 and two-color laser field $f(t) = F_1\cos\omega t + F_2\cos(2\omega t + \theta)$, where F_1 and F_2 are the magnitudes of the fundamental and second harmonic electric fields respectively, ω is the angular frequency of the fundamental laser, $\theta = 2\omega\tau$ is the relative phase between the fundamental and second harmonic with τ the corresponding time delay. For simplicity, the fields are assumed to be perpendicular to the metal surface and abruptly cut off inside the metal. The potential barrier seen by electrons inside the metal reads,

$$\phi(x,t) = \begin{cases} 0, & x < 0 \\ V_0 - ef(t)x - eF_0x, & x \geq 0 \end{cases} \tag{2}$$

where $V_0 = E_F + W_{eff}$, E_F is the Fermi energy of the metal, and $W_{eff} = W_0 - W_{Schottky}$ is the effective work function with W_0 the nominal work function and $W_{Schottky} = 2\sqrt{e^3F_0/16\pi\varepsilon_0}$ the Schottky barrier lowering due to dc field F_0, e (> 0) is the elementary charge, and ε_0 is the vacuum permittivity. By exactly solving TDSE subject to the potential barrier in Eq. (2), the time-averaged electron transmission probability from energy level ε is obtained as

$$D(\varepsilon) = \sum_{l=-\infty}^{\infty} w_l(\varepsilon) \tag{3}$$

where $w_l(\varepsilon)$ represents the electron emission through l-photon processes, with $l < 0$ being multiphoton emission, $l = 0$ direct tunneling, and $l > 0$ multiphoton absorption processes. It is important to note that although l in Eq. (3), as written, is referred to the number of fundamental photons $\hbar\omega$, it also includes the possible processes of substituting two fundamental photons $2\hbar\omega$ with a single second-harmonic photon $\hbar(2\omega)$, illustrated in the three possible pathways in Fig. 9(a), as well as arbitrary multiples of such substitutions.

By performing Fourier analysis and fitting with a simple quantum pathway model, we can obtain explicitly from the exact quantum theory in Eq. (3), the electron emission transmission probability through pathways I, II, and III, as well as through the interference terms between them I&II, II&III, and I&III.

Photoemission through each of the channels is explicitly shown in Fig. 7(b). It is clear that pathways I and II in combination, form the majority of the constant base line emission channels, around which the transmission probability oscillates with the relative phase θ. The strongest interference is between pathways I and II. Interference terms, and therefore the total transmission probability, can be strongly tuned by the phase difference θ, with maximum at $\theta \cong \pi/2$ and minimum at $\theta \cong 1.8\pi$, as shown in Fig. 7(b).

Our study provides direct theoretical foundation to confirm the coherent emission physics of replacing two fundamental photons with one second-harmonic photon despite various possible pathways. Our quantum theory and the corresponding pathways model are applicable to arbitrary driving-laser frequency, intensity (below the material damage threshold), and material properties. Our study provides insights into two-color laser-induced photoelectron emission dynamics and more general coherent control schemes of quantum systems ranging from single atoms and molecules, nano-objects, and material surfaces and interfaces. Manipulating ionization pathways and the corresponding quantum phases between pathways enable us to develop methods for controlling excitation and ionization processes in atoms, molecules, and materials under strong laser fields. Therefore, identifying and quantifying quantum pathways and corresponding quantum phases are fundamentally important to both the understanding of the photoionization dynamics and the characterization of the atomic and molecular structures. Our analysis using the exact analytical quantum model in combination with the Fourier analysis can provide a systematic investigation into the parametric dependence of each pathway as well as interference terms among them. The parametric scaling of different pathways would be helpful in the optimization of the input laser parameters to achieve coherent control through a specific pathway in a given quantum system, e.g. for advanced cathodes development.

The work is published in Physical Review B [4].

During this performance period, the PI is also serving as a Guest Editor for the Nineteenth Special Issue on High-Power Microwave and Millimeter-Wave Generation in IEEE Transactions on Plasma Science [5].

[1] Y. Luo and P. Zhang, "Ultrafast optical-field-induced photoelectron emission in a vacuum nanoscale gap: An exact analytical formulation", Appl. Phys. Lett. 119, 194101 (2021). **[Featured Article]**

[2] Y. Zhou and P. Zhang, "Theory of laser-induced photoemission from a metal surface with nanoscale dielectric coating", J. Appl. Phys. 131, 064903 (2022).

[3] Y. Luo and P. Zhang, "Optical-field-induced Electron Emission in a dc-Biased Nanogap", Phys. Rev. Applied 17, 044008 (2022).

[4] Y. Zhou, and P. Zhang, "Unraveling quantum pathways interference in two-color coherent control of photoemission with bias voltages", Phys. Rev. B. 106, 085402 (2022).

[5] J. Browning, N. M. Jordan, J. Stephens, and P. Zhang, "ANNOUNCEMENT The Nineteenth Special Issue on High-Power Microwave and Millimeter-Wave Generation", IEEE Trans. Plasma Sci., 50, 1378 (2022).

3. Findings and Conclusions

We constructed an analytical solution for nonlinear photoelectron emission in a nanoscale metal–vacuum–metal junction driven by a single-frequency laser field. Our results show the transition from direct tunneling to multiphoton induced electron emission as gap distance increases. We developed an exact quantum model for photoemission from metal surfaces coated with an ultrathin dielectric, by solving the 1D time-dependent Schrodinger equation. It is found that a flat metal surface with dielectric coating can photoemit a larger current density than the uncoated case when the dielectric has smaller relative permittivity and larger

electron affinity. We extended our exact theory for nonlinear photoelectron emission in a dc-biased metallic nanovacuum gap triggered by a laser field. Our results demonstrate that, besides the dc bias, varying the gap spacing could strongly influence the rectification on the photoelectron emission in a dc-biased metal-vacuum-metal gap. We also analyzed quantum pathways interference in two-color coherent control of photoemission. Our results will be useful to the development of advanced cathodes and electron sources with density modulation, enabling new advances for the development of high power electromagnetic sources and amplifiers.

4. Plans and Upcoming Events

We are currently applying our newly developed models for electron emission due to pulsed laser excitation to study emission current density modulation in RF field emitters. It is found that lasers, whether CW or pulsed, can provide significant modulation in RF field emitters. We plan to analyze the density profile of the emitted beam with a systematic parametric scaling analysis. This will be used to determine the optimized combination of emitter properties, laser, and RF fields to give the desired level of density modulation, which is important to the generation of short electron bunches for HPM excitation. We have been discussing with experimentalists at AFRL and University of Southern California to explore possible collaboration opportunities. We plan to explore the possibility of tailoring the emission energy spread by quantum dots. We also plan to develop new theory for beam-circuit interaction for density modulated beams using optical means. The optically modulated current from cathodes will be incorporated into the interaction with a slow wave structure to examine the RF outputs and determine the frequency optimums. We plan to develop new theory for beam-circuit interaction for density modulated beams using optical means. We will further explore the space charge effects in Pierce theory and identify the small q quantity for a realistic TWT. We also plan to run CST and XOOPIC simulations to test the beam-circuit theory and provide guidance to the source and circuit design of amplifiers and oscillators.

5. Transitions and Impacts

Not Applicable.

6. Collaborations

John Luginsland, Confluent Sciences/AFOSR.
Matt Franzi, Air Force Research Laboratory.
Steve Fairchild, Air Force Research Laboratory.
Tyson Back, Air Force Research Laboratory.
Yi Luo, international collaborator, Singapore University of Technology and Design, Singapore.
Ricky Ang, international collaborator, Singapore University of Technology and Design, Singapore.
Yee Sin Ang, international collaborator, Singapore University of Technology and Design, Singapore.
Lin Wu, international collaborator, Institute of High Performance Computing, Singapore.
Y. Y. Lau, University of Michigan.
John Verboncoeur, Michigan State University.
Rehan Kapadia, University of Southern California.
Chengkun Huang, Los Alamos National Labs.
Sneha Banerjee, Sandia National Labs.
Chunqi Jiang, Old Dominion University.
Brain Bentz, Sandia National Labs.

7. Personnel

Principal Investigator: Peng Zhang, 1 person-month, National Academy Member (N).

Team Members:
Patrick Wong (currently Scientist at Verus Research), Postdoc, 3 person-months, National Academy Member (N).
Yi Luo (currently Postdoc at SUTD, Singapore), graduate student, 3 person-months, National Academy Member (N).
Yang Zhou, graduate student, 12 person-months, National Academy Member (N).
Md. Faisal, graduate student, 6 person-months, National Academy Member (N).
Lan Jin, graduate student, 6 person-months, National Academy Member (N).

Business Contact: Casie Medina
Subs: None

8. Students

3 graduate students assisting during reporting period.

9. Technology Transfer

We have filed a US Provisional Patent on the enhancement of photoelectron emission using thin dielectric coating: P. Zhang, L. Wu, X. Xiong, and Y. Zhou, “Thin Dielectric Coated Plasmonic Photoemitter”, US Patent Provisional, filed on 5/20/2021. It was converted to nonprovisional United States application on 5/20/2022.

10. Products, Publications, Patents, License Agreements, etc.

Publications resulting from this project during the performance period of 10/1/2020-9/30/2021:

Archival Publications

1. Y. Luo and P. Zhang, "Ultrafast optical-field-induced photoelectron emission in a vacuum nanoscale gap: An exact analytical formulation", Appl. Phys. Lett. 119, 194101 (2021). **[Featured Article]**. Peer-reviewed, Distribution A, Federal Funding Acknowledged. https://doi.org/10.1063/5.0061914

2. Y. Zhou and P. Zhang, "Theory of laser-induced photoemission from a metal surface with nanoscale dielectric coating", J. Appl. Phys. 131, 064903 (2022). Peer-reviewed, Distribution A, Federal Funding Not Acknowledged. https://doi.org/10.1063/5.0078060

3. Y. Luo and P. Zhang, "Optical-field-induced Electron Emission in a dc-Biased Nanogap", Phys. Rev. Applied 17, 044008 (2022). Peer-reviewed, Distribution A, Federal Funding Acknowledged. https://doi.org/10.1103/PhysRevApplied.17.044008

4. Y. Zhou, and P. Zhang, "Unraveling quantum pathways interference in two-color coherent control of photoemission with bias voltages", Phys. Rev. B. 106, 085402 (2022). Peer-reviewed, Distribution A, Federal Funding Acknowledged. https://doi.org/10.1103/PhysRevB.106.085402

5. J. Browning, N. M. Jordan, J. Stephens, and P. Zhang, "ANNOUNCEMENT The Nineteenth Special Issue on High-Power Microwave and Millimeter-Wave Generation", IEEE Trans. Plasma Sci., 50, 1378 (2022). Peer-reviewed, Distribution A, Federal Funding Not Acknowledged. https://doi.org/10.1109/TPS.2022.3167495

Conference Papers

1. Peng Zhang, “Electron Emission Physics at Ultrafast and Ultra-Small Scale”, 2022 IVEC Mini-Courses, Twenty-Third IEEE International Vacuum Electronics Conference (April 25-28, 2022, Monterey, CA, USA). **[Invited Tutorial]** Federal Funding Acknowledged.

2. Peng Zhang, “Exact Quantum Solution for Photoemission at Ultrafast and Ultra small Scales”, Photocathode Physics for Photoinjectors Workshop (P3 2021), Nov 10-12, 2021, SLAC, Virtual, USA. **[Invited Talk]** Federal Funding Acknowledged.

3. Y. Zhou, and Peng Zhang, “PO08.00011: Quantum pathways interference in photoemission from metals induced by two-color lasers with a dc bias”, 64th Annual Meeting of the APS Division of Plasma Physics (October 17–21, 2022, Spokane, Washington, USA). [Oral] Federal Funding Acknowledged.

4. B. Bentz, K. Youngman, A. Iqbal, Y. Zhou, Peng Zhang, “DT1.00001: Photoemission induced plasma breakdown”, 75th Annual Gaseous Electronics Conference (October 3-7, 2022, Sendai, Japan). [Oral] Federal Funding Acknowledged.

5. M. Faisal, A. Iqbal, Peng Zhang, “Smith-Purcell Radiation with Different Grating Parameters and Beam Bunching Frequencies”, 49th IEEE International Conference on Plasma Science (22 - 26 May, 2022, Seattle, WA, USA). [poster] Federal Funding Acknowledged.

6. Y. Zhou and Peng Zhang, “Interference of quantum pathways in two-color laser induced photoemission with a dc bias”, 49th IEEE International Conference on Plasma Science (22 - 26 May, 2022, Seattle, WA, USA). [Oral] Federal Funding Acknowledged.

7. A. Paudel, P. Wong, Peng Zhang, J. Luginsland, and M. Franzi, “A Discrete Cavity Analysis for Coupled-Cavity Travelling Wave Tubes”, 49th IEEE International Conference on Plasma Science (22 - 26 May, 2022, Seattle, WA, USA). [poster] Federal Funding Acknowledged.

8. A. Paudel, P. Wong, Peng Zhang, J. Luginsland, and M. Franzi, “A Discrete Cavity Analysis for Coupled-Cavity Traveling Wave Tubes”, Twenty-Third IEEE International Vacuum Electronics Conference (April 25-28, 2022, Monterey, CA, USA). [Poster] Federal Funding Acknowledged.

9. M. Faisal, A. Iqbal, and Peng Zhang, “Smith-Purcell Radiation with Different Grating Parameters and Beam Bunching Frequencies”, Twenty-Third IEEE International Vacuum Electronics Conference (April 25-28, 2022, Monterey, CA, USA). [Poster] Federal Funding Acknowledged.

10. Y. Zhou, Peng Zhang, “Quantum Efficiency of Photoemission from Biased Metal Surfaces with Lasers from UV to NIR”, Twenty-Third IEEE International Vacuum Electronics Conference (April 25-28, 2022, Monterey, CA, USA). [Oral] Federal Funding Acknowledged.

11. Peng Zhang, Y. Luo, Y. Zhou, “An Exact Theory for few-Cycle Optical-Field-Induced Photoelectron Emission From Biased Surfaces”, JTh4A.16, High-Brightness Sources and Light-Driven Interactions Congress (HILAS), OPTICA (March 22-25, 2022, Budapest, Hungary). [Poster, Virtual] Federal Funding Acknowledged.

12. Y. Zhou, and Peng Zhang, “Theory of Photoelectron Emission from Metal Surfaces Coated with a Nanoscale Dielectric”, Photocathode Physics for Photoinjectors Workshop (P3 2021), Nov 10-12, 2021, SLAC, Virtual, USA. [Poster] Federal Funding Acknowledged.

Theses

1. Y. Zhou, “Photoemission from biased metal surfaces: quantum efficiency, laser heating, dielectric coatings, and quantum pathways interference”, Ph.D. dissertation, Dept. Elect. Comput. Eng., Michigan State Univ., East Lansing, MI, USA, 2022. Federal Funding Acknowledged.

Patents

1. P. Zhang, L. Wu, X. Xiong, and Y. Zhou, “Thin Dielectric Coated Plasmonic Photoemitter”, US Patent Provisional, filed on 5/20/2021; converted to nonprovisional United States application on 5/20/2022.

11. Point of Contact in Navy

Kevin Jensen, NRL, 1SEP2022; Jason Marshall, NRL, 10MAY2022

12. Acknowledgement/Disclaimer

This work was sponsored by the Office of Naval Research (ONR), under grant (or contract) number N00014-20-1-2681. The views and conclusions contained herein are those of the authors only and should not be interpreted as representing those of ONR, the U.S. Navy or the U.S. Government.

Infrared Optics with Engineered Materials

Grant No. N00014-20-1-2297

Annual Report for Fiscal Year 2022

Period of Performance: October 1, 2021 to September 30, 2022

Prepared by:

Professor Mikhail Kats, Principal Investigator
University of Wisconsin-Madison
Engineering Hall, 1415 Engineering Drive, Room 3441, Madison, WI, USA - 53706
Email: mkats@wisc.edu



Kats Group



This work was sponsored by the Office of Naval Research (ONR), under grant number N00014-20-1-2297. The views and conclusions contained herein are those of the authors only and should not be interpreted as representing those of ONR, the U.S. Navy or the U.S. Government.

Grant or Contract Number: N00014-20-1-2297
Date Prepared: January 31, 2023
Project Title: Infrared Optics with Engineered Materials
Annual Summary Report: FY22, 1 October 2021 to 30 September 2022
Principle Investigator: PI Mikhail Kats, mkats@wisc.edu, University of Wisconsin-Madison

Section I: Project Summary

1. Overview of Project

Abstract: The major goals of this project are to explore innovative ways to engineer and characterize existing and emerging optical materials to enable next-generation infrared optics for emitting, manipulating, absorbing, and detecting infrared light. The ability to emit, manipulate, absorb, and detect infrared light has substantial long-term Naval relevance, especially due to the rapid development of infrared sensors and cameras, as well as high-power lasers that may be used to blind these instruments. This document describes progress made in FY22 toward these fundamental-science goals, and includes improved understanding of the thermodynamic limits of thermal radiation, improved understanding of giant anisotropy in quasi-one dimensional perovskite materials, the demonstration of modification of oxide semiconductors and phase transitions using focused ion beams, and the demonstration of coatings that conceal information from infrared imagers including hyperspectral infrared cameras.

Objective: The proposal had three key sections. In Chapter 1, we proposed new approaches to modify materials properties, focusing on spatial control of infrared optical properties, such that they can be engineered into devices. In Chapter 2, we proposed the development of new and improved methods of materials metrology to better understand infrared optical materials and to better characterized engineered optical structures. In Chapter 3, we proposed new infrared optical and optoelectronic devices for polarization control and infrared photodetection, based on materials-engineering and characterization techniques (to be) developed in Chapters 1 and 2. Specifics goals include the development of new spectroscopic techniques for materials analysis, new types of flat and thin optical components for imaging and beam control, more-robust control over polarization of infrared light, new optical protective technologies, and new optical technology for thermoregulation using engineered thermal radiation.

Background: Our approach to reach the objectives described above is to carry out an interdisciplinary, integrated program where we simultaneously investigate new spectroscopic techniques for materials characterization, new ways of modifying materials, and new devices, with the devices building on the materials innovations developed within the project.

2. Activities and Accomplishments

Several research tasks from the start of this project have involved the engineering and measurement of thermal radiation—a physical process that has in principle been understood since the dawn of quantum theory. However, over the last two decades, a number of breakthroughs have shown that not only are new applications possible, but also our understanding of thermal radiation and related phenomena has room for improvement.

We observed that over the last decade+ there have been a number of published papers by various research groups that claim (via experiment or simulations) the demonstration of "super-Planckian" thermal radiation, in which an object held at a particular temperature emits more light in some wavelength band compared to a perfect blackbody at the same temperature. Such claims are often quite surprising, because they appear to violate the laws of thermodynamics—extremely fundamental and well-established scientific principles. We spent a considerable amount of effort to nail down the relevant physical principles and clarify how and when "super-Planckian" emission is and is not possible, resulting in a publication in Nature

Photonics titled “Super-Planckian emission cannot really be ‘thermal’”. The reference is Y. Xiao et al, *Nature Photonics* 16, 397 (2022). We looked at several ways in which super-Planckian emission may be possible; for example in Fig. 1, we reproduce one of the figures from our commentary, showing that the absorption cross-section (and hence the emission cross-section) can be larger than the geometrical area of a small emitter which features resonances. If defining the emission area as the geometrical area, then super-Planckian thermal radiation is indeed possible. However, we found that in most scenarios of practical relevance, this concept of “super-Planckian thermal radiation” is misleading. This is because the effect does not stack when many emitters are placed close to each other; instead, a macroscopic surface made of many such small “super-Planckian” emitters is indeed bound by the Planck blackbody limit.

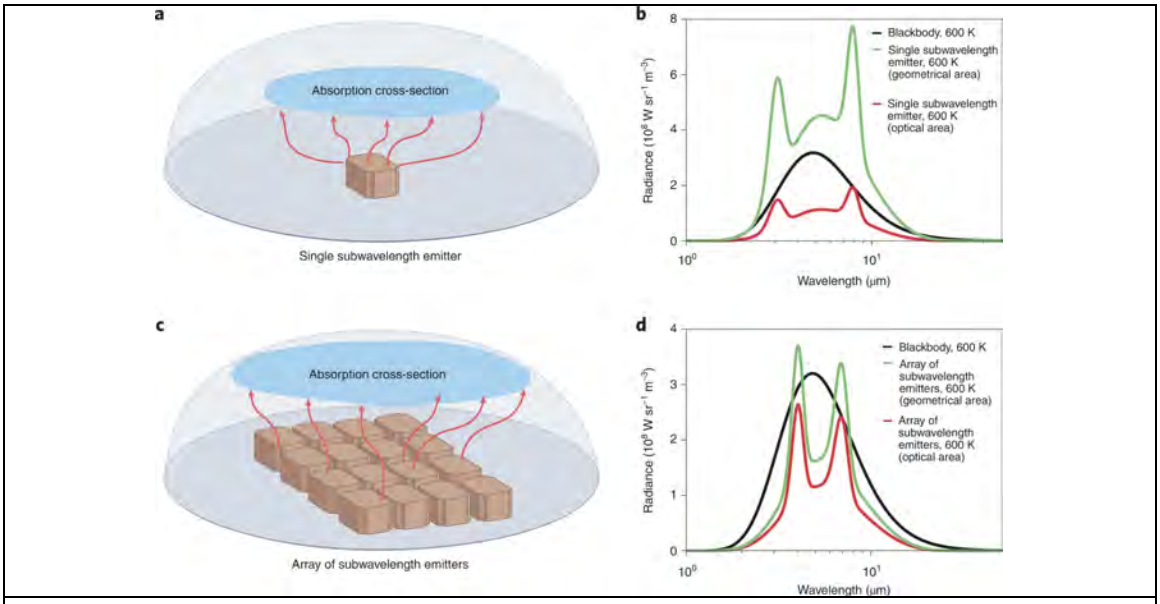


Fig. 1. (a) A subwavelength thermal emitter can radiate toward a hemisphere with an optical absorption cross-section much larger than its geometrical cross-section near its resonance wavelength. (b) Thermal emission from subwavelength objects at a particular temperature can appear super-Planckian if considering the geometrical cross-section as the emitting area, but cannot be super-Planckian if the optical-absorption cross-section is considered instead. (c,d) The apparent enhancement of the absorption cross-section decreases if multiple subwavelength emitters are positioned together side by side, for example in a tightly packed array.

A perhaps more interesting and sophisticated scenario is described in Fig. 2, below. This scenario was motivated by a theoretical paper from Purdue University (Jacob group) which calculated that a blackbody emitter with a nonlinear structure in front of it can convert some of the light from one wavelength to another, resulting in super-Planckian emission. This paper—which previously did not get much attention in the community—hit upon something quite profound. It turns out that in this case super-Planckian emission is indeed possible, if the heat bath that is in contact with the emitter is at a higher temperature than the region of space toward which it is emitting. In our paper, we put this interesting concept on much firmer footing, describing it as an example of a class of what we called “heat-powered radiation”, where the difference in temperature between the emitter and the space it is emitting can power a thermodynamic heat engine, which can do work and in doing so overcome the Planck blackbody limit. At the same time, however, we argue that this is best not called “thermal radiation” or “thermal emission”, because the emitter is no longer in thermodynamic equilibrium, and it is this nonequilibrium that allows for the Planck limit to be overcome. We are sure that future discussions will be had over which terminology is correct, but we believe our work to clarify what is and is not physically possible, which is very important.

I note that the lead author, Dr. Yuzhe Xiao, is departing our group to start a faculty position at the University of North Texas, in the Department of Physics. We are proud of him and wish him well.

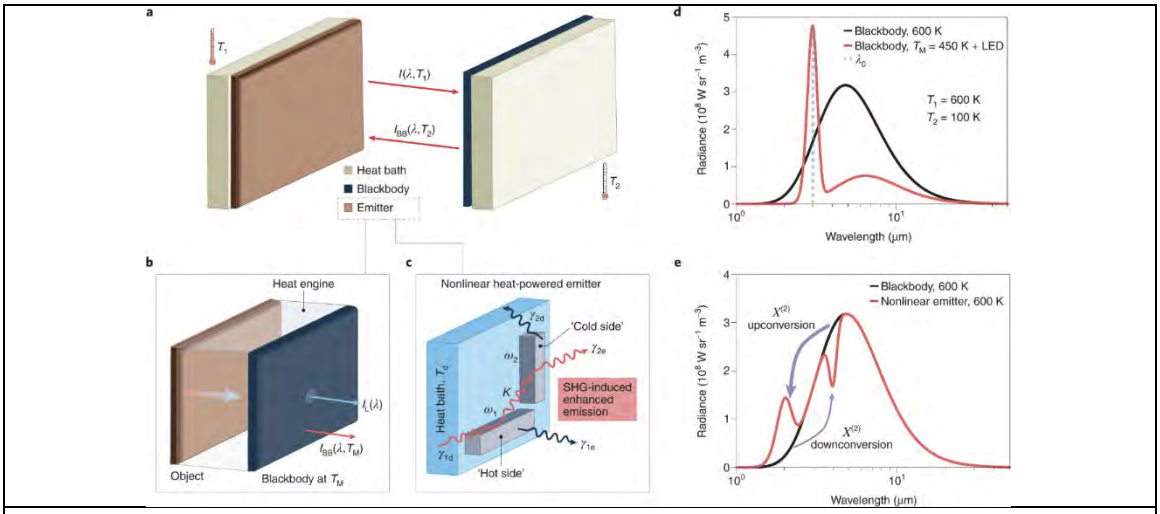


Fig. 2. Non-equilibrium heat-powered emission between a hot emitter and a cold blackbody, which are in contact with heat baths at different temperatures. b, A heat engine runs between the hot object at T_1 and a blackbody at an intermediate temperature T_M, and the work generated from the heat engine is used to power a vanishingly small LED on the surface. In this configuration, the total light emission is the combination of blackbody radiation at TM and LED light. c, Schematic of an emitter that can realize super-Planckian emission via nonlinear effects when radiating towards a cold environment. d, Super-Planckian heat-powered emission is realized near the LED center wavelength λ_0 for the configuration shown in b. e, Modification of the blackbody radiation spectrum via nonlinear effects as shown in c: non-equilibrium conditions enable selective upconversion through second-harmonic generation, thus realizing super-Planckian heat-powered emission near 2 μm.

During this performance period, we continued to work in collaboration with Jayakanth Ravichandran (USC) and Rohan Mishra (WUSTL) on highly anisotropic infrared materials, to enable sophisticated polarization control of light. During the quarterly reports, we have been reporting our discovery of colossal optical anisotropy in strontium titanium sulfide (STS), setting a world record for a uniaxial material. However, during this performance period we have not been able to fully understand the mechanism that enhances the infrared anisotropy to the degree observed experimentally. We believe we are close, and will be able to publish a paper describing the effect before the next annual report. At the same time, we have made progress in understanding the anisotropy of barium titanium sulfide (BTS), the first material where we found large infrared anisotropy (previously in N. Niu et al, *Nature Photonics* 12, 392 (2018), carried out under an ONR YIP award). Our collaborators at USC were able to synthesize BTS platelets in two different orientations [(100) and (001)], and we performed optical characterization of these materials, clearly observing in-plane optical anisotropy for the (100) BTS crystals but not for the (001) BTS crystals (Fig. 3). Time-domain thermoreflectance measurements at room temperature also found substantial thermal-conductivity anisotropy (1.7 vs 0.038 W/mK), and we identified the cause being the differences in phonon scattering rates along the different directions. This work was published as Zhao et al, *Chemistry of Materials* 34, 5680 (2022).

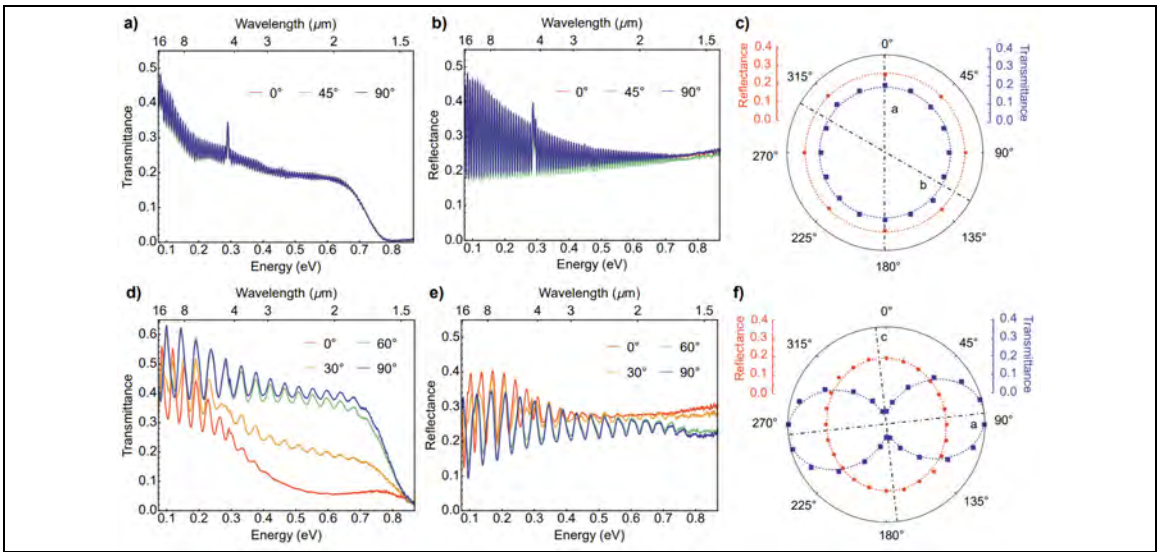
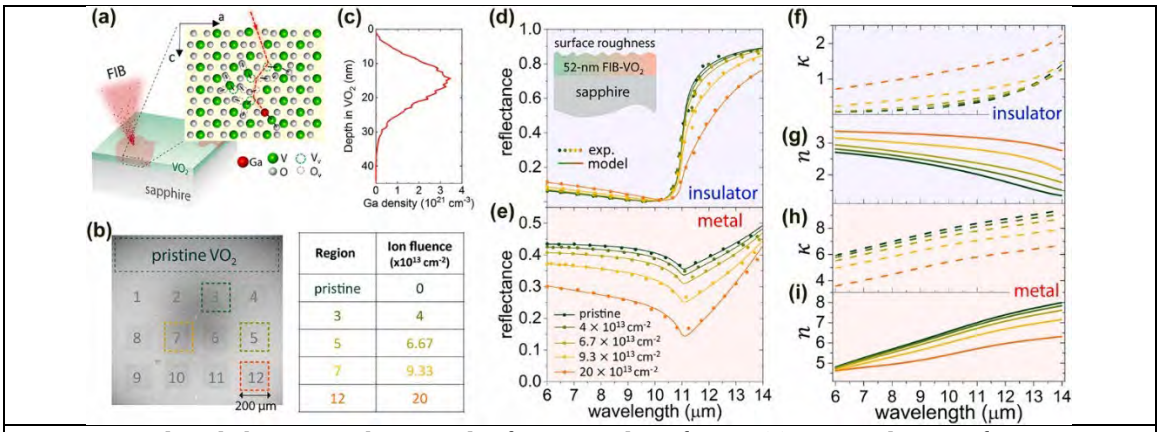


Fig. 3. (a, b, c) Transmittance and reflectance of (001) BTS crystals, showing in-plane isotropy. (d, e, f) Transmittance and reflectance of (100) BTS crystals, which clearly have substantial in-plane anisotropy. The plots in c and f are at a wavelength of 2 micron.

We also continued to work on the ion-beam modification of materials, here specifically using a commercial focused ion beam (FIB) system, or the type that is typically available at universities and corporate labs. In a recent paper (H. Mei, *Nanophotonics*, 11, 3923 (2022)) we investigated FIB modification of two materials: localized doping in ZnO, and defect engineering of vanadium dioxide ($_{VO2}$), the prototypical phase-transition material that is the subject of several tasks in the present project. Fig. 4 shows the ion-irradiation experiments, where a Ga FIB at 30 keV is used to bombard a VO_2 film. The ion irradiation modifies the optical properties of the film in both the metal and insulator phases (Fig. 4(d-i)), but not too much, as shown by reflectance measurements and mid-infrared spectroscopic ellipsometry of the films. y



Region	Ion fluence (x10^{13} cm^{-2})
pristine	0
3	4
5	6.67
7	9.33
12	20

Fig. 4. FIB-induced changes in the optical refractive index of VO_2. (a) Ion irradiation of VO_2 using a FIB, showing a collision cascade in the VO_2 lattice initiated by an energetic Ga ion. (b) SEM image of the FIB-irradiated VO_2 regions with the corresponding ion fluences listed. (c) Simulated depth profile of 30-keV Ga ions into a VO_2 thin film using TRIM. (d, e) The symbols are FTIR reflectance measurements on pristine VO_2 and regions irradiated with different ion fluences for temperatures at 25 °C (all regions in pure insulating phases) and 100 °C (all regions in pure metallic phases), respectively. The solid curves are the model fits to the FTIR measurements, where the underlying model was created based on ellipsometry of pristine VO_2. The insulator-phase (f, g) and metal-phase (h, i) refractive indices were extracted from the fittings shown in (d) and (e).

We can make some interesting observations from looking at the phase-transition temperature (Fig. 5). Intrinsic VO_2 transitions from being an insulator at room temperature to a metallic phase when heated past ~70 °C. In previous work, we discovered that the VO_2 phase transition can be modified by defect engineering via an ion beam, which can create localized strain (J. Rensberg et al, *Nano Letters* 16, 1050 (2016)). However, in that work we used an ion accelerator and tuned the ion energy such that the ions penetrated into the middle of the VO_2 film. Here, the ion penetration depth is only 15-20 nm (Fig. 4(c)), whereas the film is 50 nm. Despite this, the effect appears to be similar, with at least the majority of the film having the same transition temperature. If this were not the case, the width of the transition (T_{IMT}) would increase when the fluence first increases—but no such thing happens (Fig. 5(b)). The ability to use a low-energy FIB to locally engineer the phase transition of VO_2 opens up the possibility of making pixels directly on VO2 for infrared imaging and detection applications.

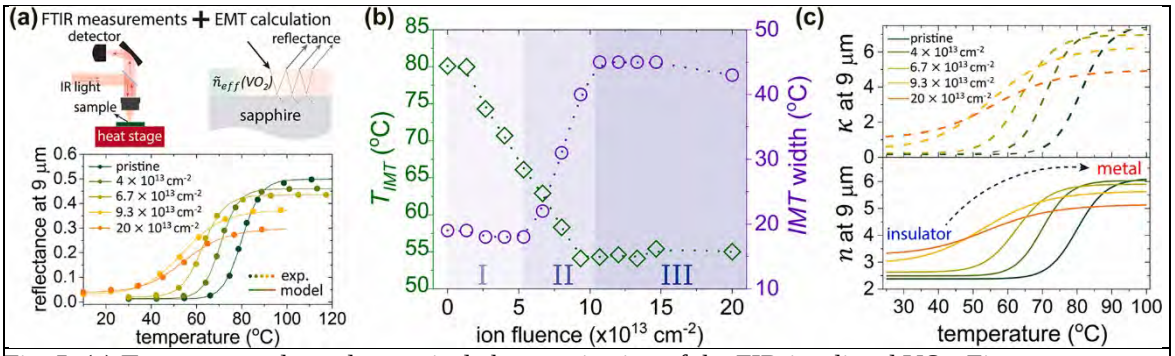


Fig. 5. (a) Temperature-dependent optical characterization of the FIB-irradiated VO_2. First, we measured temperature-dependent reflectance across the IMT for each irradiated region. Then, we applied effective-medium theory to approximate the refractive indices at intermediate temperatures and calculate the temperature-dependent reflectance. By sweeping the parameters of T_{IMT} and E—which determine the IMT width and temperature, respectively—we found the best fit between the FTIR measurements and calculation, enabling us to extract the IMT temperature and width for each irradiation ion fluence, as plotted in (b). (c) Extracted temperature-dependent refractive indices of the defect-engineered VO_2 irradiated by different ion fluences. Here we plot the results for a single wavelength of 9 μm to clearly show the evolution of refractive-index values versus temperature and ion fluence.

Finally, on the device side, we have completed and published a manuscript titled "Wavelength-by-wavelength temperature-independent thermal radiation utilizing an insulator-metal transition" (J. King et al, *ACS Photonics* 9, 2742 (2022)). In this collaborative work with Shriram Ramanathan's group (Purdue; recently moved to Rutgers), we designed the temperature-dependent spectral emissivity of a coating to counteract all the changes in the blackbody-radiation distribution over a certain temperature range, enabled by the nonhysteretic insulator-to-metal phase transition of $SmNiO_3$. At each wavelength within the long-wave infrared atmospheric-transparency window, the thermal radiance of our coating remains nearly constant over a temperature range of at least 20 °C. Our approach can conceal thermal gradients and transient temperature changes from infrared imaging systems, including those that discriminate by wavelength, such as multispectral and hyperspectral cameras. The concept and major experimental result are shown in Fig. 6, where in (c) our engineered emitter is compared to an ordinary material, which here is just a fused-silica wafer. The structure that generates this performance is a silica substrate, an ITO layer, and an $SmNiO_3$ layer with appropriate thicknesses that we optimized using conventional thin-film calculations combined with Kirchhoff's law of thermal radiation.

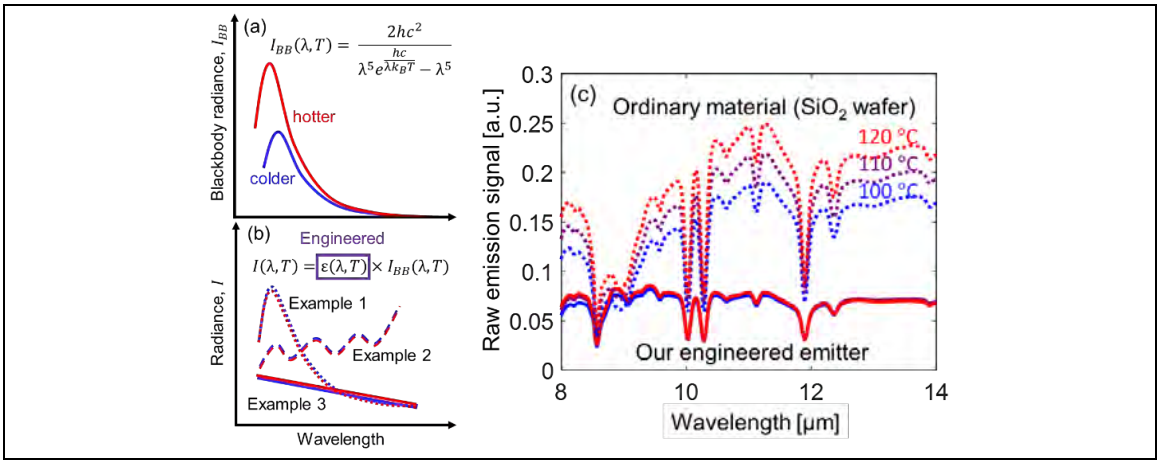


Fig. 6. (a) Blackbody spectral radiance, $I_{BB}(\lambda, T)$, at two arbitrary temperatures. (b) Several examples of temperature-dependent spectral radiance where $dI(\lambda, T)/dT = 0$ is achieved by engineering the emissivity. (c) The main experimental result of this paper: an emitter engineered to achieve $dI(\lambda, T)/dT = 0$ across the 8 – 14 μm from T = 100 °C to T = 120 °C compared to a reference SiO_2 wafer (the sharp features are due to absorption by ambient gases present in the lab on the day of the measurement).

The ability of this coating to function as a wavelength-by-wavelength zero-differential (information concealing) coating is shown in Fig. 7. Assuming a conventional surface where the emissivity does not depend much on temperature, and infrared camera easily picks up the differences between the surface at different temperatures. However, with the zero-differential coating based on $SmNiO_3$ ("ZDSE") information is concealed, and the camera picks up roughly the same signal irrespective of surface temperature. This effect persists even when different spectral filters are positioned in front of the camera, indicating that the effect is present at each wavelength within the long-wave infrared (LWIR) band of the infrared camera.

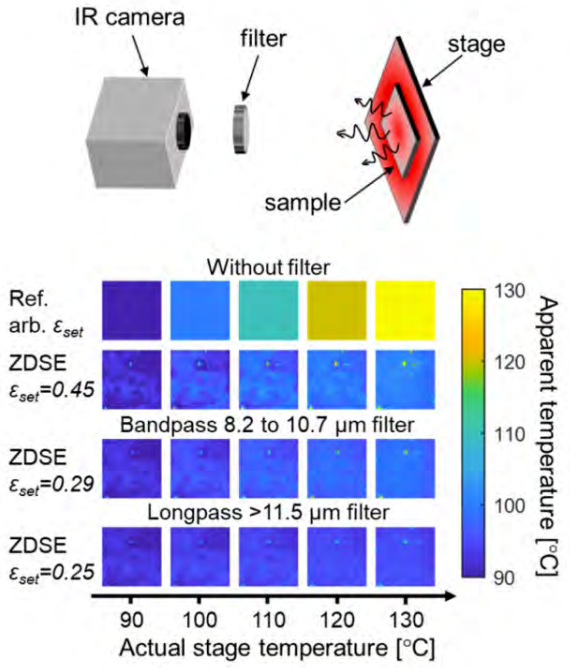


Fig. 7. Infrared imaging setup and (bottom) infrared images of the ZDSE with and without spectral filters. The "apparent temperature" is the value reported by the FLIR infrared camera when the input emissivity ε_{set} was selected such that the apparent temperature matched the stage temperature at 90 °C

3. Findings and Conclusions

- Clarified when super-Planckian emission is and is not possible, resolving confusion that exists in the literature
    - Related to a Chapter 2 objective [new and improved methods of materials metrology to better understand infrared optical materials and to better characterized engineered optical structures], given our use of thermal emission as a metrology technique elsewhere in this project

- Reported additional characterization of barium titanium sulfide (BTS), a prototypical quasi-one-dimensional material that has giant anisotropy in the infrared
    - Chapter 1 objective [new approaches to modify materials properties, focusing on spatial control of infrared optical properties]
    - Chapter 3 objective [new infrared optical and optoelectronic devices for polarization control and infrared photodetection]
- Demonstrated that a focused ion beam can be used to direct-write features on phase-transition material VO_2, locally modifying its phase-transition properties
    - Chapter 1 objective [new approaches to modify materials properties, focusing on spatial control of infrared optical properties]
- Demonstrated a coating that features "wavelength by wavelength" zero-differential thermal emission, and can therefore conceal temperature information and features from infrared cameras, even those that can hone in on specific wavelengths
    - Chapter 3 objective [new infrared optical and optoelectronic devices for polarization control and infrared photodetection]

4. Plans and Upcoming Events

The plans are unchanged from the proposal. Prof. Kats has an upcoming seminar at the University of Minnesota, which will in part cover the work on the present project. Prof. Kats also has upcoming invited talks covering material in the present project at the Optica Novel Optical Materials and Applications (NOMA) Conference in Busan (Korea), the SPIE Optics and Photonics Conference (San Diego), and the SPP10 Conference (Houston).

5. Transitions and Impacts

We hate an STTR Phase II, subcontracted from and in collaboration with Physical Sciences Incorporated, on thermochromic coatings for emissivity engineering. The research that led to that award evolved in part from the accomplishments on the present grant.

6. Collaborations

In this reporting period on this project, we have collaborated with the following groups:

- Group of Carsten Ronning, University of Jena, Germany
- Group of Shriram Ramanathan, Purdue University (moved to Rutgers)
- PIs David Woolf, Joel Hensley, and others, Physical Sciences Incorporated
- Group of Jayakanth Ravichandran, University of Southern California
- Group of Rohan Mishra, Washington University in St. Louis
- Group of Raluca Scarlat, University of California, Berkeley

7. Personnel

Principal investigator: Mikhail Kats, 0.78 person months [not a National Academy Member]

Team Members: Yuzhe Xiao, Assistant Scientist, 5.44 person months [not a National Academy Member]; Chenghao Wan, postdoc, 7.68 person months [not a National Academy Member]

8. Students

Four (4) graduate students

9. Technology Transfer

Patent application for Planck spectroscopy was submitted in a previous cycle, publish this year:

Y. Xiao, C. Wan, J. Salman, M. A. Kats, “Planck spectrometer”, Patent application filed Dec 2020; Published 2022.

10. Products, Publications, Patents, License Agreements, etc.

Publications resulting from this project:

Archival Publications (all peer reviewed)

Y. Xiao, M. Sheldon and M. A. Kats, "Super-Planckian emission cannot really be ‘thermal’", *Nature Photonics* 16, 397 (2022)

B. Zhao, M. S. B. Hoque, G. Y. Jung, H. Mei, S. Singh, G. Ren, M. Milich, Q. Zhao, N. Wang, H. Chen, S. Niu, S. J. Lee, C. T. Kuo, J. S. Lee, J. A. Tomko, H. Wang, M. A. Kats, R. Mishra, P. E. Hopkins, J. Ravichandran, "Orientation Controlled Anisotropy in Single Crystals of Quasi-1D BaTiS3", *Chemistry of Materials* 34, 5680 (2022)

J. King, A. Shahsafi, Z. Zhang, C. Wan, Y. Xiao, C. Huang, Y. Sun, P. J. Roney, S. Ramanathan, M. A. Kats, “Wavelength-by-wavelength temperature-independent thermal radiation utilizing an insulator-metal transition”, *ACS Photonics* 9, 2742 (2022)

H. Mei, A. Koch, C. Wan, J. Rensberg, Z. Zhang, J. Salman, M. Hafermann, Y. Xiao, R. Wambold, S. Ramanathan, C. Ronning, M. A. Kats, “Tuning carrier density and phase transitions in oxide semiconductors using focused ion beams”, *Nanophotonics* 11, 2923 (2022)

Conference Papers

Note: in our group/field, we typically do not submit “conference papers”, but we do have conference presentations which are either oral or poster presentations. Sometimes (but not always) the abstract is published, but we do not typically submit full conference papers.

C. Wan et al, “Diverse Tunable Nanophotonic Devices Based on Thin-Film Vanadium Dioxide”, MRS Fall Meeting, Boston (2022)

C. Wan, M. Hafermann, T. J. Park, Z. Zhang, Y. Xiao, H. Mei, S. Ramanathan; C. Ronning, M. Kats, “Tunable Threshold in VO2-based Photonic Devices Enabled by Defect Engineering”, Conference on Lasers and Electro-Optics (CLEO), San Francisco (2022) [postdeadline talk]

Books

None

Book Chapter

None

Theses

None

Websites

None

Patents

d. Inventors: Y. Xiao, C. Wan, J. Salman, M. A. Kats
e. Wisconsin Alumni Research Foundation
f. Planck spectrometer
d. US20220187134A1 (USA)
e. Filed Dec 2020; Published June 2022

Other Products: Identify any other significant products that were developed under this project. Describe the product and how it is being shared.

Prof. Kats presented a Basic Research Forum for the Office of the Under Secretary of Defense (OUSD) in 2022, covering in part work supported by this project

11. Point of Contact in Navy

None at this time

12. Acknowledgement/Disclaimer

This work was sponsored by the Office of Naval Research (ONR), under grant (or contract) number N00014-20-1-2297. The views and conclusions contained herein are those of the authors only and should not be interpreted as representing those of ONR, the U.S. Navy or the U.S. Government.

ONR Global Grant Reports

Homoepitaxial Ga_2O_3 Structures for Power Device Applications

Grant No. N62909-20-1-2055

Annual Report for Fiscal Year 2022

Period of Performance: October 1, 2021 to September 30, 2022

Prepared by:

Akito Kuramata, Principal Investigator
Novel Crystal Technology, Inc.,
2-3-1 Hirosedai, Sayama,
Saitama, 350-1328, Japan
Email: kuramata@novelcrystal.co.jp



This work was sponsored by the Office of Naval Research (ONR), under grant (or contract) number N62909-20-1-2055. The views and conclusions contained herein are those of the authors only and should not be interpreted as representing those of ONR, the U.S. Navy or the U.S. Government.

Grant or Contract Number: N62909-20-1-2055
Date Prepared: 1/31/2023
Project Title: Homoepitaxial Ga2O3 Structures for Power Device Applications
Annual Summary Report: FY22
Principle Investigator: Akito Kuramata, kuramata@novelcrystal.co.jp
Novel Crystal Technology, Inc. (http://www.novelcrystal.co.jp/index.html)
2-3-1 Hirosedai, Sayama, Saitama, 350-1328 Japan

Section I: Project Summary

1. Overview of Project

Monoclinic Gallium Oxide (β-Ga_2O_3) is a very attractive semiconducting material for next generation power devices due to its excellent material properties and ease of mass production. Ga_2O_3 has extremely large bandgap of 4.5-4.8 eV and high breakdown electric field strength of about 8 MV/cm, yielding a nearly ten-fold higher Baliga's figure of merit than that of 4H-SiC. Therefore, realization of Ga_2O_3 power devices will bring huge reduction of energy loss for industrial instruments, power plant, or military equipment, etc.

In this project, we will develop the high-quality growth of Ga_2O_3 bulk substrates by using edge-defined, film-fed growth (EFG) and homoepitaxial thick films by using halide vapor phase epitaxy (HVPE), both with large size up to 4-inch in diameter. The Ga_2O_3-based power devices will be optimized for doping scheme, termination structure, etc. to fully take advantage of the material properties. The techniques of wafer bonding onto foreign substrates with higher thermal conductivity and integrating $(Al_xGa_{1-x})_2O_3/Ga_2O_3$ heterostructures will also be developed as a solution to the heat dissipation issue in Ga_2O_3 devices. By using those techniques, we will be able to demonstrate the ultra high power Ga_2O_3 diode and transistor of kV-class.

During the first year, a total of 91 Ga_2O_3 and $(Al_xGa_{1-x})_2O_3$ substrates and epiwafers were provided to NRL as program deliverables. This number includes both custom growths for novel experiments such as $(Al_xGa_{1-x})_2O_3$ critical thickness to commercialized 100 mm Ga2O3 epiwafers. In addition, a number of boules of Ga_2O_3 are currently at Novel Crystal technology and are expected to provide additional samples of Ga_2O_3 to NRL in the near future.

Abstract:
β-Ga_2O_3 is a very attractive semiconducting material for next generation power devices due to its excellent material properties and ease of mass production. Ga_2O_3 has extremely large bandgap of 4.5-4.8 eV and high breakdown electric field strength of about 8 MV/cm, yielding a nearly ten-fold higher Baliga's figure of merit than that of 4H-SiC. Therefore, realization of Ga_2O_3 power devices will bring huge reduction of energy loss for industrial instruments, power plant, or military equipment, etc.

In this project, we will develop the high-quality growth of Ga_2O_3 bulk substrates by using EFG and homoepitaxial thick films by using HVPE, both with large size up to 4-inch in diameter. The Ga_2O3-based power devices will be optimized for doping scheme, termination structure, etc. to fully take advantage of the material properties. The techniques of wafer bonding onto foreign substrates with higher thermal conductivity and integrating $(Al_xGa_{1-x})_2O_3/Ga_2O_3$ heterostructures will also be developed as a solution to the heat dissipation issue in Ga_2O_3 devices. By using those techniques, we will be able to demonstrate the ultra-high power Ga_2O_3 diode and transistor of kV-class.

Objective:
Advance the state-of-the-art of ultra-wide bandgap steady-state and pulsed power electronics by developing benchmark device structures based on high quality homoepitaxial Ga_2O_3 on native β-Ga_2O_3 substrates. Demonstrate that high quality, large-area Ga_2O_3 substrates and low-defect density epilayers grown by Novel

Crystal Technology are a viable platform for the development of commercial β-Ga_2O_3-based high voltage, high power devices. Demonstrate a vertical Ga_2O_3 power SBD with breakdown voltage of 5-10 kV while maintaining on resistance Ron below 1 mΩ-cm^2. Building on this technology, demonstrate a vertical Ga_2O_3 power transistor with breakdown voltage limited only by the intrinsic breakdown of the dielectrics in the device.

Introduction:

The single-crystal gallium oxide (Ga_2O_3) is an advantageous material for high-power, high-temperature electronic device applications due to its high energy direct gap (~4.9 eV) and high breakdown field (8 MV/cm), yielding a nearly ten-fold higher Baliga figure of merit than that of 4H-SiC ($BFOM_{Ga2O3}$ = 3444, $BFOM_{4H\text{-}SiC}$ = 300). An additional feature of the gallium oxide technology is that commercially available large diameter gallium oxide substrates, grown inexpensively from the melt, are available with 2-inch diameter with prototype 4-inch diameter substrates having been demonstrated (Fig. 1). Additional important feature of the gallium oxide technology is that high quality homoepitaxial growth of gallium oxide epitaxial layers on gallium oxide substrates with growth rates of 8 microns/hour have been demonstrated for hydride vapor phase epitaxial (HVPE) growth. In addition, good N-type doping control has been demonstrated with doping from the range of low $10^{15}cm^{-3}$ to 10^{19} cm^{-3} (Figure 1). Highly doped N-type regions by ion implantation has also been demonstrated. Thus, the gallium oxide material technology has many of the features needed for low cost, high performance next generation high voltage power switch technology.

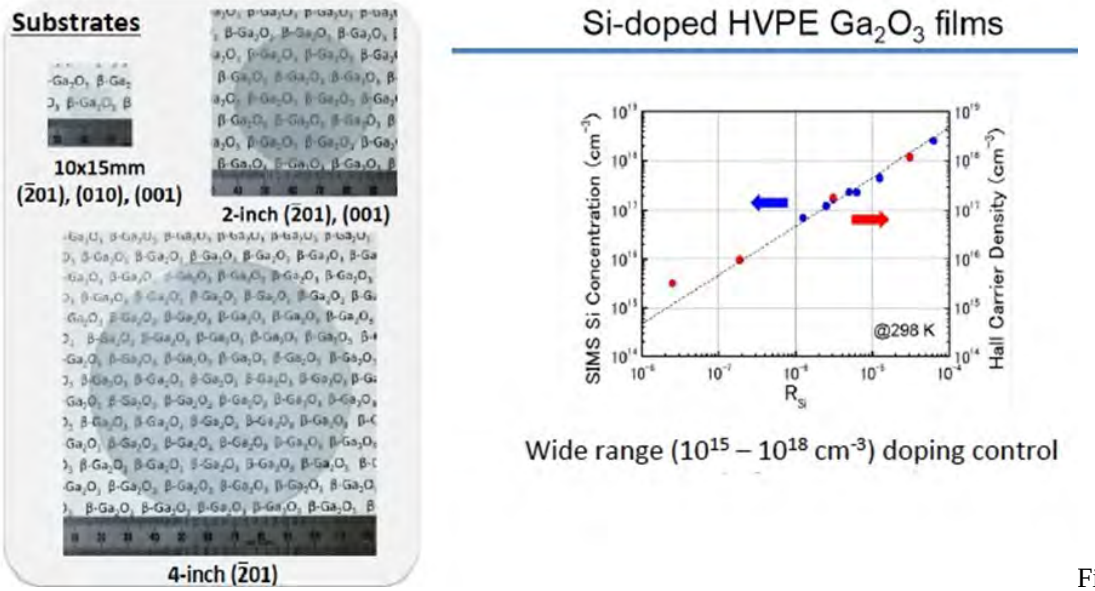


Figure 1. Examples of gallium oxide substrates and N-type doping control.

Background:

Since 2015, NCT/NRL have been a leader this field with a number of vertical Schottky barrier diode demonstrations. However, only recently has the quality of epitaxy has been sufficiently optimized to fully take advantage of the predicted 8 MV/cm critical field of Ga_2O_3. This program will aim towards extending breakdown voltage beyond the 5 kV milestone using the approaches learned in the first NICOP program, under which a 2.3 kV and 33 A SBDs were demonstrated.

2. Activities and Accomplishments

Our achievement lists of Year 2 are as below.

1. Ga_2O_3 substrates –
    a. (100) orientation substrates prepared by cleaving method
    b. (010) Fe-doped substrates, 10x15 mm^2 size
    c. (001) Sn-doped substrates, 2-inch size

2. MBE epitaxial films
    a. HFET structures for lateral power devices
    b. Thin, n+ doped MBE epilayer for impact ionization study

3. HVPE epitaxial films (all wafers are (001) orientation)
    a. 4-inch epiwafer for vertical power device development
    b. UID epiwafer on Fe-doped substrate, 10x15 mm^2 size
    c. 2-inch epiwafers for vertical power device development
    d. Epiwafer with variable doping level for impact ionization study (10x15 mm^2 size)

Specific substrate and epiwafer quantities are summarized in the table below.

Sample detail	**Qty**
Substrate, 10x15 mm2 (010) Fe-doped	3
Substrate, (100) made by cleaving	300
Epiwafer, HVPE, 100 mm	1
Epiwafer, HVPE UID, 10x15 mm2	3
Substrate 10x15 mm2 (010) Fe-doped	50
Substrate 2-inch (001) Sn-doped	8
Epiwafer, HVPE, 20 um, <1e16 cm-3	2
Epiwafer, HVPE, 2inch standard	3
Epiwafer, MBE HEMT, AlGaO/Ga2O3	4
Epiwafer, N-doped, HVPE, 2 inch	1
Epiwafer, HVPE, 10x15 mm2	2
Epiwafer, Ga2O3, MBE, 10x15 mm2	1

Specific activities and research results obtained with these sample deliverables are outlined next:

a) Characterization of homoepitaxial CIS-MOCVD β-Ga_2O_3 as a function of film thickness and substrate orientation

Monoclinic (β-phase) gallium oxide is the only ultra-wide bandgap (4.6-4.9 eV) semiconductor platform with a large area native substrate technology and the ability to grow high quality, thick (10-20 μm) homoepitaxial layers with controllable doping concentrations. These properties alone make β-Ga_2O_3 a leading candidate for next-generation power devices with ultra-high power figure of merit. The high critical field of Ga_2O_3 (6-8 MV/cm) suggests that the breakdown performance of vertical devices can be maintained using a thinner epilayer, resulting in lower specific on-resistance, faster transit times, lower switching and conduction losses, and thus higher overall efficiency. The close-injection showerhead metalorganic chemical vapor deposition (CCS-MOCVD) growth method has been demonstrated to result in high quality epitaxial Ga_2O_3 with electron mobility of nearly 200 $cm^2/V{\cdot}s$ and background compensation levels of $2{\times}10^{13}$ cm^{-3} [1, 2]. Even though a high growth rate has been demonstrated via CIS-MOCVD, device

demonstrations such as lateral transistors and vertical diodes have used relatively thin epilayers (1-2 μm) [3]. In this work, we push the limits of CIS-MOCVD epitaxy to demonstrate film growth up to 10 μm thickness, and furthermore determine the effect of substrate growth method (EFG vs. Czochralski), substrate orientation [(010) vs. (001)], and substrate doping (Fe-doped vs. Sn-doped). Fig. 2a compares the rocking curves of up to 10 μm thick epilayers on EFG (010) Ga_2O_3:Fe substrates. The full width at half maximum (FWHM) values of the (020) reflections were all in the 33-53 arcsec range without a clear thickness-dependent trend. FWHM values for 3 μm epilayers grown on co-loaded (001) and (010) EFG Sn-doped substrates were similar as well: 39.13 arcsec from the (003) reflection and 65.48 arcsec from the (020) reflection. Indeed, growth on Sn-doped (010) substrates proved more challenging and the growth temperature was further explored in the 700-780 °C range. Polarized Raman spectra from 10 μm thick epilayers confirmed the phase purity at that thickness; Fig. 3 shows polarization averaged spectra from growths on substrates from two different sources. The evolution of relatively large hillocks was observed as a function of film thickness, as illustrated via atomic force microscopy (AFM) in Fig. 4a-c. These defects were present regardless of substrate origin (Czochralski or EFG) or doping (Sn or Fe), but were not observed for films grown on the (001) orientation. Cross-sectional imaging is expected to reveal whether these defects originate from substrate nanopipes. Further experiments with growth on (100) Ga_2O_3 and electrical characterization of these epilayers are in progress. References: [1] S. Seryogin et al., Appl. Phys. Lett. 117, 262101 (2020). [2] L. Meng et al., Cryst. Growth & Des., 2022, in press. [3] M.J. Tadjer et al., J. Phys. D: Appl. Phys. 54, 034005 (2020).

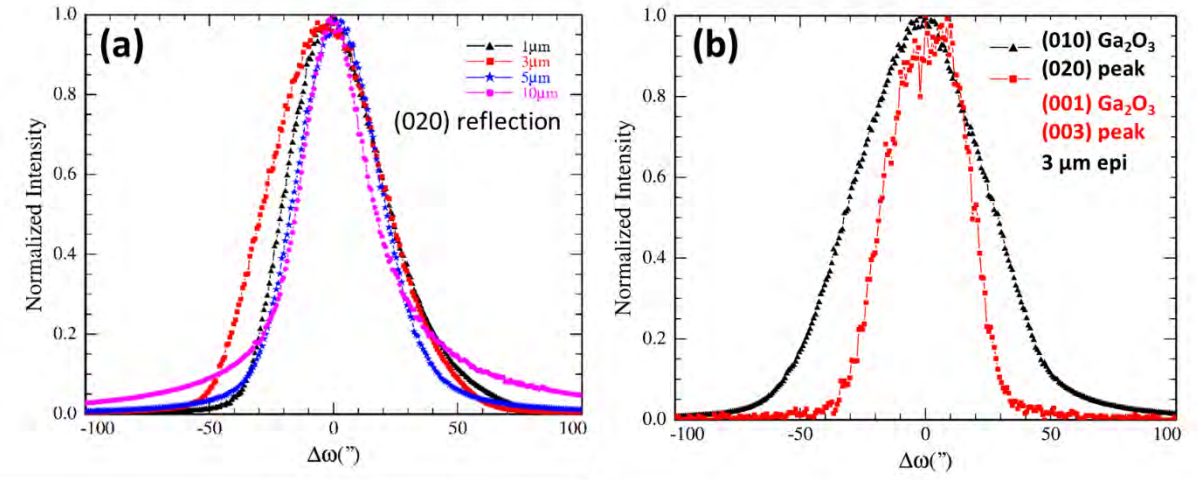


Fig. 2. Rocking curves of MOCVD homoepitaxial β-Ga_2O_3 films (a) thickness of 1, 3, 5, and 10 μm grown on EFG (010) Ga_2O_3:Fe substrates and (b) 3 μm films on (010) and (001) Ga_2O_3:Sn substrates.

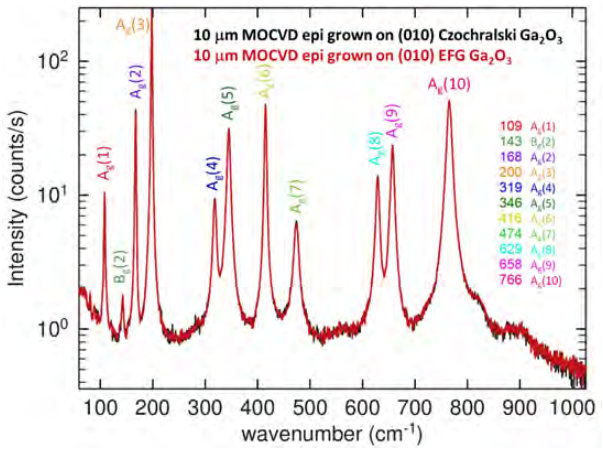


Fig. 3. Polarization-averaged Raman spectra obtained from 10 μm thick homoepitaxial β-Ga_2O_3 grown by CIS-MOCVD on both Czochralski and edge-defined, film-fed grown (EFG) (010) Ga_2O_3:Fe substrates.

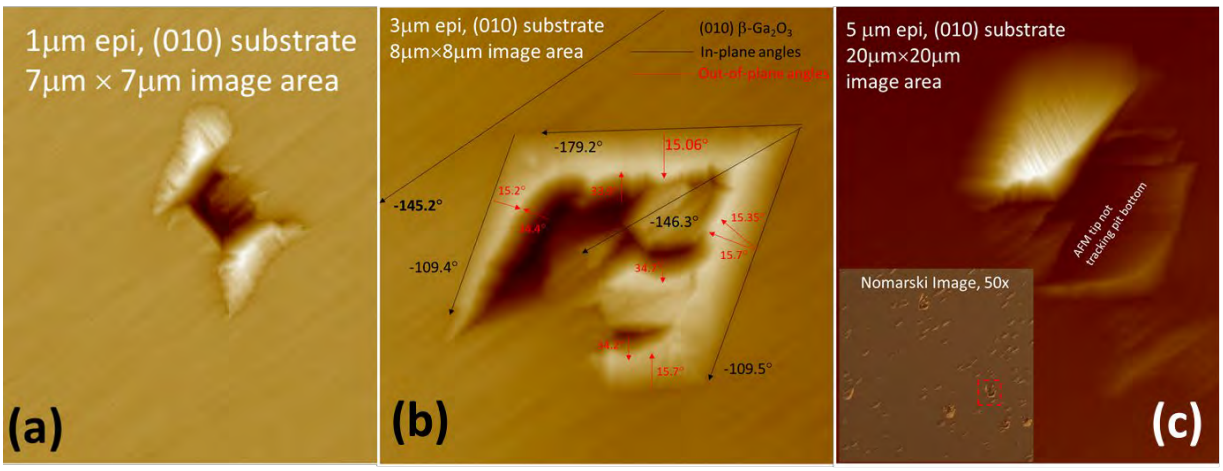


Fig. 4. Atomic force microscopy images of defect evolution as a function of epitaxial thickness for MOCVD epitaxial β-Ga_2O_3 films on EFG (010) Ga_2O_3:Fe substrates with (a) 1 μm, (b) 3 μm, and (c) 5 μm thickness.

An ultrawide bandgap energy (4.8 eV) and low-cost, high-quality growth has positioned β-Ga_2O_3 at the forefront of research for next generation power electronics and optoelectronics (deep-UV LEDs and solar-blind photodetectors). Incorporation of Al can further increase the bandgap energy offering even larger breakdown fields and a wider, tunable range (4.8 eV to >6 eV) of optoelectronic applications. [1] β-$(Al_xGa_{1-x})_2O_3/Ga_2O_3$ heterostructures are also technologically relevant for current device technologies such as β-$(Al_xGa_{1-x})_2O_3/Ga_2O_3$ modulation-doped field effect transistors (MODFETs). [2] In this work, we report the critical thickness limitations of heteroepitaxial β-$(Al_xGa_{1-x})_2O_3$ films grown by ozone-assisted molecular beam epitaxy (O_3-MBE) on (100) and (010) β-Ga_2O_3 substrates.

A series of unintentionally-doped (UID) β-$(Al_xGa_{1-x})_2O_3$ films were grown via O_3-MBE on (100) and (010) -oriented Fe-doped β-Ga_2O_3 substrates with varying Al composition and thickness (50-400 nm). Using X-ray diffraction (XRD), the Al composition (x) of the (010) films were measured (Fig. 5(a)) and ranged from $0.069 < x < 0.195$. [3] XRD of (100) films is shown in Fig. 5(b). XRD was also used to determine lattice constants and strain relative to β-Ga_2O_3 due to Al incorporation. A Nomarski microscope was used to identify any visible defects, such as cracking, in the films. Two distinct defects were observed: hillock-like defects on the (100) films (Fig. 6(a)) and cracking in the (010) films (Fig. 6(b)). The presence of cracks as a function of film thickness and Al composition for the (010) films is provided in Fig. 6(c) along with a

lower bound for critical film thickness as determined via the Griffith criterion by Mu et al. [1] No cracking was observed in the (100) films. Subsequently, atomic force microscopy (AFM) was performed to assess surface roughness and characterize the hillock-like defects in the (100) films and the cracks in the (010) films. Figs. 7(a) and 7(c) show representative surface topographies of a 100 nm thick (100) film and a 200 nm thick (010) film (x=0.136). For similar thickness and Al composition, the (100) films were rougher than their (010) counterparts. Step height profiles of the hillocks in the (100) films and cracks in the (010) films are shown in Figs. 7(b) and 7(d). The cracks in the (010) film were in the [001] direction (Fig. 7(e)). Electron backscatter diffraction (EBSD) was used to further characterize the hillocks in the (100) films to determine their crystallographic orientation. High resolution transmission electron microscopy (HR-TEM) of the hillocks and cracks was also performed to investigate the atomic-scale anatomy of the defect structures.

[1] S. Mu, M. Wang, H. Peelaers, and C. G. Van de Walle, "First-principles surface energies for monoclinic Ga_2O_3 and Al_2O_3 and consequences for cracking of $(Al_xGa_{1-x})_2O_3$," *APL Mater.*, vol. 8, no. 9, p. 91105, Sep. 2020, doi: 10.1063/5.0019915.

[2] S. Krishnamoorthy *et al.*, "Modulation-doped β-$(Al_{0.2}Ga_{0.8})_2O_3/Ga_2O_3$ field-effect transistor," *Appl. Phys. Lett.*, vol. 111, no. 2, p. 023502, 2017.

[3] Y. Oshima, E. Ahmadi, S. C. Badescu, F. Wu, and J. S. Speck, "Composition determination of β-$(Al_xGa_{1-x})_2O_3$ layers coherently grown on (010) β-Ga_2O_3 substrates by high-resolution X-ray diffraction," *Appl. Phys. Express*, vol. 9, no. 6, p. 61102, 2016.

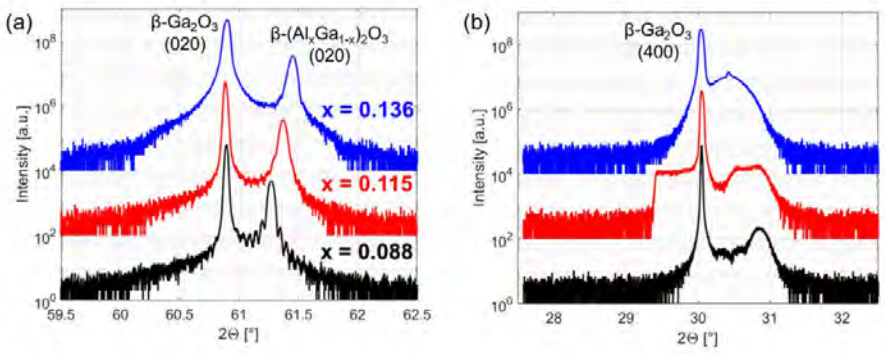


Fig. 5. ω-2Θ scans of 200 nm $(Al_xGa_{1-x})_2O_3$ films on (a) (010) and (b) (100) β-Ga_2O_3 substrates.

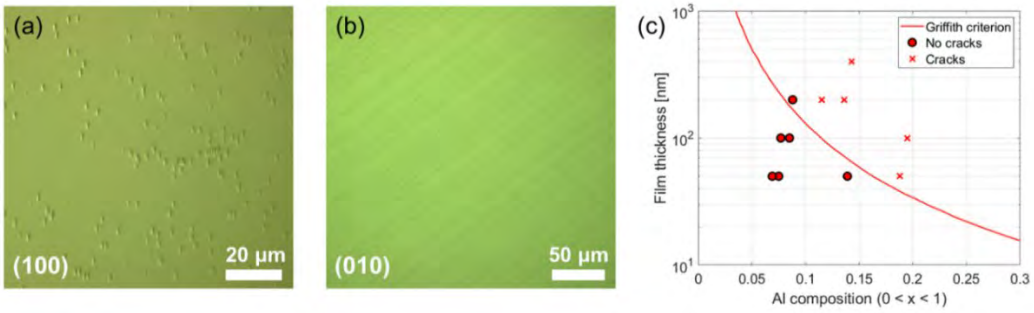


Fig. 6. Nomarski images of the (a) hillock-like defects and (b) cracks in the (100) and (010) films, respectively. (c) Identification of cracks in the (010) β-$(Al_xGa_{1-x})_2O_3$ films in comparison with lower bound of critical thickness.

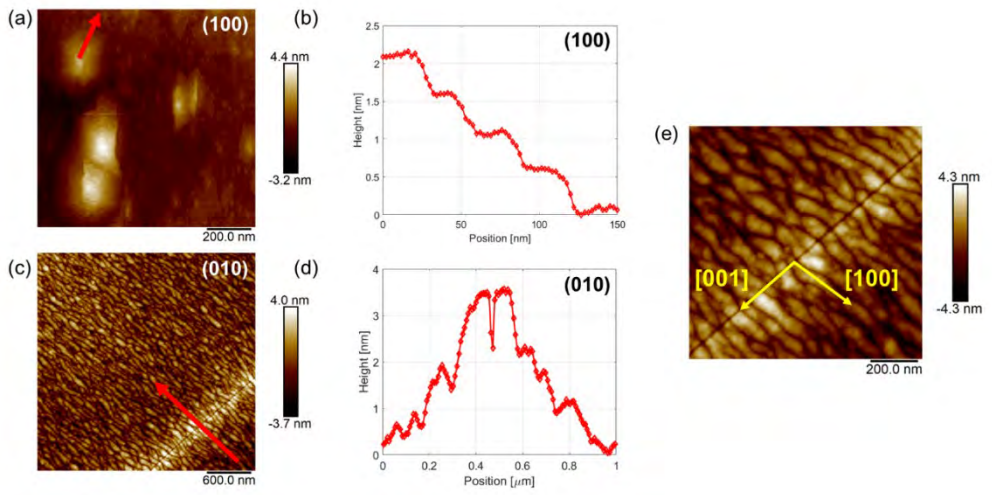


Fig. 7. (a,c) AFM of the (100) and (010) films showing the hillock-like defects and cracks and (b,d) step height profiles of the defects. (e) Direction of cracks on (010) films.

c) Nanocrystalline diamond growth on (010) β-Ga_2O_3 and β-$(Al_xGa_{1-x})_2O_3$ for thermal management of power electronics

Since the first demonstration of a β-Ga_2O_3 field-effect transistor (FET) by Higashiwaki et al. [1], extensive research has been dedicated to the development of β-Ga_2O_3 power devices. However, the expected extremely high power densities combined with the extremely low thermal conductivity of β-Ga_2O_3 creates a significant and unavoidable thermal challenge which must be addressed early in the device design process through electro-thermal co-design. In this work, we report the growth of nanocrystalline diamond (NCD) heat spreading layers (~100 nm thick) on (010) β-Ga_2O_3 substrates and epitaxial β-$(Al_xGa_{1-x})_2O_3$ heterostructures using microwave plasma enhanced chemical vapor deposition (MW-CVD) for thermal management of β-Ga_2O_3-based power devices.

To reduce thermal boundary resistance, the diamond film should be placed as close as possible to the heat source in a device. Ideally, the diamond would be grown directly on the semiconductor surface, as any barrier dielectrics would increase the thermal resistance between the active region and the diamond heat spreader. As such, initial growths were attempted directly on Ga_2O_3; however, the NCD growth conditions, namely the H_2 plasma, were destructive to the Ga_2O_3, preventing film growth. To protect the Ga_2O_3 from etching in H_2 plasma, a SiN interlayer (~50 nm) was deposited on the samples prior to diamond growth. For initial process optimization, the effect of the SiN growth conditions on (010) β-Ga_2O_3 was investigated. SiN interlayers were grown via plasma-enhanced CVD (PECVD) at 300 °C, 400 °C, 500 °C, 600 °C, 300 °C (~10 nm) followed by 600 °C (~40 nm), and 300 °C with a 600 °C anneal in N_2 (5 min). For diamond growth, all samples were first seeded for diamond nucleation using detonation nanodiamond powder. After the samples were placed in an Astex 1.5 kW MW-CVD reactor, they were pre-treated with 200 sccm of H_2 at a temperature of 100 °C and a pressure of 15 torr for 1 h. Subsequently, NCD growth was performed using a 1.5% CH_4/H_2 concentration at a temperature of 400 °C, pressure of 15 torr, and power of 800 W for ~6 h. The resultant NCD film thickness was ~100 nm. Raman spectroscopy (Fig. 8) was used to confirm the presence of an NCD film and qualitatively assess its crystalline quality. For all samples, the linewidth of the Raman mode at ~1330 cm^{-1} was narrow (~10 cm^{1}), indicating a relatively high quality NCD film was obtained for all SiN growth conditions. Using atomic force microscopy (AFM), no significant variation in grain size and surface roughness was observed for all NCD films grown (Fig. 9). While film quality and grain size were comparable amongst all films, three of the samples had visible macroscopic imperfections. Diamond growth was subsequently performed at 500 °C and 600 °C using optimal SiN interlayers (PECVD

at 400 °C, 500 °C, and 300°C with a 600 °C anneal) to determine the ideal diamond growth temperature. Diamond growth at 500 °C was also tested on β-$Al_xGa_{1-x}O_3$/Ga_2O_3 heterostructures. To test the robustness of as-fabricated device structures in NCD growth environmental conditions, Hall measurements were performed before and after a 6 h, 500 °C anneal in forming gas (N_2/H_2) to quantify any changes in electrical performance.

[1] M. Higashiwaki et al., *Appl. Phys. Lett.*, vol. 100, no. 1, p. 13504, Jan. 2012.

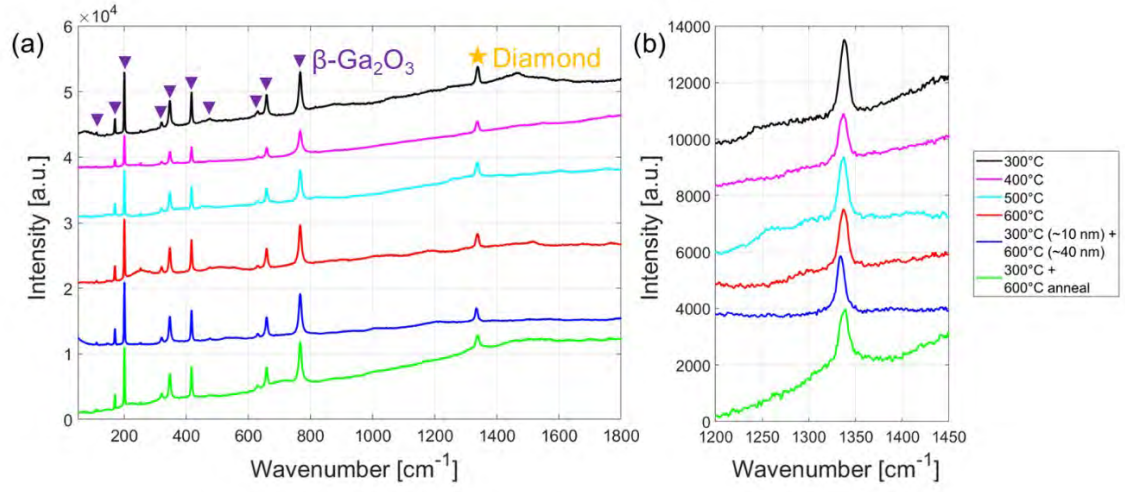


Fig. 8. (a) Raman spectra of the NCD films on β-Ga_2O_3. Raman modes of β-Ga_2O_3 and diamond are denoted by triangles and stars, respectively. (b) Raman mode of diamond. The legend details the SiN growth conditions.

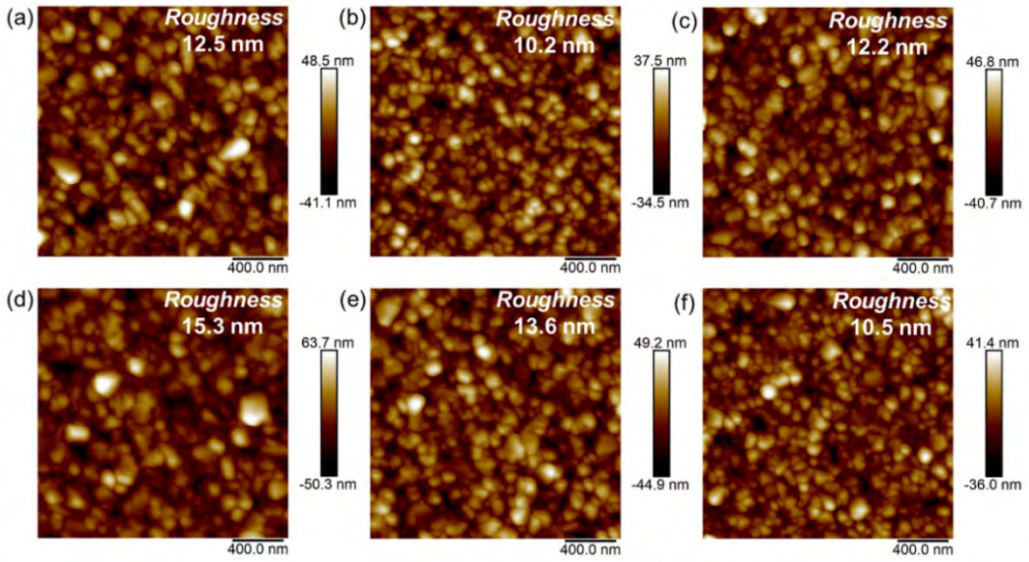


Fig. 9. AFM of the NCD films on β-Ga_2O_3. These samples had SiN interlayers grown via PECVD at (a) 300 °C, (b) 400 °C, (c) 500 °C, (d) 600 °C, (e) 300 °C (~10 nm) followed by 600 °C (~40 nm), and (f) 300 °C with a 600 °C anneal in N_2 (5 min). Inset: root-mean-square roughness.

d) Nanocrystalline Diamond-Capped β-$(Al_xGa_{1-x})_2O_3/Ga_2O_3$ Field-Effect Transistors

The low thermal conductivity of β-Ga_2O_3 is a well-known challenge for devices based on this ultra-wide bandgap semiconductor [1]. The development of high-performance β-Ga_2O_3-based power devices will require the incorporation of thermal management solutions, e.g. wafer bonding or top-side heat spreaders [2]. Here, we report the first demonstration of nanocrystalline diamond (NCD)-capped β-$(Al_xGa_{1-x})_2O_3/Ga_2O_3$ heterostructure field-effect transistor (HFET) as a potential solution for top-side device-level thermal management for Ga_2O_3 power devices.

β-$(Al_xGa_{1-x})_2O_3/Ga_2O_3$ heterostructures were grown via ozone-assisted molecular beam epitaxy (O_3-MBE) and consisted of a 125 nm thick unintentionally doped (UID) Ga_2O_3 layer followed by a 28 nm thick $(Al_{0.19}Ga_{0.81})_2O_3$ barrier layer on an Fe-doped (010) Ga_2O_3 substrate. The $(Al_{0.19}Ga_{0.81})_2O_3$ layer was delta-doped with Si ~3 nm above the interface. Si ion implantation (activation anneal: 30 min, 925 °C in N_2) and e-beam evaporation of Ti/Au (anneal: 1 min, 470 °C in N_2) was used to form ohmic source/drain contacts. The specific contact resistivity, mobility, sheet carrier concentration, and sheet resistance at room temperature were measured to be 4.3×10^{-4} Ω×cm^2, 54 cm^2/V·s, 1.26×10^{13} cm^{-2}, and 9.1 kΩ/□, respectively. A ~50 nm SiN_x layer was deposited by plasma-enhanced chemical vapor deposition (PECVD) at 400ºC to protect the Ga_2O_3 from damage caused by the H_2 plasma required for NCD growth using microwave plasma enhanced CVD (MW-CVD). NCD nucleation sites were facilitated via a seeding method using detonation nanodiamond powder. The growth chamber was pre-treated with 200 sccm of H_2 at a temperature of 100 °C and a pressure of 15 torr for 1 h. NCD growth was then performed using a 1.5% CH_4/H_2 concentration at a temperature of 400 °C, pressure of 15 torr, and power of 800 W for ~6 h. The resulting NCD film thickness was ~100 nm. O_2 plasma (ICP 1000W, RF 100W) and SF_6 (ICP 200W, RF 50W) were used to etch the NCD and SiN_x layers, respectively, to expose the source/drain probing pads and the gate region. A 22nm HfO_2 gate dielectric was deposited by atomic layer deposition, and finally the gate contacts were formed by lift-off of a 20/200 nm thick Ni/Au metal stack. The resulting device cross-section schematic is shown in Fig. 10. Fig. 11 shows a secondary electron microscopy (SEM) image of the NCD crystals on the β-$(Al_xGa_{1-x})_2O_3$ sample beside a region where NCD was etched.

Fig. 12 and 13 show the DC transfer and output characteristic for the NCD-capped β-$(Al_xGa_{1-x})_2O_3/Ga_2O_3$ HFET labeled "MOS gate". A low on-state I_D (max of 4.8 mA/mm) was observed, which may be caused by SF_6-plasma overetching into the AlGaO barrier within the gate region when removing the NCD/SiN_x film. In contrast, DC transfer and output measurements are shown in Fig. 12 and 14 (labeled "Gate on NCD") for a device still capped with NCD within the gate region. On-state I_D was over 10X higher when the AlGaO barrier in the gate region was not exposed to the O_2 plasma and SF_6 etches required to remove the NCD and SiN_x layers, respectively. A maximum power density of ~6.58 W/mm, with a gate voltage of 0 V, was measured before catastrophic failure occurred on the "Gate on NCD" device. Lastly, thermal measurements were performed using a TMX Scientific T°Imager (532 nm, 100X objective); power dissipated was monitored using an oscilloscope, and the base temperature was maintained at 20 °C. Fig. 15 shows the average temperature rise at the gate as a function of power density where the slope corresponds to the device thermal resistance. A 40% reduction in the thermal resistance at the gate electrode was observed with the incorporation of the NCD heat spreading layer when compared to a reference uncapped HFET. Optimization of the NCD/SiN_x etch within the gate region will be required to maintain good device performance with the incorporation of this thermal management technique. [1] M. Higashiwaki, Phys. Status Solidi RRL, **15**, 2100357, (2021). [2] C. Yuan, *et al.*, J. Appl. Phys. **127**, 154502 (2020).

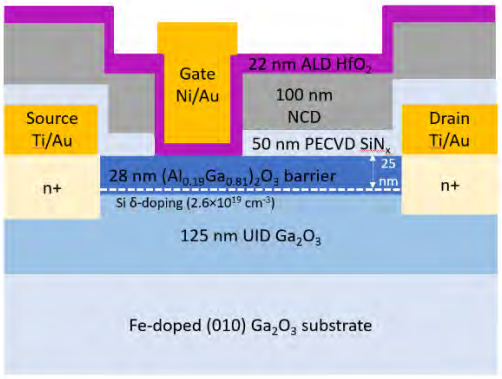


Fig. 10. Cross-section schematic of the β-Ga_2O_3 HFET with NCD heat-spreading layer.

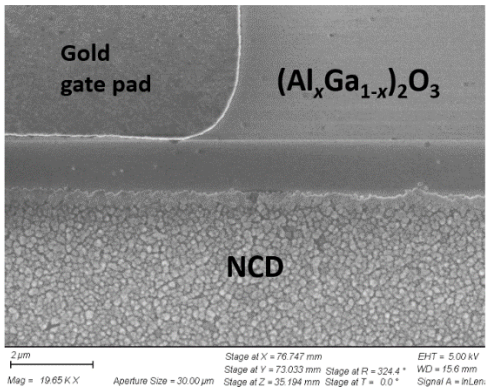


Fig. 11. SEM of NCD grown on β-$(Al_xGa_{1-x})_2O_3$, showing where NCD was etched off.

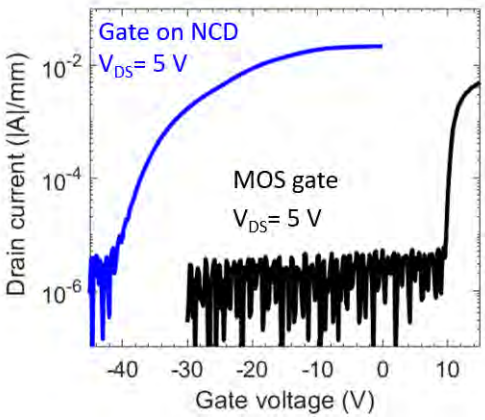


Fig. 12. DC transfer characteristics of Ga_2O_3 HFETs with MOS gate and with gate on NCD.

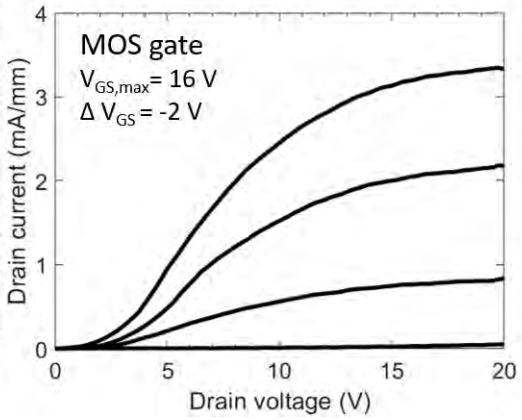


Fig. 13. DC output characteristics (I_{DS}-V_{DS}) of HFET with a MOS gate.

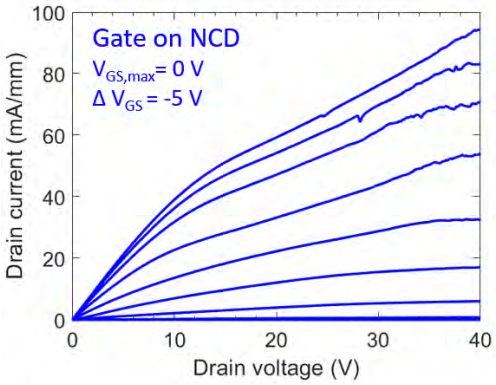


Fig. 14. DC output characteristics (I_{DS}-V_{DS}) of β-$(Al_xGa_{1-x})_2O_3/Ga_2O_3$ HFET with the gate on NCD.

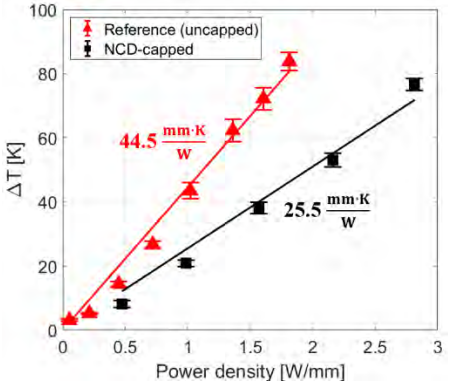


Fig. 15. Average temperature rise of gate vs. power density for HFETs with the extracted Rth values.

e) Demonstration of MOCVD Si-doped β-$(Al_xGa_{1-x})_2O_3$ Recessed-Gate MESFET

The alloying of Ga_2O_3 with Al_2O_3 has been successfully demonstrated to widen the already large bandgap of β-Ga_2O_3 showing great promise for future high-power devices. Phase pure β-$(Al_xGa_{1-x})_2O_3$ films with Al content up to 27% have been grown using metalorganic chemical vapor deposition (MOCVD) [1]. The development of β-$(Al_xGa_{1-x})_2O_3$/β-Ga_2O_3 heterostructures has resulted in the demonstration of modulation-doped field-effect transistors reaching room temperature mobilities of 180 cm^2/Vs [2]. Here, we report our results of MOCVD Si-doped β-$(Al_xGa_{1-x})_2O_3$ channel metal-semiconductor field-effect transistors.

The β-$(Al_xGa_{1-x})_2O_3$/β-Ga_2O_3 heterostructures were grown in Agnitron's Agilis 500 MOCVD reactor with trimethylaluminum (TMAl), triethylgallium (TEGa), and oxygen (5N) as precursors, and argon (6N) as carrier gas. The TMAl and TEGa precursors were used to grow ~100 nm thick Si doped β-$(Al_xGa_{1-x})_2O_3$ layer on ~300 nm UID β-Ga_2O_3 buffer layer, respectively, on a Fe doped (010) β-Ga_2O_3 1" substrate (Synoptics). The AlGaO layer was Si-doped using silane diluted in nitrogen (SiH_4/N_2) as the source with the targeted doping concentration of ~ $4x10^{17}$ cm^{-3}. The growth pressure, substrate temperature, and oxygen flow rate used for the growth of the AlGaO layer were, respectively, 15 Torr, 800 °C, and 600 sccm. The gas phase [TMAl]/([TMAl]+[TEGa]) molar flow rate ratio was ~8.4%. The resulting Al concentration was ~20.56% calculated from X-ray diffraction (XRD). Room temperature Hall measurements performed on the heterostructure indicated a sheet resistance of R_{SH} = 7636 Ω/sq., sheet carrier concentration n_s of 7.15 x 10^{12} cm^{-2}, and mobility of 114 cm^2/V·s. Conduction in the UID buffer layer is under further investigation using a control sample with the AlGaO barrier layer etched off. Mesa isolation was performed via Cl_2 plasma dry etch process (800 W ICP, 60 W RIE, 5 mT, ~30 nm/min). Ohmic contacts were formed via Si ion implantation ($3x10^{19}$ cm^{-3} dose, 100 nm box profile) with an activation anneal of 925 °C for 30 minutes in N_2 atmosphere, followed by lift-off of a 20/200 nm thick Ti/Au metal stack annealed at 475 °C for 1 minute in N_2. An approximate 30 nm gate recessed was formed via Cl_2 plasma dry etch process (100 W ICP, 150 W RIE, 5 mT, ~10 nm/min). Gate contacts were then formed by lift-off of a 20/200 nm thick Ni/Au metal stack. A cross-sectional schematic of the resulting β-$(Al_xGa_{1-x})_2O_3$ MESFET is shown in Figure 16. XRD of the β-$(Al_xGa_{1-x})_2O_3$ film is shown in Figure 17. Figure 18 shows an atomic force microscopy (AFM) image and rms roughness of the gate-recessed β-$(Al_xGa_{1-x})_2O_3$ with a depth of ~30 nm.

DC transfer and output *I-V* results from the fabricated MESFETs are shown in Figures 19(a) and (b), respectively. The on/off current ratio was ~300 and the threshold voltage was -14V due to the incorporation of the gate recess. A maximum drain current of 1.8 mA/mm was measured at a gate bias of 5 V and drain bias of 30 V, and output *I-V* results show good saturation and gate-controlled current modulation. The low on-state current can be improved with device optimization including, improved ohmic source/drain contacts, removal of plasma-damage from the gate recess etch, and minimizing the roughness of the β-$(Al_xGa_{1-x})_2O_3$ films.

[1] A. F. M. Anhar Uddin Bhuiyan, *et al.*. Appl. Phys. Lett., **115**, 120602 (2019). [2] Y. Zhang, *et al.*, Appl. Phys. Lett. **112**, 173502 (2018).

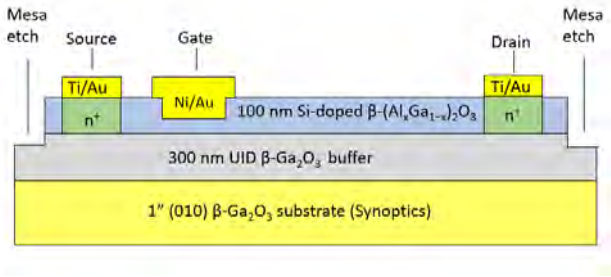


Fig. 16. Cross-section schematic of gate-recessed β-$(Al_xGa_{1-x})_2O_3$ MESFET. Gate-source and gate-drain spacing is set to 2.5 µm and 10 µm, respectively.

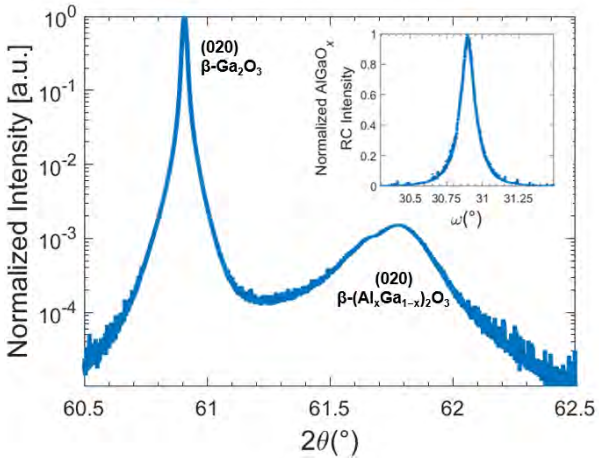


Fig. 17. XRD of the β-$(Al_xGa_{1-x})_2O_3$/β-Ga_2O_3 heterostructure. Inset shows normalized Rocking Curve intensity of the β-$(Al_xGa_{1-x})_2O_3$ film showing the (020) peak with a full width half maximum of 446".

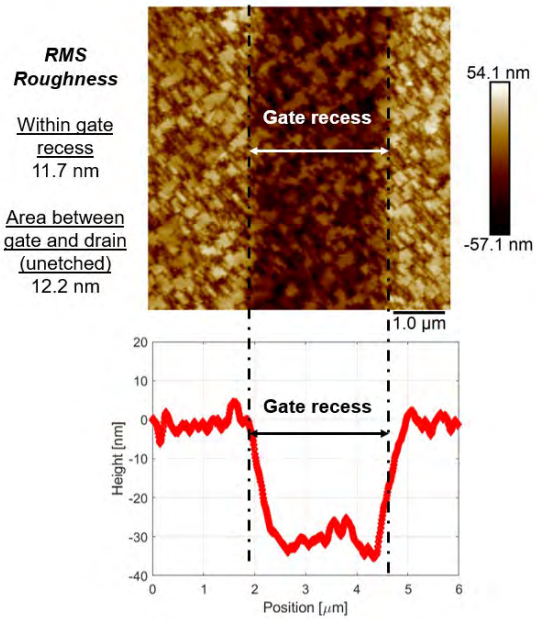


Fig. 18. AFM of the β-$(Al_xGa_{1-x})_2O_3$ channel showing a gate-recessed depth of ~30 nm and RMS roughness of 11.7 nm and 12.2 nm within and outside of the gate-recessed region, respectively.

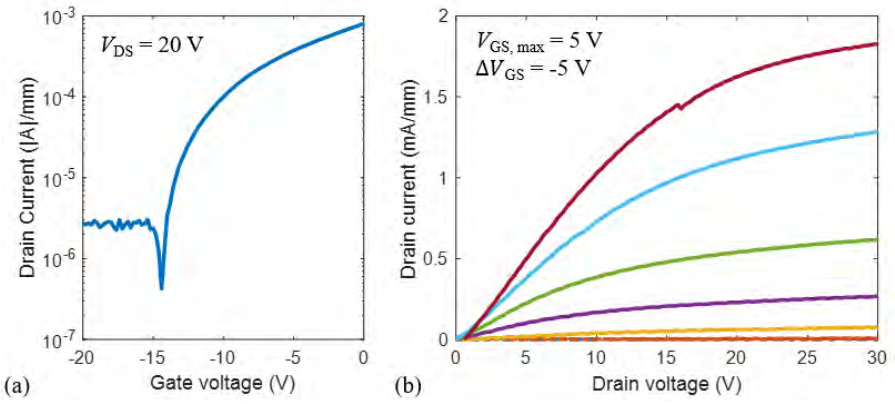


Fig. 19(a) Transfer (J_D-V_{GS}) characteristics and **(b)** Output (J_D-V_{DS}) characteristics of the fabricated gate-recessed β-$(Al_xGa_{1-x})_2O_3$ channel MESFET.

f) High Temperature Annealing Effects and Defect Populations of Ga_2O_3

Beta gallium oxide (bGO) presents great potential for next generation power and RF devices in no small part due to the large area, high quality, melt grown, bulk substrates available, something lacking in alternatives such as gallium nitride, aluminum nitride, and diamond. While bulk crystal growth is essential, so too is growth of high quality and exceedingly phase-pure single crystal epitaxial structures. Among growth techniques, molecular beam epitaxy (MBE) and metalorganic chemical vapor deposition (MOCVD) are common with differing tradeoffs in purity, crystal structure, and defect populations. MBE films are typically grown at more moderate temperatures which can benefit purity at the expense of a greatly reduced growth rate as well as reduced atomic mobility for crystal refinement. Here, we focus on the effects of high temperature annealing on the quality and defect structure of a 500nm thick MBE bGO film grown on an 010 bulk substrate. Specifically, we target annealing near typical MOCVD growth regimes at 1000C by both RTA and moderate pressure (~30 bar) annealing in nitrogen, as well as rapid heating and cooling pulses (max ~300 K/s) at moderate pressures via multicycle rapid thermal annealing (MRTA) to access intermediate (~1450C) and high temperature (1600C) states near the melting point (~1725C) with rapid quenching to assess the high temperature state. Samples were probed by Nomarski imaging, Raman scattering, X-ray diffraction, positron annihilation spectroscopy (PAS), and Rutherford backscattering spectroscopy with channeling (RBS/c).

Macroscopically, bare films annealed at low and moderate temperatures were unchanged while annealing near the melting point yielded surface reconstruction and features parallel to [001]. Suppression of surface reconstruction was achieved using a 100nm PECVD SiO2 cap during annealing. Phononic behavior was not greatly affected as measured by Raman shift and peak width, and only minor deviations in intensity ratios were notable which could be attributed to spatial anisotropy or slight deviations in substrate rotation during acquisition. High-resolution X-ray diffraction indicates consistent quality of films and substrates with no deleterious effects after quenching from any anneal condition.

At the atomic scale, PAS measures defect populations by the annihilation lifetime of injected positrons. Energy dependent PAS was obtained for all conditions yielding S and W parameters as a function of depth. This data was fit to a three layer model to capture surface mediated artifacts, a true film population (~500nm), and the bulk substrate population. Measurements on virgin material shows a greater S parameter of the MBE film and surface relative to the substrate indicating the expected greater defect concentration from the low film growth temperature. Upon annealing, the MBE film defect populations are significantly affected by both the sample temperature and presence of the cap while the bulk material defect population was relatively unaffected by any anneal condition. Film defect populations were indeed even improved upon beyond the population of the bulk substrate as indicated by the reduced S-parameter. Furthermore, plots of S vs W show a linear trend for both the MBE film and substrate for all samples indicating a similar defect or defect complex dominating the PAS signal for all films and substrates.

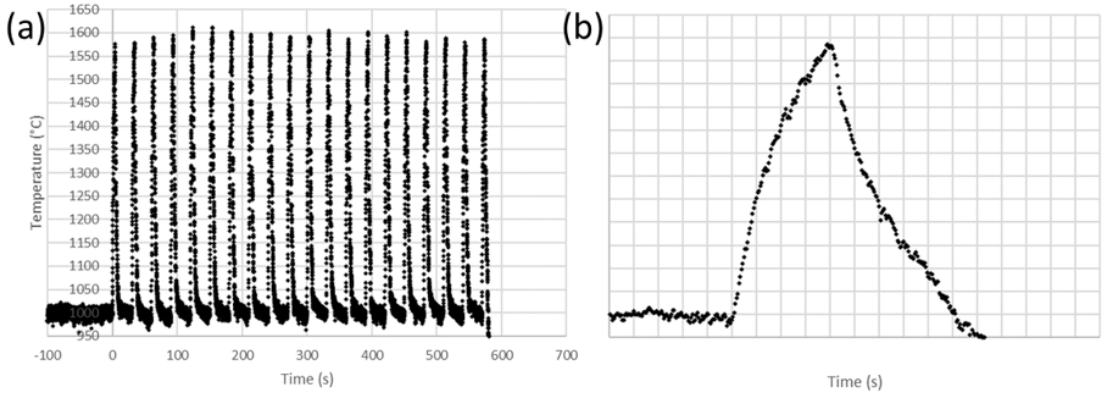


Fig. 20 Measured temperature profile for ~1600 C MRTA anneal at 50K/div showing **(a)** total pulse regime with 100s/div and **(b)** final pulse and quench to ambient with 1s/div.

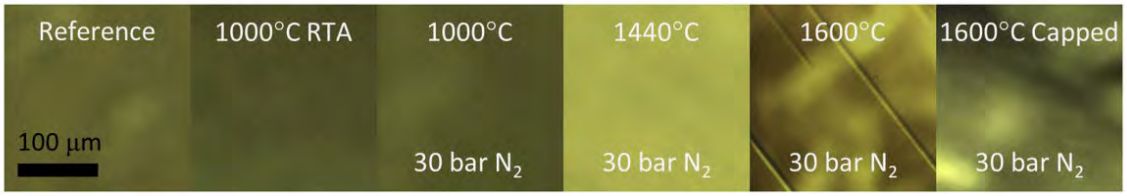


Fig. 21 Nomarksi images highlighting surface features after annealing. Sample annealed without cap at 1600°C shows significant large scale surface recombination.

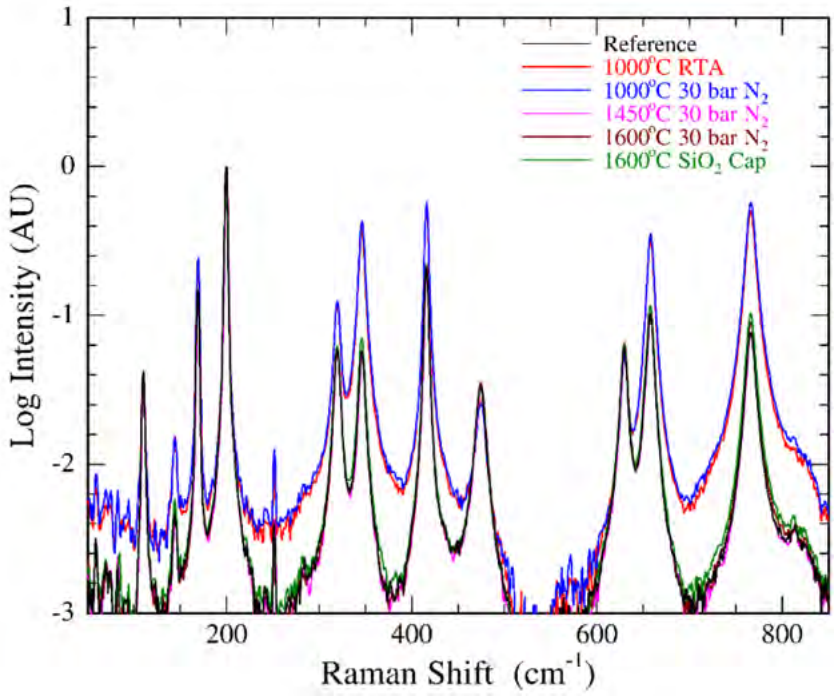


Fig. 22 Raman spectroscopy from all samples shows minimal changes in position and width. Intensity ratios shows moderate changes likely tied to sample rotation during acquisition.

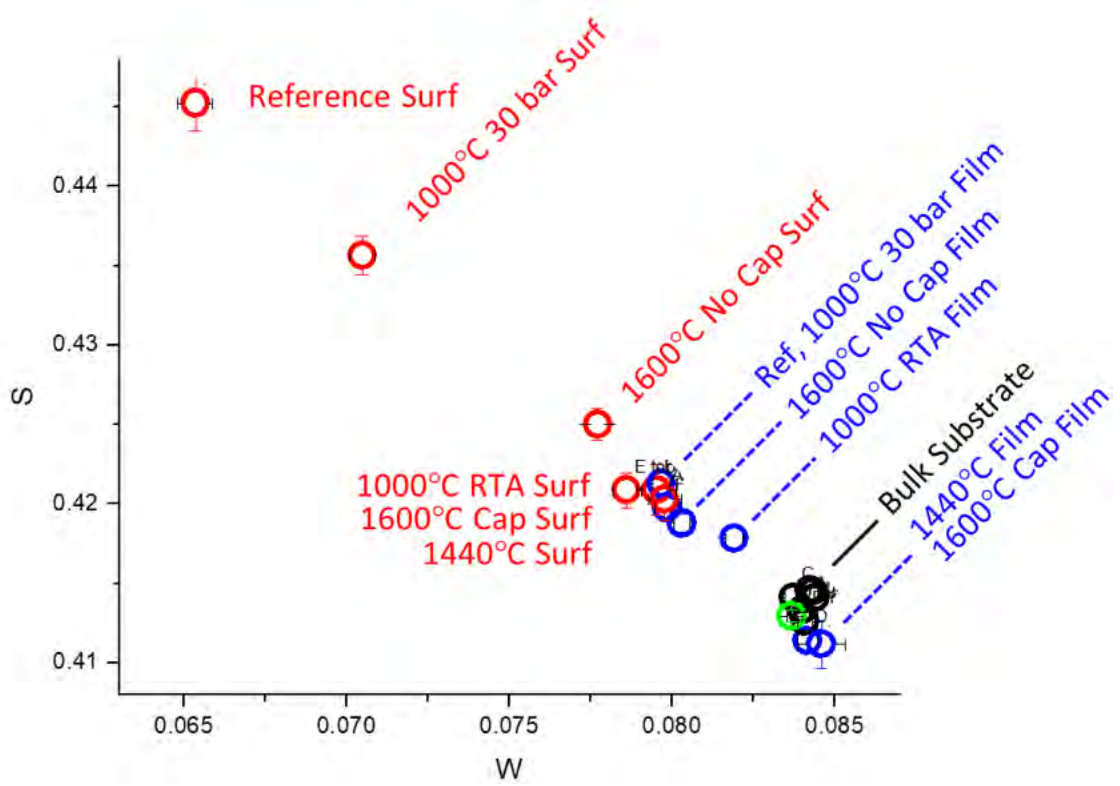


Fig. 23 Positron annihilation spectroscopy S vs W parameter for all samples. Red symbols indicate surface signals, blue symbols are from the main MBE film, and black are the substrate signals.

g) Interfacial Thermal Transport of Thinned and Chemical Mechanical Polished (201) β-Ga2O3 Direct Wafer Bonded to (001) Si

Room temperature direct wafer bonding of ($\underline{2}$01) β-Ga_2O_3 and (001) Si substrates was performed, whose bonded interface consisted of thin ~2 nm SiO_2 and ~4 nm Ti interlayers. The thermal transport characteristics of the bonded interface were measured using steady-state thermoreflectance,[1] which showed a thermal boundary conductance of ~63 MW/(m^2·K). However, because the bonded β-Ga_2O_3 substrate was initially ~700 μm thick, the β-Ga_2O_3 was thinned prior to measuring the thermal boundary conductance of the bonded interface. Post-bonding β-Ga_2O_3 thinning and polishing recipes were developed in this study and triple-axis X-ray diffraction symmetric rocking curves were employed to examine the subsurface lattice damage induced or removed by each thinning and polishing step. For all thinning (grinding and lapping) and polishing steps, ~10 kPa downward pressure and 30 RPM pad rotation speed were used. After bonding to Si, the unbonded backside of the β-Ga_2O_3 was grinded with 30 μm diamond paste. This resulted in a ($\underline{6}$03) β-Ga_2O_3 XRD rocking curve FWHM of ~170” and FW(0.0001)M of ~19000” after removing ~600 μm of material. After grinding, 5 μm then 1 μm Al_2O_3 particles were used for lapping. After lapping with 5 μm Al_2O_3, the rocking curve FWHM and FW(0.0001)M decreased to ~40” and ~1300”, respectively. 1 μm Al_2O_3 particles were then used as a finer lapping step, which further reduced the FWHM and FW(0.0001)M to ~30” and ~1000”. The reduction in rocking curve peak widths (either changing to a softer particle material or smaller size) corresponds to the removal of subsurface lattice damage induced by each previous step. Lastly, 70-nm colloidal silica was used as the final polishing step, which reduced the rocking curve FWHM and FW(0.0001)M to 20” and ~400”, respectively. The final polished surface roughness

was 0.4 nm. During the lapping and polishing steps, a wedge in the β-Ga_2O_3 was intentionally induced such that the β-Ga_2O_3 layer had a thickness gradient ranging from ~2 to ~10 μm. The thickness gradient enables a more reliable extraction of the thermal boundary conductance of the bonded interface using steady-state thermoreflectance. The thermal boundary conductance measured for these bonded β-Ga_2O_3|Si structures is comparable to our previous work[2] bonding β-Ga_2O_3 to 4H-SiC (~65 MW/(m^2·K)), and greater than other work reported in the literature that utilized mechanical tape exfoliation methods to bond (100) or ($\underline{2}$01) β-Ga_2O_3 to quartz or diamond (8-17 MW/(m^2·K)).[3-5]

References

1. J.L. Braun, et al., Rev. Sci. Instrum. 90, 024905 (2019).

2. Z. Cheng, et al., ACS Appl. Mater. Interfaces, 12(40), 44943 (2020).

3. Y. Zhang, et al., Appl. Phys. Lett., 116, 202101 (2020).

4. Y. Zhang, et al., ECS J. Solid State and Technol., 9, 055007 (2020).

5. Z. Cheng, et al., APL Mater. 7, 031118 (2019).

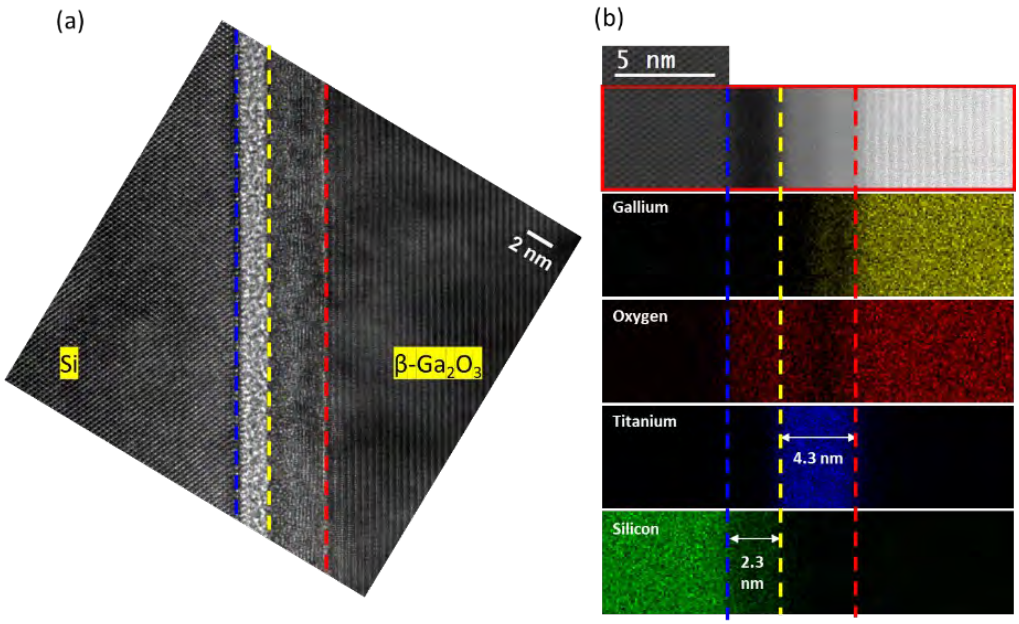


Fig. 24. (a) High-resolution transmission electron microscopy image of the bonded interface aligned to the [110] Si || [102] β-Ga_2O_3 zone axes. The bonded interface consists of a ~2 nm SiO_2 layer adjacent to the Si side and ~4 nm Ti layer adjacent to the β-Ga_2O_3. (b) High-angle annular dark field scanning transmission electron microscopy image with energy-dispersive X-ray spectroscopy color maps for Ga, O, Ti, and Si.

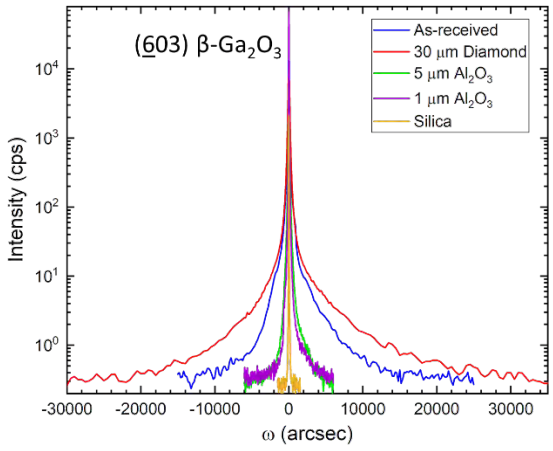


Fig. 25. Triple-axis X-ray diffraction rocking curves of the symmetric ($\underline{6}03$) β-Ga_2O_3 after each thinning (grinding and lapping) and chemical mechanical polishing step. The as-received state corresponds to a wire sawed surface, which is followed by: (1) 30-μm diamond grind, (2) 5-μm Al_2O_3 lapping, (3) 1-μm Al_2O_3 lapping, and (4) colloidal silica polishing. The decrease in both FWHM and the diffuse scatter intensity (i.e. FWXM), corresponds to removal of subsurface lattice damage.

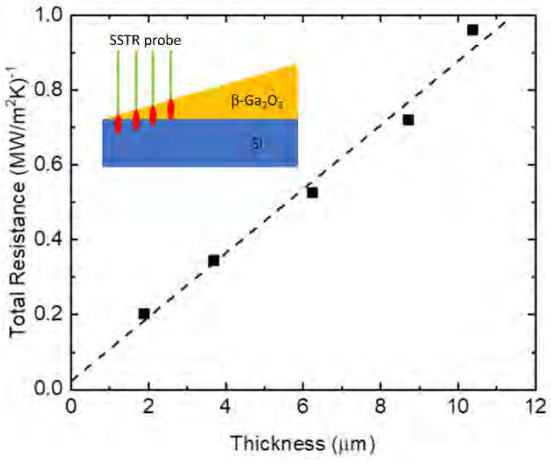


Fig. 26. Steady-state thermoreflectance measurements taken at different points along the bonded sample with varying β-Ga_2O_3 thicknesses. The thermal boundary conductance corresponds to the y-intercept, which is ~63 MW/(m^2·W). The SSTR probe has an areal diameter of 10 μm, so the β-Ga_2O_3 thickness can be considered constant for each measurement.

h) Activation of implanted Si, Ge and Sn donors in high-resistivity halide vapor phase epitaxial β-Ga2O3:N with high mobility

Activation of implanted donors into a highly-resistive, nitrogen-doped homoepitaxial β-Ga_2O_3 has been investigated. Nitrogen acceptors with concentration of ~10^{17} cm-3 were incorporated during epitaxial growth yielding low-doped (net donor concentration <10^{14} cm^{-3}) films subsequently implanted with Si, Ge, and Sn. Upon Ohmic contact formation to the implanted regions, sheet resistance values of 314, 926, and 1676 Ω/sq were measured at room temperature for the Si-, Ge-, and Sn-implanted samples, respectively. Room temperature Hall measurements resulted in sheet carrier concentrations and Hall mobilities of 2.13×10^{14} cm^{-2}/93 cm^2/(V·s), 8.58 ×10^{13} cm^{-2}/78 cm^2/(V·s), and 5.87×10^{13} cm^{-2}/63 cm^2/(V·s), respectively, for these three donor species. Secondary Ion Mass Spectroscopy showed a volumetric dopant concentration of approximately 2×10^{19} cm^{-3} for the three species, resulting in carrier activation efficiencies of 64.7%, 40.3%, and 28.2% for Si, Ge, and Sn, respectively. Temperature-dependent Hall effect measurements ranging from 15K to 300K showed a nearly constant carrier concentration in the Si-implanted sample, suggesting the formation of an impurity band indicative of degenerate doping. With a bulk carrier concentration of 1.3×10^{19} cm^{-3} for the Si implanted sample, a room temperature mobility of 93 cm^2/(V·s) is among the highest reported in Ga_2O_3 with a similar carrier concentration. The unimplanted Ga_2O_3:N regions remained highly resistive after the surrounding areas received implant and activation anneal. These results open the pathway for fabricating Ga_2O_3 devices through the selective n-type doping in highly-resistive epitaxial Ga_2O_3.

Table 1. Summary of the LTLM and room temperature Hall effect measurement data and ion implant activation efficiency determined via SIMS.

Implant	Si	Ge	Sn
R_c (Ω·mm)	1.2	3.1	2.3
R_{sh} (Ω/sq)	314	926	1676
μ (cm^2/(Vs))	93	78	63
n_{sh} (cm^{-2})	2.13 x 10^{14}	8.59 x 10^{13}	5.87 x 10^{13}
Activation %	64.7	40.3	28.2

i) Gallium Oxide Junction Barrier Schottky Diodes with Sputtered P-Type Nickel Oxide

Junction barrier Schottky (JBS) diodes are unique vertical diodes that have been realized in both SiC and GaN. The anode metal forms both a Schottky and an ohmic contact to the semiconductor(s), allowing for low power losses in the on-state, and higher breakdown voltage in the off state. Gallium oxide, an ultra-wide bandgap (UWBG) semiconductor (4.8 eV) has been researched heavily for vertical power diodes due to its favorable material properties including melt and homoepitaxial growth, doping control, and the prospect of a high breakdown field strength (6-8 MV/cm). However, due to the flat valence band and strong self-trapping of holes, the realization of p-type conductivity within gallium oxide (Ga_2O_3) has thus far been unsuccessful. This means that a p-type semiconductor with favorable band offsets to Ga_2O_3 must be used in order to form a PN junction and JBS diode. Nickel oxide (NiO) has been shown to form a heterojunction with Ga_2O_3 due to its wide bandgap (3.7 eV) and p-type conductivity. NiO is most commonly deposited using reactive sputtering, where variation of the oxygen partial pressure allows for control of the hole concentration. In this work, have demonstrated the fabrication of a Ga_2O_3 NiO JBS diode, taking advantage of a lower on-state power losses than a PN diode and a higher breakdown voltage than a schottky barrier diode.

Prior to JBS diode fabrication, thin films of sputtered NiO were characterized in order to observe how the sputtering conditions affected properties such as deposition rate, band gap, resistivity, and carrier concentration. The sputtering power, chamber pressure, and oxygen partial pressure were varied. The p-type conductivity of NiO stems from the Ni vacancies. These vacancies are increased as the oxygen partial pressure is increased during the reactive sputtering process. A highly doped NiO film is desirable underneath the anode in order to induce strong lateral depletion and protection of the Schottky contact, while a lowly doped NiO is desired for JTE in order to mitigate the electric field.

Fabrication of the JBS diodes consisted of two lithography processes. The first process utilized a traditional lithography approach where the samples were re-patterned after each step. A 10 µm thick epitaxial layer grown using Halide Vapor Phase Epitaxy was etched using BCl_3 in order to achieve a 400 nm deep trench. A warm phosphoric (80°C) acid clean was used to remove etch damage. After etching, the samples were re-patterned for NiO deposition and lift-off. Due to the small (2 µm) features, misalignment between the etched regions and the deposited NiO occurred. Due to the observed misalignment between etching and sputtering, a self-aligned lithography process was then implemented utilizing a double mask and XeF_2 lift-off. Ellipsometry was used to determine the optical constants, band gap, and thickness of the sputtered NiO thin films. Hall Effect measurements were carried out using a LakeShore Cryogenic Hall system in order to determine the hole concentration. Due to the low mobility (< 1 cm^2/Vs) and high resistivity of the NiO films, the measured carrier concentration values were inaccurate and inconclusive. Attempts at increasing the Hall voltage in order to improve the accuracy of the Hall Effect measurements have thus far been unsuccessful. Electrical testing of the JBS diodes was performed in order to evaluate the on-resistance and breakdown voltage. Schottky barrier and PN diodes

were fabricated alongside the JBS diodes in order to confirm the successful fabrication of the JBS diode. Fig. 27a shows the forward *J-V* measurements of all three diodes fabricated using the self-aligned process. The JBS diode exhibits behavior similar to the Schottky barrier diode with lower on-state power losses than the PN diode. All measured JBS diodes exhibited ideality factors less than 1.10. The 100 µm diameter devices had on-resistances between 5.6-7.6 mΩ*cm^2. Fig 27b shows the breakdown voltage testing of the JBS diodes in comparison to the Schottky and PN diodes. As expected, JBS diodes exhibits higher breakdown voltage (1 kV) and lower leakage than the Schottky barrier diode. All breakdown measurements were performed using Fluorinert. When comparing the *J-V* data of both lithography processes, it was shown that the forward *J-V* was similar. However, when comparing the breakdown measurements it was shown that the self-aligned process resulted in higher breakdown voltages by almost and lower leakage current. A breakdown voltage of 1 kV was achieved under the self-aligned process while the standard lithography process only achieved ~600 V. We currently attribute this improvement to the reduction of NiO/trench misalignment as well as a likely reduction in hole concentration for NiO used in the self-aligned process. Further optimization of both the NiO sputter recipes and characterization are needed, as well as improving the self-aligned lithography process.

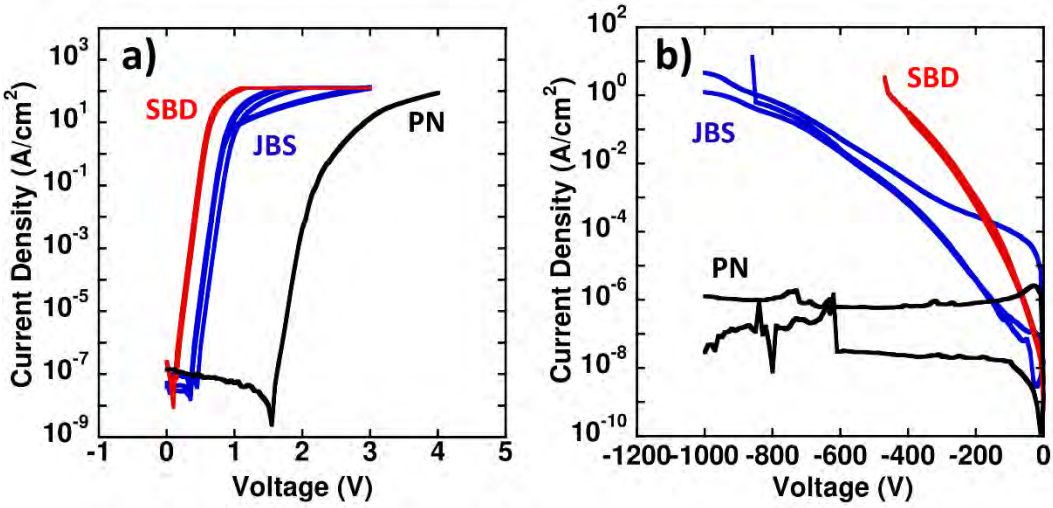


Fig. 27. *J-V* measurements of Ga2O3 Schottky, pn, and JBS diodes for a) forward bias testing and b) reverse bias testing.

j) Full-wafer Structural and Electrical Characterization of Gallium Oxide Wafer

Gallium oxide substrate and epitaxy technology has advanced tremendously since the first device demonstration a decade ago [1]. In 2022, crystal growth using several different methods (EFG, Czochralski, Vertical Bridgman) have yielded high quality crystals that have commercialized the 4-inch substrate technology required for device commercialization [2]. High growth rate epitaxial techniques such as MOCVD and HVPE have pushed commercial drift layer thicknesses with the expectation that high quality and low defect density epilayers will enable ultra-high voltage (>20 kV) vertical diodes and transistors [3].

A 100 mm diameter HVPE β-Ga2O3 epiwafer (9.6 µm, 1.5x1016 cm-3) on an n+ (001) Ga2O3 substrate was supplied by Novel Crystal Technology, Inc. X-Ray topography (XRT) was performed at NRL using Rigaku XRTmicron X-ray topography system. Schottky barrier diodes were fabricated using a blanket substrate-side Ti/Au cathode annealed at 470 °C for 1 minute, followed by epi-side gridded Ni/Au anodes in order to facilitate defect characterization under bias. Electrical characterization of >3000 devices over the full 100 mm wafer (10 mm exclusion zone) was performed using a computer-controlled wafer prober and a Keithley 4200SCS semiconductor parameter analyzer. Reverse breakdown voltage measurements and on-state hyperspectral electro-luminescence imaging were also performed on selected devices based on the preliminary XRT and electrical data.

Figure 28a shows the g=(224) XRT, image of the wafer, using Cu K□ radiation, showing a number of structural defects such as slip planes near the edge of the wafer. Thus, a 10 mm exclusion zone was implemented in the electrical characterization of this wafer. Other regions of interest, shown in purple squares, exhibited dislocation bundles that will be discussed in detail at the meeting. The g=(020) XRT image, using Mo K□, in Figure 28b shows diffraction data from the substrate as well as the epitaxial layer on the wafer.

Fig. 28c shows a photograph of the 100 mm wafer with fabricated vertical Schottky barrier diodes (SBDs). Electrical characterization plots obtained by I-V and C-V measurements are shown in Fig. 29. While the on-state resistance from the largest devices was about 2× higher (15-17 mΩ-cm2) than the small SBDs in the PCM areas, the ideality factor was very uniform across the wafer. Reverse bias measurements (leakage current IREV at -10 V, capacitance-voltage) confirmed the uniformity of the wafer. Breakdown voltage and electroluminescence imaging results will be presented at the conference. These results present the first report of 4-inch Ga2O3 epiwafer X-ray topography characterization and device electrical characterization, further elucidating the device reliability challenges that must be addressed for the commercialization of β-Ga2O3 power electronics [4, 5].

References:

[1] M. Higashiwaki et al., Appl. Phys. Lett. 100, 034101 (2012).
[2] A. Kuramata et al., Jpn. J. Appl. Phys. 55, 1202A2 (2016).
[3] H. Murakami et al., Appl. Phys. Expr. 8, 015503 (2014).
[4] N.A. Mahadik et al., APL Materials 7, 022513 (2019).
[5] A.J. Green et al., APL Materials 10, 029201 (2022).

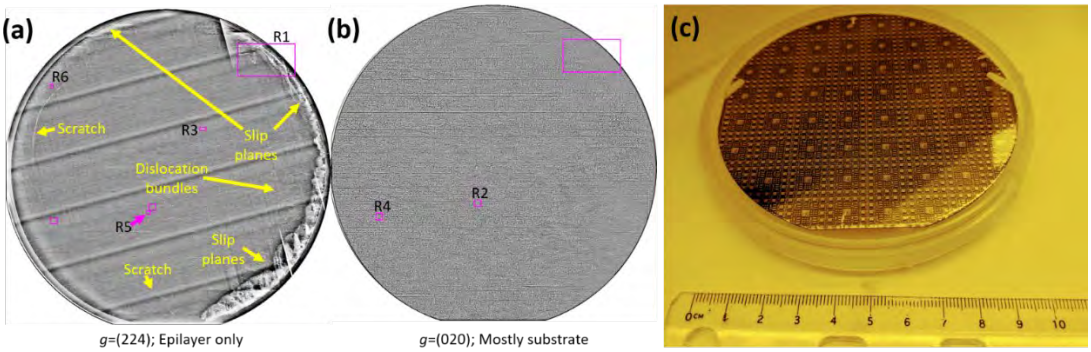


Figure 28. X-Ray topographs of 100 mm β-Ga2O3 HVPE epiwafer along the (a) (224) and (b) (020) reflections obtaining signal from epilayer and substrate, respectively. (c) Photograph of same epiwafer processed with vertical Schottky barrier diodes.

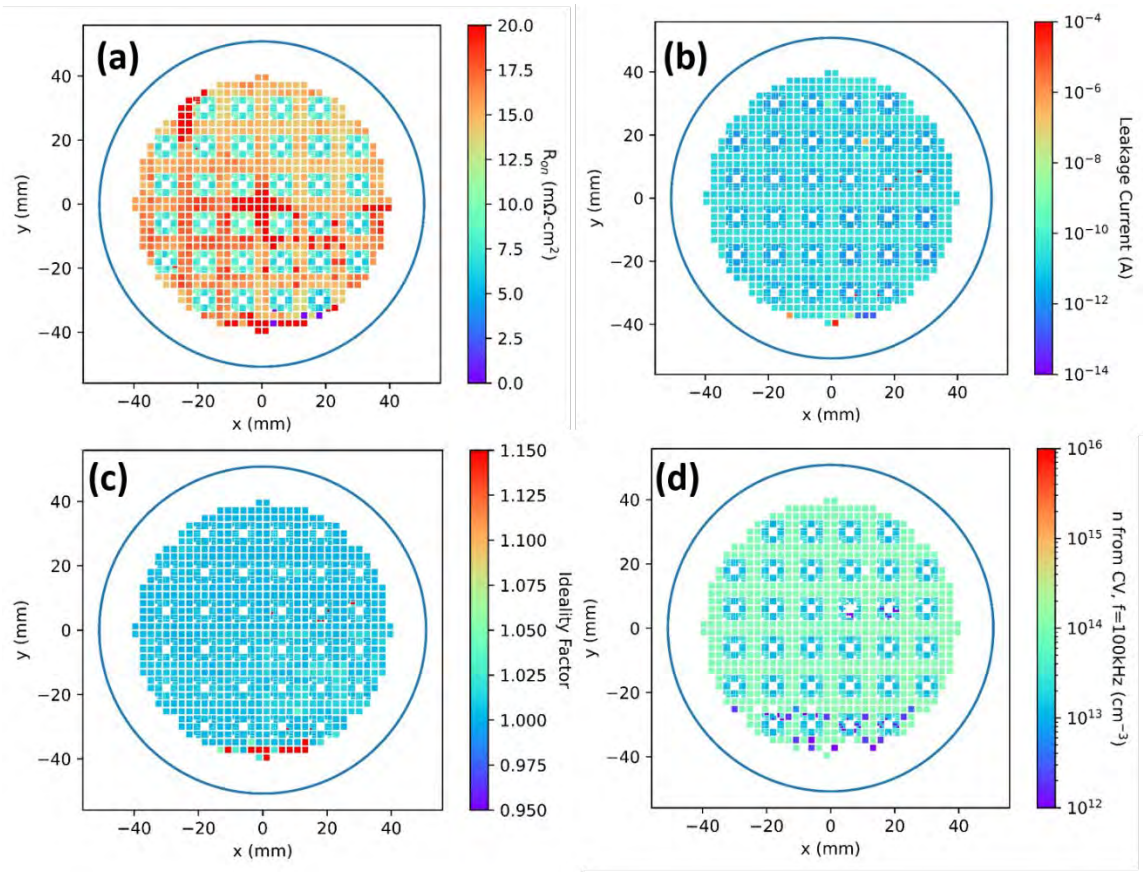


Figure 29. Wafer-level automatic characterization of Schottky diode (a) on-resistance, (b) reverse leakage current at -10 V bias, (c) ideality factor, and (d) carrier concentration extracted from 100 kHz capacitance-voltage measurements. Large-area devices show up in orange and red color in (a).

3. Findings and Conclusions

A number of fundamental studies in Ga_2O_3 were carried out addressing challenges for this material system. For MOCVD Ga_2O_3 homoepitaxy on EFG substrates provided by Novel Crystal Technology, we have detailed for the first time extended defects in thick epilayers. In thin heteroepitaxial AlGaO, we have detailed critical thickness limitations governed by crystal fracture theory (Griffith criterion). The low thermal conductivity of Ga_2O_3 is a challenge particularly for lateral devices which must be mitigated via high thermal conductivity material integration, such as diamond. NRL has carried out comprehensive studies of diamond growth on Ga_2O_3 and have demonstrated lateral devices coated with diamond. Another approach via wafer bonding to Silicon has been studied using a direct bonding technique and steady-state thermoreflectance measurements after thinning of the Ga_2O_3 layer. The lack of p-type conductivity is of less concern for lateral devices but for vertical devices it is of critical importance. We have developed a self-aligned JBS diode process integrating p-type NiO. Hall measurements of implanted Ga_2O_3 were performed for the first time. Finally, a large area wafer device demonstration was carried out via Schottky diode fabrication and full-wafer X-Ray topography characterization.

4. Plans and Upcoming Events

In year 3, growth efforts of epitaxial Ga2O3 and (AlxGa1-x)2O3 films are expected to continue. Deliverables will focus on:

4.1. Ga2O3 substrates (2-inch, 10x15 mm) for epitaxial MOCVD efforts at NRL
4.2. Ga2O3 substrates (2-inch, 4-inch) for wafer-bonding efforts at NRL for back-side thermal management of Ga2O3 devices
4.3. Ga2O3 substrates grown via novel methods such as Vertical Bridgman and/or Float Zone growth
4.4. (AlxGa1-x)2O3/Ga2O3 heterostructure field effect transistors grown by molecular beam epitaxy for lateral power electronic devices with top-side thermal management
4.5. Thick Ga2O3 homoepitaxial films on conductive substrates grown by halide vapor phase epitaxy for vertical power devices
4.6. Additional performance of growth and characterization depending on experimental needs:

- custom growths for unique experiments, such as Nitrogen-doped Ga2O3
- custom services such as wafer dicing and secondary ion-mass spectroscopy
- characterization such as X-Ray diffraction and electrochemical capacitance-voltage measurements.

5. Transitions and Impacts

The current and prior NICOPs with Novel Crystal Technology have supported internal research at NRL in the field of Ga_2O_3 for several years now. The prior NICOP has impacted almost every research publication on Ga2O3 at NRL in the 2016-2020 period, and we expect research under the present NICOP to elevate Ga_2O_3 technology to TRL 4 where transition opportunities can be identified.

6. Collaborations

Agency/Org	Performer	Project Name	Purpose of Research/ Collaboration
ONR	Capt. Lynn Petersen	Homoepitaxial Ga_2O_3 Structures for Power Device Applications	Program Co-sponsor
ONR Global	Richard Yamada	Homoepitaxial Ga_2O_3 Structures for Power Device Applications	Program Co-sponsor
ARL	Aivars Lelis, Tim Leong	Homoepitaxial Ga_2O_3 Structures for Power Device Applications	Program Co-sponsor (year 3 only)

7. Personnel

Principal investigator: Akito Kuramata
Business Contact: kuramata@novelcrystal.co.jp
Novel Crystal Technology, Inc., 2-3-1 Hirosedai, Sayama, Saitama, 350-1328, Japan
Team Members: Kohei Sasaki

8. Students

Not applicable.

9. Technology Transfer

Not applicable.

10. Products, Publications, Patents, License Agreements, etc.

Publications resulting from this project:

Archival Publications

a. Growth and characterization of α-Ga_2O_3 on sapphire and nanocrystalline β-Ga_2O_3 on diamond substrates by halide vapor phase epitaxy
b. Journal of Vacuum Science and Technology A: Vacuum, Surfaces, and Films
c. Sushrut Modak, James Spencer Lundh, Nahid Sultan Al-Mamun, Leonid Chernyak, Aman Haque, Thieu Quang Tu, Akito Kuramata, Marko J Tadjer, Stephen J Pearton
d. Gallium oxide, diamond, halide vapor phase epitaxy
e. Distribution Statement A: Approved for public release. Distribution unlimited.
f. Published
g. DOI
h. 10.1116/6.0002115
i. 3 November 2022
j. Volume 40
k. Issue 6
l. First Page Number 062703
m. American Vacuum Society: https://avs.scitation.org/doi/full/10.1116/6.0002115
n. Acknowledgement of Federal Support? Yes
o. Peer Reviewed? Yes

a. Activation of implanted Si, Ge, and Sn donors in high-resistivity halide vapor phase epitaxial β-Ga_2O_3:N with high mobility
b. Applied Physics Letters
c. Joseph A Spencer, Marko J Tadjer, Alan G Jacobs, Michael A Mastro, John L Lyons, Jaime A Freitas Jr, James C Gallagher, Quang T Thieu, Kohei Sasaki, Akito Kuramata, Yuhao Zhang, Travis J Anderson, Karl D Hobart
d. Gallium oxide, acceptors, donors, ion implantation, halide vapor phase epitaxy
e. Distribution Statement A: Approved for public release. Distribution unlimited.
f. Published
g. DOI
h. 10.1063/5.0120494
i. 7 November 2022
j. Volume 121
k. Issue 19
l. First Page Number 192102
m. American Physical Society: https://aip.scitation.org/doi/full/10.1063/5.0120494
n. Acknowledgement of Federal Support? Yes
o. Peer Reviewed? Yes

Conference Papers

a. AlN-capped β-(AlxGal-x)2O3/Ga2O3 heterostructure field-effect transistors for near-junction thermal management of next generation power devices
b. James Spencer Lundh, Hannah N Masten, Kohei Sasaki, Alan G Jacobs, Zhe Cheng, Joseph Spencer, Lei Chen, James Gallagher, Andrew D Koehler, Keita Konishi, Samuel Graham, Akito Kuramata, Karl D Hobart, Marko J Tadjer

c. Device Research Conference
d. June 26, 2022
e. Columbus, OH
f. Published
g. August 19, 2022
h. DOI
i. 10.1109/DRC55272.2022.9855809
j. Acknowledgement of Federal Support? Yes/No

11. Point of Contact in Navy

Dr. Marko J. Tadjer
Naval Research Laboratory, Code 6881
4555 Overlook Ave SW
Washington, DC 20375
Marko.tadjer@nrl.navy.mil

12. Acknowledgement/Disclaimer

This work was sponsored by the Office of Naval Research (ONR), under grant (or contract) number N62909-20-1-2055. The views and conclusions contained herein are those of the authors only and should not be interpreted as representing those of ONR, the U.S. Navy or the U.S. Government.

Compact High-Power Microwave Oscillators

Contract No. N62909-18-1-2122

Annual Report for Fiscal Year 2022

Period of Performance: October 1, 2021 to September 30, 2022

Prepared by:

Dr. Alan Phelps, Principal Investigator
Physics Department
University of Strathclyde
John Anderson Building
107 Rottenrow East
Glasgow, Scotland, UK G4 0NG
Email: a.d.r.phelps@strath.ac.uk

This work was sponsored by the Office of Naval Research (ONR), under grant number N00014 -18-1-2122. The views and conclusions contained herein are those of the authors only and should not be interpreted as representing those of ONR, the U.S. Navy or the U.S. Government.

Grant or Contract Number: N62909-18-1-2122-GRANT12538355, N00014-18-S-B001
Date Prepared: 31 January 2023
Project Title: Compact high-power microwave oscillators
Annual Summary Report: FY22
Principal Investigator: Alan Phelps, a.d.r.phelps@strath.ac.uk
University of Strathclyde, Scotland, UK

Section I: Project Summary

1. Overview of Project

Abstract:
The ABP group, of the University of Strathclyde, Scotland, UK, have been investigating the operation of a novel high-power microwave oscillator. Designed to operate in the X-band ($8-12GHz$) without the application of external magnetic insulation, the source radiates Cherenkov radiation due to efficient modulation of an electron beam, propagated solely under the influence of the beam's self-forces. Numerical modeling of this design indicates efficiencies of $\eta\sim25\%$, corresponding to $\sim220MW$ from a $500keV$, $1.7kA$ electron beam, with efficiencies of $\eta\sim30\%$ obtained as the quality of the electron beam improves (e.g. through revision of the electron accelerator, to be informed by the results of the experimental program). Named the 'Self-Insulating Backward-Wave Oscillator', the prototype design has been progressed to manufacture for proof of principle experiments. During the operation of the prototype both the electron beam and the microwave output have been measured. The observed output mode TM_{01} and the measured frequency of $9.25GHz$ are both in good agreement with the numerical model. The full-width-half-maximum microwave pulse duration $\sim50ns$ was shorter and the microwave power $\sim8MW$ was significantly less than in the numerical simulations. Analysis of these experimental results has identified the modifications needed to achieve improved output parameters in future work.

Objective:
Develop an X-band High Power Microwave (HPM) source that operates without the use of externally applied magnetic insulation. Over the reporting period the aim was to complete the current work program, extended by NCE due to the impact of the Covid-19 pandemic.

Introduction:
The work presented was undertaken as part of a project which concluded during the current reporting period on June 14 2022. All work was undertaken at the University of Strathclyde (UoS) with full technical reporting provided in [1].

This work was sponsored by the Office of Naval Research (ONR), under grant (or contract) number N62909-18-1-2122, GRANT 12538355, N00014-18-S-B001. The views and conclusions contained herein are those of the authors only and should not be interpreted as representing those of ONR, the U.S. Navy, or the U.S. Government.

ABP group	Atoms Beams and Plasma research group, based in the Physics Department of the University of Strathclyde.
A-K gap	Anode – Cathode (German "Kathode") gap: refers to the spacing between the cathodic emitter and anode plane of the electron accelerating diode
BWO	Backward-Wave Oscillator
GHz	Giga-Hertz: 1,000,000,000 Hertz or 1,000,000,000 full-wave oscillations of the field-pattern per second.
HPM	High Power Microwave: refers to microwave sources / amplifiers with output powers >100MW
keV / kA	Kilo-electron-Volt / kilo-ampere: 1000 Volts / 1000 Amperes
MW	Mega-Watt: 1,000,000 Watts
ns	Nano-second: 0.000,000,001 seconds
PiC	Particle in Cell: a numerical code that considers both the electromagnetic fields and discrete particles within the "cells" used to define the simulation volume.
PY	Project Year: refers to the period running from June 15 in one year till June 14 in the following year
S-band	A region of the EM spectrum between 2 – 4 GHz
SIBWO	Self-Insulating Backward-Wave Oscillator
UoS	University of Strathclyde.
X-band	A region of the EM spectrum between 8 – 12GHz
PPS	Pulsed Power Supply: a high voltage, high current single-shot power supply located at the UoS, capable of producing $\sim 200 - 250ns$ long pulses of up to $750kV$ (max as configured) at multiple tens of kiloamperes of current

Table 1: List of abbreviations / terminology

Background:

The SIBWO is a novel variant of the conventional relativistic BWO, operating at electron energies of $\gtrsim 500keV$. The concept originated in work conducted at the Institute of High Current Electronics (IHCE) Russia at ~3GHz [2,3]. A variation of the concept was investigated, at X-band, at the National University of Defense Technology (NUDT) China [4]. Over the same time period the UoS undertook an investigation of an S-band SIBWO variant, with results presented at the 2015 Joint UK / US Directed Energy Workshop [5]. The current project involves theRese development of an X-band variant of the UoS work, shown in schematic cross-section in Figure 7.

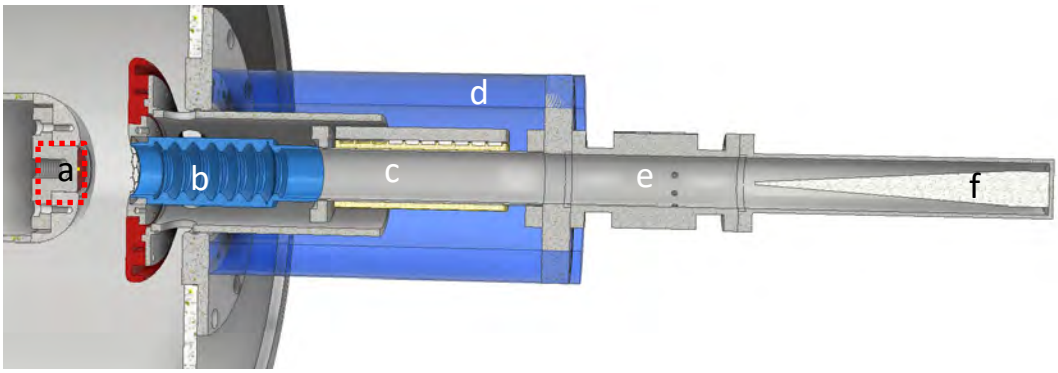


Figure 1. Schematic cross-section of SIBWO prototype assembly noting (a) A-K gap of accelerating diode (b) interaction region (c) beam dump (d) linear-stage location for A-K gap adjustment (e) field probe diagnostics (f) attenuating load termination

This includes the incorporation of klystron-like elements to enhance efficiency [6 – 11], though the dominant characteristics remain BWO-like. Results from the project have been presented at conferences [12 – 16].

References

1. MacInnes, P., et al., 2022, "Compact high-power microwave oscillators", Final Technical Report, DTIC Accession Number: AD1181792, 30 Sept. 2022.
2. Totmeninov, E.M. et al., 2009, IEEE Trans. Plasma Sci., 37(7), pp. 1242 – 1245.
3. Totmeninov, E.M., et al., 2011, IEEE Trans. Plasma Sci., 39(4), pp. 1150 – 1153.
4. Guo, L.M., et al., 2017, Rev. Sci. Instrum., 88(2), article 024708.
5. MacInnes, P., et al., 2015, 15-19 June 2015 UK / US Directed Energy Workshop, Swindon, UK.
6. Phelps, A.D.R., 2018, ONR HPM Program FY 2018 Report.
7. Phelps, A.D.R., 2019, ONR HPM RPPR 2019.
8. Phelps, A.D.R., 2019, ONR HPM Program FY 2019 Report.
9. Phelps, A.D.R. 2020, ONR, HPM RPPR 2020.
10. Phelps, A.D.R. 2021, ONR, HPM Program FY 2020 Report.
11. Phelps, A.D.R. 2021, ONR, HPM RPPR 2021.
12. MacInnes. P., et al., 2019, UK / US Directed Energy Workshop, Swindon, UK, 22-26 July 2019.
13. MacInnes, P., et al., 2020, 47th Int. Conf. on Plasma Sci. (ICOPS 2020), 6-10 Dec. 2020.
14. Crampsey, B., et al., 2020, 47th Int. Conf. on Plasma Sci. (ICOPS 2020), 6-10 Dec. 2020.
15. MacInnes, P., et al., 2021, UK Institute of Physics, 47th Plasma Physics Conference, 6-9 April 2021.
16. MacInnes, P. et al., 2022, UK/ US Directed Energy Workshop, Swindon, UK, 18-22 July 2022.

2. Activities and Accomplishments

Concluding the numerical work package, a mode converting horn antenna was designed to provide a Gaussian output field pattern. The antenna was optimized for best performance at 9.4GHz, with an operational bandwidth of +/- ~100MHz. The transverse output field patterns for 9.3 – 9.5GHz can be seen in Figure 2, with the launch mode being the HE_{11}, formed by a mode mixture of the TE_{11} and TM_{11} at weightings of ~85% to ~15% respectively, with Gaussian output obtained where the constituent modes differ in phase by $\sim 180^0$ (see Figure 3).

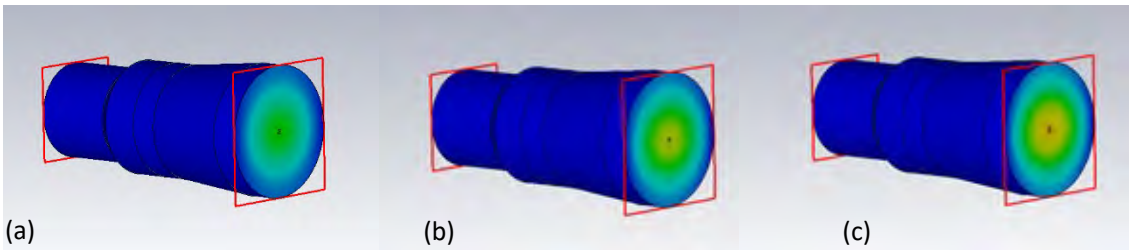


Figure 2. 'Satoh' launch antenna, designed to provide a near Gaussian output field pattern at ~9.4GHz. (a) – (c) show the transverse field pattern at 9.3GHz, 9.4GHz and 9.5GHz respectively**.**

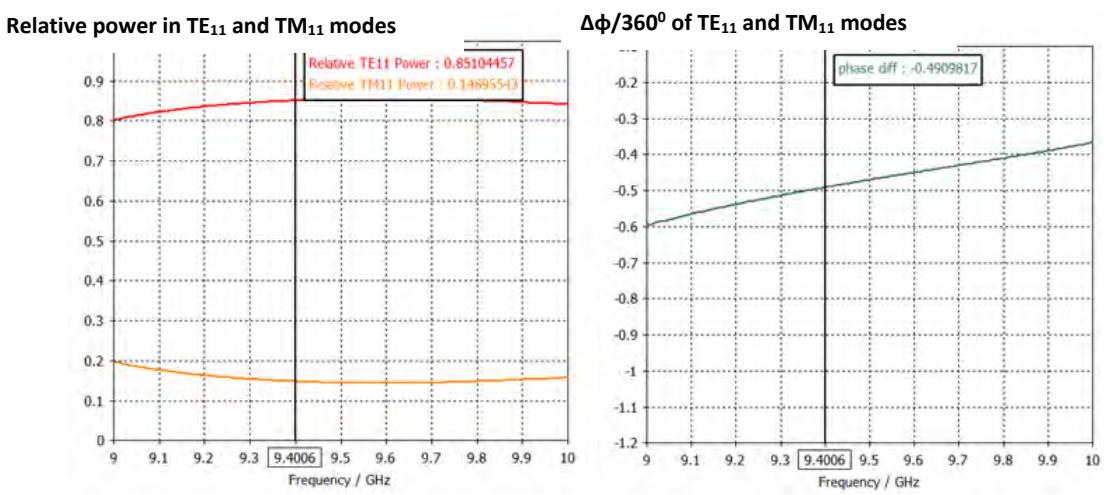


Figure 3. (a) Shows the relative strength of the TE_{11} and TM_{11} modes at the output (b) shows the corresponding phase difference between the two modes. A value of +/- 0.5 corresponds to a phase difference of 180^0 between modes.

The mode conversion required to turn the output TM_{01} mode of the SIBWO into the TE_{11} input for the Satoh horn is straight forward, with options such as co-axial or serpentine mode converters, providing a means or depositing any remaining electron beam to the drift-tube wall prior to output.

Hot testing of the SIBWO prototype began in April 2022, concluding with the end of the current project in mid-June 2022.

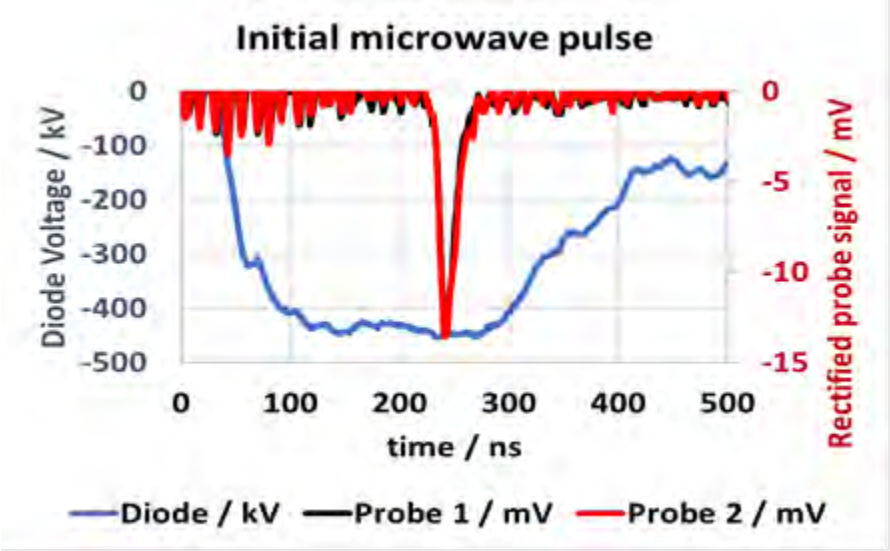


Figure 47. First microwave output experimental results from the SIBWO prototype. Probes 1 and 2 are orthogonal and share the same axial plane. Agreement in terms of temporal location and pulse magnitude are a strong indication the operating mode is the expected TM_{01} mode.

The power envelopes shown in Figure 4 were obtained using rectifying crystal detectors, placed on two orthogonal D-dot probes at the SIBWO output. The probes were axially co-located, meaning the AC signal detected at both probes should present at the same magnitude and phase for output in the TM_{01} mode (i.e. the envelopes recorded should be "identical" within experimental limits). This was clearly observed, though pulse shortening was equally evident. This was determined to be due to issues within the electron accelerator, with the cathodic emitter showing evidence of excessive emission and rapid aging.

Following improvements to the accelerating diode assembly the pulse width was extended though signs of pulse shortening remained (see Figure 5). Examination of the Fourier content (Figure 6) showed strong resonance at a single frequency of $\sim 9.24GHz$; this is consistent with TM_{01} operation from the SIBWO at lower electron beam energy ($\sim 410keV$) and higher than expected beam current ($> 2kA$), both of which would contribute to a down-shift in the intended operating frequency of $\sim 9.4GHz$ at $500keV, 1.7kA$. The purity of the output spectrum indicates the SIBWO interaction was growing as intended (without significant mode competition etc.) until the on-set of pulse shortening.

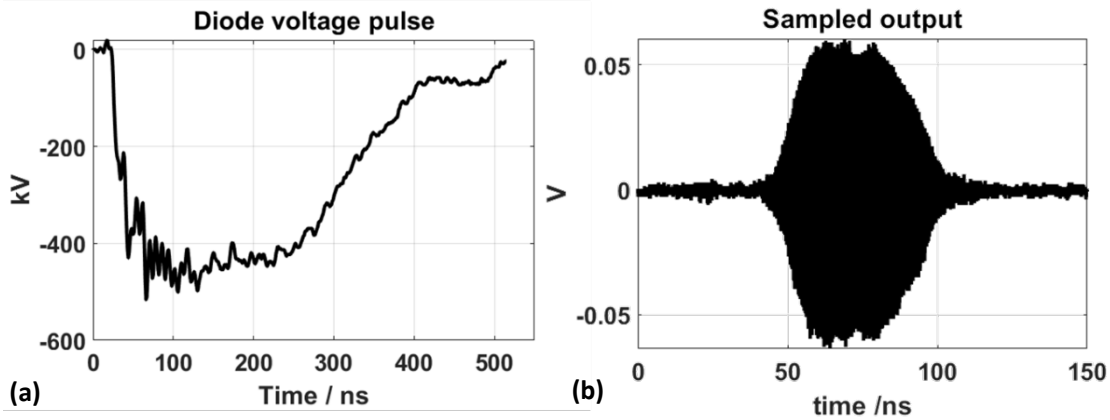


Figure 5 Shows (a) the applied diode pulse (b) the measured microwave output from the SIBWO.

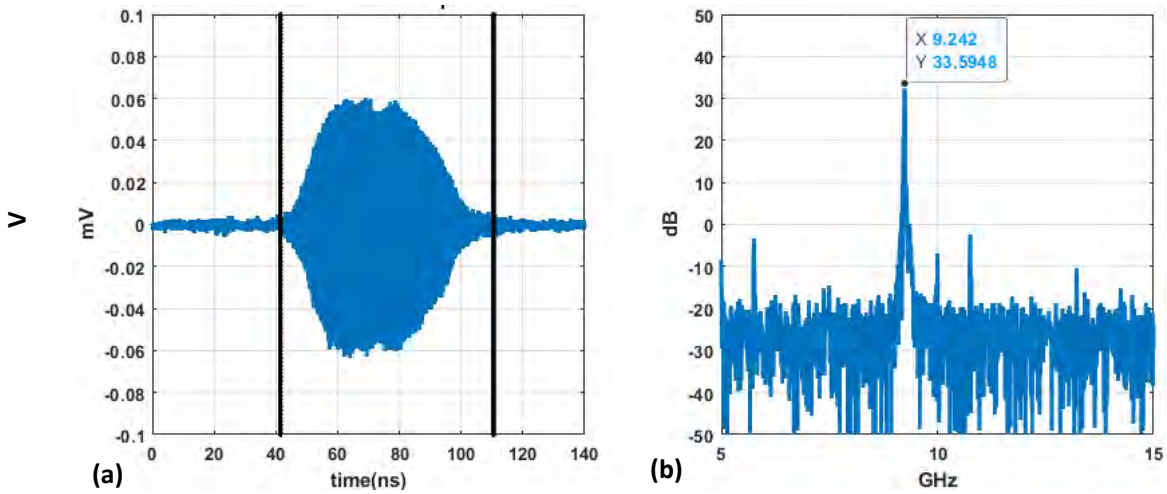


Figure 6. Shows (a) windowing of the AC waveform, (b) spectral content in the pulse.

To provide some insight a series of simulations were undertaken with e-beam injection (at $\sim 410keV$) curtailed at various points in the simulation runtime (Figure 7). While this is a rough analogue to any likely plasma-shorting processes occurring in the experiment the agreement between the predicted and measured spectra is clear.

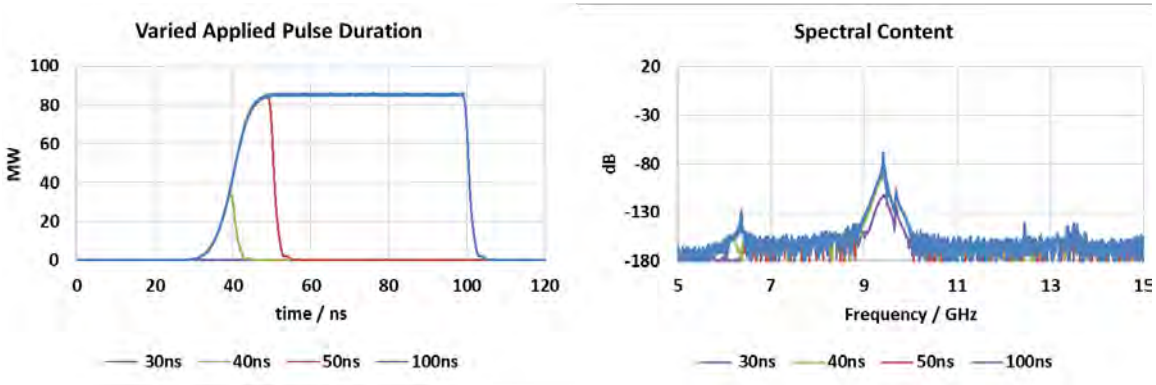


Figure 7. Shows the change in the output power envelope, and associated spectral content, for a fixed set of e-beam parameters with varying beam-pulse duration.

Accounting for the attenuation in the diagnostic line the SIBWO output was determined to have grown to at least $8MW$ before pulse-shortening. At the time of writing it is unknown whether the measured signals were curtailed due to "shorting" of the probe tip(s) or "shorting" within the interaction region and / or accelerating diode. Evidence of damage within the accelerating diode (albeit at reduced level) remained evident at the conclusion of the experimental program, indicating issues there were at least partly responsible for the measured performance.

3. Findings and Conclusions

The predicted electronic efficiency from the SIBWO, as currently developed, was in the range $20-30\%$, depending on the applied potential and resulting electron beam parameters. The predicted efficiency for the design progressed to experiment was 25%, corresponding to $\sim 220MW$ at $\sim 9.4GHz$ extracted from a high-quality $500keV, \sim 1.8kA$ electron beam.

In the experiment two outstanding issues were identified.

1) Degradation of performance in the accelerating diode
2) Lower than predicted output power

Issues in the accelerating diode were significantly reduced (but not eliminated) through additional processing of the electrode surfaces. Further iteration of the diode design, coupled with consideration of different materials (e.g. tungsten for the electrodes, carbon nanotube arrays for the emitter), would address the remaining issues surrounding rapid aging of the emitter velvet.

Issues associated with the accelerating diode were considered to be, at least in part, responsible for the lower than predicted output power measurement. An in-depth analysis of the experimental results, against the predicted trends in performance, indicates there may also be an issue with the output diagnostic when placed under sufficient electrical stress. As this could not be confirmed within the time-frame of the current program the UoS would consider the stated output power of $\sim 8MW$ at $\sim 9.24GHz$ as being representative of the <u>minimum</u> power generated in the experiment, not an indication of the maximum attainable (or attained).

4. Plans and Upcoming Events

Submission of paper to the 49th UK Institute of Physics, Plasma Physics Conference planned (27 – 30 March 2023, Oxford, UK).

Recommendations for Future Work:

The UoS considers the following to be areas of interest in further developing the SIBWO.

- Optimization of the electron accelerating diode
  - Operation of the SIBWO is reliant on the delivery of a suitably high-quality electron beam
  - Resolve remaining issue with aging of emitter material
    - Investigate use of different materials for electrodes and emitter
  - Knowledge gained directly applicable to the accelerating diodes of a range of HPM sources

- Investigate operation of field diagnostic at high-power
  - Test using high-power signals from other sources
  - Develop secondary diagnostic for cross-checking in SIBWO 'hot' tests
- Numerical investigation of X-band SIBWO at lower accelerating potentials
  - Reduce E-field stress in accelerating diode
  - Determine potential output powers and efficiencies for $200 - 300keV$ electron beams

5. Transitions and Impacts

Not applicable

6. Collaborations

Collaboration with Drs. Simon Cooke and Igor Chernyavskiy at NRL in modeling and design of the electron accelerator and SIBWO interaction region.

7. Personnel

Principal investigator: Prof. Dr. Alan D. R. Phelps
Person months worked: 4
National Academy Member: Yes
Nationality: UK

Co-investigator or Co-PI: Prof. Dr. Kevin Ronald
Person months worked: 4
National Academy Member: Yes
Nationality: UK

Business Contact: RKES, University of Strathclyde

Team Members: Dr. Philip MacInnes
Person months worked: 12
National Academy Member: No
Nationality: UK

8. Students

Not applicable

9. Technology Transfer

In the collaboration with NRL the UoS provided both examples files and support documentation for the configuration of commercial numerical software to model the SIBWO and its associated accelerating diode.

10. Products, Publications, Patents, License Agreements, etc.

Publications resulting from this project:

Conference Papers

(1) First Experimental operation of an X-band Self-Insulating Backward Wave Oscillator, P. MacInnes, K. Ronald, C.G. Whyte, B. Crampsey, S.J. Cooke, I.A. Chernyavskiy, A.D.R Phelps, UK/ US Directed Energy Workshop, Swindon, UK, 18-22 July 2022

11. Point of Contact in Navy

Ryan Hoffman ONR, ryan.hoffman@navy.mil

Tim Andreadis NRL, tim.andreadis@nrl.navy.mil
Jesus GilGil NRL, jesus.gilgil@nrl.navy.mil
Simon Cooke NRL, simon.cooke@nrl.navy.mil
Igor Chernyavskiy NRL, igor.chernyavskiy@nrl.navy.mil
Matthew McQuage NSWC, matthew.mcquage@navy.mil
Predrag Milojkovic ONRG (before 2021), predrag.milojkovic.civ@mail.mil
Charles Eddy ONRG (2021 onwards) chip.eddy@nrl.navy.mil ; charles.r.eddy12.civ@mail.mil

Geodesic Luneburg Lenses for High Power Applications

Grant No. N62909-20-1-2040

Annual Report for Fiscal Year 2022

Period of Performance: October 1, 2021 to September 30, 2022

Prepared by:

Dr. Oscar Quevedo-Teruel, Principal Investigator
KTH Royal Institute of Technology
Brinellvägen 8, 114 28
Stockholm, Sweden
Email: oscarqt@kth.se





This work was sponsored by the Office of Naval Research (ONR), under grant number N62909-20-1-2040. The views and conclusions contained herein are those of the authors only and should not be interpreted as representing those of ONR, the U.S. Navy or the U.S. Government.

Grant or Contract Number: N62909-20-1-2040
Date Prepared: 25th Jan. 2023
Project Title: Geodesic Luneburg Lenses for High Power Application
Annual Summary Report: FY22
PI: Prof. Oscar Quevedo-Teruel, oscarqt@kth.se
KTH Royal Institute of Technology

Section I: Project Summary

1. Overview of Project

Abstract:

This project investigates the suitability of fully metallic geodesic Luneburg lens antennas for high-power applications. Previous reporting periods focused on the development of the ray tracing model for rotationally symmetric cases. This model has been expanded with the introduction of loss terms. Several non-rotationally symmetric profiles, which reduce the overall size of the lens while maintaining performance, have been explored within this reporting period. Investigations into an elliptical lens (where a compression has been applied along the *y*-axis) have been completed and a manuscript describing this profile has been accepted for publication in IEEE Transactions on Antennas and Propagation. The accuracy of the model depicting the half-lens case (where a mirror plane is placed along an axis of symmetry in the lens) has been improved and generalized so a compression can be introduced in addition to the mirror plane. Initial studies have been conducted on a lens with multiple compressions in the *xy*-plane. An in depth discussion on the numerical elements of the ray tracing model was presented at the European Conference on Antennas and Propagation, held onsite in Madrid. The ray tracing model for a compressed half-lens was presented at the International Symposium on Antennas and Propagation in Sydney. Future work plans include the continued investigation into the doubly-compressed profile; manufacturing of prototypes to validate the addition of loss terms to the code and doubly-compressed profile; experimental validation of the designed prototypes and investigating the introduction of a reflectarray in half-geodesic lenses.

Objective:

The primary objective of this project is to investigate the suitability of geodesic lenses for high-power antenna applications, which can be utilized in radar systems. As geodesic lenses can take a significant amount of time to model using commercial software, the development of a time-efficient model was deemed necessary. In addition to this, the project aims to determine the fundamental limitations of geodesic lenses and their limitations at high-power. The project will also explore the use of fully metallic geodesic lenses at X- and Ku- bands.

Introduction:

A Luneburg lens is a graded-index lens that perfectly transforms a spherical/cylindrical wave into a plane wave at the opposing side of the excitation. Luneburg lenses are an attractive solution for communications and radar systems since they have low scan losses. However, their principal drawback for high-power applications is that they are typically implemented with dielectric materials, which are lossy and limit the amount of handled power. Equivalents to dielectric Luneburg lenses can be achieved with geodesic lenses. As geodesic lenses are fully metallic, they can cope with high-power.

Geodesic lenses consist of two parallel curved conductive plates, with a homogenous refractive index between the plates. The refractive index profile of a conventional dielectric lens is then replicated with an

appropriate height profile. A rotationally symmetric structure is assumed during the calculation of the height profile. This lens profile can be reduced in the *z*-direction via the introduction of folds, which maintain the optical path length required of the lens.

Geodesic Luneburg lenses are highly relevant for both naval and civilian applications as they can be used in radar systems; 5G/6G communications systems and satellite communications.

Background:

Ray tracing has been successfully implemented in the design process of a wide range of microwave technologies where commercial software is either inefficient or inconvenient. In this approach the propagation of electromagnetic waves is modelled in terms of rays, where each ray is defined as the normal to the wave front at that location. In doing so, the problem is simplified allowing for the possibility of an algorithm to be developed.

The ray tracing model that has been engineered over the course of this project can be split into three regimes, firstly geometric optics to determine the ray path through the lens, secondly the concept of ray tubes to approximate the amplitude at the lens edge and finally Kirchhoff diffraction to determine the radiation pattern exhibited by the lens.

2. Activities and Accomplishments

In the previous reporting periods, the ray tracing model was developed for rotationally symmetric cases. This proved significantly faster than commercial software (running in approximately 20 seconds, compared to hours using CST). By applying a compression along the y-axis of the rotationally symmetric case and modifying the height profile to compensate for this adjustment, the lens size can be reduced in the *xy*-plane while maintaining performance. During the current reporting period, an article describing in detail this elliptical was accepted for publication in IEEE Transactions on Antennas and Propagation. Additionally, a presentation describing the numerical elements of the model for the rotationally symmetric case was given at the European Conference on Antennas and Propagation (EuCAP) 2022, held in Madrid. The accompanying paper has also been published in the conference proceedings.

Numerical elements of the ray tracing model were further developed over this reporting period with the introduction of loss terms. This takes the surface roughness and conductivity of the metal that the desired lens will be manufactured with into consideration when the radiation pattern is calculated. The example presented in Fig. 1 shows the radiation patterns determined for an ideal elliptical lens (metal plates are PEC) and realistic elliptical lens (steel metallic plates) using the ray tracing model and HFSS. These lenses have identical dimensions and operate at 30 GHz.

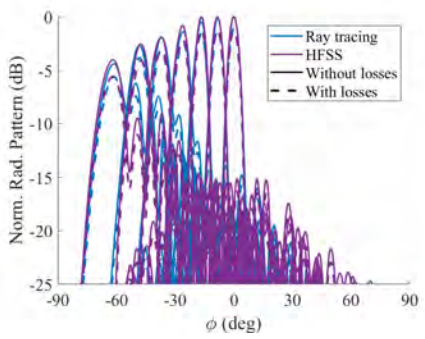
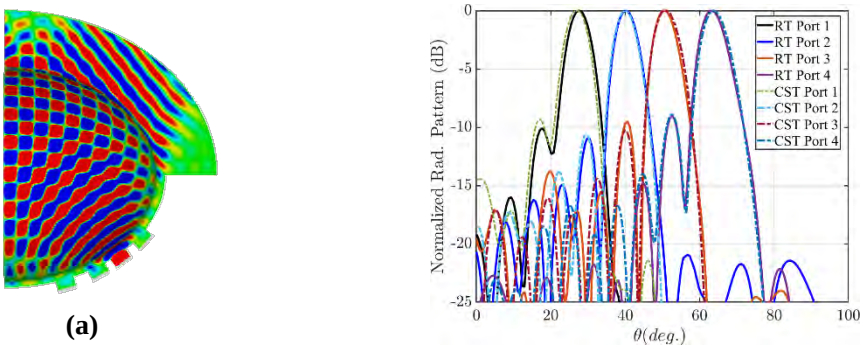


Figure 1: Radiation patterns for an ideal elliptical lens and elliptical lens manufactured with steel. The dimensions of each lens are identical and each lens has been fed from multiple source positions.

Inaccuracies with the half-lens model developed in the previous reporting period have been corrected, and the model has been further adjusted to allow for elliptical cases. The cause of these inaccuracies was found to be to an error with in how the waveguide was modeled. It should also be noted that the height profile needs to be modified from the full lens case in order to generate a planar wavefront as shown in Fig. 2 (a). An excellent agreement can be found between the ray tracing model and CST simulations for a range of different source positions (Fig. 2 (b)). These results were presented at the 2022 International Symposium on Antennas and Propagation (ISAP), held in Sydney Australia.

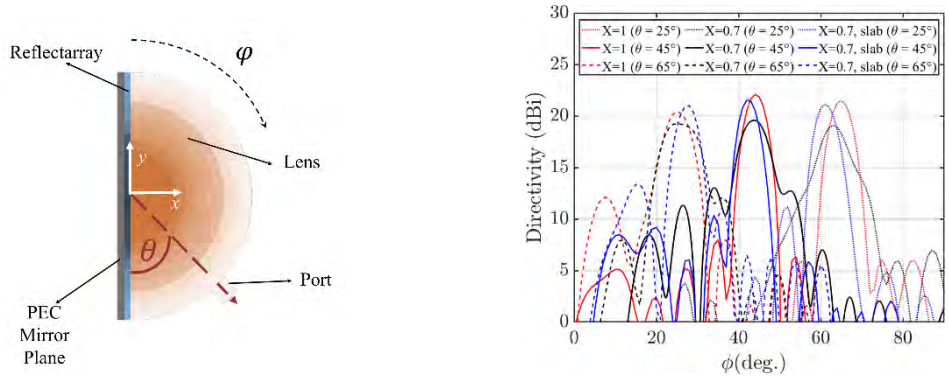


(a) **(b)**

Figure 2: (a) E-field pattern for elliptical half-lens antenna and (b) radiation patterns for the elliptical half-lens determined from ray tracing and CST simulations.

Initial studies have been performed for the integration of a reflectarray (RA) and the mirror plane of the half-lens antenna. This allows for the wavefront propagating through the lens to undergo an additional manipulation which can compensate for a lower equivalent refractive index (i.e. reduced profile height) or redirect the beam to mitigate against feed blockage. A planar half-lens case with concentric layers of dielectric was modelled in commercial software to prove the concept (Fig.3 (a)). The case investigated compensated for a lens with a refractive index profile that has a maximum value that is 70% of the ideal Luneburg lens case. Figure 3 shows the directivity for the integrated RA and half-lens antenna (operating at 30 GHz) when fed with a waveguide port at multiple positions. X is a constant that refers to the maximum refractive index value, where X =1 is the ideal Luneburg lens profile and X = 0.7 has a maximum value that is 70% of the ideal Luneburg case. The RA used here is a slab consisting of discrete dielectric layers of the same thickness and differing permittivities. The arrangement of these layers have been selected to best compensate for the reduced refractive index profile of the lens, and achieve this quite well as shown in Fig. 3 (b). The results of this proof of concept have been accepted for presentation at the next EuCAP edition (to be held in Florence, Italy). The next reporting period aims to further improve this response and also

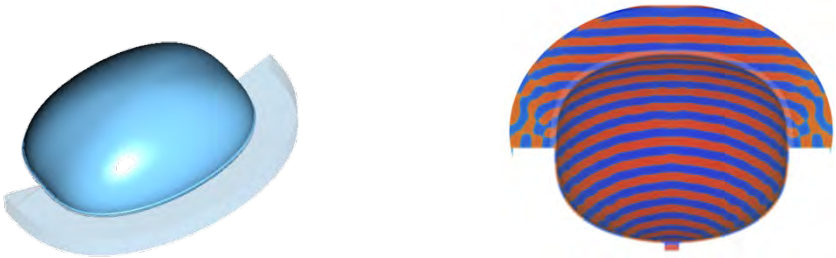
integrate this with a geodesic lens. Using a geodesic form increases the complexity of the problem as the plates are curved and no longer planar, and hence the RA design must account for this.



(a) **(b)**

Figure 3: (a) Configuration of RA and half-lens structure and (b) radiation patterns for the ideal half-Luneburg lens, lens with lower refractive index profile and the lens with a lower refractive index profile and integrated RA.

A non-rotationally symmetric full-lens structure was investigated in this reporting period. For this profile, a spline function was used to create a footprint in the *xy*-plane that reduced the size of the lens in both the *x* and *y* directions (Fig. 4). This variation in shape is more complex than the compressions applied in the elliptical lens case, and allows for the wavefront to be manipulated in a different manner when the lens is illuminated at different source positions. This was investigated with the intention of improving the lens response at more extreme positions, while reducing the full lens size. The ray tracing model required modification to the meshing of the lens profile and how the waveguide port was represented at different positions. Investigations are still on going for this structure.



(a) **(b)**

Figure 4: (a) Lens with compressions in multiple directions and (b) E-field response of lens.

3. Findings and Conclusions

Geodesic lenses with a significantly smaller profile have been shown to be capable of operating with a similar performance to the full-lens profile, however with a reduced angular range. This is of benefit for applications where there are constraints on the volume of the device i.e. in satellite communications. The ray tracing model has also been modified to account for these adjustments to the profiles, while continuing to run accurately and efficiently.

Investigations into lens structures that reduce the profile size, while maintaining angular performance are ongoing.

4. Plans and Upcoming Events

The ray tracing code will be further modified to account for the change in phase and trajectory of the wavefront propagating through the half-lens with an integrated reflectarray. This step is critical for the exploration and design of different configurations, and requires a significant modification to the model.

The prototype designed to operate from 10-20 GHz that has been sent to manufacturing, will be tested experimentally. Additionally, prototypes will be engineered and then manufactured for non-rotationally symmetric cases such as the doubly-compressed lens and a half-lens with an integrated reflectarray. An elliptical lens with a water-drop profile will be manufactured using metallic 3D printing techniques to verify the loss terms that have been added to the code.

It is anticipated that several articles will be submitted to various journals (depending on measured results) over the course of the next reporting period. The focus of these manuscripts will be the inclusion of loss terms in the code, a doubly-compressed lens and the half-lens with an integrated reflectarray.

In terms of dissemination, a paper titled ‘Reducing the Refractive Index Range of GRIN Lenses Through the Integration of a Reflectarray’, has been accepted to be presented at the 2023 European Conference on Antennas and Propagation (EuCAP) held in Florence. This is the largest European conference relevant to our research. Additionally, an abstract for a presentation called ‘Integrating Half-Lens Antennas with a Reflectarray’, has been submitted to the Swedish Microwave Days Event. This is a national conference, which has been organized by KTH.

5. Transitions and Impacts

No information to report.

6. Collaborations

The team at KTH have collaborated with Prof. Francisco Mesa (University of Seville in Spain) and Dr. Nelson Fonseca (European Space Agency) to further develop of the ray tracing tool for non-rotationally symmetric cases.

7. Personnel

All the participants in this project are at KTH Royal Institute of Technology.

Principal investigator: Prof. Oscar Quevedo-Teruel (Full Professor)
Team Members:

- Dr. Sarah Clendinning (Post-doc).
- Ms. Pilar Castillo-Tapia (PhD student).
- Ms. Shiyi Yang (PhD student).

8. Students

In 2022, Ms. Pilar Castillo-Tapia and Ms. Shiyi Yang contributed to the project. Both are PhD students.

9. Technology Transfer

No information to report.

10. Products, Publications, Patents, License Agreements, etc.

Publications resulting from this project:

Archival Publications (publication reference information (article title, authors, journal, date, volume, issue) can be automatically entered using a DOI)

a. Geodesic Lens Antennas for 5G and Beyond
b. IEEE Communications Magazine
c. Oscar Quevedo-Teruel, Qingbi Liao, Qiao Chen, Pilar Castillo-Tapia, Francisco Mesa, Kun Zhao and Nelson Fonseca
d. 5G Mobile Communication, Spatial Diversity, Dielectric Materials, Prototypes, Directive Antennas, Geometrical Optics and Propagation Losses
e. Distribution Statement: N/A
f. Published
g. DOI: 10.1109/MCOM.001.2100545
h. Publication Identifier: N/A
i. 1 January 2022
j. 60
k. 1
l. 40
m. Publication Location: N/A
n. Acknowledgement of Federal Support? (**Yes**/~~No~~)
o. Peer Reviewed? (**Yes**/~~No~~)

Archival Publications

a. Near-Field Focusing Multibeam Geodesic Lens Antenna for Stable Aggregate Gain in Far-Field
b. IEEE Transactions on Antennas and Propagation
c. Omar Orgeira, German Leon, Nelson Fonseca, Pedro Mongelos and Oscar Quevedo-Teruel
d. Lenses, Gain, Ray Tracing, Mathematical Models, Antennas, Focusing, Antenna Arrays
e. Distribution Statement: N/A
f. Published
g. DOI: 10.1109/TAP.2021.3139093
h. Publication Identifier: N/A
i. 10 January 2022
j. 70
k. 5
l. 3320
m. Publication Location: N/A
n. Acknowledgement of Federal Support? (**Yes**/~~No~~)
o. Peer Reviewed? (**Yes**/~~No~~)

Archival Publications

a. Ray-Tracing Model For Generalized Geodesic Lens Multiple Beam Antennas
b. IEEE Transactions on Antennas and Propagation
c. Qingbi Liao, Nelson Fonseca, Miguel Camacho, Angel Palomares-Caballero, Francisco Mesa and Oscar Quevedo-Teruel
d. Lens Antennas, Geodesic Lenses, Parallel Plate Waveguides, Ray Tracing and Non-Euclidean Transformation Optics

e. Distribution Statement: N/A
f. Early Access
g. DOI: 10.1109/TAP.2022.3233643
h. Publication Identifier: N/A
i. N/A
j. -
k. -
l. -
m. Publication Location: N/A
n. Acknowledgement of Federal Support? (**Yes**/~~No~~)
o. Peer Reviewed? (**Yes**/~~No~~)

Conference Papers

a. Numerical aspects of the application of ray-tracing to geodesic lenses
b. Sarah Clendinning, Shiyi Yang, Qingbi Liao, Pilar Castillo-Tapia, Francisco Mesa, Nelson Fonseca and Oscar Quevedo-Teruel
c. European Conference on Antennas and Propagation
d. 26th March – 1st April 2022
e. Madrid, Spain
f. Published
g. 11th May 2022
h. Publication Identifier Type: N/A
i. Publication Identifier: N/A
j. Acknowledgement of Federal Support? (**Yes**/~~No~~)

Conference Papers

a. Ray-Tracing Model for Elliptical Half-Geodesic Lens Antennas
b. Sarah Clendinning, Francisco Mesa and Oscar Quevedo-Teruel
c. International Symposium on Antennas and Propagation
d. 31st October – 3rd November 2022
e. Sydney, Australia
f. Published
g. 2nd January 2023
h. Publication Identifier Type: N/A
i. Publication Identifier: N/A
j. Acknowledgement of Federal Support? (**Yes**/~~No~~)

Conference Papers

a. Ka-Band Implementation of a Geodesic Half-Maxwell Fisheye Lens Antenna
b. Shiyi Yang, Qiao Chen, Francisco Mesa, Nelson Fonseca and Oscar Quevedo-Teruel
c. International Symposium on Antennas and Propagation
d. 31st October – 3rd November 2022
e. Sydney, Australia
f. Published
g. 2nd January 2023
h. Publication Identifier Type: N/A

i. Publication Identifier: N/A
j. Acknowledgement of Federal Support? (**Yes**/~~No~~)

Books

N/A

Book Chapter

N/A

Theses

N/A

Websites

N/A

Patents

N/A

Other Products: Identify any other significant products that were developed under this project. Describe the product and how it is being shared.

N/A

11. Point of Contact in Navy

The main contacts during the 2022 reporting period were:

- Navy: Ryan Hoffman (ryan.hoffman@navy.mil)
- ONR Global London: Charles R. Eddy, Jr. (charles.r.eddy12.civ@mail.mil)

12. Acknowledgement/Disclaimer

This work was sponsored by the Office of Naval Research (ONR), under grant number N62909-20-1-2040. The views and conclusions contained herein are those of the authors only and should not be interpreted as representing those of ONR, the U.S. Navy or the U.S. Government.

New Ideas for Advanced Relativistic Magnetrons

Grant No. N62909-21-1-2006

Annual Report for Fiscal Year 2022

Period of Performance: October 1, 2021 – September 30, 2022

Prepared by:

Prof. Yakov Krasik, Principal Investigator
Physics Department
Technion-Israel Institute of Technology,
Haifa 32000, Israel
Email: fnkrasik@physics.technion.ac.il





This work was sponsored by the Office of Naval Research (ONR), under grant (or contract) number N62909-21-1-2006. The views and conclusions contained herein are those of the authors only and should not be interpreted as representing those of ONR, the U.S. Navy or the U.S. Government.

Grant or Contract Number: N62909-21-1-2006
Date Prepared: 7 March 2023

Project Title: New Ideas for Advanced Relativistic Magnetrons
Annual Summary Report: 1 October 2021 to 30 September 2022
Principle Investigator: Yakov Krasik ;fnkrasik@physics.technion.ac.il
Physics Department, Technion-Israel Institute of Technology, Haifa 32000, Israel

Section I: Project Summary

1. Overview of Project

The major goal of this project was to build an efficient relativistic magnetron fed by a split cathode with no pulse shortening and enabling repetitive operation.

A relativistic magnetron (RM) is a pulsed high-power microwave (HPM) source which shows great promise because of its high efficiency in transforming the energy of electrons into electromagnetic power. Its performance, though, is marred by two main problems. One, that the duration of the high-voltage (HV) pulse is much longer than the duration of the HPM pulse, so-called pulse-shortening. This occurs because of non-uniformity of the explosive emission plasma formed at the surface of the cathode from which electrons are emitted and this plasma's radial expansion towards the anode. The latter leads to mode competition which reduces the efficiency of the RM's operation and finally to pulse-shorting. The idea we presented was that of a split-cathode which solves the problem of pulse-shortening by placing the plasma source outside the RM interaction region and by squeezing the electron charge between a cathode and a reflector placed respectively upstream and downstream from the anode and connecting the cathode and reflector by a conducting rod coaxial to the hollow anode. As the squeezed charge increases with continuous emission, its energy decreases, becoming an ideal electron source for a RM without the presence of plasma. Methods to produce this situation were proposed and tested numerically by us and our UNM collaborators.

The objectives of this project were to design by simulations, build, prove and test experimentally the concept of the split cathode fed RM. As an added value, not mentioned originally, we proposed a solution to the second important problem of RM systems, that is, the size and weight of the pulsed power system required to produce the required axial magnetic field in an RM. We have introduced an axial output design which reduces the size of the magnetron and built the magnetron anode block from segments separated by small gaps allowing fast penetration of the magnetic field. This allows using a pulsed power system orders of magnitude lighter and smaller. The segmented magnetron was simulated, built and tested and the principle was proved.

This work was sponsored by the Office of Naval Research Global (ONRG), under grant number N62909-21-1-2006. The views and conclusions contained herein are those of the authors only and should not be interpreted as representing those of ONRG, the U.S. Navy or the U.S. Government.

Abstract:

During the previous year we have shown by simulation and experiments that in contrast to a conventional solid cathode no pulse shortening develops when a split cathode is used as the electron source of a RM. The RM tested was closed and not designed to radiate HPM. During the period relevant to the present report, we designed, manufactured and tested an axial output RM fed by a split cathode and built from anode segments attached to the same HV pulse generator (200kV, 250ns pulse duration). We reconfirmed that no microwave pulse shortening appears and measured a microwave power of 25 MW at a frequency of 2.15 GHz over the entire voltage pulse length.

To operate the segmented anode RM, we designed and manufactured a one–layer solenoid powered by a low-cost pulse power supply (stored ≤300 J energy). The longitudinal slits in the magnetron's anode block, allows for fast magnetic field penetration which drastically decreased the power requirements of the pulsed generator feeding the axial insulating magnetic field producing solenoid and did not affect the operation of the magnetron. This results not only in a compact system but also in overall high electrical efficiency and the possibility to operate the RM in a repetitive mode.

We also carried out experiments and theoretical modeling of the diocotron instability the development of which seems to govern the electron dynamics in the split cathode-fed RM's operation. The diocotron instability has been observed in the pure electron plasma formed in a split cathode coaxial diode. A model of the electron squeezed state, which allows the calculation of the equilibrium plasma density, was developed. The model was applied in an analysis of the experimental data, and the presence of the diocotron instability was unambiguously confirmed.

Objective:

The objectives of the research during 10.01.2021 -09.30.2022, was to examine the operation of the split cathode segmented anode RM on the refurbished linear induction accelerator (LIA) and start a research to understand the effect of the diocotron instability on the performance of the RM.

Introduction and background:

Our thesis explaining the idea of a split cathode supported by numerical simulations and first experiments with a coaxial diode confirming that the principle is correct, was published in Leopold *et al*., Phys. Plasmas **27**, 103102 (2020). The second step was to test the performance of a RM fed by a split cathode and compare it to a solid cathode. In this work [Leopold *et al*., J. Appl. Phys. **130**, 034501 (2021)] we replaced the coaxial diode with an A6 magnetron. This setup was not designed to radiate microwaves and calibrated B-dot probes were used to measure the microwaves developing in the resonators. The microwaves pulse generated by the solid cathode arrangements stopped at ~110 ns, whereas with a split cathode it continued for ~220 ns which means that with a split cathode no pulse shortening appears.

In our proposal we suggested to test a diffraction output magnetron (MDO) similar to that suggested by Xu, *et al*. [see Phys. Plasmas **25**, 083301 (2018)] which is compact and simpler to manufacture. Also, this design contains a conical tube which captures electrons escape downstream which otherwise would have reached and damaged the microwave's output dielectric window.

We have adjusted this design to fit into our experimental tube, around which a solenoid already existed, and performed PIC simulations to test it. The simulations confirmed the design and showed that with a solid cathode the efficiency of the microwave production is ~50% compared to ~36% obtained with a split cathode.

A **compact** relativistic magnetron was an additional goal which we have only mentioned in passing in our original proposal. Incorporating a split cathode in a magnetron with axial output design does reduce the size of the system which is the main impeding factor of size, weight and overall efficiency of the RM. The required amplitude of the axial magnetic fields is 0.2 – 0.5 T along ~30 - 50 cm. This is typically produced by a solenoid forming magnetic fields on the millisecond timescale necessary for the magnetic field to diffuse through the magnetron's anode. These times require a high-power supply and limit the repetition rate of the magnetron's operation. Modern permanent magnets can provide such fields, but the magnetron system is still too large to be considered compact. Permanent magnets can also be incorporated inside the hollowed magnetron anode vanes and the hollow cathode, but this arrangement is limited by the available magnetic field.

We realized that this problem has a simple solution which no one thought of before. Cutting longitudinal slits through the entire conducting volume making up the magnetron system, causes the magnetic field penetration not to be restricted by the diffusion rate. Thus, one can apply a microsecond timescale magnetic field produced by a solenoid powered by a considerably smaller power supply. We tested the axial output design with an anode block built from three segments separated by longitudinal slits and found that fast magnetic field penetration does not interfere with the microwave generation. This is a breakthrough idea, which affects not only the size, weight and the overall efficiency of the system, but also allows it to operate in repetitive mode. Our simulation work confirming the axial output magnetron design operating with a split cathode and built from anode segments has been published in Leopold *et* al., IEEE Trans. Electron Dev. **68**, 5227 (2021).

2. Activities and Accomplishments

During the period of the present report (10/01/2021 – 09/30/2022) we manufactured and tested the performance of the axial output segmented anode magnetron fed by a split cathode experimentally and started the study needed to optimize the design.

In these experiments [Ya. E. Krasik *et al.*, J. Appl. Phys. **131**, 023301 (2022)] we used our Marx pulse generator (~200 kV, 250 ns, ~120 Ω). The experimental setup is shown in Fig. 1. The axial output A6 RM designed by simulations, was placed inside a 400 mm long Perspex tube (inner radius 60 mm). The aluminum anode was 40 mm long (21 mm/42 mm inner/outer anode radii) is surrounded by a cylindrical tube followed by a closed conical section separating it axially from the rest of the downstream region [Fig. 1(a)]. The cylindrical part of this section has radial slots so that all six magnetron cavities are open [Fig. 1(b)]. Three vanes are continued radially into the space outside this tube and reach the outer radius of the system. The space outside the magnetron becomes divided into three sectors. Three 4^0 (2 mm wide) angular slits are cut radially at the center angle of three vanes [Figs. 1(a) and 1(b)]. This conical structure transforms the axial output to a TM_{01} waveguide mode. The electron source of the split cathode consists of 5 mm long carbon capillary tubes placed in holes drilled in a 40 mm diameter cathode holder and symmetrically distributed along a 16 mm diameter circle. This emitter is connected to the 40 mm diameter downstream reflector by a 6.5 mm diameter rod. The axial distance between the upstream edge of the anode and the

edge of the carbon capillaries was 23 mm. The solid cathode was a 20 mm long explosive emission cathode made of a 13 mm diameter carbon rod in which eight 1 mm deep longitudinal grooves, symmetrically distributed azimuthally, were drilled. This cathode was placed at the longitudinal center of the anode and connected by the rod between upstream and downstream reflectors which were positioned at a distance of 35 mm from the anode edges. This structure was placed inside the Perspex tube and a vacuum of 10^{-3} Pa was maintained by a turbo-molecular pump. A solenoid was constructed from a single wire layer wound around the Perspex tube. The solenoid, is energized by a current pulse of 90 μs half-period, produced by a discharge of a 25 μF capacitor charged to a voltage ranging from 2.5 – 5 kV (total stored energy 78 – 312 J), which produced a magnetic field 0.125 – 0.25 T distributed axially as seen in Fig. 1b.

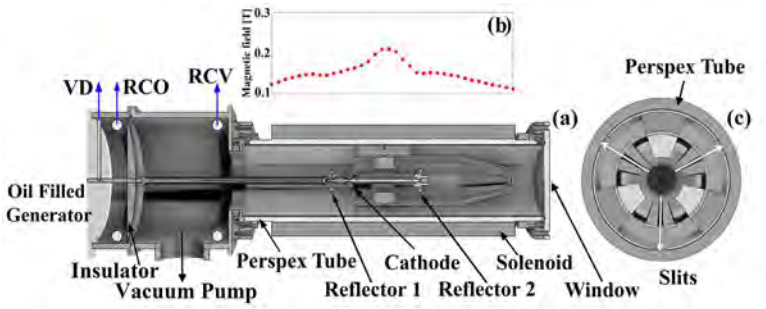


Fig. 1. Longitudinal (a) cross section of the experimental setup and the axial magnetic field distribution (b) for 4 kV charging voltage of the pulsed power supply. Azimuthal cross section at the magnetron center (c).

Waveforms of the voltage and the current measured by the RCV and that of the microwave measured by the D-dot probe for the magnetron fed by either a solid cathode or a split cathode are shown in Fig. 2. The D-dot probe was placed ~16 cm from the cover of the conical anode section which is close to the far-field (≥19 cm). One can that the voltage and current waveforms and amplitudes for both cathode types are similar with slightly larger current and smaller voltage amplitudes for the carbon cathode. With the carbon cathode, the microwave pulse duration is ~90 ns because of pulse shortening, whereas with the split cathode the microwaves generation continues for ~210 ns until the voltage becomes ≤100 kV. The maximum amplitude of the electric field's radial component reaches ~460 kV/m for the solid cathode and ~350 kV/m for the split cathode. For the solid cathode the dominant frequency is 2.15 GHz (λ~14 cm) during ~80 ns [Fig. 2(c)].

The total power of the HPM was calculated by integration of the measured radial distribution of electric field (horizontal and vertical polarization) carried out at a distance of 30 cm from the Perspex output window. These measurements give the total power of 25 MW and the maximal electric field at that the distance of ~250 kV/m. With the carbon cathode, a similar power density distribution was obtained resulting in the total power of ~42 MW.

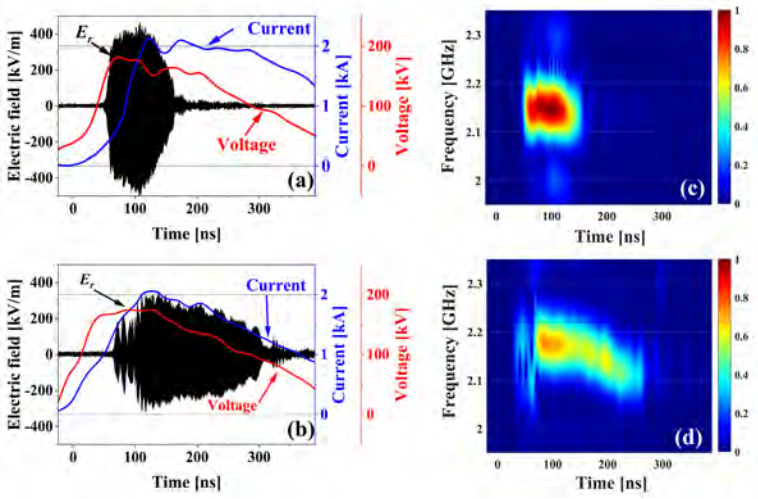


Fig. 2. Typical waveforms of the voltage and current and radial electric field for a solid carbon cathode, B_z = 0.25 T (a) and for a split cathode, B_z = 0.15 T (b). (c) and (d) are the normalized frequency/time contours of the microwave signals (a) and (b) respectively.

This work demonstrated the success of two new ideas, namely, that the split cathode eliminates microwave pulse shortening and a segmented magnetron anode block with axial slits allows fast magnetic field penetration into the interaction region and operates as well as an ordinary magnetron. This increases considerably the total efficiency of the system because the magnetic field power supply requirements are drastically lowered. Such a RM is also suitable for repetitive operation.

We mentioned in the interim report of June 2022 that we wish to study two theoretical issues in an attempt to understand the dynamics of the electron flow in a split cathode fed magnetron and to be able to better control its operation. One, is the connection of the special electron dynamics, that is, the electron cloud trapped inside the potential well consisting the cathode and the reflector, and the connecting rod between the cathode and reflector inside the anode, and what is known as the squeezed state. This was theoretically modeled and analyzed by us and published in Bliokh *et* al., Phys. Plasmas **28**, 072106 (2021). It was shown that a squeezed state can develop when electrons are continuously injected at one or both edges of a longitudinal potential well. The properties of this state of an electron cloud are similar to that of a one-dimensional quasi-neutral plasma where the external electrostatic potential substitutes the role of the ions. Quasi-neutrality of an ordinary, two-component plasma, is replaced by an equilibrium between the confining external potential field and the repulsive Coulomb force of the space-charge. It is important to note that our interpretation of the equilibrium condition allows one to determine the maximum number of charged particles, which can be accumulated in a given potential trap.

The second dynamical issue which we wished to investigate is related to the diocotron instability. The dynamics of the split cathode fed RM is different from that of a solid cathode, not only because of the longitudinal oscillations of the continuously injected accumulated charge but also because the diocotron bunching appears to be different. This is seen in Fig. 3 where the spokes of the π-mode developing for a solid cathode is compared to that appearing when the solid cathode is replaced by a split cathode. The diocotron instability with respect to the electron dynamics in $E\times B$ devices such as the RM has been treated in a vast volume of literature but is out of the scope of the present report. A detailed analysis of the diocotron

mode (the number of azimuthal bunches) development and its connection to the magnetron mode will be discussed in our next report.

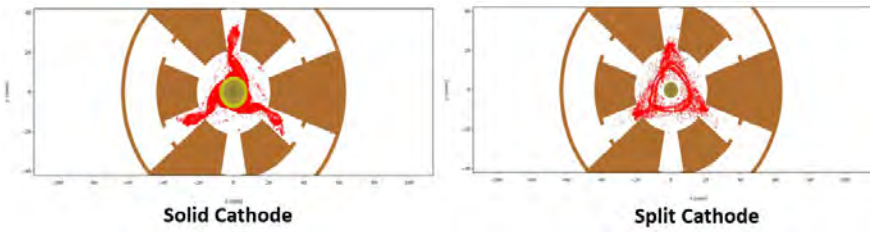


Fig. 3. The spokes of the π-mode developing in a solid cathode fed magnetron (left panel) and the same mode around the non-emitting rod of a split cathode (right panel).

During the period of the present report we have though carried out experiments seeking the diocotron instability in the longitudinally oscillating and azimuthally expanding electron plasma forming inside a split cathode.

Experiments were carried out using the setup sketched in Fig. 4. The experiment was performed in a 124 mm diameter long stainless-steel tube at the center of which a 40 mm diameter, 62 mm long stainless-steel hollow anode was placed. An axial magnetic field, of up to 1.2 T and half-period of 15 ms was produced by a solenoid. The high voltage pulse (~200 kV, ~250 ns) was applied to the same split cathode as that used for the magnetron experiments. The distance between the reflector and the anode downstream edge was 40 mm. The diocotron instability should appear as a rotating periodic azimuthal modulation of the electron density. These modulations were measured by two probes inserted through holes drilled at the longitudinal center of the anode and separated from each other by 180^0.

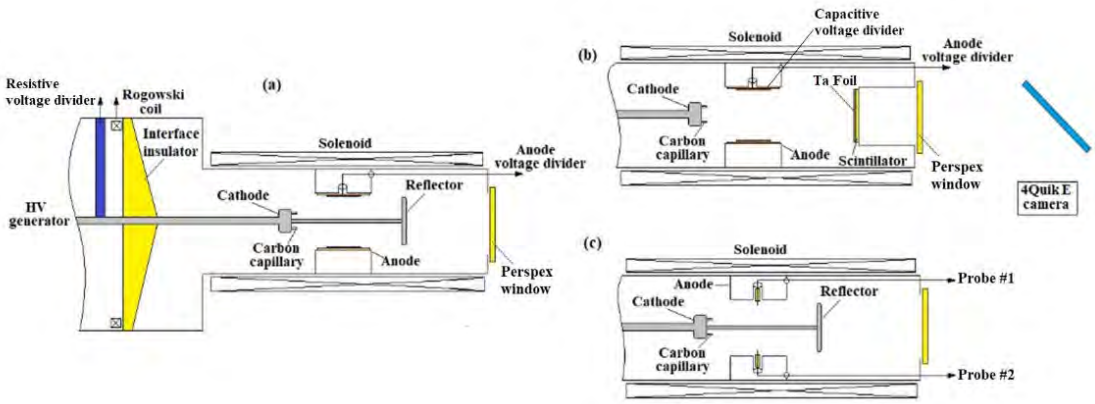


Fig. 4**.** The experimental setup for (a) a wire grid reflector, (b) to record the beam in the absence of the reflector and rod and (c) with the probes #1 and #2.

The temporal and spatially resolved transverse distribution of the electron-beam current density was obtained by fast x-ray imaging of the beam. The images were obtained at a distance of 100 mm from the anode where a 2 mm thick fast EJ-200 scintillator was placed, attached to the back of a grounded 80 μm-thick Ta foil. The interaction of these x-rays with the scintillator produces an image recorded using a 4QuikE camera (of 1.2 ns frame duration). X-ray images were obtained only in the absence of the reflector and registered at different times relative to the onset of the voltage as seen in Fig. 5. Similar images were obtained for other magnetic field values as well, independent of whether the rod was present or absent.

One can see that the electron beam pattern is not azimuthally uniform and bunching is discernible, typical for a diocotron instability.

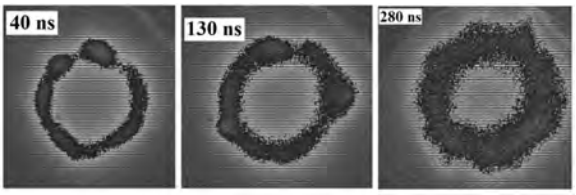


Fig. 5. Framing images of the luminescence pattern appearing on the plastic scintillator due to the interaction of the electron beam with a 127-μm-thick Ta foil placed in front of the scintillator. Frame duration 1.2 ns, magnetic field 8 kG.

The existence of the diocotron instability in a split cathode geometry is confirmed by the high frequency oscillations observed on the probe signals shown, for example, in Fig. 6. Experiments with probes #1 and #2 were carried out in three configurations: (a) the split cathode; (b) no reflector and rod; and (c) no reflector but rod present. In all these cases, high frequency oscillations were observed in the probe signals.

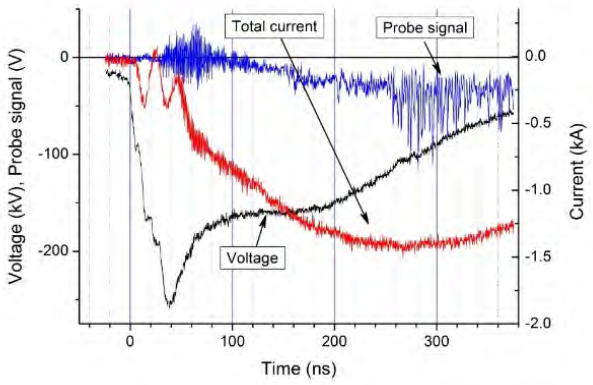


Fig. 6. The probe signal, voltage, and current waveforms. Split cathode configuration, magnetic field 8 kG.

The oscillating component of the probe signals was separated from the slowly varying and a wavelet analysis of the normalized filtered signals was performed. The resulting spectrograms of two probe signals (see Fig. 7) show a sharp change in the spectra in the time interval 275 – 300 ns. The resulting correlation functions between the signals from two probes in thee intervals [see Fig. 7 (a)] show that the oscillating signals are in-phase in the time domain 220 ns < t < 270 ns, and out of phase in the time domain 275ns< t <300ns. The latter is explained by the fast transformation of the azimuthally rotating azimuthal bunches of electrons from even to odd number.

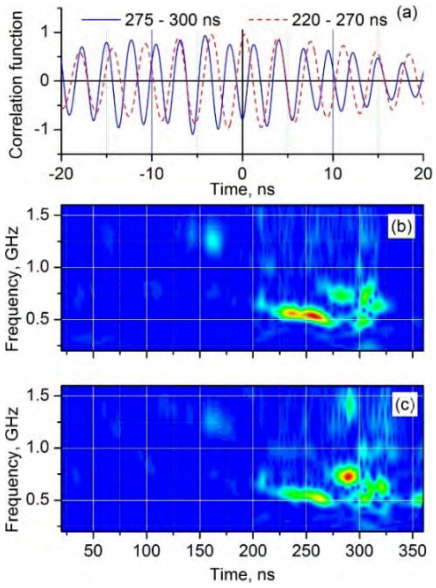


Fig. 7. (a) Correlation functions of the signals within the time intervals 275-300 ns and 220-270 ns; (b) and (c) Time dependent spectrograms of the signals registered by the two probes.

Periodic probe signals appear as the result of rotating electron density modulation produced by the diocotron instability. The rotation frequency of the density modulation is defined by the drift velocity $v_d = cE/H$ in the crossed radial electric, E, and axial magnetic, H, fields. In order to support this hypothesis, we superimpose a spectrogram and an appropriately scaled voltage waveform as shown in Fig. 8(left) and one can see that the time dependence of the voltage waveform coincidences with the variation in the spectrum over a long period of time. This indicates that the diocotron instability can indeed be responsible for the observed oscillating signal behavior. Calculation of the rotation frequency, f(r) = ω(r)/2π, was performed using our model described in Phys. Plasmas 29, 123901 (2022). The frequency jump occurs when the voltage is ~75 kV and the corresponding electron density of the squeezed state at this moment is ~6.9×10^{10} cm-3. The calculated dependence f(r) for these values of the voltage and the electron density for the experimental system dimensions is shown in Fig. 8(c). The calculated frequency value agrees with the defined experimentally difference $\Delta f = 0.25$ GHz between frequencies, shown in Fig. 8(a). The minor frequency from the considered is nearly twice as large as the rotation frequency, while the higher frequency is approximately three times larger. It means, that the lower frequency corresponds to the electron cloud configuration with two (even!) azimuthal bunches, the higher frequency corresponds to configuration with three (odd!) bunches. The latter agrees with the result of correlation analysis, presented in Fig.7(a).

This work [Bliokh *et* al., Phys. Plasmas **29**, 123901 (2022)] confirms the appearance of the diocotron instability in a split cathode fed coaxial diode. We expect that for a corresponding magnetron, the diocotron instability and the magnetron eigenmodes could act simultaneously and influence each other.

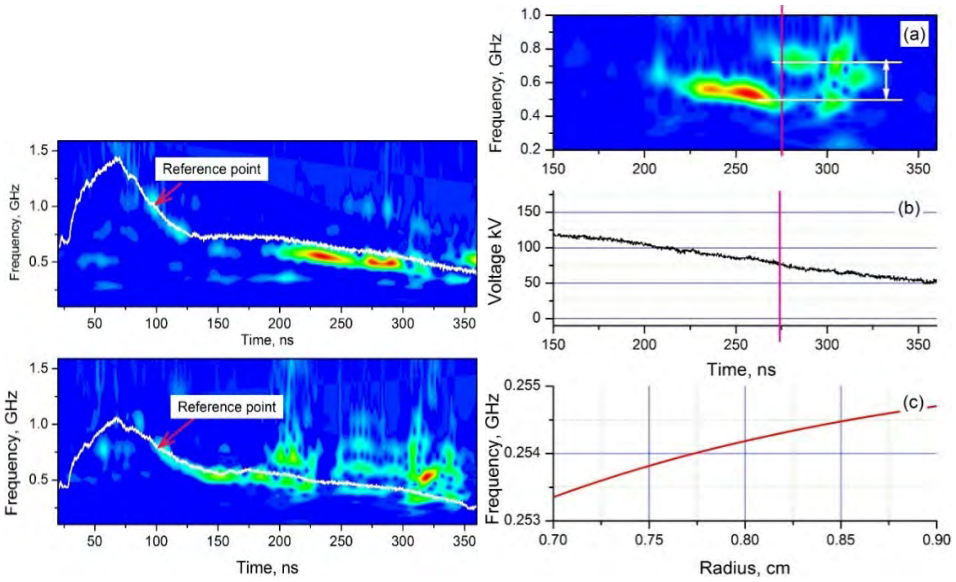


Fig. 8. (left)Two different spectrograms and the corresponding scaled voltages. The voltage waveforms $U(t)$ are scaled so that they coincide with the dominant frequency at some point marked as the reference point. (right) Experimental determination of the rotation frequency of the bunches. (a) Spectrogram. Vertical red line marks the point in time when the frequency jump occurs. The horizontal white lines mark the values of the frequencies. (b) The voltage waveform. Vertical red line marks the voltage value at the time the frequency jump occurs. (c) The rotation frequency, calculated using the theoretical model, described in Phys. Plasmas **29**, 123901 (2022).

3. Findings and Conclusions

- We have demonstrated the success of two new ideas, namely that the split cathode eliminates microwave pulse shortening and a segmented magnetron anode block with axial slits allows fast magnetic field penetration into the interaction region, and operates as well as an ordinary magnetron. This increases considerably the total efficiency of the system because the magnetic field power supply requirements are drastically lowered. Such a RM is also suitable for repetitive operation.
- We also demonstrated by experiments and theoretical modeling the importance of the diocotron instability in a system with split cathode. This can affect the parameter choices for optimal performance.

4. Plans and Upcoming Events

Significant future experiments:

- Operating the segmented anode, split cathode fed, axial output magnetron in repetitive mode.

Significant milestones:

- Analytical and numerical effort to gain more understanding of the electron dynamics

Upcoming significant events:

- Plenary talk at the ICOPS 2023 conference, Santa Fe, NM. The split cathode fed RM will be one chapter of this talk.

5. Transitions and Impacts

NA

6. Collaborations

Prof. Edl Schamiloglu, University New Mexico, New Mexico, USA.

7. Personnel

Key Personnel:
Principal investigator: Yakov Krasik (fnkrasik@physics.technion.ac.il; +972-545509951), 1.8 Person Months, National Academy Member – No, Israel

Team Members:
Dr. John Leopold (leopoldjg@technion.ac.il)
Dr. Yurii Bliokh (bliokh@physics.technion.ac.il)
Engineer Yevgene Flyat (flyat@technion.ac.il)
Engineer Svetlana Gleizer (sgleizer@technion.ac.il)

8. Students

PhD student Yang Cao
PhD student Meital Siman Tov

9. Technology Transfer

We have no technology to transfer. All the results of our research were summarized in our published papers. Prof. Edl Schalomiglu, University New Mexico is responsible for any technology transfer to the NAVY relevant person.

10. Products, Publications, Patents, License Agreements, etc.

1. **Title:** An advanced relativistic magnetron operating with a split cathode and separated anode segments
   Journal: Journal of Applied Physics
   Authors: Yakov E. Krasik, John G. Leopold, Yoav Hadas, Yang Cao, Svetlana Gleizer, Eugene Flyat, Yurii P. Bliokh, Dmitrii Andreev, Andrey Kuskov, and Edl Schamiloglu,
   Keywords: microwave, high power, relativistic magnetron, plasma
   Distribution Statement: no restriction, public domain
   Publication Status: Published Online: 11 January 2022, Journal of Applied Physics **131**, 023301 (2022). https://doi.org/10.1063/5.0080421
   Acknowledgement of Federal Support? Yes
   Peer Reviewed? Yes

2. **Title:** “Observation of the diocotron instability in a diode with split cathode
   Journal: Physics of Plasmas
   Authors: Yurii P. Bliokh, Yakov E. Krasik, John G. Leopold, Edl Schamiloglu,
   Keywords: diocotron instability, electron beam, relativistic magnetron, plasma
   Distribution Statement: no restriction, public domain
   Publication Status: Published Online: 06 December 2022, Physics of Plasmas **29**, 123901 (2022). https://doi.org/10.1063/5.0080421
   Acknowledgement of Federal Support? Yes
   Peer Reviewed? Yes

Conference Papers

We have participated with oral presentations of our results related to a split cathode segmented relativistic magnetron in two international conferences:

a. PPC SOFE 2021, December 12-16, Denver, CO USA
b. ICOPS 2022, May 22-26, Seattle, Washington USA

11. Point of Contact in Navy

Charles R. “Chip” Eddy, Jr.
Science Director - Power & Energy, Materials
Office of Naval Research Global - London

ONR FY22 Grant and Contract Summaries

ONR FY22 Grant Summaries

Grant or Contract Number: N00014-17-1-2702
Date Prepared: 4/28/2023
Project Title: Novel High-Power Microwave System Designs Using Nonlinear Transmission Lines
Annual Summary Report: FY22
Period of Performance: 15 Apr 2018 to 31 Dec 2021
Principle Investigator: Allen L. Garner, algarner@purdue.edu ,
Purdue University, 516 Northwestern Ave. West Lafayette, IN 47906

Nonlinear transmission lines (NLTLs) are of great interest to the Navy for solid state high repetition rate directed energy systems. This grant has investigated the suitability of novel composite materials for NLTLs in a high-power microwave (HPM) source. Since understanding the current state of NLTL research will guide potential areas of improvement, we first performed an extensive review of current NLTL technology and topologies and published a review paper in IEEE Access, which has already been cited 32 times. In parallel with that effort, we developed techniques for designing and constructing composites containing various volume loadings of barium strontium titanate (BST) and/or nickel zinc ferrite (NZF), which exhibit nonlinear permittivity and permeability, respectively, and examined their linear and nonlinear electrical and
magnetic properties. We first measured the linear permittivity and permeability of BST, NZF, and BST/NZF composites as functions of volume loading and frequency and the linear permeability. We observed notable increases in permeability for NZF composites about 15% volume loading and for BST/NZF composites containing above 10% NZF. We also developed effective medium theories (EMTs) and finite element simulations using CST Microwave Studios to compare with experimental composite measurements from 1 to 4 GHz. We then further tested the resulting NLTLs using a Blumlein generator, an inductive adder, and then with the NLTLs acting simultaneously as a pulse forming line and high-power microwave source. These efforts provide the potential for developing compact NLTL systems for generating RF for multiple applications, including biomedical applications or those that may require man-portable (or nearly so) systems.

Grant or Contract Number: N00014-19-1-2262
Date Prepared: 7/24/2022
Project Title: Theory and Experiments on Magnetically Insulated Line Oscillator (MILO)
Annual Summary Report: FY22
Period of Performance: 15 Apr 2018 to 31 Dec 2021
Principle Investigator: Ronald Gilgenbach, rongilg@umich.edu,
University of Michigan, Ann Arbor, MI 48109-2014

We have produced a broad theory of the flow of crossed field devices, which applies to several geometries of interest. Using this theory, the Buneman-Hartree condition for the coaxial MILO geometry has been derived from Brillouin flow theory for the first time. In addition, the Brillouin flow profiles produced have yielded important analytic results that were very useful in the design of the L-band, S-band, and Harmonic MILOs. Through this theory and our experiments, we found that MILOs differ markedly from magnetrons in that they operate much closer to the Hull cutoff than to the Buneman-Hartree condition. Additionally, this theory predicted the unexpected result that MILOs can operate below the Hull cutoff current, in a “double-valued” region of the magnetic flux ratio where the total current decreases as the insulation increases. This was also

observed in particle-in-cell simulations in CST Particle Studio. This theory was used to design an L-band MILO capable of operation at moderate current and voltage (~10 kA, ~250 kV), and was corroborated by simulations in ICEPIC and CST Particle Studio. It was also used to interpret MILO experiments performed elsewhere, at the Air Force Research Laboratory, in the UK, France, and China.

We have designed, simulated, fabricated, tested, and interpreted the high-impedance L-band MILO. In experiments with a 240-kV, 10-kA generator, the 1 GHz MILO operated at 25-30 Ohms and produced up to 25 MW at 1.017 GHz. This device marks the first demonstration of a MILO at less than 10 kA of total current. An S-band MILO was demonstrated at 2.082 GHz, producing over 1 MW and exploring a variety of cathode materials and geometries. Building upon this work, we demonstrated a dual-band Harmonic MILO, producing 3.2 +/- 0.8 MW at 2.075 GHz and 13 ± 3.9 MW at 0.985 GHz.

Grant or Contract Number: N00014-18-1-2384
Date Prepared: 7/15/2022
Project Title: A High Repetition Rate, Long Lifetime Magnetically Insulated Line Oscillator (MILO)
Annual Summary Report: FY22
Period of Performance: 15 Apr 2018 to 31 Dec 2021
Principle Investigator: John Mankowski, john.mankowski@ttu.edu,
Texas Tech University (TTU), Lubbock, TX 79409.

The design, simulation, implementation, and testing of a 1 GW class, S-band, Magnetically Insulated Line Oscillator (MILO) capable of high repetition rates. were presented. The simulation work confirmed that the design could produce an output signal greater than a Giga-Watt peak power with over 10% efficiency. A test bed was then constructed with a compact Marx generator as the pulsed power source capable of 800 kV open-circuit voltage pulse. Testing the MILO revealed issues with the original ceramic feedthrough not being capable of holding off the input voltage. The gathered data with the original feedthrough did confirm that the MILO produced an output within the S-Band with a narrow bandwidth. After altering the design to improve the voltage hold-off, new issues arose as the output frequency of the MILO dropped by nearly 1 GHz with a 1 GHz bandwidth. This may indicate that the SWS has become over-moded with a non-axial symmetric plasma formation. Plans for future testing involve changing the test bed to one with a pulse forming line, which will shape the input pulse into the MILO. A low-cost process to fabricate carbon fiber velvet cathodes was presented, along-side computer simulation and experimental data to characterize the effectiveness of the cathodes as electron beam emitters for HPM devices. This research shows that the methods used to create the carbon fiber velvet on a wooden mechanical loom are viable to produce cathodes for high-power microwave devices at a fraction of the cost of commercially available options. The shot-to-shot variance of the custom velvets was also less than the commercial option, resulting in consistent pulses which is important for HPM devices.

Grant or Contract Number: N00014-22-1-2483
Date Prepared: 4/24/2023
Project Title: New Anode Materials for High Lethality HPM Sources
Annual Summary Report: [FY22]
Period of Performance: 1 June 2022 to 30 April 2025
Principle Investigator: Ravi P Joshi, Email: ravi.joshi@ttu.edu
Texas Tech University, Lubbock, TX 79409.

This proposal is a three year period project to carry out fundamental research directly tied to the advancement of effective high lethality HPM sources. It involves developing anode materials that reduce the number of adsorbates on the surface which can limit both the repetition rate of HPM sources and the pulse length. It is not known a priori if long pulse or high repetition sources will have a greater effect on the target – this needs to be tested. What is known is that electromagnetic energy is required to affect a target, and designing electrodes with lower adsorbate load will increase the energy and hence, very likely, the lethality of HPM sources. This work is multipronged and has at its heart a novel idea, for which we will apply for a patent on reducing the adsorbate load content. In one part of this collaborative research project, the nature, ionization level of these neutrals will be determined by careful experimental measurements of the adsorbate load on cathode and anode materials on UNMs LTD test bed by utilizing time and spatially resolved diagnostics. A second parallel part will involve Molecular Dynamics (MD), Monte Carlo and first principle atomic physics Density Functional Theory (DFT) simulations on the likely hydrogen and other adsorbate content on these materials and how these will be reduced. Reduction techniques could include shock loading of the first few monolayers of the material, or laser surface cleaning. This parallel paired collaborative proposal is between Dr. Salvador Portillo at the University of New Mexico (UNM) and Dr. Ravi Joshi at Texas Tech University (TTU). UNM will lead the experimental effort, and TTU will lead the material numerical simulations for quantitative predictions, experimental validation and optimization. The efforts and achievements at TTU to date have been to set up and successfully apply simulation capability for the following tasks: (a) determination of thermal profiles within anode targets subject to electron-beam or laser excitation, (b) calculations of binding energies of some select carbon or oxygen-based adsorbates based on DFT, (c) successful modeling of outgassing of hydrogen at different temperatures, and (d) MD based laser-driven surface desorption and/or dissociation of adsorbates towards surface cleaning.

Grant or Contract Number: N00014-22-1-2490
Date Prepared: 4/24/2023
Project Title: An Accessible platform for simultaneous Macro, Meso and Microscopic Measurements of Polymeric Materials at High Loading Rates and Temperatures
Annual Summary Report: FY22
Period of Performance: 1 July 2022 to 30 June 2025
Principle Investigator: Sal Portillo, Email: sportil@unm.edu
University of New Mexico, Albuquerque, NM 87131-0001

This proposal is a three year period project to carry out fundamental research directly tied to the advancement of effective high lethality HPM sources. It involves developing anode materials that reduce the number of adsorbates on the surface which can limit both the repetition rate of HPM sources and the pulse length. It is not known a priori if long pulse or high repetition sources will have a greater effect on the target – this needs to be tested. What is known is that electromagnetic energy is required to affect a target, and designing electrodes with lower adsorbate load will increase the energy and hence, very likely, the lethality of HPM sources. This work is multipronged and has at its heart a novel idea, for which we will apply for a patent on reducing the adsorbate

load content. In one part of this collaborative research project, the nature, ionization level of these neutrals will be determined by careful experimental measurements of the adsorbate load on cathode and anode materials on UNMs LTD test bed by utilizing time and spatially resolved diagnostics. Specifically, UNM will employ a time resolved Mach Zehnder interferometer utilizing a CW 532 nm laser, with one half of the beam passing through the AK gap of our anode experiments. The resultant combination of this arm with the reference beam will be captured with a high speed framing camera yielding results in the nano second regime. This set up will be adjusted to a Moire interferometric set up to yield additional imaging. Similarly, the time resolved spectroscopic measurements from a spatially resolved fiber array are captured by a pico/nano second streak camera coupled to a high resolution triple grating spectrometer. X-ray diagnostics will measure the X-ray production and energy deposition on the anode -these include time resolved radiation detectors and time resolved imaging plates. Three additional diagnostics will be developed to aid in the measurement of plasma evolution in the AK gap of our test bed as well as in a yet to be designed high frequency MILO. These are a time resolved Photon Doppler Velocimetry based on a 1550 CW laser and a small shifted laser, a Thomson scattering system based on a Nano second 1 joule slm laser and finally a faraday rotation instrument to measure the fields inside the charged particle beam. Laser peening and treatment of surfaces will be based on a 900nm CW energy variable laser scanned over the surface of the material.

A second parallel part will involve Molecular Dynamics (MD), Monte Carlo and first principle atomic physics Density Functional Theory (DFT) simulations on the likely hydrogen content on these materials and how these will be reduced via shock loading of the first few monolayers of the material. This parallel paired collaborative proposal is between Dr. Salvador Portillo at the University of New Mexico (UNM) and Dr. Ravi Joshi at Texas Tech University (TTU). UNM will lead the experimental effort, and TTU will lead the material numerical simulations for quantitative predictions, experimental validation and optimization.

ONR FY22 Industry Grant Summary

Grant or Contract Number: N00014-22-1-2694
Date Prepared: April 25, 2023
Project Title: Implementation of Tunable Dielectric and Multiferroic Materials For High Power Microwave Applications
Annual Summary Report: FY22
Period of Performance: 1 August 2022 to 31 Jan 2024
Principle Investigator: Somnath Sengupta,
somnath@powerhouseconsultinggroup.com; Small Business

Based on our Phase II work, Powerhouse proposes to evaluate tunable delay lines fabricated from tunable dielectric materials and tunable multiferroic materials on application specific systems. The two tasks focus on the development of tunable delay lines for NRL and NSWCDD. The metrics goals are to demonstrate a 100% bandwidth tunable group delay device that will offer a maximum of 50 ps of group delay over a 2 GHz bandwidth at high RF incident powers in the 20 kW - 200 kW (instantaneous peak power) range. For the multiferroic materials, the goal of this effort is to provide experimental data for evaluation against design criteria by current DoN S&T development efforts. In addition to the power level measurements, the relevant magneto-dielectric properties of the materials including the P vs E, B vs H, dE/dH, dB/dE values, and saturation magnetization of the materials, all at relevant voltage (50 to 100 kV) and current levels (100s of amps) used in HPM systems will be measured. The proposal is for a PoP of 18 months.

ONR FY22 Industry Contract Summaries

Contract Number: N00014-19-C-1008
Project Title: Active/Passive Limiters for High Power Radio Frequency (HPRF)
Contract Period of Performance: 23 Jan. 2019 – 22 Jan. 2023
Principle Investigator: Dr. Sameer Hemmady, sameer.hemmady@verusresearch.net
Organization: Verus Research, Albuquerque, NM

Project Summary
In this body of research, Verus studied physical mechanisms for High Power Radio-Frequency induced nonlinear responses of front-end components typically found in RF receivers. Verus categorized the physical mechanisms from the small-signal linear regime of operation to the large signal nonlinear regime which comprises a continuum of states spanning non-persistent effects and persistent effects (which includes degradation and eventual damage). Similar responses were characterized for other RF front-end components, such as mixers and analog-to-digital convertors (ADCs). This body of research is anticipated to benefit the Navy's High Power Electronic Warfare (HPEW) applications and missions by way of developing prescriptions for more effective HPRF waveforms against RF receivers of interest.

Contract Number: N00014-20-C-1083
Project Title: Leveraging Predictive Effects for Devising Collaborative HPRF/Cyber Engagement Paradigms
Contract Period of Performance: 9 June 2020 – 8 June 2023
Principal Investigator: Dr. Sameer Hemmady, sameer.hemmady@verusresearch.net
Organization: Verus Research, Albuquerque, NM

Project Summary
The focus of this research effort is to leverage recent advancements in predictive effects research for devising collaborative High Power Radio Frequency (HPRF)/Cyber engagement paradigms for complex electronic targets of interest. In the current base effort, Verus Research has focused on performing experiments that establish how software pre-conditioning of an electronic asset can demonstrably alter its HPRF susceptibility, as quantified through its empirically generated Probability of Effects (Pe) curves. In the current Option, Verus Research has utilized predictive effects to devise agile attack waveforms. This has direct implications to mission-level concept of operations (CONOPS) for HPRF platforms in terms of extending its range to effect or alternatively increase its ability to penetrate and affect electronic assets housed deeper inside targeted infrastructure facilities.

SBIR/STTR Summaries

SBIR/STTR Summaries

Grant or Contract Number: N68335-19-C-0255, SBIR Phase II
Project Title: Miniaturization of High Average Power, High Peak Power, Wide Bandwidth Antennas and DSRDs
Period of Performance: 3 Jul 2019 to 22 Jun 2023
Principle Investigator: Michael Abdalla, mda@asrcorporation.com
Organization: ASR Corporation

Project Summary
The ultimate goal of the Phase II effort is to build drift step recovery diodes (DSRDs) that can meet specific requirements of interest to pulsed-power source developers and the development of an appropriate antenna for use with a DSRD based pulsed-power source. During the Phase II base effort, the team has made significant progress toward these goals. The ESA antenna effort has resulted in the development of a true ESA array and a moderate bandwidth array. DSRDs were fabricated with a graded-epitaxy growth method for the first time. Further development of the DSRD and the antenna in Option II is discussed below.

The overall problem addressed here is one of dopant and heterostructure optimization of tried-and-true silicon DSRDs, with decreased rise time and increased reverse current density ratings from junction structures and packaging that enables higher current and lower internal impedance operation. Silicon is the material of choice, as it provides a sustainable commercial path and can perform at the required performance metrics. New DSRD fabrication process flows have been developed and implemented, with focus on leveraging gas-phase epitaxy, as well as traditional diffused-junction diode manufacturing. New wet processing methods for beveling and passivating DSRDs have been developed to address the voltage-holding reliability, improved pulse lifetime, and die-to-die consistency issues seen in prior work. Potential advantages of the new DSRD process flow over traditional methods have been analyzed and described in two patent applications and three presentations at conferences. Pulsed power from DSRD circuits designed by the Missouri Institute for Defense & Energy has been demonstrated.

The primary area of research focus in Phase II Base was to investigate strategies to incorporate focusing into the antennas to reduce overall volume. True electrically small antennas (ESA) have been considered. Due to bandwidth limitations for true ESA designs, alternate compact antennas have been considered.

The ESA work will thus be transitioned to bi-conical resonators or comparable ultra-wide-band and high-power radiating structures. In the Phase II Option I, these radiating structures shall include TEM horns, bi-cones, quarter-wave oscillators and continued advances in high efficiency wideband resonant radiators. These antennas will be larger with higher radiating efficiency. As the DSRD pulse generator parameters become clearer, the antenna design will be finalized.

Grant or Contract Number: N68335-21-C-0435, SBIR Phase II
Project Title: Solid-state, Sub-nanosecond Pulse Sharpener for Generating High Power Impulses
Period of Performance: 27 July 2021 to 31 July 2023
Principle Investigator: Dr. Jason Sanders, jason@transientplasmasystems.com
Organization: Transient Plasma Systems, Inc.

Project Summary
The Office of Naval Research issued this SBIR topic to fund the development of a solid-state closing switch capable of producing high power ultra-wideband (UWB) electrical pulses. This proposed effort will investigate Semiconductor Avalanche Shaping (SAS) device structures for both Si and SiC, with Si being viewed as the conservative approach for achieving the threshold specifications of this topic. SiC material properties suggest it is likely well suited for impact-ionization avalanche switching inherent to SAS, which does not rely on long minority carrier lifetime for practical implementation in the same way that other wideband opening switches, such as Drift Step Recovery Diodes (DSRDs), do. The significantly shorter intrinsic region that can be achieved with a SiC SAS-type device is expected to result in higher dV/dt capability compared to Si due to shorter transit distance through the device and reduced effective resistance. Devices have been designed and simulated during Phase I. In Phase II solid-state devices capable of switching kW-MW power pulses with risetimes faster than 300 ps at high pulse repetition rate are in development. Si parts are currently being fabricated at Transient Plasma Systems, and they are expected to provide the near-term capability required by ONR and NRL. Research into edge termination techniques and packaging continues for SiC SAS parts in partnership with GE Global Research, who is subcontracting for this effort. During the Phase II Base effort, TPS will manufacture high TRL SAS and work with GE to fabricate an initial run of experimental SiC SAS. Follow-on Phase II Option funding will assist in further maturation of the Si design so that parts can be provided to potential DOD customers, as well as additional development of a next generation SiC based SAS. These devices will add to the United States' high power UWB technology portfolio and enable compact, reliable UWB directed energy systems with advanced capabilities.

Grant or Contract Number: N68335-23-C-0010, SBIR Phase II
Project Title: Improved Marx Pulse Generator for HPM Systems
Period of Performance: 20 Oct 2021 to 03 Mar 2025
Principle Investigator: Sam Dickerson, sdickerson@sara.com
Organization: Scientific Applications & Research Associates, Inc.

Project Summary
SARA intends to help usher in a new generation of US sourced high-power microwave (HPM) systems by developing an innovative, solid-state, semiconductor opening switch (SOS) based pulse generator. The pulse generator is made up of an SOS driver and the opening switch itself. The driver system is intended to adequately pump the opening switch diodes allowing generation of very high peak power, fast risetime pulses. The driver system consists of a solid-state Marx generator, saturating transformer, and pumping capacitor. The solid-state Marx generator serves as the primary energy store for the system and is switched by state-of-the-art high voltage silicon carbide (SiC) MOSFETs. The improved switching characteristics of SiC devices allow SOS arrays to be adequately pumped by only a single magnetic switching component, the saturating transformer. The Phase II base effort (presently underway) will fabricate, assemble, characterize and demonstrate a scaled version of the SOS driver. In addition, the design for a full-scale gigawatt (GW) class SOS based pulse generator will be crafted. A Phase II Option effort will use recently developed US sourced SOS diodes to assemble and demonstrate a solid-state, GW class SOS based pulse

generator capable of pulses in excess of 300 kV with sub 10 ns risetimes at pulse repetition rates in excess of 300 Hz.

Grant or Contract Number: N68335-21-C-0062, SBIR Phase II
Project Title: Drift Step Recovery Diode (DSRD) for Wideband (WB) and Ultra-Wideband (UWB) Pulse Generation
Period of Performance: 8 Oct 2020 to 31 Oct 2022
Principal Investigator: Ranbir Singh, ranbir.singh@genesicsemi.com
Organization: GeneSiC Semiconductor Inc.

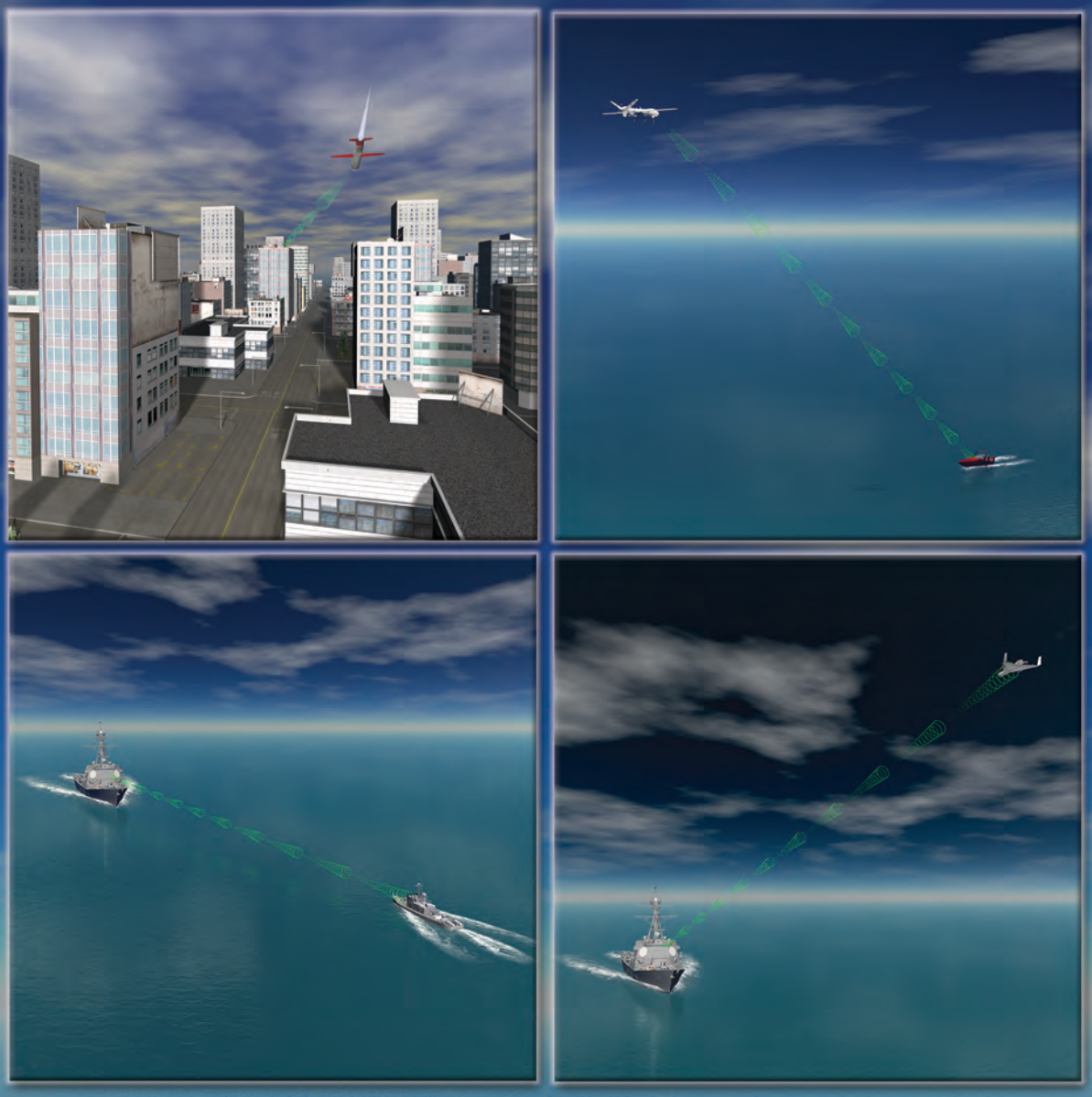
Project Summary
Drift step recovery diodes (DSRDs) are the fastest semiconductor opening switches reported to-date and are a critical enabling technology for realizing ultra-wide band (UWB) high-power microwave sources which are of great interest for US Navy applications. The main goal of this two-Phase SBIR project is to develop silicon carbide drift step recovery diodes as a reliable and qualified product for insertion into the next-generation ultra-wide band, high-power microwave sources. Capitalizing on the superior intrinsic advantages of the semiconductor material silicon carbide (SiC) over silicon, this project will develop ultra-high speed SiC based DSRDs with single-chip ratings of > 2 kV and ≥ 100 A, with significantly faster switching capability. This will reduce the number of series-connected devices necessary to realize ultra-high voltage 20-50 kV pulse generators with sub-nanosecond switching capability.

Grant or Contract Number: N68335-22-C-0642, SBIR Phase II
Project Title: Next-Gen Solid-State Power Module for High Power Microwave Drivers
Period of Performance: 29 Aug 2022 to 29 Aug 2024
Principle Investigator: Landon Collier, lcollier@sara.com
Organization: Scientific Applications & Research Assoc., Inc.

Project Summary
High power microwave (HPM) sources have conventionally been driven by gas-switched pulsed power generators due to high voltage, high current, and fast rise-time requirements. However, these traditional technologies impose significant limitations on advancements in HPM technology due to low repetition rate, short lifetime, limited waveshaping capabilities, and difficulty of synchronization. Recent advancements in solid state device technology, including wide bandgap semiconductors such as silicon carbide (SiC), have opened the door for development of a next generation of pulsed power drivers capable of overcoming these limitations, with rep-rates in the 10's to 100's of kHz, million-shot lifetime, arbitrary waveform capability, and sub-ns jitter. Further, optimization of solid-state device characteristics and packaging techniques tailored towards pulsed power application can result in smaller, lighter, and more efficient systems than can currently be achieved with commercially available devices. A solid-state alternative to traditional HPM drivers was developed during Phase I leveraging SARA's ability to evaluate, test, and package state-of-the-art (SotA) silicon carbide die into large pulsed power systems. Further, characterization of SotA semiconductor devices demonstrated exceptional rise time performance and peak current handling capabilities. Building upon this initial development effort, the modulator design is undergoing refinement in preparation for experimental demonstration during Phase II.

Contract Number: N68335-19-C-0445, SBIR Phase II
Project Title: Navy-Electronic Battle Damage Indicator (eBDI) Tool for Non-Kinetic High-Power Radio-Frequency (RF) Engagements
Period of Performance: 29 Aug 2019 to 30 April 2024
Principal Investigator: Donald Voss, donv@vosssci.com
Organization: Voss Scientific, LLC

Project Summary
A critical need exists for a compact and reliable electronic Battle Damage Indicator (eBDI) tool for use in a directed energy (DE) battlefield in which High Power Radio Frequency (HPRF) devices are employed. In the Phase I effort, Voss Scientific demonstrated the feasibility of building an Autonomous Damage Assessment Module (ADAM) capable of meeting the Navy electronic Battle Damage Indicator (eBDI) requirements by utilizing a man- or UAV-portable electronics package with multiple methods of emplacement, both covert and overt. In the Phase II work, the ADAM Gen-I system was assembled and tested in the laboratory to verify it could successfully meet all performance requirements regarding temperature, RF measurement, and communication. Subsequent field testing in two live HPM experiments demonstrated ADAM's ability to withstand and characterize the HPM attack, detect battle damage, detect target recovery, and identify targets affected. With these successful field tests in both damp, winter environments and hot desert conditions, the ADAM Gen-I system has demonstrably reached the TRL-7 level of development.



Office of Naval Research
875 N. Randolph Street
Arlington, VA 22203-1995
www.onr.navy.mil